Ministry of Science and Higher Education of the Russian Federation
ITMO University

ISSN 2220-8054

NANOSYSTEMS:
PHYSICS, CHEMISTRY, MATHEMATICS

2026, volume 17 (2)

Наносистемы: физика, химия, математика

2026, том 17, № 2

NANOSYSTEMS:
PHYSICS, CHEMISTRY, MATHEMATICS

ADVISORY BOARD MEMBERS

Chairman: V.N. Vasiliev *(St. Petersburg, Russia)*,
V.M. Buznik *(Moscow, Russia)*; V.M. Ievlev *(Voronezh, Russia)*, P.S. Kop'ev*(St. Petersburg, Russia)*, V.N. Parmon *(Novosibirsk, Russia)*, A.I. Rusanov *(St. Petersburg, Russia)*,

EDITORIAL BOARD

Editor-in-Chief: I.Yu. Popov *(St. Petersburg, Russia)*

Section Co-Editors:
Physics – V.M. Uzdin *(St. Petersburg, Russia)*,
Material science – V.V. Gusarov *(St. Petersburg, Russia);* O.V. Al'myasheva *(St. Petersburg, Russia)*;
Chemistry – V.K. Ivanov *(Moscow, Russia)*,
Mathematics – I.Yu. Popov *(St. Petersburg, Russia).*

Editorial Board Members:
A.P. Alodjants *(St. Petersburg, Russia)*; S. Bechta *(Stockholm, Sweden)*; J. Behrndt *(Graz, Austria)*; A. Chatterjee (*Hyderabad, India)*; A.V. Chizhov *(Dubna, Russia)*; A.N. Enyashin *(Ekaterinburg, Russia)*, E.A. Gudilin *(Moscow, Russia)*; A.R. Kaul *(Moscow, Russia)*; Yu.S. Kivshar *(Canberra, Australia)*; S.A. Kozlov *(St. Petersburg, Russia)*; P.A. Kurasov *(Stockholm, Sweden)*; A.V. Lukashin *(Moscow, Russia)*; G.P. Miroshnichenko *(St. Petersburg, Russia)*; I.Ya. Mittova *(Voronezh, Russia)*; H. Najar *(Monastir, Tunisia),* Nguyen Anh Tien *(Ho Chi Minh, Vietnam)*; V.V. Pankov *(Minsk, Belarus)*; K. Pankrashkin *(Oldenburg, Germany)*; V. Rajendran *(Tamil Nadu, India)*; A.A. Rempel *(Ekaterinburg, Russia)*; A.A. Rogachev *(Minsk, Belarus)*; V.Ya. Rudyak *(Novosibirsk, Russia)*; H.M. Sedighi (*Ahvaz, Iran*); D Shoikhet *(Karmiel, Israel)*; M.N.Smirnova *(Moscow, Russia)*; P. Stovicek *(Prague, Czech Republic)*; V.M. Talanov *(Novocherkassk, Russia)*; A.Ya. Vul' *(St. Petersburg, Russia)*; A.V. Yakimansky (*St. Petersburg, Russia*), V.A. Zagrebnov *(Marseille, France).*

Editors:
I.V. Blinova; A.I. Popov; E.S. Trifanova *(St. Petersburg, Russia),*
R. Simoneaux *(Philadelphia, Pennsylvania, USA).*

Address: ITMO University, Kronverkskiy pr., 49, St. Petersburg 197101, Russia.
Phone: +7(812)607-02-54, **Journal site:** http://nanojournal.ifmo.ru/,
E-mail: nanojournal@itmo.ru

AIM AND SCOPE

The scope of the journal includes all areas of nano-sciences. Papers devoted to basic problems of physics, chemistry, material science and mathematics inspired by nanosystems investigations are welcomed. Both theoretical and experimental works concerning the properties and behavior of nanosystems, problems of its creation and application, mathematical methods of nanosystem studies are considered.

The journal publishes scientific reviews (up to 30 journal pages), research papers (up to 15 pages) and letters (up to 5 pages). All manuscripts are peer-reviewed. Authors are informed about the referee opinion and the Editorial decision.

CONTENT

MATHEMATICS

PHYSICS

CHEMISTRY AND MATERIAL SCIENCE

NANOSYSTEMS:
PHYSICS, CHEMISTRY, MATHEMATICS

Lakaev S.N., et al. *Nanosystems: Phys. Chem. Math.*, 2026, **17** (2), 143–152.
http://nanojournal.ifmo.ru
DOI 10.17586/2220-8054-2026-17-2-143-152

Original article

Two-fermion lattice Schrödinger operators with first and second nearest-neighboring-site interactions

Saidakhmat N. Lakaev[1,2,a], Saidakbar Kh. Abdukhakimov[1,2,b], Adkham B. Khasanov[1,c]

[1]Samarkand State University, Samarkand, Uzbekistan

[2]V. I. Romanovskiy Institute of Mathematics, Uzbekistan Academy of Sciences, Tashkent, Uzbekistan

[a]slakaev@mail.ru, [b]abduxakimov93@mail.ru, [c]atham.xasanov@mail.ru

Corresponding author: S. Kh. Abdukhakimov, abduxakimov93@mail.ru

Abstract We study the Schrödinger operators $H_{\lambda\mu}(K)$ that model a two-fermion system on the three-dimensional lattice $\mathbb{Z}^3$, where total quasimomentum is fixed at $K \in \mathbb{T}^3$, and the particles interact through nearest- and next-nearest-neighbor couplings with strengths $\lambda, \mu \in \mathbb{R}$. For $K = 0$, we establish that $H_{\lambda\mu}(0)$ admits reducing invariant subspace whose restriction depends solely on the parameter $\mu \in \mathbb{R}$. This μ parameter line contains two *critical* points corresponding to the lower and upper spectral thresholds; at each of these points, the Fredholm determinant of the restricted operator vanishes. Each of these critical points divides the parameter line into two infinite intervals, where the number of eigenvalues lying below (or above) the essential spectrum remains constant. Depending on μ, the corresponding reduced operator has exactly one discrete eigenvalue, located either below the bottom or above the top of the essential spectrum. Moreover, we derive a lower bound on the number of discrete eigenvalues of $H_{\lambda\mu}(K)$ for all $K \in \mathbb{T}^3$.

Keywords Two-fermion system; lattice Schrödinger operator; discrete eigenvalues; essential spectrum; reduced subspaces.

Acknowledgements The authors acknowledge support of this research by Ministry of Higher Education, Science and Innovation of the Republic of Uzbekistan (Grant No. FL-9524115052).

For citation Lakaev S.N., Abdukhakimov S.Kh., Khasanov A.B. Two-fermion lattice Schrödinger operators with first and second nearest-neighboring-site interactions. *Nanosystems: Phys. Chem. Math.*, 2026, **17** (2), 143–152.

1. Introduction

Lattice models play a central role in many areas of modern physics. Among these are the two-body and three-body lattice Hamiltonians, which represent simplified formulations of the Bose- and Fermi-Hubbard models respectively, and describe systems with fixed number of identical particles. For one-particle lattice Schrödinger operators defined on one-, two-, and three-dimensional lattices, the existence, finiteness, and localization of discrete eigenvalues relative to the essential spectrum have been established; see, for example, the one- and two-dimensional cases in [1, 2] and the three-dimensional setting in [3]. These results were subsequently extended to two-particle lattice systems. In particular, for Hamiltonians on one-, two-, and three-dimensional lattices on-site (zero-range) interactions and one-step nearest-neighbor interactions, the existence of discrete eigenvalues below and above the essential spectrum was rigorously proved. Moreover, at zero total quasi-momentum $K = 0$, the threshold phenomena such as the appearance of an eigenvalue or a virtual level at the spectral edges were analyzed in detail [4–7]. These studies also revealed a pronounced dependence on bound states on the total quasi-momentum and covered both bosonic and fermionic symmetry classes. The three-particle problem was subsequently investigated for lattice Schrödinger Hamiltonians on one- and three-dimensional lattices with zero-range (on-site) interactions. In this setting, the structure of the essential spectrum and the finiteness or infiniteness of the discrete spectrum were described, and, in the presence of a zero-range resonance in the corresponding two-particle subsystems, Efimov-type effects and asymptotic laws for the distribution of eigenvalues were established [8–14]. Moreover, these discrete Hamiltonians may be viewed as natural approximations to their continuous counterparts [15]. By discretizing configuration space, one obtains bounded operators on the lattice Hilbert spaces whose spectral behaviour approximates that of the continuous few-body Schrödinger operators in the continuum limit; this observation allows a rigorous treatment of few-body quantum systems within the framework of bounded operator theory and often simplifies technical aspects of the spectral analysis. However, unlike the continuous setting, the few-body lattice Hamiltonian does not admit a full separation of the center-of-mass motion: the lattice discretization breaks the continuous translation (and Galilean) symmetry and couples center-of-mass and relative degrees of freedom. Nevertheless, the system retains discrete translational invariance, which makes it possible to apply the Floquet-Bloch decomposition. As a result, the full lattice Hamiltonian decomposes into a direct integral of fiber operators $H(K)$ parameterized by the quasimomentum $K \in \mathbb{T}^d$, so that spectral questions may be reduced to the analysis of these fiber operators (see, for example, [16, Section 4]). In the current paper, we investigate the spectral properties of a family of Hamiltonians describing two-fermion lattice systems with nearest- and next-nearest-neighbor interactions. In particular, the Hamiltonian studied here represents the three-dimensional case of the model presented in [16]. In the momentum representation, after a von Neumann direct integral decomposition over the quasi-momentum $K \in \mathbb{T}^3$, the two-fermion system is described by the fiber Schrödinger operator (see [4, 16])

$$H_{\lambda\mu}(K) = H_0 + V_{\lambda\mu}, \qquad \lambda, \mu \in \mathbb{R}, \tag{1}$$

acting in the subspace

$$L^{2,o}(\mathbb{T}^3) = \{f \in L^2(\mathbb{T}^3) : f(-p) = -f(p)\},$$

of odd functions on the torus $\mathbb{T}^3 = (-\pi, \pi]^3$ with Haar measure.

The free Hamiltonian part is the multiplication operator

$$H_0(K)f(p) = \mathcal{E}_K(p)f(p), \quad \mathcal{E}_K(p) = \varepsilon\left(\frac{K}{2} + p\right) + \varepsilon\left(\frac{K}{2} - p\right), \quad \varepsilon(p) = 2\sum_{i=1}^{3}(1 - \cos p_i), \tag{2}$$

and interaction $V_{\lambda\mu}$ is an integral operator in $L^{2,o}(\mathbb{T}^3)$ with smooth kernel

$$v_{\lambda\mu}(p) = \mu\left(\sum_{i=1}^{3}\cos p_i\right)^2 + \mu\sum_{i=1}^{3}\cos^2 p_i + \lambda\sum_{i=1}^{3}\cos p_i - 3\mu, \qquad p \in \mathbb{T}^3,$$

in particular, the rank of $V_{\lambda\mu}$ depends on the values $\lambda, \mu \in \mathbb{R}$ and does not exceed 12.

For $K = 0$, since the operator $H_0(0)$ is multiplication by an even, permutation-symmetric function and the parity structure of $V_{\lambda\mu}$, one obtains the decomposition

$$L^{2,o}(\mathbb{T}^3) = \bigoplus_{\theta \in \{\mathrm{eeo}, \mathrm{eoe}, \mathrm{oee}, \mathrm{ooo}\}} L^{2,\theta}(\mathbb{T}^3) \tag{3}$$

where, for example, $\theta = \mathrm{eeo}$ means that the function is even in the first two coordinates and odd in the third.

In the case $\theta = \mathrm{ooo}$ the interaction vanishes, so this subspace does not contribute to the discrete spectrum. For each $\theta \in \{\mathrm{eeo}, \mathrm{eoe}, \mathrm{oee}\}$, the subspace $L^{2,\theta}(\mathbb{T}^3)$ is naturally associated with a distinguished transposition $\sigma = \sigma_\theta$ of the coordinate variables, defined by

$$\sigma_{\mathrm{eeo}}(p_1, p_2, p_3) = (p_2, p_1, p_3), \qquad \sigma_{\mathrm{eoe}}(p_1, p_2, p_3) = (p_3, p_2, p_1), \qquad \sigma_{\mathrm{oee}}(p_1, p_2, p_3) = (p_1, p_3, p_2).$$

With respect to the action of this transposition σ_θ, the space $L^{2,\theta}(\mathbb{T}^3)$ admits the orthogonal decomposition

$$L^{2,\theta}(\mathbb{T}^3) = L^{2,\theta,\mathrm{sym}}(\mathbb{T}^3) \oplus L^{2,\theta,\mathrm{asym}}(\mathbb{T}^3), \tag{4}$$

where

$$L^{2,\theta,\mathrm{sym}}(\mathbb{T}^3) = \{f \in L^{2,\theta}(\mathbb{T}^3) : f \circ \sigma_\theta = f\}, \quad L^{2,\theta,\mathrm{asym}}(\mathbb{T}^3) = \{f \in L^{2,\theta}(\mathbb{T}^3) : f \circ \sigma_\theta = -f\}.$$

We focus on the antisymmetric subspaces

$$L^{2,\theta,\mathrm{asym}}(\mathbb{T}^3), \qquad \theta \in \{\mathrm{eeo}, \mathrm{eoe}, \mathrm{oee}\}$$

and, by unitary equivalence, reduce the analysis to the representative case $\theta = \mathrm{eeo}$.

Our main results are as follows:

(i) Unitary equivalence of $H_\mu^{\theta,\mathrm{asym}}(0)$ for $\theta \in \{\mathrm{eeo}, \mathrm{eoe}, \mathrm{oee}\}$;
(ii) Exact determination of the eigenvalues of $H_\mu^{\theta,\mathrm{asym}}(0)$ outside the essential spectrum;
(iii) Bounds on the number of eigenvalues of $H_{\lambda\mu}(K)$ for arbitrary $K \in \mathbb{T}^3$.

Further, we study the class of rank-one self-adjoint perturbations V for which the perturbed Schrödinger operator $H_\mu^{\theta,\mathrm{asym}}(0)$ possesses a prescribed number of eigenvalues lying to the left or right of its essential spectrum. The model is exactly solvable, and its discrete spectrum demonstrates the creation and annihilation of bound states triggered by small perturbations of potential V supported on finite subsets of the three dimensional lattice $\mathbb{Z}^3$. When such a phenomenon of emergence and disappearance occurs at the lower (resp. upper) edge of the essential spectrum of $H_\mu^{\theta,\mathrm{asym}}(0)$, we say that the operator is *critical* at that edge. We prove that the set of perturbations V leading to criticality consists of a single point on the parameter line. This yields a precise algebraic-geometric framework for analyzing the stability and bifurcation of bound states in the lattice Schrödinger operators. Finally, since the eigenvalues of $H_\mu^{\theta,\mathrm{asym}}(0)$ are in one-to-one correspondence with the zeros of the Fredholm determinant $\Delta_\mu(z)$ (see [7]), the problem reduces to the study of the zeros of $\Delta_\mu(z)$.

Previous works [2, 3, 7, 16] have studied the two-particle Schrödinger operator $H_{\lambda\mu}(K)$, where $K \in \mathbb{T}^d$ denotes the total quasimomentum of the two-particle system. This operator naturally emerges in the framework of the Bose-Hubbard model, which describes the quantum dynamics of two identical particles bosons or fermions on a discrete lattice $\mathbb{Z}^d$ in spatial dimensions ($1 \le d \le 3$). The particle interactions are governed by two real parameters, λ and μ, representing the strengths of the interaction at the same site and between nearest-neighbor sites, respectively. For the three-dimensional lattice $\mathbb{Z}^3$, the bosonic operator $H_{\gamma\lambda\mu}(K)$ with on-site (γ) and nearest-neighbor (λ,μ) interactions was analyzed in [17]. It was shown that its restriction to a certain invariant subspace depends only on the interaction parameters λ and μ; the mechanisms of eigenvalue emergence and disappearance are described in terms of the critical operator. Moreover, conditions ensuring the existence of exactly α eigenvalues below and β eigenvalues above the essential spectrum, with $\alpha+\beta \leq 2$, were established. For the two-dimensional lattice $\mathbb{Z}^2$, the same operator structure was considered in [18] with on-site (γ), nearest-neighbor (λ,μ), and next-nearest-neighbor (μ) interactions. It was proved that, for suitable interaction parameters, the operator has exactly seven eigenvalues outside the essential spectrum for all $K \in \mathbb{T}^2$.

The structure of the paper is as follows. In Section 2, we introduce the two-fermion Schrödinger operator in the quasimomentum representation. In Section 3, several preliminary results are established. The main results of the paper are formulated in Section 4. Finally, Section 5 is devoted to the detailed proofs of these results.

2. Schrödinger operator of a two-fermion system on lattices

2.1. The two-fermion Schrödinger operator in the quasimomentum representation

We denote by $\mathbb{T}^3=(\mathbb{R}/2\pi\mathbb{Z})^3\equiv(-\pi,\pi]^3$ the three-dimensional torus. It can be naturally identified with the Pontryagin dual group of $\mathbb{Z}^3$ and is equipped with the Haar measure $\mathrm{d}p$.

In the quasimomentum representation, the lattice Schrödinger operator $H_{\lambda\mu}(K), K\in\mathbb{T}^3$ of the two-fermion system acting in the subspace $L^{2,o}(\mathbb{T}^3)$ of odd functions on $\mathbb{T}^3$, $L^{2,o}(\mathbb{T}^3)=\{f\in L^2(\mathbb{T}^3): f(-p)=-f(p)\}$ (see [4, 16]).

The operator $H_{\lambda\mu}(K)$ is given by

$$H_{\lambda\mu}(K) := H_0(K)+V_{\lambda\mu}, \qquad \lambda,\mu\in\mathbb{R}, \tag{5}$$

where $H_0(K)$ is the multiplication operator associated with the function defined by (2) and the potential $V_{\lambda\mu}$ is an integral operator of the form

$$\begin{aligned}[V_{\lambda\mu}f](p) &= \frac{\lambda}{4\pi^3}\sum_{i=1}^{3}\sin p_i\int_{\mathbb{T}^3}\sin q_i f(q)\mathrm{d}q+\frac{\mu}{4\pi^3}\sum_{i=1}^{3}\sin 2p_i\int_{\mathbb{T}^3}\sin 2q_i f(q)\mathrm{d}q+\\ &+\frac{\mu}{2\pi^3}\sum_{1\leq i<j\leq 3}\left(\cos p_i\sin p_j\int_{\mathbb{T}^3}\cos q_i\sin q_j f(q)\mathrm{d}q+\cos p_j\sin p_i\int_{\mathbb{T}^3}\cos q_j\sin q_i f(q)\mathrm{d}q\right).\end{aligned} \tag{6}$$

Both operators $H_0(K)$ and $V_{\lambda\mu}$ are bounded and self-adjoint. In scientific literature, the parameter $K\in\mathbb{T}^3$ is commonly referred to as the *two-particle quasimomentum*, while $H_{\lambda\mu}(K)$ is usually called the *discrete Schrödinger operator* associated with the two-particle Hamiltonian $\hat{\mathbb{H}}_{\lambda\mu}$.

3. Some preliminaries

3.1. Analyzing the essential spectrum of discrete Schrödinger operators

The rank of the operator $V_{\lambda\mu}$, which depends on the values of λ and μ, is at most twelve. Due to this, and by applying Weyl's theorem, the essential spectrum of $H_{\lambda\mu}(K)$ is the same as the spectrum of $H_0(K)$ for any $K\in\mathbb{T}^3$. This means that $\sigma_{\mathrm{ess}}(H_{\lambda\mu}(K))$ equals the spectrum of $H_0(K)$, i.e.,

$$\sigma_{\mathrm{ess}}(H_{\lambda\mu}(K))=\sigma(H_0(K))=[\mathcal{E}_{\min}(K),\mathcal{E}_{\max}(K)], \tag{7}$$

where the minimum and maximum values of the essential spectrum are given by:

$$\mathcal{E}_{\min}(K):=\min_{p\in\mathbb{T}^3}\mathcal{E}_K(p)=4\sum_{i=1}^{3}\left(1-\cos\frac{K_i}{2}\right)\geq\mathcal{E}_{\min}(0)=0,$$

$$\mathcal{E}_{\max}(K):=\max_{p\in\mathbb{T}^3}\mathcal{E}_K(p)=4\sum_{i=1}^{3}\left(1+\cos\frac{K_i}{2}\right)\leq\mathcal{E}_{\max}(0)=24,$$

and the function $\mathcal{E}_K(p)$ is defined as:

$$\mathcal{E}_K(p):=4\sum_{i=1}^{3}\left(1-\cos\frac{K_i}{2}\cos p_i\right). \tag{8}$$

3.2. Decomposition into invariant subspaces and unitary equivalence

For each $\theta \in \{\mathrm{eeo}, \mathrm{eoe}, \mathrm{oee}, \mathrm{ooo}\}$, let $L^{2,\theta}(\mathbb{T}^3) \subset L^{2,o}(\mathbb{T}^3)$ denote the subspaces of odd functions defined by

$$L^{2,\mathrm{eeo}}(\mathbb{T}^3) = \{f \in L^{2,o}(\mathbb{T}^3) : f(p_1,p_2,p_3) = f(-p_1,p_2,p_3) = f(p_1,-p_2,p_3)\}$$
$$L^{2,\mathrm{eoe}}(\mathbb{T}^3) = \{f \in L^{2,o}(\mathbb{T}^3) : f(p_1,p_2,p_3) = f(-p_1,p_2,p_3) = f(p_1,p_2,-p_3)\}$$
$$L^{2,\mathrm{oee}}(\mathbb{T}^3) = \{f \in L^{2,o}(\mathbb{T}^3) : f(p_1,p_2,p_3) = f(p_1,-p_2,p_3) = f(p_1,p_2,-p_3)\}$$
$$L^{2,\mathrm{ooo}}(\mathbb{T}^3) = \{f \in L^{2,o}(\mathbb{T}^3) : f(p_1,p_2,p_3) = -f(-p_1,p_2,p_3) = -f(p_1,-p_2,p_3)\}$$

for a.e $(p_1,p_2,p_3) \in \mathbb{T}^3$.

Lemma 1. *The equality*

$$L^{2,\mathrm{o}}(\mathbb{T}^3) = \bigoplus_{\theta\in\{\mathrm{eeo},\mathrm{eoe},\mathrm{oee},\mathrm{ooo}\}} L^{2,\theta}(\mathbb{T}^3) \tag{9}$$

holds true.

Proof. Let $f \in L^{2,o}(\mathbb{T}^3)$. Define the following four functions:

$$f^{\mathrm{eeo}}(p_1,p_2,p_3) = \frac{1}{4}\big[f(p_1,p_2,p_3) + f(-p_1,p_2,p_3) + f(p_1,-p_2,p_3) - f(p_1,p_2,-p_3)\big] \in L^{2,\mathrm{eeo}}(\mathbb{T}^3),$$
$$f^{\mathrm{eoe}}(p_1,p_2,p_3) = \frac{1}{4}\big[f(p_1,p_2,p_3) + f(-p_1,p_2,p_3) - f(p_1,-p_2,p_3) + f(p_1,p_2,-p_3)\big] \in L^{2,\mathrm{eoe}}(\mathbb{T}^3),$$
$$f^{\mathrm{oee}}(p_1,p_2,p_3) = \frac{1}{4}\big[f(p_1,p_2,p_3) - f(-p_1,p_2,p_3) + f(p_1,-p_2,p_3) + f(p_1,p_2,-p_3)\big] \in L^{2,\mathrm{oee}}(\mathbb{T}^3),$$
$$f^{\mathrm{ooo}}(p_1,p_2,p_3) = \frac{1}{4}\big[f(p_1,p_2,p_3) - f(-p_1,p_2,p_3) - f(p_1,-p_2,p_3) - f(p_1,p_2,-p_3)\big] \in L^{2,\mathrm{ooo}}(\mathbb{T}^3).$$

By direct calculation, we have $f = f^{\mathrm{eeo}} + f^{\mathrm{eoe}} + f^{\mathrm{oee}} + f^{\mathrm{ooo}}$.

Let $h = f^{\theta_1}\overline{f^{\theta_2}}$, where $\theta_1 \neq \theta_2$ and $\theta_1, \theta_2 \in \{\mathrm{eeo}, \mathrm{eoe}, \mathrm{oee}, \mathrm{ooo}\}$. The function $h = f^{\theta_1}\overline{f^{\theta_2}}$ is odd in at least one variable, hence, its integral over $\mathbb{T}^3$ vanishes. Therefore, $\langle f^{\theta_1} f^{\theta_2}\rangle = 0$, which proves orthogonality. □

By the structure of the perturbation operator $V_{\lambda\mu}$, its restriction to $L^{2,\mathrm{ooo}}(\mathbb{T}^3)$ vanishes. Therefore, it suffices to analyze the remaining three subspaces $L^{2,\mathrm{eeo}}(\mathbb{T}^3)$, $L^{2,\mathrm{eoe}}(\mathbb{T}^3)$ and $L^{2,\mathrm{oee}}(\mathbb{T}^3)$, each admitting a decomposition into symmetric and antisymmetric components with respect to the corresponding transposition:

$$\sigma_\theta = \begin{cases} (12), & \text{if } \theta = \mathrm{eeo}, \\ (13), & \text{if } \theta = \mathrm{eoe}, \\ (23), & \text{if } \theta = \mathrm{oee}. \end{cases}$$

Lemma 2. *For any $f \in L^{2,\theta}(\mathbb{T}^3), \theta \in \{\mathrm{eeo}, \mathrm{eoe}, \mathrm{oee}\}$, there exists an orthogonal decomposition $f = f^{\mathrm{sym}} + f^{\mathrm{asym}}$ where f^{sym} is symmetric and f^{asym} is antisymmetric under the transposition σ.*

Proof. For $f \in L^{2,\theta}(\mathbb{T}^3)$, define:

$$f^{\mathrm{sym}} := \frac{1}{2}\left(f(p) + f(\sigma_\theta p)\right)$$
$$f^{\mathrm{asym}} := \frac{1}{2}\left(f(p) - f(\sigma_\theta p)\right)$$

These satisfy:

- $f = f^{\mathrm{sym}} + f^{\mathrm{asym}}$ (by direct computation)
- $f^{\mathrm{sym}}(\sigma_\theta p) = f^{\mathrm{sym}}(p)$ (symmetric)
- $f^{\mathrm{asym}}(\sigma_\theta p) = -f^{\mathrm{asym}}(p)$ (antisymmetric)

□

We define the symmetric and antisymmetric subspaces of $L^{2,\theta}(\mathbb{T}^3)$ with respect to the σ transposition as

$$L^{2,\theta,\mathrm{sym}}(\mathbb{T}^3) := \left\{f \in L^{2,\theta}(\mathbb{T}^3) : f(p) = f(\sigma_\theta p)\right\},$$
$$L^{2,\theta,\mathrm{asym}}(\mathbb{T}^3) := \left\{f \in L^{2,\theta}(\mathbb{T}^3) : f(p) = -f(\sigma_\theta p)\right\}.$$

The operator $H_0(0)$ is a multiplication operator defined by the even function $\mathcal{E}_0(p)$, that is symmetric with respect to permutation of the variables p_1, p_2, p_3. This operator acts on the space $L^{2,o}(\mathbb{T}^3)$. Hence, for each parity type θ, the subspaces $L^{2,\theta,\mathrm{sym}}(\mathbb{T}^3)$ and $L^{2,\theta,\mathrm{asym}}(\mathbb{T}^3)$ are invariant with respect to $H_0(0)$.

According the equalities

$$2\cos p_1 \cos q_1 + 2\cos p_2 \cos q_2 = (\cos p_1 + \cos p_2)(\cos q_1 + \cos q_2) + (\cos p_2 - \cos p_1)(\cos q_2 - \cos q_1),$$
$$2\cos p_1 \cos q_1 + 2\cos p_3 \cos q_3 = (\cos p_1 + \cos p_3)(\cos q_1 + \cos q_3) + (\cos p_3 - \cos p_1)(\cos q_3 - \cos q_1),$$
$$2\cos p_2 \cos q_2 + 2\cos p_3 \cos q_3 = (\cos p_2 + \cos p_3)(\cos q_2 + \cos q_3) + (\cos p_3 - \cos p_2)(\cos q_3 - \cos q_2),$$

the operator $V_{\lambda\mu}$ in (6) can be written as

$$
\begin{aligned}
[V_{\lambda\mu}f](p) = {} & \frac{\lambda}{4\pi^3}\sum_{i=1}^{3}\sin p_i\int\limits_{\mathbb{T}^3}\sin q_i f(q)\mathrm{d}q + \frac{\mu}{4\pi^3}\sum_{i=1}^{3}\sin 2p_i\int\limits_{\mathbb{T}^3}\sin 2q_i f(q)\mathrm{dq} \\
& + \sum_{\substack{i,j,k\,\in\{1,2,3\}\\ i\neq j\neq k}} \frac{\mu}{4\pi^3}[\sin p_i(\cos p_j+\cos p_k)\int\limits_{\mathbb{T}^3}\sin q_i(\cos q_j+\cos q_k)f(q)\mathrm{d}q \\
& + \sin p_i(\cos p_j-\cos p_k)\int\limits_{\mathbb{T}^3}\sin q_i(\cos q_j-\cos q_k)f(q)\mathrm{d}q].
\end{aligned}
\tag{10}
$$

From (10), it follows that the subspaces $L^{2,\theta,\mathrm{sym}}(\mathbb{T}^3)$ and $L^{2,\theta,\mathrm{asym}}(\mathbb{T}^3)$ are invariant subspaces of the operator $V_{\lambda\mu}$. Consequently, these subspaces are also invariant with respect to $H_{\lambda\mu}(0)$, and hence, they provide a reduction of this operator. Therefore, the spectrum of the operator $H_{\lambda\mu}(0)$ satisfies

$$
\sigma\big(H_{\lambda\mu}(0)\big) = \bigcup_{\theta\in\{\mathrm{eeo},\,\mathrm{eoe},\,\mathrm{oee}\}} \sigma\big(H_{\lambda\mu}(0)\big|_{L^{2,\theta,\mathrm{sym}}(\mathbb{T}^3)}\big)\cup\sigma\big(H_{\lambda\mu}(0)\big|_{L^{2,\theta,\mathrm{asym}}(\mathbb{T}^3)}\big). \tag{11}
$$

Let us denote by $V_\mu^{\theta,\mathrm{asym}}$ the restriction of the operator $V_{\lambda\mu}$ to the antisymmetric subspaces $L^{2,\theta,\mathrm{asym}}(\mathbb{T}^3)$; note that this restriction does not depend on λ, since the coupling constant λ appears only in the symmetric part of $V_{\lambda\mu}$. Applying the representation (10) of the $V_{\lambda\mu}$ yields

$$
[V_\mu^{\mathrm{eeo,asym}}f](p) = \frac{\mu}{4\pi^3}\sin p_3(\cos p_2-\cos p_1)\int_{\mathbb{T}^3}\sin q_3(\cos q_2-\cos q_1)f(q)\mathrm{d}q,
$$

$$
[V_\mu^{\mathrm{eoe,asym}}f](p) = \frac{\mu}{4\pi^3}\sin p_2(\cos p_3-\cos p_1)\int_{\mathbb{T}^3}\sin q_2(\cos q_3-\cos q_1)f(q)\mathrm{d}q,
$$

$$
[V_\mu^{\mathrm{oee,asym}}f](p) = \frac{\mu}{4\pi^3}\sin p_1(\cos p_3-\cos p_2)\int_{\mathbb{T}^3}\sin q_1(\cos q_3-\cos q_2)f(q)\mathrm{d}q.
$$

Let us introduce the notation

$$
H_\mu^{\theta,\mathrm{asym}}(0) := H_{\lambda\mu}(0)\mid_{L^{2,\theta,\mathrm{asym}}(\mathbb{T}^3)} = H_0 + V^{\theta,\mathrm{asym}}.
$$

Lemma 3. *Let*

$$
\mathbb{U}_1 : L^{2,\mathrm{eoe,asym}}(\mathbb{T}^3)\to L^{2,\mathrm{eeo,asym}}(\mathbb{T}^3), \qquad \mathbb{U}_2 : L^{2,\mathrm{oee,asym}}(\mathbb{T}^3)\to L^{2,\mathrm{eeo,asym}}(\mathbb{T}^3)
$$

be the permutation operators defined for almost all $(p_1,p_2,p_3)\in\mathbb{T}^3$ *by*

$$
(\mathbb{U}_1 f)(p_1,p_2,p_3) = f(p_1,p_3,p_2), \qquad (\mathbb{U}_2 f)(p_1,p_2,p_3) = f(p_2,p_3,p_1).
$$

Then

$$
\mathbb{U}_1 V_\mu^{\mathrm{eoe,asym}}\mathbb{U}_1^* = V_\mu^{\mathrm{eeo,asym}}, \qquad \mathbb{U}_2 V_\mu^{\mathrm{oee,asym}}\mathbb{U}_2^* = V_\mu^{\mathrm{eeo,asym}}.
$$

Consequently, the Hamiltonians

$$
H_\mu^{\theta,\mathrm{asym}}(0), \qquad \theta\in\{\mathrm{eeo},\mathrm{eoe},\mathrm{oee}\},
$$

are unitarily equivalent, and hence have identical spectra. It is therefore sufficient to analyze the case $\theta = \mathrm{eeo}$.

Proof. The operators $\mathbb{U}_1$ and $\mathbb{U}_2$ are unitary since coordinate permutations preserve the Lebesgue measure on $\mathbb{T}^3$. By construction, $V_\mu^{\theta,\mathrm{asym}}$ is defined by the same formula $\mathcal{V}_\mu$, with the role of the variables permuted according to θ. Conjugating $V_\mu^{\mathrm{eoe,asym}}$ by $\mathbb{U}_1$ relabels the coordinates (p_2,p_3), yielding $V_\mu^{\mathrm{eeo,asym}}$, and similarly for $\mathbb{U}_2$. Since $H_\mu^{\theta,\mathrm{asym}}(0)$ is the sum of the same free part and the corresponding $V_\mu^{\theta,\mathrm{asym}}$, these conjugation relations extend directly to the full Hamiltonians, proving their unitary equivalence. □

Remark 1. *This lemma establishes that the Hamiltonians associated with the labels* eeo, eoe *and* oee *are unitarily equivalent, as they differ only by permutations of coordinates. Consequently, their spectra coincide, and it is sufficient to carry out the spectral analysis for any one of these Hamiltonians.*

Remark 2. *The main objective of this work is to characterize the eigenvalues of* $H_\mu^{\mathrm{eeo,asym}}(0)$ *that lie outside the essential spectrum. In particular, we aim to estimate the number of eigenvalues of the operator* $H_{\lambda\mu}(K)$ *for any* $K\in\mathbb{T}^3$.

4. Main results of the work

It is known that the essential spectrum of the operator $H_\mu^{\mathrm{eeo,asym}}(0)$ coincides with the interval $[0,24]$. To identify discrete eigenvalues of $H_\mu^{\mathrm{eeo,asym}}(0)$, we aim to derive an implicit equation using Fredholm determinant theory. To determine the discrete eigenvalues, it suffices to consider the eigenvalue equation

$$H_\mu^{\mathrm{eeo,asym}}(0)f = zf$$

for $z \in \mathbb{R}\setminus[0,24]$ and nontrivial functions $f \in L^{2,\mathrm{eeo,asym}}(\mathbb{T}^3)$. The Fredholm determinant associated with the operator $H_\mu^{\mathrm{eeo,asym}}(0)$, denoted by $\Delta_\mu(z)$, is given by

$$\Delta_\mu(z) = 1 + \mu a(z), \tag{12}$$

where

$$a(z) = \frac{1}{4\pi^3}\int\limits_{\mathbb{T}^3} \frac{\sin^2 p_1(\cos p_3 - \cos p_2)^2 \mathrm{d}p}{\mathcal{E}_0(p) - z}. \tag{13}$$

Lemma 4. *A number $z \in \mathbb{R}\setminus[0,24]$ is an eigenvalue of the operator $H_\mu^{\mathrm{eeo,asym}}(0)$ if and only if the condition*

$$\Delta_\mu(z) = 0 \tag{14}$$

is satisfied. Furthermore, within $\mathbb{R}\setminus[0,24]$ the function $\Delta_\mu(z)$ admits at most one root.

The proof of this lemma is quite standard (cf., e.g., [3, 7]).

Lemma 5. *The functions $\Delta_\mu(z)$ and $a(z)$ defined in $\mathbb{R}\setminus[0,24]$ are real-valued. Moreover, $a(z)$ is strictly increasing and positive in $(-\infty,0)$, strictly increasing and negative in $(24,+\infty)$, and satisfies the following asymptotic relations:*

$$\lim_{z\nearrow 0} a(z) = a(0), \quad \lim_{z\searrow 24} a(z) = -a(0), \quad \lim_{z\to\pm\infty} a(z) = 0,$$

and

$$\lim_{z\nearrow 0} \Delta_\mu(z) = 1 + a(0)\mu, \quad \lim_{z\searrow 24} \Delta_\mu(z) = 1 - a(0)\mu, \quad \lim_{z\to\pm\infty} \Delta_\mu(z) = 1.$$

Proof. The asymptotic formulas for the function $a(z)$, defined in (13) can be proved as in Lemma 4.7 of [16]. Hence, we omit the corresponding calculations. The asymptotic behavior of the function $\Delta_\mu(z)$ follows directly from (12) together with the asymptotic of $a(z)$. ☐

Remark 3. *The value $a(0)$ is given by the integral representation (see (13))*

$$a(0) = \frac{1}{4\pi^3}\int_{\mathbb{T}^3} \frac{\sin^2 p_1(\cos p_3 - \cos p_2)^2}{\mathcal{E}_0(p)}\,dp.$$

A numerical evaluation using a standard quadrature on a uniform grid (with mesh size $N\times N\times N$ and convergence check in N) gives

$$a(0) \approx 0.0891,$$

with accuracy about 10^{-4} (stable under further grid refinement).

The following theorem presents the first main result of this paper, which gives one a complete description of the discrete spectrum of the operator $H_\mu^{\mathrm{eeo,asym}}(0)$.

Theorem 1. *Let $\mu \in \mathbb{R}$. Then the following statements hold for $H_\mu^{\mathrm{eeo,asym}}(0)$.*

(i) *For any $\mu \in [-\frac{1}{a(0)}, \frac{1}{a(0)}]$ the operator $H_\mu^{\mathrm{eeo,asym}}(0)$ has no eigenvalues outside the essential spectrum.*

(ii) *For any $\mu < -\frac{1}{a(0)}$ the operator $H_\mu^{\mathrm{eeo,asym}}(0)$ has a unique simple eigenvalue $z(\mu;0) < 0$ and the associated eigenfunction can be written as*

$$f_\mu(p) = C\frac{\sin p_3(\cos p_2 - \cos p_1)}{\mathcal{E}_0(p) - z(\mu;0)}, \quad p \in \mathbb{T}^3, \tag{15}$$

where $C \in \mathbb{R}$ is a (nonzero) normalization constant.

(iii) *For any $\mu > \frac{1}{a(0)}$, the operator $H_\mu^{\mathrm{eeo,asym}}(0)$ has a unique simple eigenvalue $z(\mu;0) > 24$ and the associated eigenfunction can be written as*

$$f_\mu(p) = C\frac{\sin p_3(\cos p_2 - \cos p_1)}{z(\mu;0) - \mathcal{E}_0(p)}, \quad p \in \mathbb{T}^3, \tag{16}$$

where $C \in \mathbb{R}$ is a (nonzero) normalization constant.

4.1. Critical operators

To clarify the mechanisms responsible for eigenvalue emergence and annihilation, we introduce the notion of a *critical* operator.

Definition 1. *We say that the operator* $H_{\mu}^{\mathrm{eeo,asym}}(0)$ *is critical at a point* $\mu_0 \in \mathbb{R}$ *if the map*

$$\mathbb{R} \ni \mu \ \mapsto \ \mathrm{tr}\ E_{H_{\mu}^{\mathrm{eeo,asym}}(0)}\left(\mathbb{R} \setminus \sigma_{\mathrm{ess}}(H_{\mu}^{\mathrm{eeo,asym}}(0))\right) \tag{17}$$

is discontinuous at μ_0*. Here* $E_H(\cdot)$ *denotes the spectral projection of the operator* $H_{\mu}^{\mathrm{eeo,asym}}(0)$*.*

Similarly, we say that $H_{\mu}^{\mathrm{eeo,asym}}(0)$ *is critical at an endpoint* $z = 0$ *or* $z = 24$ *of the essential spectrum if there exist points* $\mu_0^{(-)}, \mu_0^{(+)} \in \mathbb{R}$ *such that the maps*

$$\begin{aligned} &\mathbb{R} \ni \mu \ \mapsto \ \mathrm{tr}\ E_{H_{\mu}^{\mathrm{eeo,asym}}(0)}\left((-\infty, \inf \sigma_{\mathrm{ess}}(H_{\mu}^{\mathrm{eeo,asym}}(0)))\right), \textit{and} \\ &\mathbb{R} \ni \mu \ \mapsto \ \mathrm{tr}\ E_{H_{\mu}^{\mathrm{eeo,asym}}(0)}\left((\sup \sigma_{\mathrm{ess}}(H_{\mu}^{\mathrm{eeo,asym}}(0)), \infty)\right) \end{aligned} \tag{18}$$

are discontinuous at $\mu_0^{(-)}$ *and* $\mu_0^{(+)}$*, respectively.*

Remark 4. *Since the map in* (17) *takes only integer values, we obtain the following equivalent characterization: The operator* $H_{\mu}^{\mathrm{eeo,asym}}(0)$ *is critical at* $\mu_0 \in \mathbb{R}$ *if the number of its eigenvalues outside the essential spectrum fails to remain constant in any neighborhood of* μ_0*. Likewise,* $H_{\mu}^{\mathrm{eeo,asym}}(0)$ *is critical at the lower endpoint* $z = 0$ *(resp. the upper endpoint* $z = 24$*) if there exists* $\mu_0 \in \mathbb{R}$ *such that the number of eigenvalues below (resp. above) the essential spectrum is not constant in any neighborhood of* μ_0*.*

The following theorem provides a precise characterization of the criticality of the operator $H_{\mu}^{\mathrm{eeo,asym}}(0)$ in terms of the real parameter μ.

Theorem 2. *The operator* $H_{\mu}^{\mathrm{eeo,asym}}(0)$ *is critical at the lower threshold* $z = 0$ *(resp., the upper threshold* $z = 24$*) of the essential spectrum if and only if the leading asymptotic terms of the determinant* $\Delta_{\mu}(z)$ *at the corresponding endpoint satisfy*

$$1 + a(0)\mu = 0 \quad \textit{(resp., } 1 - a(0)\mu = 0\textit{).}$$

In other words, the determinant $\Delta_{\mu}(z)$ *vanishes at* $z = 0$ *or* $z = 24$ *according to these asymptotics.*

According to the min-max principle, the number of eigenvalues of the operator $H_{\lambda\mu}(K)$ located outside the essential spectrum is not fixed but remains bounded above by twelve.

Theorem 3. *Assume that* $K \in \mathbb{T}^3$ *and* $(\lambda, \mu) \in \mathbb{R}^2$*.*

(i) *If* $\mu < -\dfrac{1}{a(0)}$*, then the operator* $H_{\lambda\mu}(K)$ *has at least three eigenvalues located below the essential spectrum.*

(ii) *If* $\mu > \dfrac{1}{a(0)}$*, then the operator* $H_{\lambda\mu}(K)$ *has at least three eigenvalues located above the essential spectrum.*

5. Proofs of the main results

We first prove the following lemma on the roots of the function Δ_{μ}, which will be used to establish the main result.

Lemma 6. *Let* $\mu \in \mathbb{R}$*.*

(i) *If* $\mu < -\dfrac{1}{a(0)}$*, then the function* $\Delta_{\mu}(\cdot)$ *has a unique root* $\xi_1(\mu)$ *in* $(-\infty, 0)$*.*

(ii) *If* $\mu \in [-\dfrac{1}{a(0)}, \dfrac{1}{a(0)}]$*, then the function* $\Delta_{\mu}(\cdot)$ *has no roots in* $\mathbb{R} \setminus [0, 24]$*.*

(iii) *If* $\mu > \dfrac{1}{a(0)}$*, then the function* $\Delta_{\mu}(\cdot)$ *has a unique root* $\xi_2(\mu)$ *in* $(24, +\infty)$*.*

Proof. Let us prove the item (i). If $\mu < -\dfrac{1}{a(0)}$, then according to Lemma 5

$$\lim_{z \nearrow 0} \Delta_{\mu}(z) < 0$$

and

$$\lim_{z \to -\infty} \Delta_{\mu}(z) = 1.$$

Hence there exists a number $\xi_1(\mu)$ in $(-\infty, 0)$ such that

$$\Delta_{\mu}(\xi_1(\mu)) = 0.$$

Since the rank of the operator $V_{\mu}^{\mathrm{eeo,asym}}$ is equal to one, there exists a unique root.

If $\mu \in [-\frac{1}{a(0)}, \frac{1}{a(0)}]$, then according to Lemma 5, the inequalities

$$\lim_{z \nearrow 0} \Delta_\mu(z) > 0, \quad \lim_{z \searrow 24} \Delta_\mu(z) > 0$$

hold. Since

$$\lim_{z \to \pm\infty} \Delta_\mu(z) = 1,$$

the functions $\Delta_\mu(\cdot)$ has no roots.

Finally, if $\mu > \frac{1}{a(0)}$, then according to Lemma 5,

$$\lim_{z \searrow 24} \Delta_\mu(z) < 0$$

and

$$\lim_{z \to +\infty} \Delta_\mu(z) = 1.$$

Hence there exists a number $\xi_2(\mu)$ in $(24, +\infty)$ such that

$$\Delta_\mu(\xi_2(\mu)) = 0.$$

Since the rank of the operator $V_\mu^{\text{eeo,asym}}$ is equal to one, there exists a unique root. □

Proof of Theorem 1 follows from Lemma 4 and 6. □

Proof of Theorem 2. We establish the result for the lower threshold; the case of the upper threshold follows by a similar argument.

Let μ_0^- be a point such that $1 + a(0)\mu = 0$. By Theorem 1, parts (i) and (ii), for every neighborhood of μ_0^- there exists a value of μ for which the number of eigenvalues of $H_\mu^{\text{eeo,asym}}(0)$ lying below the essential spectrum is not constant. Equivalently, by Remark 4, the mapping

$$V_\mu^{\text{eeo,asym}} \longmapsto \operatorname{tr} E_{H_\mu^{\text{eeo,asym}}(0)}\big((-\infty, \inf \sigma_{\text{ess}}(H_\mu^{\text{eeo,asym}}(0)))\big)$$

is discontinuous at μ_0^-. According to Definition 1, this implies that whenever the equality $1 + a(0)\mu = 0$ holds, the operator $H_\mu^{\text{eeo,asym}}(0)$ is critical at the lower threshold of the essential spectrum.

Conversely, assume that $H_\mu^{\text{eeo,asym}}(0)$ is critical at the lower edge of the essential spectrum. Then there exists a point μ_0^- at which the function

$$V_\mu^{\text{eeo,asym}} \longmapsto \operatorname{tr} E_{H_\mu^{\text{eeo,asym}}(0)}\big((-\infty, \inf \sigma_{\text{ess}}(H_\mu^{\text{eeo,asym}}(0)))\big)$$

is discontinuous. Suppose that $\mu_0^- \neq -\frac{1}{a(0)}$. In this case, by Theorem 1, parts (i) and (ii), one can find a neighborhood $U(\mu_0^-)$ in which the number of eigenvalues of $H_\mu^{\text{eeo,asym}}(0)$ lying below its essential spectrum does not vary, contradicting the assumption of criticality. From this contradiction, it follows that $\mu_0^- = -\frac{1}{a(0)}$. □

5.1. Analysis of the discrete spectrum of the operator $H_{\lambda\mu}(K)$

For any $n \geq 1$, we define two quantities: $e_n(K; \lambda, \mu)$ and $E_n(K; \lambda, \mu)$. These are defined using a min-max approach.

The first quantity, $e_n(K; \lambda, \mu)$, is the largest lower bound for the expectation value of the operator $H_{\lambda\mu}(K)$ with respect to a normalized vector ψ, where ψ is orthogonal to a set of $n-1$ vectors $\phi_1, \ldots, \phi_{n-1}$ from the space $L^{2,o}(\mathbb{T}^3)$.

The second quantity, $E_n(K; \lambda, \mu)$, is the smallest upper bound for the same expectation value, under the same conditions.

According to the min-max principle, we have the inequalities $e_n(K; \lambda, \mu) \leq \mathcal{E}_{\min}(K)$ and $E_n(K; \lambda, \mu) \geq \mathcal{E}_{\max}(K)$.

Since the rank of the operator $V_{\lambda\mu}$ is at most twelve, one can choose a set of twelve vectors, $\phi_1, \phi_2, \ldots, \phi_{12}$, from its range. Consequently for all $n \geq 13$, the following equalities hold: $e_n(K; \lambda, \mu) = \mathcal{E}_{\min}(K)$ and $E_n(K; \lambda, \mu) = \mathcal{E}_{\max}(K)$.

Lemma 7. *Assume that* $n \geq 1$ *and* $i \in \{1, 2, 3\}$. *The following two properties hold:*

(i) *For fixed values of* K_j *where* $j \neq i$, *the function*

$$K_i \mapsto \mathcal{E}_{\min}((K_1, K_2, K_3)) - e_n((K_1, K_2, K_3); \lambda, \mu)$$

is non-increasing in the interval $(-\pi, 0]$ *and non-decreasing in* $[0, \pi]$.

(ii) *Similarly, for fixed* K_j *with* $j \neq i$, *the function*

$$K_i \mapsto E_n((K_1, K_2, K_3); \lambda, \mu) - \mathcal{E}_{\max}((K_1, K_2, K_3))$$

also exhibits the same monotonic behavior, being non-increasing in $(-\pi, 0]$ *and non-decreasing in* $[0, \pi]$.

Proof. We may,without loss of generality, assume that $i = 1$. Let $\psi \in L^{2,o}(\mathbb{T}^3)$ be an arbitrary vector. Consider the quadratic form associated with shifted operator $(H_0(K) - \mathcal{E}_{\min}(K))$:

$$((H_0(K) - \mathcal{E}_{\min}(K))\psi, \psi) = \int\limits_{\mathbb{T}^3} \sum_{i=1}^{3} \cos \tfrac{K_i}{3} \left(1 - \cos q_i\right) |\psi(q)|^2 \, \mathrm{d}q, \quad K := (K_1, K_2, K_3).$$

If we regarded expression as a function of the single variable $K_1 \in \mathbb{T}$, it is evident that it is non-decreasing in $(-\pi, 0]$ and non-increasing in $[0, \pi]$. This monotonicity follows directly from the properties of the cosine function. Since the potential operator $V_{\lambda\mu}$ does not depend on K, the corresponding function

$$K_1 \mapsto e_n(K; \lambda, \mu) - \mathcal{E}_{\min}(K)$$

inherits the same monotonic behavior. Therefore,for each $n \geq 1$, this function is non-decreasing in $(-\pi, 0]$ and non-increasing in $[0, \pi]$.

An entirely analogous argument applies to the functions

$$K_i \mapsto E_n(K; \lambda, \mu) - \mathcal{E}_{\max}(K),$$

demonstrating the monotonicity of the shifted eigenvalues from above. □

Theorem 4. *Let $\lambda, \mu \in \mathbb{R}$. Suppose that the operator $H_{\lambda\mu}(0)$ has n eigenvalues (counting multiplicities) located below (respectively, above) its essential spectrum. Then, for every $K \in \mathbb{T}^3$, the operator $H_{\lambda\mu}(K)$ also possesses at least n eigenvalues lying below (respectively, above) its essential spectrum.*

Proof. We rely on Lemma 7, which establishes certain monotonicity properties of the eigenvalues with respect to K. Specifically, for any $K \in \mathbb{T}^3$ and any integer $m \geq 1$, the following inequalities hold:

$$0 \leq \mathcal{E}_{\min}(0) - e_m(0; \lambda, \mu) \leq \mathcal{E}_{\min}(K) - e_m(K; \lambda, \mu),$$

$$E_m(K; \lambda, \mu) - \mathcal{E}_{\max}(K) \geq E_m(0; \lambda, \mu) - \mathcal{E}_{\max}(0) \geq 0.$$

Assume that for some $\lambda, \mu \in \mathbb{R}$, the value $e_n(0; \lambda, \mu)$ is a discrete eigenvalue of the operator $H_{\lambda\mu}(0)$. By definition of a discrete eigenvalue, this implies

$$\mathcal{E}_{\min}(0) - e_n(0; \lambda, \mu) > 0.$$

Combining this observation with the inequalities above, we immediately deduce that for any $K \in \mathbb{T}^3$, the eigenvalue $e_n(K; \lambda, \mu)$ remains strictly below $\mathcal{E}_{\min}(K)$, i.e.,

$$e_n(K; \lambda, \mu) < \mathcal{E}_{\min}(K).$$

Since the eigenvalues are arranged in increasing order,

$$e_1(K; \lambda, \mu) \leq \ldots \leq e_n(K; \lambda, \mu) < \mathcal{E}_{\min}(K),$$

it follows that the operator $H_{\lambda\mu}(K)$ possesses at least n discrete eigenvalues lying below its essential spectrum.

An entirely analogous argument applies to the eigenvalues $E_n(K; \lambda, \mu)$, establishing the corresponding result for eigenvalues above the essential spectrum. □

Proof of Theorem 3 will prove by combining the results of Theorem 4 and Theorem 1. □

6. Conclusion

In this work, we performed a detailed spectral analysis of the two-fermion lattice Schrödinger operators $H_{\lambda\mu}(K)$ on the three-dimensional lattice $\mathbb{Z}^3$ with nearest- and next-nearest-neighbor interactions. By reducing the problem to invariant subspaces and studying the associated Fredholm determinant, we identified two critical spectral points that determine the behavior and number of discrete eigenvalues. Our results demonstrate that the reduced operator possesses exactly one discrete eigenvalue depending on the interaction strength and provide explicit bounds for the number of eigenvalues for arbitrary quasimomentum. Furthermore, we described a class of rank-one self-adjoint perturbations that induce the creation or annihilation of bound states, offering a clear algebraic-geometric framework for understanding stability and bifurcation phenomena. These findings deepen the understanding of spectral properties of lattice Schrödinger operators and contribute to the mathematical foundations of interacting quantum systems.

References

[1] Kholmatov Sh.Yu., Lakaev S.N., Almuratov F. Bound states of discrete Schrödinger operators on one and two dimensional lattices. *J. Math. Anal. Appl.*, 2021, **503**(1), P. 125280.

[2] Lakaev S.N., Özdemir E. The existence and location of eigenvalues of the one particle Hamiltonians on lattices. *Hacettepe J. Math. Stat.*, 2016, **45**, P. 1693–1703.

[3] Lakaev S.N., Bozorov I.N. The number of bound states of a one-particle Hamiltonian on a three-dimensional lattice. *Theoret. and Math. Phys.*, 2009, **158**, P. 360–376.

[4] Albeverio S., Lakaev S.N., Makarov K.A., Muminov Z.I. The Threshold Effects for the Two-particle Hamiltonians on Lattices. *Communications in Mathematical Physics*, 2006, **262**, P. 91–115.

[5] Faria Da Veiga P.A., Ioriatti L., O'Carroll M. Energy-momentum spectrum of some two-particle lattice Schrödinger Hamiltonians. *Physical Review E*, 2002, **66**, P. 016130.

[6] Lakaev S.N., Abdukhakimov S.Kh. Threshold effects in a two-fermion system on an optical lattice. *Theoret. and Math. Phys.*, 2020, **203**(2), P. 251–268.

[7] Lakaev S.N., Kholmatov Sh.Yu., Khamidov Sh.I. Bose-Hubbard model with on-site and nearest-neighbor interactions, exactly solvable case. *J. Phys. A: Math. Theor.*, 2021, **54**, P. 245201.

[8] Albeverio S., Lakaev S.N., Muminov Z.I. Schrödinger operators on lattices. The Efimov effect and discrete spectrum asymptotics. *Ann. Henri Poincaré*, 2004, **5**(4), P. 743–772.

[9] Albeverio S., Lakaev S.N., Khalkhujaev A.M. Number of Eigenvalues of the Three-Particle Schrodinger Operators on Lattices, Markov *Process. Relat. Fields.*, 2012, **18**, P. 387–420.

[10] Bach V., de Siqueira Pedra W., Lakaev S.N. Bounds on the discrete spectrum of lattice Schrödinger operators. *Journal of Mathematical Physics*, 2017, **59**(2), P. 022109.

[11] Lakaev S.N. The Efimov's effect of the three identical quantum particle on a lattice. *Funct. Anal. Appl.*, 1993, **27**, P 15–28.

[12] Lakaev S.N., Dell'Antonio G., Khalkhuzhaev A. Existence of an isolated band in a system of three particles in an optical lattice. *J. Phys. A: Math. Theor.*, 2016, **49**(52), P. 15.

[13] Lakaev S.N., Lakaev Sh.S. The existence of bound states in a system of three particles in an optical lattice. *J.Phys. A: Math. Theor.*, 2017, **50**, P. 335202.

[14] Muminov Z.I., Aktamova V.U. The point spectrum of the three-particle Schrödinger operator for a system comprising two identical bosons and one fermion on $\mathbb{Z}$. *Nanosystems: Phys.Chem.Math.*, 2024, **15**, P. 438–447.

[15] Faddeev L.D., Merkuriev S.P. *Quantum Scattering Theory for Several Particle Systems*, Kluwer Academic Publishers, Petersburg, 1993.

[16] Lakaev S.N., Motovilov A.K., Abdukhakimov S.Kh. Two-fermion lattice Hamiltonian with first and second nearest-neighboring-site interactions. *J. Phys. A: Math.*, 2023, **56**, P. 315202.

[17] Akhmadova M.O., Azizova M.A. Spectral analysis of two-particle Hamiltonians with short-range interactions. *Nanosystems: Phys. Chem.Math.*, 2025, **16**(5), P. 577–585.

[18] Lakaev S.N., Latipova D.A., Akhmadova M.O. On the existence of the maximum number of isolated eigenvalues for a lattice Schrödinger operator. *Nanosystems: Phys. Chem.Math.*, 2025, **16**(6), P. 737–748.

Submitted 14 October 2025; revised 26 January 2026; accepted 19 February 2026

Information about the authors:

Saidakhmat N. Lakaev – Samarkand State University, Samarkand, 140104, Uzbekistan; V. I. Romanovskiy Institute of Mathematics, Uzbekistan Academy of Sciences, Tashkent, Uzbekistan; ORCID 0000-0003-4951-9340; slakaev@mail.ru

Saidakbar Kh. Abdukhakimov – Samarkand State University, Samarkand, 140104, Uzbekistan; V. I. Romanovskiy Institute of Mathematics, Uzbekistan Academy of Sciences, Tashkent, Uzbekistan; ORCID 0009-0008-0400-7193; abduxakimov93@mail.ru

Adkham B. Khasanov – Samarkand State University, Samarkand, 140104, Uzbekistan; ORCID 0000-0003-4734-8920; atham.xasanov@mail.ru

Conflict of interest: the authors declare no conflict of interest.

NANOSYSTEMS:
PHYSICS, CHEMISTRY, MATHEMATICS

Original article

Tukhtabaev A.M. *Nanosystems: Phys. Chem. Math.*, 2026, **17** (2), 153–164.
http://nanojournal.ifmo.ru
DOI 10.17586/2220-8054-2026-17-2-153-164

Weakly periodic measure and phase transition: q-state p-adic Potts model on the Cayley tree of order k

Akbarkhuja M. Tukhtabaev[1,2]

[1]Namangan State University, P.O. Box, 160107, 161 Bobursho street, Namangan, Uzbekistan

[2]Kimyo International University in Tashkent Branch Namangan, 75 A Chortoq street, Namangan, Uzbekistan

akbarxoja.toxtaboyev@mail.ru

Corresponding author: A. M. Tukhtabaev, akbarxoja.toxtaboyev@mail.ru

PACS 517.98

ABSTRACT In this paper, we investigate weakly periodic p-adic quasi Gibbs measures for the q-state Potts model on the Cayley tree of order k. Furthermore, we demonstrate that for all $q \geq 3$ and $k \geq 2$, there exist a prime number p and a parameter θ that guarantee the occurrence of a phase transition.

KEYWORDS p-adic numbers; Potts model; p-adic quasi Gibbs measure; translation-invariant, periodic, weakly periodic Gibbs measure; phase transition.

ACKNOWLEDGEMENTS The author is grateful to Professor M.M. Rahmatullaev for his many helpful suggestions during the preparation of this paper. The author also thanks the anonymous referee for the careful reading of the manuscript and for many valuable comments and suggestions that helped to improve the quality of the paper.

FOR CITATION Tukhtabaev A.M. Weakly periodic measure and phase transition: q-state p-adic Potts model on the Cayley tree of order k. *Nanosystems: Phys. Chem. Math.*, 2026, **17** (2), 153–164.

1. Introduction

The application of p-adic analysis in the study of complex physical systems, particularly nanosystems, is motivated by the non-Archimedean nature of hierarchical structures [1, 2]. Nanomaterials often exhibit fragmented, fractal, or hierarchical energy landscapes where traditional Euclidean geometry fails to capture the underlying dynamics [3]. In this context, the p-adic metric provides a more natural framework for describing the ultrametricity inherent in disordered systems, such as spin glasses and polymers at the nanoscale [4]. This aligns with the fundamental work of G. Parisi and his collaborators, who established that the state space of complex disordered systems possesses a hierarchical, ultrametric structure [5, 6].

In nanoscience, the relaxation processes in complex molecules (e.g., proteins or nanoclusters) often occur through a hierarchy of energy barriers. As noted in the work of Avetisov (et al.), the transition dynamics between states in these systems can be modeled using p-adic diffusion equations [7]. The p-adic Gibbs measure, as explored in this paper, provides the statistical foundation for understanding equilibrium states in such hierarchical models, offering a more accurate representation of thermodynamic stability in non-Archimedean state spaces [8].

The p-adic Potts model on a Cayley tree serves as a powerful mathematical abstraction for analyzing interactions within branched polymers and dendrimers [9]. Dendrimers are nanoscopic, highly branched macromolecules whose structural symmetry is perfectly mirrored by the topology of the Cayley tree, also known as the Bethe lattice. The topological congruence between these nanostructures and the Cayley tree makes the study of phase transitions-specifically the existence of multiple Gibbs measures-essential for predicting how “information” or “energy” is distributed across these molecular networks under non-Archimedean temperature constraints. Such theoretical insights are increasingly crucial for the development of molecular electronics and the design of functional nanomaterials [10]. By investigating the q-state p-adic Potts model, this research provides a rigorous mathematical framework to evaluate the stability of thermodynamic phases in hierarchical molecular assemblies, offering a predictive toolset for future simulations of nanostructured systems.

While traditional statistical mechanics uses the field of real numbers $\mathbb{R}$, p-adic mathematical physics, as pioneered by Volovich and Khrennikov, suggests that at the Planck scale or within specific disordered media, the geometry of space-time or state-space may be non-Archimedean [1, 11]. For Nanosystems, this is particularly relevant in:
Quantum dots and tunneling: Where discrete energy levels and hierarchical transitions dominate [12].
Molecular dynamics: Where the “basins of attraction” in a protein’s folding landscape form an ultrametric space [7, 13].

By analyzing the q-state p-adic Potts model, this research contributes to the theoretical understanding of phase transitions in systems where interactions follow a hierarchical logic. This provides a rigorous mathematical toolset for future simulations of nanostructured materials and hierarchical molecular assemblies [14].

The Potts model is used in many areas, including magnetism, physics, image processing, medicine, sociology, biology and social dynamics (see e.g., [15]).

The p-adic Potts model was initially studied on the integers $\mathbb{Z}$ (see [16]), and the existence of a phase transition was proven when $| q |_p < 1$. This model was first studied on a Cayley tree in [17]. In that paper, it has been proven that there is a unique Gibbs measure when $| q |_p = 1$, and at least two Gibbs measures when $| q |_p < 1$. Subsequently, the research moved forward with [18], which introduced the notion of a p-adic quasi Gibbs measure. Furthermore, this paper achieved two significant goals: it classified the p-adic interpretation of phase transition into three separate categories, and it provided a rigorous demonstration of a strong phase transition for the model when situated on the binary tree.

Subsequent academic contributions have concentrated on various specialized aspects of the model, including: the examination of the chaotic behavior associated with the p-adic Potts-Bethe mapping ([19–21]), the analysis of translation-invariant p-adic Gibbs measures ([22, 23]), studies related to periodic p-adic quasi Gibbs measures ([24–26]), the construction and study of non-periodic, constructive measures ([25, 27–29]). Related investigations also addressed weakly periodic Gibbs measures defined over the real numbers ([30, 31]) and explored weakly periodic p-adic quasi Gibbs measures as applied to the Ising model ([32, 33]). Most recently, for the 3-state Potts model on the binary tree, [34] successfully demonstrated that a phase transition occurs when $p > 3$, and a quasi phase transition is present when $p = 3$.

Several recent studies [35–37] have extensively investigated various lattice models, such as the mixed spin-1/2 and spin-1 Ising model, the three-state SOS model with one-level competing interactions, and the Hard-Core-Potts model. These investigations were primarily conducted within the framework of the real number field $\mathbb{R}$, where the authors established specific conditions for the occurrence of phase transitions on the Cayley tree.

In [38], the authors investigated translation-invariant p-adic quasi Gibbs measures for the q-state Potts model with an external field on a Cayley tree of order two and established the conditions for phase transitions. In contrast, the present paper explores a broader class of weakly periodic p-adic quasi Gibbs measures for the q-state Potts model without an external field on a Cayley tree of an arbitrary order $k \geq 2$, rigorously demonstrating that a phase transition always occurs under certain parameter regimes.

This paper extends the foundational work of [34] by focusing on weakly periodic p-adic quasi Gibbs measures for the q-state Potts model defined on the Cayley tree of order k. Detailed in Sections 4 and 5, a significant discovery is the proof establishing the occurrence of a phase transition phenomenon for all configurations where $q \geq 3$ and $k \geq 2$, provided certain values of p and θ are present.

2. Preliminaries

2.1. p-adic numbers and measures

For the field of rational numbers, $\mathbb{Q}$, and a predetermined prime p, any $x \in \mathbb{Q} \setminus \{0\}$ possesses a representation $x = p^r \dfrac{n}{m}$, where $r \in \mathbb{Z}$, $m \in \mathbb{Z}^+$, and n, m are integers such that $\gcd(n, p) = \gcd(m, p) = 1$.

The p-adic norm on $\mathbb{Q}$, defined as $| x |_p = p^{-r}$ for non-zero $x = p^r \dfrac{n}{m}$ and $| 0 |_p = 0$, is a non-Archimedean valuation. Consequently, it adheres to the strong triangle inequality, which states that $| x + y |_p \leq \max\{| x |_p, | y |_p\}$.

Later, we will use the following important properties of the p-adic norm:
1) if $| x |_p \neq | y |_p$, then $| x \pm y |_p = \max\{| x |_p, | y |_p\}$;
2) if $| x |_p = | y |_p$, then $| x \pm y |_p \leq | x |_p$.

The field of rational numbers, $\mathbb{Q}$, is incomplete with respect to the p-adic norm. The completion of $\mathbb{Q}$ under this norm results in the construction of the field of p-adic numbers, $\mathbb{Q}_p$. Every non-zero p-adic number y possesses a unique canonical expansion:

$$y = p^{\gamma(y)}(y_0 + y_1 p + y_2 p^2 + ...),$$

where the p-adic valuation $\gamma(y) \in \mathbb{Z}$ and the coefficients y_j satisfy $0 < y_0 \leq p - 1$ and $0 \leq y_j \leq p - 1$ for $j \geq 1$. The p-adic norm is extended to $\mathbb{Q}_p$ as $| y |_p = p^{-\gamma(y)}$, where $\gamma(y)$ is also denoted as $\mathrm{ord}_p(y)$.

Let a be an element of the p-adic field $\mathbb{Q}_p$ and let $r > 0$. We define the open ball $B(a, r)$, the closed ball $\overline{B(a, r)}$, and the sphere $S(a, r)$ centered at a with radius r as the sets:

$$B(a, r) = \{x \in \mathbb{Q}_p : | x - a |_p < r\},$$
$$\overline{B(a, r)} = \{x \in \mathbb{Q}_p : | x - a |_p \leq r\},$$
$$S(a, r) = \{x \in \mathbb{Q}_p : | x - a |_p = r\}.$$

The sets $\mathbb{Z}_p := \overline{B(0, 1)}$ and $\mathbb{Z}_p^* = S(0, 1)$ are respectively called *p-adic integers* and *p-adic units*.

p-adic *exponential* is defined by

$$\exp_p(x) = \sum_{n=0}^{\infty} \frac{x^n}{n!},$$

which converges for $x \in B(0, p^{-1/(p-1)})$.

Put

$$\mathcal{E}_p = \left\{ x \in \mathbb{Q}_p : \mid x - 1 \mid_p < p^{-1/(p-1)} \right\}.$$

The set $\mathcal{E}_p$ is a range of exponential. A more detailed see [39], [1].

Lemma 1. *(Hensel's lemma) [40,41] Let $F(x)$ be a polynomial whose coefficients are p-adic integers. Let x^* be a p-adic integer such that for some $i \geq 0$ one has*

$$F(x^*) \equiv 0 (\operatorname{mod} p^{2i+1}), \quad F'(x^*) \equiv 0 (\operatorname{mod} p^i), \quad F'(x^*) \not\equiv 0 (\operatorname{mod} p^{i+1}).$$

Then $F(x)$ has a p-adic integer root x_* such that $x_* \equiv x^* (\operatorname{mod} p^{i+1})$.

The symbol $o[x]$ was adopted in the work [42] to facilitate simplified computations. By definition, $z = o[x]$ means that $\mid z \mid_p < \mid x \mid_p$.

Let $\mathbb{F}_p = \{1, 2, ...p - 1\}$. It is known [43] that, $\mathbb{F}_p$ is a group under the multiplication. Let $a \in \mathbb{Z}_p^*$, $k = mp^s$ and

$$Sol_p(x^k - a) = \{\xi \in \mathbb{F}_p : \xi^k - a = o[1]\}, \quad \kappa_p = card(Sol_p(x^k - a)) = (m, p - 1),$$

here (c, d) is the greatest common divisor of c and d.

Theorem 1. *[42,44] Let $p \geq 3$ and let $k = mp^s$, where $(p, m) = 1$, $s \geq 0$. Suppose that $a \in Z_p^*$ and it has the following canonical form:*

$$a = a_0 + a_1 p + a_2 p^2 + ...$$

with $Sol_p(x^k - a) \neq \emptyset$. Then the followings conditions are equivalent:

i) *$x^k = a$ has a solution;*

ii) *$a = a_0^{p^s} + o[p^s]$;*

iii) *for any $\xi \in Sol_p(x^k - a)$ the equation $x^k = a$ has a unique solution in $B(\xi, 1)$.*

Moreover, if the equation $x^k = a$ has a solution, then its number of solutions equals $\kappa_p = (m, p - 1)$.

Note that, if $a \in \mathbb{Q}_p \setminus \mathbb{Z}_p^*$, after substituting $x = \dfrac{x_*}{\mid x \mid_p}$, $a = \dfrac{a_*}{\mid a \mid_p}$, we obtain the equation $x_*^k = a_*$ under condition $k \mid ord_p(a)$ (k divides $ord_p(a)$). Clear that here $a_* \in \mathbb{Z}_p^*$.

In [45], the equation $x^k = a$ was studied in $\mathbb{Q}_2$.

Let $(X, \mathcal{B})$ be a measurable space, where $\mathcal{B}$ represents an algebra of subsets of X. A function $\mu : \mathcal{B} \to \mathbb{Q}_p$ is termed a p-adic measure if it satisfies the property of finite additivity: for any finite collection of pairwise disjoint sets $A_1, A_2, \ldots, A_n \in \mathcal{B}$, the following equality holds:

$$\mu\left(\bigcup_{j=1}^{n} A_j\right) = \sum_{j=1}^{n} \mu(A_j).$$

Furthermore, if the total measure is unity ($\mu(X) = 1$), the p-adic measure is specifically referred to as a p-adic probability measure. A p-adic measure μ is defined as bounded if the supremum of the p-adic norm of the measures of all sets in the algebra is finite:

$$\sup\{\mid \mu(A) \mid_p : A \in \mathcal{B}\} < \infty.$$

2.2. Cayley tree

The Cayley tree Γ^k (where $k \geq 1$) is an infinite $(k + 1)$-regular graph, meaning every vertex has a degree of $k + 1$. Let V and L denote the vertex and edge sets, respectively. An edge $l = \langle x, y \rangle$ signifies that x and y are nearest neighbors. Given a fixed root $x_0 \in \Gamma^k$, $d(x, y)$ represents the length of the shortest path between x and y. We define the shells $W_n = \{x \in V : d(x, x_0) = n\}$ and the finite subgraph $V_n = \{x \in V : d(x, x_0) \leq n\}$, with L_n being the corresponding set of edges in V_n. For any vertex $x \in W_n$, $S(x)$ is the set of its direct successors (neighbors in W_{n+1}): $S(x) = \{y \in W_{n+1} : d(y, x) = 1\}$. The set of all neighbors of x is $S_1(x) = \{y \in V : d(y, x) = 1\}$, and the unique parent of x (the neighbor closer to the root) is denoted $x \downarrow = S_1(x) \setminus S(x)$ (see [46]).

3. p-adic quasi Gibbs measure for the Potts model

The model is defined over the p-adic numbers ($\mathbb{Q}_p$). States (Φ): Each vertex x on the graph V can be in one of q possible states, $\Phi = \{1, 2, \ldots, q\}$. Configuration ($\sigma$): A configuration is an assignment of states to the vertices. Ω_A is the set of all possible configurations on a subset A of vertices. Configuration union: The operation $(\sigma_{n-1} \vee \varphi^{(n)})$ provides a way to define a configuration on a larger set V_n by combining an existing configuration σ_{n-1} on the smaller set V_{n-1} with a configuration $\varphi^{(n)}$ on the boundary or complement $W_n = V_n \setminus V_{n-1}$. This is crucial for building the measure step-by-step toward the infinite system.

The (formal) Hamiltonian of the p-adic Potts model is defined by

$$H(\sigma)=J\sum_{\langle x,y\rangle\in L}\delta_{\sigma(x)\sigma(y)} \tag{1}$$

where $J\in B(0,p^{-1/(p-1)})$ is a coupling constant, $\langle x,\, y\rangle$ stands for nearest neighbor vertices and δ_{ij} is the Kronecker's symbol, i.e.

$$\delta_{ij}=\begin{cases}0, & \text{if } i\neq j,\\ 1, & \text{if } i=j.\end{cases}$$

Assume that $\mathbf{h}:V\to\mathbb{Q}_p^q$ is a mapping, i.e. $\mathbf{h}_x=(h_{1,x},h_{2,x},...,h_{q,x})$, where $h_{i,x}\in\mathbb{Q}_p$, $i\in\Phi$ and $x\in V$. Given $n\in\mathbb{N}$, we consider a sequence of p-adic probability measures $\mu_{\mathbf{h}}^{(n)}$ on Ω_{V_n} defined by

$$\mu_{\mathbf{h}}^{(n)}(\sigma)=\frac{1}{Z_n^{(\mathbf{h})}}\exp_p\{H_n(\sigma)\}\prod_{x\in W_n}h_{\sigma(x),x}, \tag{2}$$

where $\sigma\in\Omega_{V_n}$, and $Z_n^{(\mathbf{h})}$ is the corresponding normalizing factor

$$Z_n^{(\mathbf{h})}=\sum_{\sigma\in\Omega_{V_n}}\exp_p\{H_n(\sigma)\}\prod_{x\in W_n}h_{\sigma(x),x}. \tag{3}$$

We say that p-adic probability measures (2) are compatibly if all $n\in\mathbb{N}$ and $\sigma_{n-1}\in\Omega_{V_{n-1}}$:

$$\sum_{\varphi^{(n)}\in\Omega_{W_n}}\mu_{\mathbf{h}}^{(n)}(\sigma_{n-1}\vee\varphi^{(n)})=\mu_{\mathbf{h}}^{(n-1)}(\sigma_{n-1}). \tag{4}$$

We notice that a non-Archimedean analogue of the Kolmogorov's extension theorem was proved in [16]. According to this theorem if (4) holds, then there exists a unique splitting p-adic measure μ_h on Ω such that for all $n\in\mathbb{N}$ and $\sigma\in\Omega_{V_{n-1}}$,

$$\mu(\sigma\in\Omega:\sigma|_{V_n}\equiv\sigma_n)=\mu_{\mathbf{h}}^{(n)}(\sigma_n),\ \text{for all } \sigma_n\in\Omega_{V_n},\ n\in\mathbb{N}.$$

Such measure is called a *p-adic quasi Gibbs measure* corresponding to the Hamiltonian (1) and vector-valued function $\mathbf{h}_x$, $x\in V$. By $QG(H)$ we denote the set of all p-adic quasi Gibbs measure associated with function $\mathbf{h}=\{\mathbf{h}_x,x\in V\}$. If all values of h_x belong to the set $\mathcal{E}_p$ then corresponding measure be *p-adic Gibbs measure* (see [18]).

The following statement is equivalent to compatibility of $\mu_{\mathbf{h}}^{(n)}$.

Theorem 2. *[18] The p-adic probability measures $\mu_h^{(n)}, n\in\mathbb{N}$ are defined by* (2) *satisfy the compatibility condition* (4) *if and only if for any $n\in\mathbb{N}$ the following equation holds:*

$$\widehat{\boldsymbol{h}_x}=\prod_{y\in S(x)}F(\widehat{\boldsymbol{h}_y},\theta), \tag{5}$$

here a vector $\widehat{\boldsymbol{h}}=\left(\widehat{h}_1,\widehat{h}_2,...,\widehat{h}_{q-1}\right)\in\mathbb{Q}_p^{q-1}$ is defined by a vector $\boldsymbol{h}=(h_1,h_1,...,h_q)\in\mathbb{Q}_p^q$ as follows

$$\widehat{h}_i=\frac{h_i}{h_q},\ i=1,2,...,q-1 \tag{6}$$

and mapping
$F:\mathbb{Q}_p^{q-1}\times\mathbb{Q}_p\to\mathbb{Q}_p^{q-1}$ is defined by $F(x;\theta)=(F_1(x;\theta),...,F_{q-1}(x;\theta),1)$ with

$$F_i(x;\theta)=\frac{(\theta-1)x_i+\sum\limits_{j=1}^{q-1}x_j+1}{\sum\limits_{j=1}^{q-1}x_j+\theta},\quad x=(x_1,x_2,...,x_{q-1})\in\mathbb{Q}_p^{q-1}, i=\overline{1,q-1}. \tag{7}$$

It is easy to check that the set of vectors $(\underbrace{h,...,h,h}_{m},1,...,1)$, $(m=1,...,q-1)$ is invariant for the right side of (5) as a mapping. Therefore, in what follows, we restrict ourselves to ones of such lines, let us say $(h,h,...,h,1)$.

4. Weakly periodic p-adic quasi Gibbs measure

Let G_k be a group of the free product of $k+1$ cyclic groups of the second order with generators $a_1,a_2,...,a_{k+1}$, respectively. There exists a one-to-one correspondence between the set of vertices V of the Cayley tree Γ^k and the group G_k (see [47]). Let G_k^* be a normal subgroup of the group G_k and $G_k/G_k^*=\{H_1,H_2,...,H_r\}$, $r\geq 1$ is a quotient group of G_k by G_k^*.

Definition 1. *A set $h=\{h_x,x\in G_k\}$ of quantities is called G_k^*-periodic if $h_x=h_i$, for all $x\in H_i$. A G_k-periodic quantities are called translation-invariant.*

Definition 2. *A set of quantities* $h = \{h_x, x \in G_k\}$ *is called* G_k^**-weakly periodic if* $h_x = h_{ij}$*, for any* $x \in H_i$ *and* $y_\downarrow \in H_j$.

Definition 3. *A* p*-adic quasi Gibbs measure* μ *is said to be* G_k^**-(weakly) periodic if it corresponds to a* G_k^**-(weakly) periodic* h*. A* G_k*-periodic measure is called a translation-invariant measure.*

Let

$$H_A = \{x \in G_k : \sum_{i \in A} \omega_x(a_i) \text{ is an even number}\},$$

where $\emptyset \neq A \subseteq N_k = \{1, 2, 3, ..., k+1\}$, and $\omega_x(a_i)$ is the number of letters a_i in a word $x \in G_k$. Note that H_A is a normal subgroup of the G_k (see [46]). It can be checked that weakly periodic Gibbs measure depends on choosing the normal subgroup of G_k. In real case, different weakly periodic Gibbs measures are found (see [30], [31]). The set of weakly periodic Gibbs measures also includes the set of periodic (in particular translation-invariant) Gibbs measures.

H_A is a normal divisor of index 2 in G_k, i.e. $G_k/H_A = \{H_0, H_1\}$ (see [46]). If $\mid A \mid = k+1$ (where $\mid A \mid$ is the number of elements of the set A), i.e. $A = N_k$, then weakly periodic measure coincides with $G_k^{(2)}$-periodic measure. Therefore, we consider $A \subset N_k$ such that $A \neq N_k$. H_A-weakly periodic collection $\mathbf{h}_x$ has the following form

$$\mathbf{h}_x = \begin{cases} \mathbf{h}_1, & \text{if } x \in H_0, \ x_\downarrow \in H_0, \\ \mathbf{h}_2, & \text{if } x \in H_0, \ x_\downarrow \in H_1, \\ \mathbf{h}_3, & \text{if } x \in H_1, \ x_\downarrow \in H_0, \\ \mathbf{h}_4, & \text{if } x \in H_1, \ x_\downarrow \in H_1, \end{cases} \tag{8}$$

where $H_0 = H_A$ and $H_1 = G_k \setminus H_A$ [46].
We assume that $\mathbf{h}_i = \left(h_i^{(1)}, h_i^{(2)}, ..., h_i^{(q-1)}, 1\right)$. Let $h_i^{(j)} = h_i, \ j = \overline{1, q-1}, \ i = \overline{1, 4}$. Using (5) and (8), we can obtain following system of the equations

$$\begin{cases} h_1 = \left(\frac{(\theta+q-2)h_1+1}{(q-1)h_1+\theta}\right)^{k-|A|} \cdot \left(\frac{(\theta+q-2)h_2+1}{(q-1)h_2+\theta}\right)^{|A|}, \\ h_2 = \left(\frac{(\theta+q-2)h_3+1}{(q-1)h_3+\theta}\right)^{|A|-1} \cdot \left(\frac{(\theta+q-2)h_4+1}{(q-1)h_4+\theta}\right)^{k+1-|A|}, \\ h_3 = \left(\frac{(\theta+q-2)h_1+1}{(q-1)h_1+\theta}\right)^{k+1-|A|} \cdot \left(\frac{(\theta+q-2)h_2+1}{(q-1)h_2+\theta}\right)^{|A|-1}, \\ h_4 = \left(\frac{(\theta+q-2)h_3+1}{(q-1)h_3+\theta}\right)^{|A|} \cdot \left(\frac{(\theta+q-2)h_4+1}{(q-1)h_4+\theta}\right)^{k-|A|}. \end{cases} \tag{9}$$

For simplicity, let $\mid A \mid = 1$. In this case, we denote by H_{A_1} the set

$$H_{A_1} = \{x \in G_k : \omega_x(a_1) \text{ is an even number}\}.$$

Then (9) gives one

$$\begin{cases} h_1 = \left(\frac{(\theta+q-2)h_1+1}{(q-1)h_1+\theta}\right)^{k-1} \cdot \frac{(\theta+q-2)h_2+1}{(q-1)h_2+\theta}, \\ h_2 = \left(\frac{(\theta+q-2)h_4+1}{(q-1)h_4+\theta}\right)^{k}, \\ h_3 = \left(\frac{(\theta+q-2)h_1+1}{(q-1)h_1+\theta}\right)^{k} \\ h_4 = \frac{(\theta+q-2)h_3+1}{(q-1)h_3+\theta} \cdot \left(\frac{(\theta+q-2)h_4+1}{(q-1)h_4+\theta}\right)^{k-1}. \end{cases} \tag{10}$$

We consider the following operator $\mathcal{A} : \mathbb{Q}_p^4 \to \mathbb{Q}_p^4$ defined as

$$\begin{cases} h_1' = \left(\frac{(\theta+q-2)h_1+1}{(q-1)h_1+\theta}\right)^{k-1} \cdot \frac{(\theta+q-2)h_2+1}{(q-1)h_2+\theta}, \\ h_2' = \left(\frac{(\theta+q-2)h_4+1}{(q-1)h_4+\theta}\right)^{k}, \\ h_3' = \left(\frac{(\theta+q-2)h_1+1}{(q-1)h_1+\theta}\right)^{k} \\ h_4' = \frac{(\theta+q-2)h_3+1}{(q-1)h_3+\theta} \cdot \left(\frac{(\theta+q-2)h_4+1}{(q-1)h_4+\theta}\right)^{k-1}. \end{cases} \tag{11}$$

It is obvious that the sets of vectors

$$I_1 = \{\mathbf{h} = (h, h, h, h) \mid h \in \mathbb{Q}_p\}, \ \ I_2 = \{\mathbf{h} = (h_1, h_2, h_2, h_1) \mid h_1, h_2 \in \mathbb{Q}_p\}$$

are invariant in respect to the operator $\mathcal{A}$.

Clearly, the fixed points of the operator $\mathcal{A}$ on invariant set I_1 are translation-invariant solutions of (5), i.e.

$$h = \left(\frac{(\theta+q-2)h+1}{(q-1)h+\theta}\right)^{k}. \tag{12}$$

To find the fixed points of the operator $\mathcal{A}$ on the invariant set I_2, one should solve the following system of equations

$$\begin{cases} h_1 = \left(\frac{(\theta+q-2)h_1+1}{(q-1)h_1+\theta}\right)^{k-1} \cdot \frac{(\theta+q-2)h_2+1}{(q-1)h_2+\theta}, \\ h_2 = \left(\frac{(\theta+q-2)h_1+1}{(q-1)h_1+\theta}\right)^{k}. \end{cases} \tag{13}$$

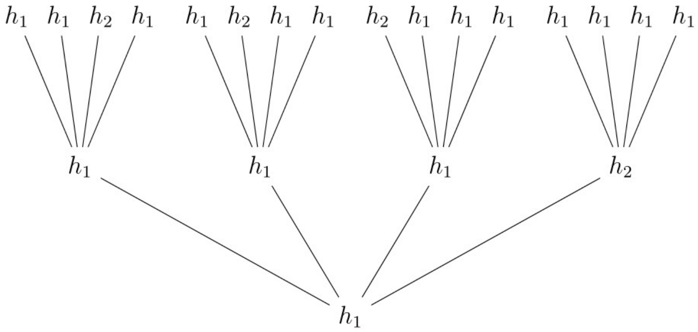

FIG. 1. This figure depicts the placement of values h_1 and h_2 associated with the invariant set I_2 on the Cayley tree of order four.

Using group representation of Cayley tree Γ^k, the values $h_x, x \in V$ corresponding to the invariant set I_2 are defined as follows:

(A). If at vertex x, we have $h_x = h_1$ then

$$h_y = \begin{cases} h_1, \text{ on } \ k-1 \ \text{ vertices of S(x)}; \\ h_2, \text{ on } \ 1 \ \text{ vertex of S(x)}, \end{cases} \tag{14}$$

(B). If at vertex x, we have $h_x = h_2$ then $h_y = h_1$, where $y \in S(x)$ (see Figure 1).

By the notation $\sqrt[k]{h_2} = x$, we get $h_1 = \frac{1-\theta x}{(q-1)x-(\theta+q-2)}$. It follows from the first equation of (13) that

$$\frac{1-\theta x}{(q-1)x-(\theta+q-2)} = x^{k-1} \cdot \frac{(\theta+q-2)x^k+1}{(q-1)x^k+\theta},$$

or

$$(q-1)(\theta+q-2)x^{2k} - (\theta+q-2)^2 x^{2k-1} + \theta(q-1)x^{k+1} - (\theta+q-2)x^{k-1} + \theta^2 x - \theta = 0. \tag{15}$$

Using notation $\sqrt[k]{h_2} = x$, one obtains from (12) that

$$(q-1)x^{k+1} - (\theta+q-2)x^k + \theta x - 1 = 0. \tag{16}$$

Factoring the left hand side of (15), we have

$$\big((q-1)x^{k+1} - (\theta+q-2)x^k + \theta x - 1\big) \cdot \big((\theta+q-2)x^{k-1} + \theta\big) = 0. \tag{17}$$

Finding non-translation weakly periodic solutions of (15) is equivalent to solving the following equation

$$x^{k-1} = -\frac{\theta}{\theta+q-2}, \tag{18}$$

where $\theta+q-2 \neq 0$.

Remark 1. *It is easy to see that if* k *is odd and* x^* *is a solution of* (18) *then* $-x^*$ *is also a solution of* (18).

Let $\theta = 1 + p^l(\theta_l + \theta_{l+1}p + ...), l \geq 1$, $a = -\dfrac{\theta}{\theta+q-2} = p^{\gamma(a)}(a_0 + a_1 p + ...), a_0 \neq 0$, (b,c) be the greatest common divisors of b, c and $k-1 = mp^s$, where $(m,p) = 1$, $s \in \{0,1,2,...\}$.

Theorem 3. *Let* $\mid q-1 \mid_p < 1$. *Then the following assertions hold*

- *if* $\mid \theta-1 \mid_p \neq \mid q-1 \mid_p$ *then the equation* (18) *is solvable iff*
  (1) $k-1$ *divides* $\gamma(a)$*;*
  (2) $a_0^{\frac{p-1}{(m,p-1)}} \equiv 1 (\operatorname{mod} p)$*;*
  (3) $a_0^{p^s} \equiv a \mid a \mid_p (\operatorname{mod} p^{s+1})$.

  Moreover, (18) *has* $\kappa_p = (m, p-1)$ *solutions and these solutions belong to* $p^{\frac{\gamma(a)}{k-1}}\mathbb{Z}_p^*$. *Here,* $\gamma(a) = -\min\{ord_p(\theta-1), ord_p(q-1)\}$ *and* $a_0 = (1-\theta) \mid \theta-1 \mid_p (\operatorname{mod} p)$ *if* $\mid \theta-1 \mid_p > \mid q-1 \mid_p$*;* $a_0 = (1-q) \mid q-1 \mid_p (\operatorname{mod} p)$ *if* $\mid \theta-1 \mid_p < \mid q-1 \mid_p$.
- *if* $\mid \theta-1 \mid_p = \mid q-1 \mid_p$, $\theta_l + q_l \neq p$ *or* $\mid \theta-1 \mid_p = \mid q-1 \mid_p$, $\theta_l + q_l = p$, $1 + \theta_{l+1} + q_{l+1} \neq p$ *then* (18) *is solvable iff*
  (1) $k-1$ *divides* $\gamma(a)$*;*
  (2) $a_0^{\frac{p-1}{(m,p-1)}} \equiv 1 (\operatorname{mod} p)$*;*
  (3) $a_0^{p^s} \equiv a \mid a \mid_p (\operatorname{mod} p^{s+1})$.

  Moreover, (18) *has* $\kappa_p = (m, p-1)$ *solutions and these solutions belong to* $p^{\frac{\gamma(a)}{k-1}}\mathbb{Z}_p^*$. *Here,* $q = 1 + p^l(q_l + q_{l+1}p + ...)$, $\gamma(a) = -ord_p(\theta-1)$, $a_0 = \dfrac{-1}{\theta_l + q_l} (\operatorname{mod} p)$ *if* $\theta_l + q_l \neq p$*;* $\gamma(a) = -ord_p(\theta-1) - 1$, $a_0 = \dfrac{-1}{1 + \theta_{l+1} + q_{l+1}} (\operatorname{mod} p)$ *if* $1 + \theta_{l+1} + q_{l+1} \neq p$.
- *if* $\mid \theta-1 \mid_p = \mid q-1 \mid_p$, $\theta_l + q_l = p$, $1 + \theta_{l+j} + q_{l+j} = p, j = 1,2,3,...r-1$, $r \geq 2$, $1 + \theta_{l+r} + q_{l+r} \neq p$ *then equation* (18) *is solvable iff*
  (1) $k-1$ *divides* $\gamma(a)$*;*
  (2) $a_0^{\frac{p-1}{(m,p-1)}} \equiv 1 (\operatorname{mod} p)$*;*
  (3) $a_0^{p^s} \equiv a \mid a \mid_p (\operatorname{mod} p^{s+1})$.

  Moreover, (18) *has* $\kappa_p = (m, p-1)$ *solutions and these solutions belong to* $p^{\frac{\gamma(a)}{k-1}}\mathbb{Z}_p^*$. *Here,* $q = 1 + p^l(q_l + q_{l+1}p + ...)$, $\gamma(a) = -ord_p(\theta-1) - r$, $a_0 = \dfrac{-1}{1 + \theta_{l+r} + q_{l+r}} (\operatorname{mod} p)$.
- *if* $\mid \theta-1 \mid_p = \mid q-1 \mid_p$, $\theta_l + q_l = p$, $1 + \theta_{l+j} + q_{l+j} = p, j \in \mathbb{N}$ *then the equation* (18) *does not have any solution.*

Proof. **Case 1.** Let $\mid \theta-1 \mid_p \neq \mid q-1 \mid_p$. We rewrite a as follows

$$a = \max\{\mid \theta-1 \mid_p, \mid q-1 \mid_p\} \cdot \begin{cases} \dfrac{1}{(1-\theta) \mid \theta-1 \mid_p} (\operatorname{mod} p) + o[1], & \text{if } \mid \theta-1 \mid_p > \mid q-1 \mid_p, \\ \dfrac{1}{(1-q) \mid q-1 \mid_p} (\operatorname{mod} p) + o[1], & \text{if } \mid \theta-1 \mid_p < \mid q-1 \mid_p. \end{cases} \tag{19}$$

(19) gives one that $\gamma(a) = -\min\{ord_p(\theta-1), ord_p(q-1)\}$ and $a_0 = (1-\theta) \mid \theta-1 \mid_p (\operatorname{mod} p)$ if $\mid \theta-1 \mid_p > \mid q-1 \mid_p$; $a_0 = (1-q) \mid q-1 \mid_p (\operatorname{mod} p)$ if $\mid \theta-1 \mid_p < \mid q-1 \mid_p$.

According to Theorem 1, (18) is solvable iff

- $k-1$ divides $\gamma(a)$;
- $a_0^{\frac{p-1}{(m,p-1)}} \equiv 1 (\operatorname{mod} p)$;
- $a_0^{p^s} \equiv a \mid a \mid_p (\operatorname{mod} p^{s+1})$.

Moreover, (18) has $\kappa_p = (m, p-1)$ solutions and these solutions belong to $p^{\frac{\gamma(a)}{k-1}}\mathbb{Z}_p^*$.

Case 2. $\mid \theta - 1 \mid_p = \mid q - 1 \mid_p$, i.e. $\theta = 1 + p^l(\theta_l + \theta_{l+1}p + ...)$ and $q = 1 + p^l(q_l + q_{l+1}p + ...)$. We rewrite a as follows

$$a = p^{-l}\left(-\frac{1 + p^l(\theta_l + \theta_{l+1}p + ...)}{(\theta_l + q_l) + (\theta_{l+1} + q_{l+1})p + ...}\right). \tag{20}$$

Case 2.1. Let $\theta_l + q_l \neq p$. In this case, we get $\gamma(a) = -ord_p(\theta - 1),\ a_0 = \frac{-1}{\theta_l + q_l}(\mathrm{mod}\, p)$. Due to Theorem 1, equation (18) is solvable iff

- $k - 1$ divides $\gamma(a)$;
- $a_0^{\frac{p-1}{(m,p-1)}} \equiv 1(\mathrm{mod}\, p)$;
- $a_0^{p^s} \equiv a \mid a \mid_p (\mathrm{mod}\, p^{s+1})$.

Moreover, (18) has $\kappa_p = (m, p-1)$ solutions and these solutions belong to $p^{\frac{\gamma(a)}{k-1}}\mathbb{Z}_p^*$.

Case 2.2. Let $\theta_l + q_l = p,\ 1 + \theta_{l+1} + q_{l+1} \neq p$. In this case, we get $\gamma(a) = -ord_p(\theta - 1) - 1,\ a_0 = \frac{-1}{1 + \theta_l + q_l}(\mathrm{mod}\, p)$. Due to Theorem 1, equation (18) is solvable iff

- $k - 1$ divides $\gamma(a)$;
- $a_0^{\frac{p-1}{(m,p-1)}} \equiv 1(\mathrm{mod}\, p)$;
- $a_0^{p^s} \equiv a|a|_p(\mathrm{mod}\, p^{s+1})$.

Moreover, (18) has $\kappa_p = (m, p-1)$ solutions and these solutions belong to $p^{\frac{\gamma(a)}{k-1}}\mathbb{Z}_p^*$.

Case 2.3. Let $\theta_l + q_l = p,\ 1 + \theta_{l+j} + q_{l+j} = p, j = 1, 2, 3, ...r - 1,\ r \geq 2,\ 1 + \theta_{l+r} + q_{l+r} \neq p$. In this case, we get $\gamma(a) = -l - r,\ a_0 = \frac{-1}{1 + \theta_{l+r} + q_{l+r}}(\mathrm{mod}\, p)$.

Again, due to Theorem 1, equation (18) is solvable iff

- $k - 1$ divides $\gamma(a)$;
- $a_0^{\frac{p-1}{(m,p-1)}} \equiv 1(\mathrm{mod}\, p)$;
- $a_0^{p^s} \equiv a|a|_p(\mathrm{mod}\, p^{s+1})$.

Moreover, (18) has $\kappa_p = (m, p-1)$ solutions and these solutions belong to $p^{\frac{\gamma(a)}{k-1}}\mathbb{Z}_p^*$.

Case 2.4. Let $\theta_l + q_l = p,\ 1 + \theta_{l+j} + q_{l+j} = p, j \in \mathbb{N}$. In this case, we have $\theta = 2 - q$ and equation (18) does not have any solution. □

The following example ensures that the set satisfying the conditions in Theorem 3 is nonempty.

Example 1. *a) Let* $p = 3,\ q = 2 \cdot 3^6 + 1,\ \theta = 3^{12} + 1,\ k = 7$. *Then we have* $x^6 = 3^{-6}(1 + o[1])$. *Therefore, in this case according to Theorem 1, equation* (18) *has two solutions in* $3^{-1}\mathbb{Z}_3^*$.

b) Let $p = 5,\ q = 1 + 2 \cdot 5^{20},\ \theta = 1 + 2 \cdot 5^{20} + 5^{21},\ k = 11$. *Then we have* $x^{10} = 5^{-20}(1 + o[1])$. *Therefore, in this case according to Theorem 1, equation* (18) *has two solutions in* $5^{-2}\mathbb{Z}_5^*$.

Theorem 4. *Let* $\mid q - 1 \mid_p = 1$. *Then equation* (18) *is solvable iff*

(1) $a_0^{\frac{p-1}{(m,p-1)}} \equiv 1(\mathrm{mod}\, p)$;
(2) $a_0^{p^s} \equiv a(\mathrm{mod}\, p^{s+1})$.

Moreover, equation (18) *has* $\kappa_p = (m, p-1)$ *solutions and these solutions belong to* $\mathbb{Z}_p^*$. *Here* $a_0 = \frac{1}{1-q}(\mathrm{mod}\, p)$.

Proof. Let $\mid q - 1 \mid_p = 1$. We rewrite a as follows

$$a = \frac{1}{1-q} + o[1], \tag{21}$$

where $\gamma(a) = 0$, $a_0 = \frac{1}{1-q}(\mathrm{mod}\, p)$. Again, due to Theorem 1, equation (21) gives one that equation (18) is solvable iff

- $a_0^{\frac{p-1}{(m,p-1)}} \equiv 1(\mathrm{mod}\, p)$;
- $a_0^{p^s} \equiv a(\mathrm{mod}\, p^{s+1})$.

Moreover, equation (18) has $\kappa_p = (m, p-1)$ solutions and these solutions belong to $\mathbb{Z}_p^*$. □

The following example ensures that the set satisfying the conditions in Theorem 4 is nonempty.

Example 2. *a) Let* $q = 5,\ p = 11,\ k = 6$. *Then we have* $x^5 = \dfrac{-\theta}{\theta+3}$ *and* $a_0 = 8$, $m = 5$, $s = 0$,

$$a_0^{\frac{p-1}{(m,p-1)}} \equiv 8^{\frac{10}{(5,10)}} (\bmod 11) \equiv 8^2 (\bmod 11) \not\equiv 1 (\bmod 11).$$

Therefore, according to Theorem 1, the equation $x^5 = \dfrac{-\theta}{\theta+3}$ *does not have any solution in* $\mathbb{Q}_{11}$.

b) Let $q = 5,\ p = 7,\ k = 6$. *Then we have* $x^5 = \dfrac{-\theta}{\theta+3}$ *and* $a_0 = 5$, $m = 5$, $s = 0$,

$$a_0^{\frac{p-1}{(m,p-1)}} \equiv 5^{\frac{6}{(5,6)}} (\bmod 7) \equiv 5^6 (\bmod 7) \equiv 1 (\bmod 7),$$

$a_0^{p^s} \equiv \dfrac{-\theta}{\theta+3} (\bmod 7)$ *or* $5 \equiv \dfrac{-\theta}{\theta+3} (\bmod 7)$, $1 + 6\theta \equiv 0 (\bmod 7)$. *Clearly, the last congruence holds. By Theorem 1, the equation* $x^5 = \dfrac{-\theta}{\theta+3}$ *has a unique solution in* $\mathbb{Q}_7$.

c) Let $q = 9,\ p = 7,\ k = 4$. *Then we have* $x^3 = \dfrac{-\theta}{\theta+7}$ *and* $a_0 = 6$, $m = 3$, $s = 0$,

$$a_0^{\frac{p-1}{(m,p-1)}} \equiv 6^{\frac{6}{(6,3)}} (\bmod 7) \equiv 6^2 (\bmod 7) \equiv 1 (\bmod 7),$$

$a_0^{p^s} \equiv \dfrac{-\theta}{\theta+7} (\bmod 7)$ *or* $6 \equiv \dfrac{-\theta}{\theta+7} (\bmod 7)$, $42 + 6\theta \equiv 0 (\bmod 7)$. *Clearly, the last congruence holds. By Theorem 1, the equation* $x^3 = \dfrac{-\theta}{\theta+7}$ *has tree solutions in* $\mathbb{Q}_7$.

Corollary 1. *Let* $p \geq 3$ *and* $\mid q \mid_p < 1$. *Then the following assertions hold*

- *if* $\mid k-1 \mid_p \leq \mid 2(\theta-1)+q \mid_p$, *then* (18) *does not have any solution;*
- *if* $\mid k-1 \mid_p > \mid 2(\theta-1)+q \mid_p$, *then* (18) *has exactly* $\kappa_p = (m, p-1)$ *solutions* $x_{\xi_i} \in B(\xi_i, 1)$, $i = 1, 2, ..., \kappa_p$, $\xi_i \in Sol_p(x^{k-1} - a)$. *Moreover, one of solutions of* (18) *belongs* $\mathcal{E}_p$.

Proof. The proof is straightforward by Corollary 3.5 in [42]. □

The following example ensures that the set satisfying the conditions in Corollary 1 is nonempty.

Example 3.

- *Let* $k = 10$, $p = 3$, $q = 6$, $\theta = 4$. *Then* $\mid k-1 \mid_p = \mid 9 \mid_3 = \dfrac{1}{9} < \dfrac{1}{3} = \mid 12 \mid_3 = \mid 2(\theta-1)+q \mid_p$ *and* (18) *does not have any solution.*
- *Let* $k = 10$, $p = 3$, $q = 6$, $\theta = 25$. *Then* $\mid k-1 \mid_p = \mid 9 \mid_3 = \dfrac{1}{9} > \dfrac{1}{27} = \mid 54 \mid_3 = \mid 2(\theta-1)+q \mid_p$ *and* (18) *has a unique (* $\kappa_3 = (m, p-1) = (1, 2) = 1$*) solution in* $\mathcal{E}_3$.
- *Let* $k = 19$, $p = 3$, $q = 6$, $\theta = 25$. *Then* $\mid k-1 \mid_p = \mid 18 \mid_3 = \dfrac{1}{9} > \dfrac{1}{27} = \mid 54 \mid_3 = \mid 2(\theta-1)+q \mid_p$ *and* (18) *has two (* $\kappa_3 = (m, p-1) = (2, 2) = 2$*) solutions. Moreover, one of them belongs to* $\mathcal{E}_3$, *another has the form* $-1 + o[1]$.

Theorem 5. *Let* $k \geq 2$, $q \geq 3$ *be fixed natural numbers. Then there exist prime* p *and* $\theta \in \mathcal{E}_p$, *such that equation* (18) *has at least one solution such that* $x^* \in Z_p^* \setminus \mathcal{E}_p$.

Proof. Let p be any prime such that

$$\mid q - i \mid_p = 1,$$

where $i = 0, 1, 2$. Note that there exists such a prime p, for instance, any prime greater than q may be such p ($p > q$). For this prime p, $k - 1 = mp^s$, where $s = 0, 1, 2, ...$

We can choose θ as follows

$$\theta = \frac{2 - q + (2-q)(1-q)^{p^s} p^{s+1}}{1 + (1-q)^{p^s} + (1-q)^{p^s} p^{s+1}}.$$

Since $(1-q)^{p^s} \equiv (1-q)(\bmod p)$, we have $\theta \in \mathcal{E}_p$. Then

$$a = -\frac{\theta}{\theta + q - 2} = \frac{1}{(1-q)^{p^s}} + p^{s+1},$$

i.e.

$$a = a_0^{p^s} + o[p^s],$$

where $a_0 = \dfrac{1}{1-q}(\bmod p)$. Since $a_0^{p^s} \equiv a_0 (\bmod p) \equiv \dfrac{1}{1-q}(\bmod p)$, we get $a \in \mathbb{Z}_p^* \setminus \mathcal{E}_p$. Therefore, in this case, according to Theorem 1, equation (18) has $\kappa_p = (m, p-1) \geq 1$ solutions in $\mathbb{Z}_p^* \setminus \mathcal{E}_p$. Because if the solution $x^* \in \mathcal{E}_p$ then ${x^*}^{k-1} = a \in \mathcal{E}_p$. However, $a \in \mathbb{Z}_p^* \setminus \mathcal{E}_p$. □

The following example demonstrates the practical application of Theorem 5.

Example 4. *Let* $k = 16$, $q = 9$. *We can choose prime* $p = 5$. *Then we get*

$$x^{15} = 268.$$

Let $w(x) := x^{15} - 268$, *then* $w(2) \equiv 0(\bmod 5^4)$, $w'(2) \equiv 0(\bmod 5) \not\equiv 0(\bmod 5^2)$. *Thanks to Hensel's lemma, the equation* $x^{15} = 268$ *has a unique solution such that* $x = 2 + o[5] \notin \mathcal{E}_5$.

5. A phase transition

If there are at least two distinct p-adic quasi Gibbs measures $\mu, \nu \in QG(H)$ such that μ is bounded and ν is unbounded, then we say that *a phase transition* occurs. Moreover, if there is a sequence of sets A_n such that $A_n \in \Omega_{V_n}$ with $| \mu(A_n) |_p \to 0$ and $| \nu(A_n) |_p \to \infty$ as $n \to \infty$, then we say that there occurs *a strong phase transition*. If all p-adic quasi Gibbs measures are bounded (or unbounded) it is said that *a quasi phase transition* occurs (see [18]).

In the present paper, we only investigate the phase transition for the p-adic Potts model.

The lemma below plays a key role in demonstrating the boundedness of the measure.

Lemma 2. *Let* $x^* \in Z_p^* \setminus \mathcal{E}_p$ *be the solution of* (18) *in Theorem 5. Then for* h_1 *and* h_2 *corresponding to* x^*, *the following statements hold*

(1) $| h_1 |_p = | h_2 |_p = 1$,
(2) $| (\theta + q - 2)h_1 + 1 |_p < 1$, $| (\theta + q - 2)h_2 + 1 |_p = 1$,

here p and θ *are defined as in the proof of Theorem 5.*

Proof. Since $x^* \in Z_p^* \setminus \mathcal{E}_p$, one has $| q - 1 |_p = 1$.

(1) By the notation given above $h_2 = {x^*}^k$, $h_1 = \dfrac{1 - \theta x^*}{(q-1)x^* - (\theta + q - 2)}$, we have

$$| h_2 |_p = | x^* |_p^k = 1,$$

$$| h_1 |_p = \frac{| 1 - \theta x^* |_p}{| (q-1)(x^* - 1) - (\theta - 1) |_p} = 1,$$

(2)

$$| (\theta + q - 2)h_2 + 1 |_p = | (\theta + q - 2){x^*}^k + 1 |_p = 1,$$

$$| (\theta + q - 2)h_1 + 1 |_p = \left| \frac{(\theta + q - 2)(1 - \theta x^*)}{(q-1)x^* - (\theta + q - 2)} + 1 \right|_p = \frac{| (1 - \theta)(\theta + q - 1)x^* |_p}{| (q-1)(x^* - 1) - (\theta - 1) |_p} < 1.$$

□

Theorem 6. *Weakly periodic p-adic quasi Gibbs measure* H_{A_1} *corresponding to pair* $\{h_1, h_2\}$ *in Lemma 2 is unbounded.*

Proof. Let $\mathcal{A}_1^{(n)}$, $\mathcal{A}_2^{(n)}$ be numbers of h_1, h_2 in V_n, respectively. (A) and (B) rules show that $\mathcal{A}_1^{(n)} \to \infty$, $\mathcal{A}_2^{(n)} \to \infty$ as $n \to \infty$. According to formula (66) in [34] and Lemma 2, we get

$$\lim_{n\to\infty} | \mu^{(n)}(\sigma) |_p = \lim_{n\to\infty} \frac{1}{| Z_1 |_p} \cdot \frac{| h_1 |_p^{\mathcal{A}_1^{(n)}} | h_2 |_p^{\mathcal{A}_2^{(n)}}}{| (\theta + q - 2)h_1 + 1 |_p^{\mathcal{A}_1^{(n)}} | (\theta + q - 2)h_2 + 1 |_p^{\mathcal{A}_2^{(n)}}}$$
$$= +\infty.$$

□

Remark 2. $h_0 = (1, 1, ...1)$ *is a translation invariant solution of* (5). *Using formula (66) in [34], it is easy to see that the measure* μ_0 *(corresponding to* h_0*) is bounded iff* $| q |_p = 1$. *For the considering case, due to Theorem* (5), *one has* $| q - i |_p = 1$, $i = 0, 1, 2$. *We deduce that* μ_0 *is bounded.*

Theorem 7. *Let* $k \geq 2$, $q \geq 3$ *be fixed natural numbers. Then for q-state Potts model on the Cayley tree of order k, there exist a prime p and a parameter* $\theta \in \mathcal{E}_p$ *that ensure a phase transition phenomenon.*

Proof. The proof is straightforward from Theorem 6 and Remark 2. □

Remark 3. *One should note that in the present paper, we solved the first open problem from [34] not only for binary tree, but also for the Cayley tree of order* $k \geq 2$.

6. Conclusion

In this paper, we have investigated the existence of p-adic Gibbs measures for the q-state p-adic Potts model on a Cayley tree of order k. By analyzing the functional equations associated with the model, we have rigorously proven the existence of weakly periodic p-adic quasi Gibbs measures. Our main result demonstrates a phase transition phenomenon for this model whenever $q \geq 3$ and $k \geq 2$, under specific conditions governed by the prime p and the model parameter θ. Unlike traditional Archimedean models, the p-adic approach allows for the capturing of non-Archimedean symmetries and ultrametricity, which are essential features of disordered complex systems.

From a broader perspective, these findings have significant implications for nanoscience, particularly in the study of nanostructured macromolecules such as dendrimers and branched polymers. Since the topological structure of a Cayley tree perfectly reflects the hierarchical branching of these nanomaterials, our results provide theoretical insights into how energy or information is distributed across such networks. The identification of phase transitions in p-adic models helps in understanding the stability of thermodynamic states in nanoscale systems where interactions follow a hierarchical rather than a purely Euclidean logic. This is crucial for predicting self-assembly processes and critical phenomena in molecular electronics.

Furthermore, the transition dynamics identified in this work provide a mathematical foundation for modeling relaxation processes in complex molecular landscapes, such as protein folding basins. Future research may extend this approach to explore p-adic models with competing interactions, external fields, or more complex lattice structures to further uncover the rich phase behavior of non-Archimedean physical systems.

References

[1] Vladimirov V.S., Volovich I.V., Zelenov E.V. *p-Adic Analysis and Mathematical Physics*. World Sci. Publ., Singapore, 1994, 392 p.

[2] Khrennikov A. *Non-Archimedean Analysis: Quantum Paradoxes, Subquantum Dynamics and Chaotic Dynamics*. Kluwer Academic Publishers, Dordrecht, 1997, 370 p.

[3] Anashin V., Khrennikov A. *Applied Algebraic Dynamics*. Walter de Gruyter, Berlin, 2009, 434 p.

[4] Rammal R., Toulouse G., Virasoro M.A. Ultrametricity for physicists. *Reviews of Modern Physics*, 1986, **58**(3), P. 765–788.

[5] Mezard M., Parisi G., Sourlas N., Toulouse G., Virasoro M. Nature of the spin-glass state. *Physical Review Letters*, 1984, **52**(13), P. 1156–1159.

[6] Mezard M., Parisi G., Virasoro M. *Spin Glass Theory and Beyond*. World Scientific Publishing Company, Singapore, 1987, 476 p.

[7] Avetisov V.A., Bikulov A.H., Kozyrev S.V., Osipov V.A. p-adic models of ultrametric diffusion constrained by hierarchical energy landscapes. *Journal of Physics A: Mathematical and General*, 2002, **35**(2), P. 177–189.

[8] Khrennikov A. *Information Dynamics in Cognitive, Psychological, Social, and Anomalous Phenomena*. Kluwer Academic Publishers, Dordrecht, 2004, 304 p.

[9] Khamraev M., Mukhamedov F.M., Rozikov U.A. On the uniqueness of Gibbs measure for p-adic Potts model on Bethe lattice. *Letters in Mathematical Physics*, 2004, **70**(1), P. 17–28.

[10] Grosberg A.Y., Khokhlov A.R. *Statistical Physics of Macromolecules*. AIP Press, New York, 1994, 350 p.

[11] Volovich I.V. p-adic string. *Classical and Quantum Gravity*, 1987, **4**(6), P. 83–87.

[12] Dragovich B., Volovich I.V. p-Adic models in quantum field theory and quantum cosmology. *Theoretical and Mathematical Physics*, 2008, **157**, P. 1625–1633.

[13] Frauenfelder H., Chan S.S., Chan W.Y. *Complexity and Hierarchy in Biochemistry*. American Institute of Physics, New York, 1991, 440 p.

[14] Kozyrev S.V. *Methods and Applications of Ultrametric and p-adic Analysis: From Theoretical Physics to Biology*. Selected topics, 2010, 156 p.

[15] Rozikov U.A. *Gibbs measures in biology and physics: The Potts model*. World Sci. Publ., Singapore, 2023, 368 p.

[16] Ganikhodjayev N.N., Mukhamedov F.M., Rozikov U.A. Existence of phase transition for the Potts p-adic model on the set $\mathbb{Z}$. *Theor. Math. Phys.*, 2002, **130**(3), P. 425–431.

[17] Mukhamedov F.M., Rozikov U.A. On Gibbs measures of p-adic Potts model on the Cayley tree. *Indag. Mathem., N.S.*, 2004, **15**(1), P. 85–100.

[18] Mukhamedov F. On dynamical systems and phase transitions for $q + 1$-state p-adic Potts model on the Cayley tree. *Math. Phys. Anal. Geom.*, 2013, **16**, P. 49–87.

[19] Mukhamedov F., Khakimov O. Phase transition and chaos: p-adic Potts model on a Cayley tree. *Chaos, Solitons and Fractals*, 2016, **87**, P. 190–196.

[20] Mukhamedov F., Khakimov O. Chaotic behavior of the p-adic Potts-Bethe mapping II. *Ergodic Theory and Dynamical Systems*, 2021, **41**, P. 2153–2177.

[21] Mukhamedov F., Khakimov O. Chaotic behavior of the p-adic Potts-Bethe mapping. *Discrete and Continuous Dynamical Systems - Series S*, 2018, **38**(1), P. 231–245.

[22] Rozikov U.A., Khakimov O.N. Description of all translation-invariant p-adic Gibbs measures for the Potts model on a Cayley tree. *Markov Processes and Related Fields*, 2015, **21**(1), P. 177–204.

[23] Saburov M., Ahmad M.A.K. On descriptions of all translation invariant p-adic Gibbs measures for the Potts model on the Cayley tree of order three. *Math. Phys. Anal. Geom.*, 2015, **18**, P. 26–44.

[24] Mukhamedov F., Khakimov O. On periodic Gibbs measure of p-adic Potts model on a Cayley tree. *p-Adic Num. Ultrametr. Anal. Appl.*, 2016, **3**, P. 225–235.

[25] Tukhtabaev A.M. On G_2-periodic quasi Gibbs measures of p-adic Potts model on a Cayley tree. *p-Adic Numbers, Ultrametric Analysis and Applications*, 2021, **13**, P. 291–307.

[26] Rahmatullaev M.M., Tukhtabaev A.M. On periodic p-adic generalized Gibbs measures for Ising model on a Cayley tree. *Letters in Mathematical Physics*, 2022, **112**, P. 1–18.

[27] Rahmatullaev M.M., Khakimov O.N., Tukhtaboev A.M. A p-Adic generalized Gibbs measure for the Ising model on a Cayley tree. *Theor. Math. Phys.*, 2019, **201**(1), P. 1521–1530.

[28] Rahmatullaev M.M., Tukhtabaev A.M. Non periodic p-adic generalized Gibbs measure for the Ising model. *p-Adic Numbers Ultrametric Anal. Appl.*, 2019, **11**, P. 319–327.

[29] Rahmatullaev M.M., Tukhtabaev A.M. Some non-periodic p-adic generalized Gibbs measures for the Ising model on a Cayley tree of order k. *Math. Phys. Anal. Geom.*, 2023, **26**(22), P. 1–23.

[30] Rozikov U.A., Rahmatullaev M.M. Description of weakly periodic Gibbs measures for the Ising model on a Cayley tree. *Theor. Math. Phys.*, 2008, **156**(2), P. 1218–1227.

[31] Rahmatullaev M.M. The existence of weakly periodic Gibbs measures for the Potts model on a Cayley tree. *Theor. Math. Phys.*, 2014, **180**(3), P. 1019–1029.

[32] Abdukaxorova Z.T. The existence of weakly periodic p-adic generalized Gibbs measures for Ising model on a Cayley tree of order two. *Bulletin of the Institute of Mathematics*, 2023, **6**, P. 1–7.

[33] Rahmatullaev M.M., Abdukaxorova Z.T. H_A-weakly periodic p-adic generalized Gibbs measures for Ising model on a Cayley tree. *Lobachevskii Journal of Mathematics*, 2024, **1**, P. 504–517.

[34] Rahmatullaev M.M., Tukhtabaev A.M., Samijonova N.D. Weakly periodic p-adic quasi-Gibbs measures for the Potts model on a Cayley tree. *Letters in Mathematical Physics*, 2024, **114**, P. 129–148.

[35] Rahmatullaev M.M., Egamov D.O. Translation-invariant Gibbs measures for the mixed spin-1/2 and spin-1 Ising model with an external field on a Cayley tree. *Nanosystems: Phys. Chem. Math.*, 2024, **15**(5), P. 576–585.

[36] Karshiboev O.Sh., Rahmatullaev M.M. The phase transition for the three-state SOS model with one-level competing interactions on the binary tree. *Nanosystems: Phys. Chem. Math.*, 2025, **16**(2), P. 134–141.

[37] Khakimov R.M., Makhammadaliev M.T., Mutalliev N.N. Phase transition and thermodynamic properties of the Hard-Core-Potts model. *Nanosystems: Phys. Chem. Math.*, 2026, **17**(1), P. 5–16.

[38] Rahmatullaev M.M., Samijonova N.D. Translation-invariant p-adic quasi Gibbs measures for the Potts model with an external field on the Cayley tree. *Nanosystems: Phys. Chem. Math.*, 2025, **16**(2), P. 164–175.

[39] Schikhof W.H. *Ultrametric Calculus*. Cambridge Univ. Press, Cambridge, 1984, 318 p.

[40] Borevich Z.I., Shafarevich I.R. *Number Theory*. Academic Press, New York, 1966, 435 p.

[41] Koblitz N. *p-Adic Numbers, p-Adic Analysis, and Zeta-Functions*. Springer, Berlin, 1977, 122 p.

[42] Mukhamedov F., Khakimov O. p-adic monomial equations and their perturbations. *Izvestiya Math.*, 2020, **84**(2), P. 348–360.

[43] Rosen K.H. *Elementary Number Theory and Its Applications*. Pearson, 2011, 768 p.

[44] Mukhamedov F.M., Saburov M. On equation $x^k = a$ over $\mathbb{Q}_p$. *Journal of Number Theory*, 2013, **133**, P. 55–58.

[45] Khakimov O.N., Abdullaeva G.Sh. On dynamics of 2-adic Ising-Potts mapping and its applications. *Bull. Inst. Math.*, 2021, **4**(5), P. 9–17.

[46] Rozikov U.A. *Gibbs measures on Cayley trees*. World Sci. Publ., Singapore, 2013, 404 p.

[47] Ganikhodjayev N.N. The group representation and automorphisms of the Cayley tree. *DAN Uz*, 1994, **4**, P. 3–5.

Submitted 4 December 2025; revised 22 March 2026; accepted 26 March 2026

Information about the authors:

Akbarkhuja M. Tukhtabaev – Namangan State University, P.O. Box, 160107, 161 Boburshoh street, Namangan, Uzbekistan; Kimyo International University in Tashkent Branch Namangan, 75 A Chortoq street, Namangan, Uzbekistan; ORCID 0000-0001-8855-9199; akbarxoja.toxtaboyev@mail.ru

Conflict of interest: the authors declare no conflict of interest.

NANOSYSTEMS:
PHYSICS, CHEMISTRY, MATHEMATICS

Original article

Anbarasu P., et al. *Nanosystems: Phys. Chem. Math.*, 2026, **17** (2), 165–171.
http://nanojournal.ifmo.ru
DOI 10.17586/2220-8054-2026-17-2-165-171

Oscillation results for second-order delay differential equation with several deviating arguments

P. Anbarasu[1,a], R. Sakthivel[1,b]

[1]PG & Research Department of Mathematics, Pachaiyappa's College, Chennai-600030, India

[a]isomorpanbu@gmail.com, [b]varshusakthi@gmail.com

Corresponding author: P. Anbarasu, isomorpanbu@gmail.com

Abstract The oscillatory behaviour of all solutions to the second-order delay differential equation with several deviating arguments and non negative coefficients is studied. Some sufficient oscillation conditions are obtained. An example is also given to illustrate the significance of our main results.

Keywords second-order delay differential equation; non-monotone arguments; oscillatory solution.

Acknowledgements The authors sincerely thank the anonymous referee for the careful evaluation, insightful remarks, and constructive suggestions, which have greatly enhanced the structure and overall quality of the manuscript.

For citation Anbarasu P., Sakthivel R. Oscillation results for second-order delay differential equation with several deviating arguments. *Nanosystems: Phys. Chem. Math.*, 2026, **17** (2), 165–171.

1. Introduction

Delay differential equations (DDEs) play an essential role in the mathematical modeling of dynamical systems where aftereffects, memory, or delayed responses are inherent. In nanosystems, delay effects frequently appear in nanoelectromechanical systems (NEMS), where the coupling between electronic circuits and mechanical oscillators introduces time-delayed feedback that significantly influences system stability and oscillatory behavior. For instance, time-delayed feedback control has been shown to govern the dynamics of nonlinear nanomechanical resonators and can induce or suppress oscillations depending on system parameters. Moreover, nanoscale heat transport and thermodynamic processes often exhibit memory effects that are effectively described using delay-differential formulations, especially in materials with internal relaxation and thermal lag.

Delay differential models also arise in nanoscale chemical kinetics and nanoparticle synthesis processes, where reaction rates and precipitation mechanisms depend on delayed interactions and diffusion effects. Such delay-driven models have been successfully applied to describe precipitation reactions, industrial chemical synthesis, and nanoscale reaction-diffusion systems. A comprehensive overview of the relevance of delay differential equations in nanoscale systems and their applications in physics and engineering can be found in recent interdisciplinary studies linking delay dynamics with nanoscience, see for example [1–5] and the references therein.

Motivated by both theoretical significance and practical applications in nanoscale systems, this paper investigates the oscillatory behavior of solutions of the second-order delay differential equation with several deviating arguments of the form

$$y''(x)+\sum_{i=1}^{m}p_i(x)y(u_i(x))=0, \qquad for \quad x\geq x_0>0, \tag{1}$$

where, p_i, $i=1,2,3,...,m$, are functions of non negative real numbers and u_i, $1\leq i\leq m$ are non-monotone functions of positive real numbers such that

$$u_i(x)<x,\, x\geq 0 \quad and \quad \lim_{x\to\infty} u_i(x)=\infty,\, 1\leq i\leq m. \tag{2}$$

and

$$\begin{aligned} v_i(x)=\sup_{s\leq x} u_i(s), \quad v(x)=\max_{1\leq i\leq m} v_i(x), \quad x\geq x_0,\\ u(x)=\max_{1\leq i\leq m} u_i(x) \quad with \quad u_i(x)\leq v_i(x). \end{aligned} \tag{3}$$

A continuously differentiable function defined on $[x_0,\infty)$, is called a solution of (1), if it satisfies (1) for almost all $x>x_0$. Any solution of (1) belongs oscillate class, if it has infinitely many zeros or large number of zeros, otherwise it is non oscillatory. Our equation (1) is oscillatory if all of its solutions oscillate, otherwise it is non oscillatory.

The first systematic study for the oscillation of all solutions of the first order delay differential equation,

$$y'(x) + p(x)y(u(x)) = 0, \quad x > x_0 > 0, \tag{4}$$

was made by Myshkis [6]. Later, several authors have studied (4) the situation when $u(x)$ is non-increasing and not necessarily monotone see, for example [7–10]. Some authors obtained oscillation results for (4) with constant delay $\beta_i > 0$, see [11]. A few authors have also investigated (4) with variable delays of the form $(x - \alpha_i(x))$, see [12]. In recent years, Gyori and Ladas studies (4) under the assumptions that $\alpha_i(x)$ are non-decreasing functions, for details, see [13]. Later, many authors considered the equation

$$y'(x) + \sum_{i=1}^{m} p_i(x)y(u_i(x)) = 0, \tag{5}$$

and investigated oscillation properties for non-decreasing and non-monotone arguments $u_i(x)$, for example, see [14–22]. Some authors have discussed the special case of (1) when $m = 1$, see [23] for more details.

In the present paper, we are interested in obtaining oscillation conditions for (5) instead of the first-order equation we take the second-order equation of the form (1).

2. Main results

The proof of our main results are essentially based on the following Lemmas.

Gronwall Inequality: If $y'(x) + p(x)y(x) \le 0,\ x \ge x_0$ where $p(x) > 0$ and $y(x) \ge 0$, then one has

$$y(x) \le y(t) \exp\left\{ \int_{x}^{t} p(s)ds \right\},\ x \ge t \ge x_0. \tag{6}$$

Lemma 1. *Suppose that* $\Delta > 0$ *and* (3) *holds. Then*

$$\liminf_{x\to\infty} \int_{v(x)}^{x} \sum_{j=1}^{m} \int_{v_j(s)}^{s} \sum_{i=1}^{m} p_i(s_1)ds_1ds = \liminf_{x\to\infty} \int_{u(x)}^{x} \sum_{j=1}^{m} \int_{u_j(s)}^{s} \sum_{i=1}^{m} p_i(s_1)ds_1ds = \Delta. \tag{7}$$

Proof. Use Lemma 2.2.1 in [24], to complete the proof. □

Lemma 2. *Let* (3) *hold and* $y(x)$ *be an eventually positive solution of* (1).

If $\Delta > \dfrac{1}{e}$ *then*

$$\liminf_{x\to\infty} \frac{y(v(x))}{y(x)} = \infty,$$

If $\Delta \le \dfrac{1}{e}$ *then*

$$\liminf_{x\to\infty} \frac{y(v(x))}{y(x)} \ge \Theta, \tag{8}$$

where Θ *is the least root of*

$$\Theta = e^{\Delta\Theta}. \tag{9}$$

Proof. Use Lemma 2.2.2 in [24], to complete the proof. □

Lemma 3. *Assume that* $y(x)$ *is a positive solution of* (1). *Denote,*

$$\varphi_{r+1}(x,t) := \exp\left\{ \int_{t}^{x} \sum_{j=1}^{m} \int_{v_j(s)}^{s} \sum_{i=1}^{m} p_i(s_1)\varphi_r(s_1, u_i(s_1))ds_1ds \right\}, \quad r \in \mathbb{N}. \tag{10}$$

with $\varphi_0(x,t) = 1$. *Then*

$$y(x)\varphi_r(x,t) \le y(t), \quad 0 \le t \le x. \tag{11}$$

Proof. The proof is similar to that of Lemma 1, in [15]. □

Theorem 1. *Assume that* $p_i(x) \ge 0,\ 1 \le i \le m$ *and* (2), (3) *are valid. If*

$$\liminf_{x\to\infty} \int_{v(x)}^{x} \sum_{j=1}^{m} \int_{v_j(s)}^{s} \sum_{i=1}^{m} p_i(s_1)ds_1ds > 1, \tag{12}$$

then all solutions of (1) *oscillate.*

Proof. Assume that $y(x)$ be an eventually positive solution of (1). From (1), $y''(x) \leq 0$ and then $y'(x) > 0$, if suppose, $y' < 0$, then for some $l \in \mathbb{R}^+$ we see $y'(x) = -l$ and integrating this over $[x_1, x]$, we obtain

$$y(x) = (y(v(x_1)) - lx_1) - x.$$

Hence, $y(x) \to -\infty$ as $x \to \infty$ but this makes no sense with $y(x) > 0$, as was assumed. So $y'(x) > 0$ which means $y(x)$ is non-decreasing. Integrating (1) over $[u_j(x), x]$, one gets

$$y'(x) - y'(v(x)) \leq y'(x) \leq -y(v(x)) \int\limits_{v_j(x)}^{x} \sum_{i=1}^{m} p_i(s_1) ds_1 \leq - \int\limits_{v_j(x)}^{x} \sum_{i=1}^{m} p_i(s_1) y(u_i(s_1)) ds_1 ds. \tag{13}$$

From the above inequality, one takes

$$\sum_{j=1}^{m} \int\limits_{v_j(x)}^{x} \sum_{i=1}^{m} p_i(s_1) y(u_i(s_1)) ds_1 \leq y'(v(x)).$$

Again integrating over $[v(x), x]$,

$$\left\{ \int\limits_{v(x)}^{x} \sum_{j=1}^{m} \int\limits_{v_j(s)}^{s} \sum_{i=1}^{m} p_i(s_1) ds_1 ds \right\} y(v(x)) \leq y(v(x)) - y(v(v(x))) \tag{14}$$

For $y(x) > 0$, finally, we reach

$$\liminf_{x \to \infty} \int\limits_{v(x)}^{x} \sum_{j=1}^{m} \int\limits_{v_j(s)}^{s} \sum_{i=1}^{m} p_i(s_1) ds_1 ds \leq 1,$$

a contradiction to (10), and hence the proof is completed. □

Theorem 2. *Assume that* $p_i(x) \geq 0,\ 1 \leq i \leq m$ *and* (2), (3) *are valid. If*

$$\liminf_{x \to \infty} \int\limits_{v(x)}^{x} \sum_{j=1}^{m} \int\limits_{v_j(s)}^{s} \sum_{i=1}^{m} p_i(s_1) ds_1 ds > \frac{1}{e} \tag{15}$$

then all solutions of (1) *oscillate.*

Proof. Assume that $y(x)$ be an eventually positive solution of (1). Divide (13) by $y(x)$ and integrate over $[v(x), x]$, then by taking simple steps, one obtains

$$\int\limits_{v(x)}^{x} \sum_{j=1}^{m} \int\limits_{v_j(s)}^{s} \sum_{i=1}^{m} p_i(s_1) ds_1 ds \leq \ln \left[\frac{y(v(x))}{y(x)} \right]. \tag{16}$$

In view of (15), there exists a constant $c > 0$ such that

$$\int\limits_{v(x)}^{x} \sum_{j=1}^{m} \int\limits_{v_j(s)}^{s} \sum_{i=1}^{m} p_i(s_1) ds_1 ds \geq c > \frac{1}{e}.$$

Using the above inequality in (16) and then taking exponential, one comes to the following inequality

$$y(v(x))/y(x) \geq e^c > ec > 1.$$

Repeating the above argument for large x, one obtains

$$y(v(x)) \geq (ec)^2 y(x).$$

Continuing these steps, we come to the issue that there exists a number $a \in \mathbb{N}$, satisfying $a > 2(\ln 2 - lnc)/(1 + \ln c)$, such that for sufficiently large x, we obtain

$$\frac{y(v(x))}{y(x)} > (ec)^a > \frac{4}{c^2}. \tag{17}$$

There exists a number $x_* \in (v(x), x)$ which satisfies the condition $y(v(x_*)) \leq v(x_*) \leq y(x)$. Consider this point as the splitting point of the integral in (15) into two equal parts as follows,

$$\int\limits_{v(x)}^{x_*} \sum_{j=1}^{m} \int\limits_{v_j(s)}^{s} \sum_{i=1}^{m} p_i(s_1) ds_1 ds \geq \frac{c}{2}; \qquad \int\limits_{x_*}^{x} \sum_{j=1}^{m} \int\limits_{v_j(s)}^{s} \sum_{i=1}^{m} p_i(s_1) ds_1 ds \geq \frac{c}{2}. \tag{18}$$

Integrating (13) over $[v(x), x_*]$ then using (18) with simple steps, one shows that

$$y(c(x_*)) \times \frac{c}{2} \leq y(v(x)). \tag{19}$$

Similarly, integrating (13) over $[x_*, x]$, by the same calculations as above we reach

$$y(v(x)) \times \frac{c}{2} \leq y(x_*). \tag{20}$$

Combining (19) and (20), we see the contradiction

$$\frac{y(v(x_*))}{y(x_*)} \leq \frac{4}{c^2}$$

to the inequality (17), and hence the Theorem is proved. □

Theorem 3. *Assume that* $p_i(x) \geq 0,\ 1 \leq i \leq m$, (2), (3) *and* (7) *hold. If, for some* $r \in \mathbb{N}$

$$\liminf_{x\to\infty} \int\limits_{v(x)}^{x} \sum_{j=1}^{m} \int\limits_{v_j(s)}^{s} \sum_{i=1}^{m} p_i(s_1)\varphi_r(v(s_1), u_i(s_1))ds_1 ds > \frac{1-\ln\Theta}{\Theta}, \tag{21}$$

where Θ *and* φ_r *are defined by* (9) *and* (10), *respectively. Under these conditions, all solutions of* (1) *oscillate.*

Proof. Assume that $y(x)$ be an eventually positive solution of (1). By Lemma 2, the inequality (8) is fulfilled. Therefore, for an arbitrary real number $0 < \epsilon < \Theta$ and for some $x^* \in (v(x), x)$, one gets for all $x > x_1 > x_0$

$$\frac{y(v(x))}{y(x)} > (\Theta - \epsilon); \qquad \frac{y(v(x))}{y(x^*)} = (\Theta - \epsilon). \tag{22}$$

Applying (11) to (1), one obtains

$$y''(x) + \sum_{i=1}^{m} p_i(x)\varphi_r(v(x), u_i(x))y(v(x)) = 0 \tag{23}$$

Integrating (23) over $[v_j(x), x]$, one gets

$$y'(x) - y'(v(x)) + \int\limits_{v_j(x)}^{x} \sum_{i=1}^{m} p_i(s_1)\varphi_r(v(s_1), u_i(s_1))y(v(s_1))ds_1 \leq 0 \tag{24}$$

Since $y'(x) > 0$, this implies

$$-y'(x) \leq y'(x) - y'(v(x)) + \int\limits_{v_j(x)}^{x} \sum_{i=1}^{m} p_i(s_1)\varphi_r(v(s_1), u_i(s_1))y(v(s_1))ds_1 \leq 0,$$

and, hence,

$$\int\limits_{v_j(x)}^{x} \sum_{i=1}^{m} p_i(s_1)\varphi_r(v(s_1), u_i(s_1))y(v(s_1))ds_1 \leq y'(x) \tag{25}$$

Let us divide (25) by $y(x)$ and integrate over $[v(x), x^*]$ for $v(x) < x^* < x$. Then using (22), we get

$$\int\limits_{v(x)}^{x^*} \sum_{j=1}^{m} \int\limits_{v_j(s)}^{s} \sum_{i=1}^{m} p_i(s_1)\varphi_r(v(s_1), u_i(s_1))ds_1 ds \leq -\frac{\ln(\Theta-\epsilon)}{(\Theta-\epsilon)} \tag{26}$$

Let us integrate (25) over $[x^*, x]$ once again. Using (22), we can obtain

$$\int\limits_{x^*}^{x} \sum_{j=1}^{m} \int\limits_{v_j(s)}^{s} \sum_{i=1}^{m} p_i(s_1)\varphi_r(v(s_1), u_i(s_1))ds_1 ds \leq \frac{1}{(\Theta-\epsilon)} \tag{27}$$

Adding (26) to (27), we get

$$\int\limits_{v(x)}^{x} \sum_{j=1}^{m} \int\limits_{v_j(s)}^{s} \sum_{i=1}^{m} p_i(s_1)\varphi_r(v(s_1), u_i(s_1))ds_1 ds \leq \frac{1-\ln(\Theta-\epsilon)}{(\Theta-\epsilon)}.$$

Then, for large x, letting $\epsilon \to 0$ and taking $liminf$, we get a contradiction with (21) and this completes the proof of the Theorem.

□

Corollary 1. *Assume that* $p_i \geq 0, 1 \leq i \leq m$, *and equations* (2), (3) *hold. If*

$$\limsup_{x\to\infty} \int\limits_{v(x)}^{x} \sum_{j=1}^{m} \int\limits_{v_j(s)}^{s} \sum_{i=1}^{m} p_i(s_1)\varphi_r(v(s_1), u_i(s_1))ds_1 ds > \frac{1}{\Theta}, \tag{28}$$

then all solutions of (1) *oscillate.*

Proof. Assume that $y(x)$ be an eventually positive solution of (1), so that by Lemma 2, the inequality (8) is fulfilled. Integrating (25) over $[v(x), x]$, we reach, for $y(x) > 0$,

$$\left[\int\limits_{v(x)}^{x} \sum_{j=1}^{m} \int\limits_{v_j(s)}^{s} \sum_{i=1}^{m} p_i(s_1)\varphi_r(v(s_1), u_i(s_1))ds_1 ds\right] y(v(x)) \leq y(x).$$

Then taking $limsup$ and using (8), we get

$$\limsup_{x\to\infty} \int\limits_{v(x)}^{x} \sum_{j=1}^{m} \int\limits_{v_j(s)}^{s} \sum_{i=1}^{m} p_i(s_1)\varphi_r(v(s_1), u_i(s_1))ds_1 ds \leq \frac{1}{\Theta},$$

which contradicts with (28). Hence, the Corollary is proved. □

3. Example

Example 4. *Consider the delay differential equation*

$$y''(x) + \frac{13}{100}y(u_1(x)) + \frac{21}{100}y(u_2(x)) = 0, \tag{29}$$

where

$$u_1(x) = \begin{cases} -x + 4n - 3.5, & \textit{if} \quad x \in [2n+1, 2n+2], \\ 3x - 4n - 11.5, & \textit{if} \quad x \in [2n+2, 2n+3] \end{cases} \quad \textit{and} \quad u_2(x) = u_1(x) - 1, \quad n \in \mathbb{N}.$$

Proof. From the equation and by (3)

$$v_1(x) = \begin{cases} 2n - 4.5, & \text{if} \quad x \in [2n+1, 2n+2.33], \\ 3x - 4n - 11.5, & \text{if} \quad x \in [2n+2.33, 2n+3] \end{cases} \quad \textit{and} \quad v_2(x) = v_1(x) - 1 \quad n \in \mathbb{N}.$$

Here, $v(x)$ attains its maximum at $x = 2n+3$, so $v(2n+3) = 2n - 2.5$ and by simple calculations, we get $\Delta = 19.635$. Hence $\Delta > 1$ so that the conditions (12) and (15) are satisfied, (29) is oscillatory and oscillation of solution of (29) is plotted in Fig.1(B). □

Example 5. *Consider the equation*

$$y''(x) + \frac{1}{2.2e}y(u_1(x)) + \frac{1}{2.4e}y(u_2(x)) = 0, \tag{30}$$

where

$$u_1(x) = \begin{cases} -2x + 6n + 2, & \textit{if} \quad x \in [2n+1, 2n+2], \\ 4x - 6n - 10, & \textit{if} \quad x \in [2n+2, 2n+3] \end{cases} \quad \textit{and} \quad u_2(x) = u_1(x) - 1, \quad n \in \mathbb{N}.$$

Proof. From the equation and by (3), it follows that

$$v_1(x) = \begin{cases} 2n, & \text{if} \quad x \in [2n+1, 2n+2.5], \\ 4x - 6n - 10, & \text{if} \quad x \in [2n+2.5, 2n+3] \end{cases} \quad \textit{and} \quad v_2(x) = v_1(x) - 1, n \in \mathbb{N}.$$

From (3), $\Delta = 0.3205$. Clearly, $\Delta \leq \frac{1}{e} = (0.3678)$. By (9), $\Theta \approx 1.755$. Define $f_r(x) : [1, \infty) \to (0, \infty)$ as

$$f_r(x) = \int\limits_{v(x)}^{x} \sum_{j=1}^{2} \int\limits_{v_j(s)}^{s} \sum_{i=1}^{2} p_i(s_1)\varphi_r(v(s_1), u_i(s_1))ds_1 ds.$$

Thus, for $r = 1$ and $v(2n+3) = 2n+2$, we have $f_1(x) = 26.0111$. Hence, conditions (21) and (28) are satisfied, hence, (30) is oscillatory. □

Example 6. *Consider the delay differential equation*

$$y''(x) + \frac{5}{x^3} y(u_1(x)) + \frac{7}{x^3} y(u_2(x)) = 0, \tag{31}$$

where

$$u_1(x) = \begin{cases} -x + 4n + 3, & \textit{if} \quad x \in [2n+1, 2n+2], \\ 3x - 4n - 5, & \textit{if} \quad x \in [2n+2, 2n+3] \end{cases} \quad \textit{and} \quad u_2(x) = u_1(x) - 1, n \in \mathbb{N}.$$

Proof. From the equation and by (3),

$$v_1(x) = \begin{cases} 2n + 2, & \text{if} \quad x \in [2n+1, 2n+2.35], \\ 3x - 4n - 5, & \text{if} \quad x \in [2n+2.35, 2n+3] \end{cases} \quad \textit{and} \quad v_2(x) = v_1(x) - 1, n \in \mathbb{N}.$$

Here $v(x)$ attains its maximum at $x = 2n+3$, so $v(2n+3) = 2n+4$. By simple calculation, we show that $\Delta < 0$ and so that the conditions (12) and (15) are not satisfied. Also we cannot apply conditions (21) and (28) for (31), which implies that it is non oscillatory, also non oscillation of solution of (31) is plotted in Fig.1(B). ☐

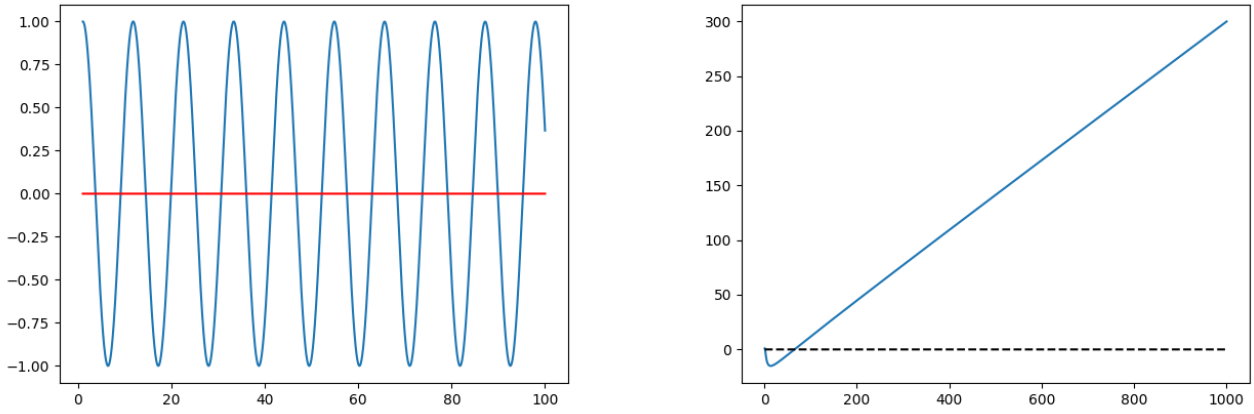

Oscillation of solution of (29)

Nonoscillation of solution of (31)

FIG. 1. Graphical representations

References

[1] Khasanov J., Muminov S., Iskandarov S. Mathematical modelling of industrial ammonia synthesis using nonlinear reaction-diffusion equations. *Nanosystems: Phys. Chem. Math.*, 2025, **16**(6), P. 749–754.

[2] Kumar S., Gandhi K.S. Modeling of precipiation reactions with time delays. *Chemical Engineering Science*, 1995, **50**(18), P. 2935–2948.

[3] Kyrychko Y.N., Blyuss K.B. Delay differential equations in nanoscale systems: From theory to applications. *Philosophical Traansactions of the Royal Society A*, 2020, **378**(2179), P. 20190275.

[4] Sellitto A., et. al. Heat transport with memory: A delay differential approach. *European Physical Journal B*, 2015, **88**, P. 210.

[5] Zhang W.M., et al. Time-delayed feedback control of a nonlinear nonmachanical resonator. *Physical Review B*, 2013, **87**(11), P. 115439.

[6] Myshkis A.D. Linear homogeneous differential equations of first order with deviating arguments. *Uspekhi Mat. Nauk*, 1950, **5**, P. 160–162.

[7] Agarwal R.P., Grace S.R. Oscillation theorems for certain neutral differential equations. *Comp. Math. Appl.*, 1999, **38**, P. 10–11.

[8] Arino O., Gyori I. Jawhari A. Oscillation criteria in delay equations. *J.Differential Equations*, 1984, **53**, P. 115–123.

[9] Koplatadze R.G., Chanturija T.A. Oscillating and monotone solutions of first order differential equations with deviating arguments (Russian). *Differentsial'nye Uravneniya*, 1982, **8**, P. 1463–1465.

[10] Laddas G., Lakshmikantham V., Papadakis J.S. Oscillations of higher-order retarded differential equations generated by retarded arguments. *Delay and Functional Differential Equations and Their Applications, Academic press, New York*, 1972, P. 219–231.

[11] Li B. Oscillations of first order delay differential equations. *Proc. Amer. Math. Soc.*, 1996, **124**, P. 3729–3737.

[12] Hunt B.R., Yorke, J.A. When all solutions of $x' = \sum q_i(t)x(t - T_i(t))$ oscillate.*J. Differential Equations*, 1984, **53**, P. 139–145.

[13] Gyori I., Ladas G. *Oscillation Theory of Delay Differential Equations With Applications*. Clarendon Press, Oxford, 1991.

[14] Akca H., Chatzarakis G.E., and Savroulakis I.P. An oscillation criteria for delay differential equations with several non-monotone arguments. *Appl. Math. Lett.*, 2016, **59**, P. 101–108.

[15] Braverman E., Chatzarakis G.E., Stavroulakis I.P. Iterative oscillation test for differential equations with several non-monotone arguments. *Advances in Difference equation*, 2016, **87**, P. 1–18.

[16] Chatzarakis G.E., Ocalan O., Ozturk S. Oscillations for differential equations with several deviating arguments. *Pacific Journal of Applied Mathematics*, 2015, **7**(2), P. 119–131.

[17] Chatzarakis G.E., Peicks H. Differential equation with several non-monotone arguments: An oscillation result. *Appl. Math. lett.*, 2017, **68**, P. 20–26.

[18] Braverman E., Karpuz B. On Oscillation of Differential and Difference Equations with non-monotone delays. *Appl. Math. Comp.*, 2011, **218**, P. 3880–3887.

[19] Fukagai N., Kusano T. Oscillation theory of first order functional differential equations with deviating arguments. *Ann. Mat. Pura Appl.*, 1984, **136**, P. 95–117.

[20] Stavroulakis I.P. A survey on the oscillation of differential equations with several deviating arguments. *J. Inequalities and Applications*, 2014, **2014**, P. 399.

[21] Ocalan O., Kilic N., Sahin S., Ozkan U.M. Oscillation of Nonlinear Delay Differential Equations with Non-monotone Arguments.*Int. Jour. of Anal. and Appl.* 2017, **14**(2), P. 147–154.

[22] Ocalan O., Kilic N., Kilic U., Ozkan U.M., Ozturk S. Oscillatory behaviour for nonlinear differential equations with several non-monotone arguments. *Comp. Meth. for Diff. Equa.*, 2020, **8**(01), P. 14–27.

[23] Baculikova B. Oscillation for second order differential equation with delay.*Elec. J. Diff. Equa.*, 2018, **96**, P. 1–9.

[24] Agarwal R.P., Bohner M., Li W.T. *Nonoscillation and oscillation: Theory for Functional Differential Equations*, Marcel Decker, New York, 2004.

Submitted 23 January 2026; revised 26 February 2026, 16 March 2026; accepted 17 March 2026

Information about the authors:

P.Anbarasu – PG & Research Department of Mathematics, Pachaiyappa's College, Chennai-600 030, India; ORCID 0009-0007-4402-7036; isomorpanbu@gmail.com

R.Sakthivel – PG & Research Department of Mathematics, Pachaiyappa's College, Chennai-600 030, India; ORCID 0000-0002-4973-5310; varshusakthi@gmail.com

Conflict of interest: the authors declare no conflict of interest.

NANOSYSTEMS:
PHYSICS, CHEMISTRY, MATHEMATICS

Original article

Irgashev B.Yu., et al. *Nanosystems: Phys. Chem. Math.*, 2026, **17** (2), 172–178.
http://nanojournal.ifmo.ru
DOI 10.17586/2220-8054-2026-17-2-172-178

The Cauchy problem for a fourth-order equation involving a fractional derivative in the Caputo sense

B. Yu. Irgashev[1,2]

[1]University of Business and Science, Namangan, Uzbekistan

[2]Institute of Mathematics named after V.I.Romanovsky of the Academy of Sciences of the Republic of Uzbekistan

bahromirgasev@gmail.com

Corresponding author: B. Yu. Irgashev, bahromirgasev@gmail.com

ABSTRACT In this article, the Cauchy problem in a half-plane is studied for a fourth-order inhomogeneous equation with a fractional derivative in the Caputo sense. The uniqueness of the solution is demonstrated using the Laplace transform. In constructing the solution, partial solutions expressed in terms of Wright functions are first found. Green's functions are then constructed using these partial solutions. The solution is constructed explicitly using the Green function. An explicit form of the fundamental solution is also obtained.

KEYWORDS Fourth-order equation, Cauchy problem, Caputo derivative, Wright function, asymptotics, fundamental solution, existence, uniqueness.

FOR CITATION Irgashev B.Yu. The Cauchy problem for a fourth-order equation involving a fractional derivative in the Caputo sense. *Nanosystems: Phys. Chem. Math.*, 2026, **17** (2), 172–178.

1. Introduction and statement of the problem

In recent decades, fractional calculus has evolved from a field of purely mathematical research into a powerful tool for modeling real physical processes. Fractional derivatives become particularly significant when describing phenomena in media with complex internal structures, memory, and nonlocal properties. As noted in [1], fractional dynamics investigates the behavior of objects and systems characterized by power-law nonlocality, power-law long-term memory, or fractal properties. Classical continuum models based on integer-order derivatives often prove inadequate when transitioning to the nanoscale, where effects of structural heterogeneity, anomalous transport, and viscoelastic relaxation begin to dominate. Work [2] provides a rigorous stochastic justification for this fact: the non-exponential relaxation of a single nanoobject naturally leads to the description of nanoparticle kinetics using differential equations with fractional derivatives.

It is noteworthy that the equation studied in this work is of particular interest for nanomechanics. Fourth-order equations traditionally describe the bending vibrations of beams, membranes, and plates [3]. In the nanoscale range, such models are applied to analyze the dynamics of nanobeams, nanofilms, and filamentary nanostructures situated in complex viscoelastic media. Study [4] investigates waves in magneto-elastic nanobeams using a fractional derivative to model internal damping, while nonlocal elasticity theory allows for the consideration of nanoscale size effects. In [5], a new mathematical model of thermoelasticity is proposed for analyzing coupled thermomechanical waves in functionally graded viscoelastic nanobeams. Works [6–8] also demonstrate that introducing fractional derivatives effectively accounts for the rheological properties of materials: [6] investigates nonlinear vibrations of beams made of fractional-order Zener viscoelastic material; [7] examines the vibrations of a nanobeam on a fractional-order viscoelastic Winkler-Pasternak foundation using nonlocal elasticity theory. In study [9], dedicated to an inverse problem for the heat conduction equation with a load, variable coefficients, and fractional integral operators, a mathematical method for analyzing heat transfer processes at the nanoscale is developed. Thus, the investigation of equations of type (1) holds not only theoretical but also direct applied significance for nanotechnologies.

This paper investigates the initial value problem for a fourth-order equation involving the Caputo fractional derivative. The Cauchy problem for second-order equations with a fractional derivative with respect to spatial variables (diffusion-wave equations) has been studied in considerable detail in works [10–14]. For equations with the Laplace operator and the Dzhrbashyan-Nersesyan fractional derivative of order $(0, 2)$, analogous results were obtained in [15], and for equations of odd order – in [16]. In [17], a solution to the Cauchy problem for an even-order equation with the Riemann-Liouville derivative of order $(0, 1)$ was obtained. A boundary value problem with the Caputo fractional derivative with applications in nanotechnologies was also investigated in [18].

Closely related to the topic of this work is the study [19], where the Cauchy problem for a homogeneous fourth-order equation with the Caputo fractional derivative was reduced to a Schrödinger equation by lowering the order of the fractional derivative. However, [19] did not consider the inhomogeneous equation, and the question of solution uniqueness remained open.

In contrast to the previous works, this paper proves a uniqueness theorem for the solution of the Cauchy problem, constructs particular solutions using the Wright function and, based on them, formulates the Green function, obtains an explicit integral representation of the solution for both the homogeneous and inhomogeneous equations, and provides the explicit form of the fundamental solution.

The proposed approach can be extended to equations of arbitrary even order, which opens up prospects for further research in the field of mathematical modeling of nanosystems, including problems concerning the dynamics of nanobeams, nanofilms, membranes, and other nanostructures in complex media with memory and nonlocal properties.

Let us proceed directly to the formulation of the problem. Consider the equation in the domain $\Omega = \{(x,y) : -\infty < x < \infty, 0 < y \le T\}$

$$L[u] \equiv \left({}_C D_{0y}^{\alpha} + \frac{\partial^4}{\partial x^4} \right) u = f(x,y), \tag{1}$$

where ${}_C D_{0y}^{\alpha}$ is the operator of fractional (in the Caputo sense) integro-differentiation of order α, $1 < \alpha < 2$, defined by the relation

$${}_C D_{0y}^{\alpha} u = D_{0y}^{\alpha-2} u_{yy} = \frac{1}{\Gamma(2-\alpha)} \int\limits_0^y \frac{\frac{\partial^2}{\partial \tau^2} u(x,\tau)}{(y-\tau)^{\alpha-1}} d\tau,$$

here $D_{0y}^{\alpha-2}$ is the operator of fractional differentiation in the sense of Riemann-Liouville [20].

A regular solution of equation (1) in the domain Ω is defined as a function $u = u(x,y)$ satisfying the conditions: $\frac{\partial^k u}{\partial x^k} \in C\left(\overline{\Omega}\right)$, $k = \overline{0,3}$; $\frac{\partial^4 u}{\partial x^4} \in C(\Omega)$; $\frac{\partial^m u}{\partial y^m} \in C\left(\overline{\Omega}\right)$, $m = \overline{0,1}$; ${}_C D_{0y}^{\alpha} u \in C(\Omega)$.

Cauchy Problem. Find a regular solution $u(x,y)$ of equation (1) in the domain Ω satisfying the initial conditions

$$\lim_{y \to +0} u(x,y) = \varphi(x), \lim_{y \to +0} \frac{\partial u(x,y)}{\partial y} = \psi(x), \tag{2}$$

where $\varphi(x), \psi(x)$ are given functions.

2. Uniqueness of solution

Theorem 1. The Cauchy problem with homogeneous initial conditions, in the class of functions satisfying the conditions $\left| \frac{\partial^m u}{\partial y^m} \right| \le M e^{\sigma y}$, $0 < M = const.$, $m = 0, 1$, where σ is a fixed constant, has only the trivial solution.

Proof. Let $u(x,y)$ be a solution of the Cauchy problem with zero initial conditions. Consider the Laplace transform of this function

$$v(x,p) = \int\limits_0^{+\infty} e^{-py} u(x,y)\, dy,$$

hence

$$|v(x,p)| \le M \int\limits_0^{+\infty} e^{-(p-\sigma)y} dy = \frac{M}{p-\sigma}.$$

Let us find the fourth-order partial derivative with respect to the variable x of the transform

$$\frac{\partial^4 v(x,p)}{\partial x^4} = \int\limits_0^{+\infty} e^{-py} \frac{\partial^4 u(x,y)}{\partial x^4} dy = -\int\limits_0^{+\infty} e^{-py} {}_C D_{0y}^{\alpha} u\, dy = -p^{\alpha} v(x,p).$$

From this, we obtain the problem

$$\begin{cases} \dfrac{\partial^4 v(x,p)}{\partial x^4} = -p^{\alpha} v(x,p), \\ |v(x,p)| \le \dfrac{M}{p-\sigma}. \end{cases} \tag{3}$$

The general solution of problem (3) has the form

$$v(x,p) = e^{Bx} (c_1 \cos Bx + c_2 \sin Bx) + e^{-Bx} (c_3 \cos Bx + c_4 \sin Bx), \quad B = \frac{\sqrt{2}}{2} p^{\frac{\alpha}{4}}.$$

By virtue of the condition of problem (3), we obtain

$$v(x,p) \equiv 0,$$

and consequently

$$u(x,y)\equiv 0.$$

Theorem 1 is proved.

3. Construction of the Solution

First, we construct some particular solutions. The following lemma holds.

Theorem 2. Functions of the form

$$u_j\left(x,y\right)=y^b\phi\left(-\frac{\alpha}{4},b+1;\lambda_jxy^{-\frac{\alpha}{4}}\right),\quad j=1,2,$$

where

$$\phi\left(-\delta,\varepsilon;z\right)=\sum_{k=0}^{\infty}\frac{z^k}{k!\Gamma\left(-\delta k+\varepsilon\right)}$$

is the Wright function;

$$x,y>0,b\in R,\lambda_1=e^{\frac{3\pi}{4}i},\lambda_2=e^{-\frac{3\pi}{4}i},$$

satisfy equation (1).

Proof. By direct calculation, we obtain

$$\frac{\partial^4u_j\left(x,y\right)}{\partial x^4}=-y^{b-\alpha}\phi\left(-\frac{\alpha}{4},b+1-\alpha;\lambda_jxy^{-\frac{\alpha}{4}}\right),\tag{4}$$

$$\frac{\partial^2u_j\left(x,y\right)}{\partial y^2}=y^{b-2}\phi\left(-\frac{\alpha}{4},b-1;\lambda_jxy^{-\frac{\alpha}{4}}\right).$$

Furthermore, since

$$\frac{1+\frac{\alpha}{4}}{2}\pi<\left|\arg\lambda_j\right|<\pi,$$

using formula [16]

$$D_{0y}^{\nu}y^{\varepsilon-1}\phi\left(-\delta,\varepsilon;\lambda y^{-\delta}\right)=y^{\varepsilon-\nu-1}\phi\left(-\delta,\varepsilon-\nu;\lambda y^{-\delta}\right),\tag{5}$$

for

$$0<\delta<1,\quad \frac{1+\delta}{2}\pi<\left|\arg\lambda\right|\leq\pi;\quad \varepsilon,\nu\in R,$$

we have

$$_CD_{0y}^{\alpha}u_j=D_{0y}^{\alpha-2}\left\{y^{b-2}\phi\left(-\frac{\alpha}{4},b-1;\lambda_jxy^{-\frac{\alpha}{4}}\right)\right\}=$$
$$y^{b-\alpha}\phi\left(-\frac{\alpha}{4},b+1-\alpha;\lambda_jxy^{-\frac{\alpha}{4}}\right).\tag{6}$$

From (4) and (6) the validity of Theorem 2 follows.

Theorem 2 is proved.

Let us recall some known properties (see [16]) of the Wright function:

$$\frac{d}{dz}\phi\left(\delta,\varepsilon;z\right)=\phi\left(\delta,\varepsilon+\delta;z\right),\quad (\delta>-1).\tag{7}$$

$$\left|\phi\left(-\delta,\varepsilon;z\right)\right|\leq C\exp\left(-\nu|z|^{\frac{1}{1-\delta}}\right),\quad |z|\to\infty,\tag{8}$$

where

$$C=C\left(\delta,\varepsilon,\nu\right),\quad \delta\in\left(0,1\right),\quad \varepsilon\in R,$$
$$\nu<\left(1-\delta\right)^{\frac{\delta}{1-\delta}}\cos\frac{\pi-|\arg z|}{1-\delta};\quad \frac{1+\delta}{2}\pi<|\arg z|\leq\pi.$$

$$\int\limits_0^{+\infty}\phi\left(-\delta,\varepsilon;\lambda x\right)dx=-\frac{1}{\lambda\Gamma\left(\delta+\varepsilon\right)},\quad \frac{1+\delta}{2}\pi<|\arg\lambda|\leq\pi.\tag{9}$$

Following works [16],[17], consider the following function

$$G_b\left(x-\xi,y-\eta\right)=-\frac{\lambda_1(y-\eta)^b}{4}\phi\left(-\frac{\alpha}{4},b+1;\lambda_1\frac{|x-\xi|}{(y-\eta)^{\frac{\alpha}{4}}}\right)-$$
$$-\frac{\lambda_2(y-\eta)^b}{4}\phi\left(-\frac{\alpha}{4},b+1;\lambda_2\frac{|x-\xi|}{(y-\eta)^{\frac{\alpha}{4}}}\right),\quad b\in R.\tag{10}$$

The following theorem holds.

Theorem 3. Let $\varphi(x)\in C^4(\mathbb{R})$, $\psi(x)\in C(\mathbb{R})$ and $\left|\varphi^{(k)}(x)\right|, |\psi(x)|\leq M=\text{const.}$, $k=0,\ldots,4$. Then the representation

$$u(x,y)=\int\limits_{-\infty}^{+\infty}G_{-\frac{\alpha}{4}}(x-\xi,y)\,\varphi(\xi)\,d\xi+\int\limits_{-\infty}^{+\infty}G_{-\frac{\alpha}{4}+1}(x-\xi,y)\,\psi(\xi)\,d\xi, \tag{11}$$

is a regular solution of the following Cauchy problem

$$\begin{cases} {}_CD_{0y}^{\alpha}u+u_{xxxx}=0,\\ \lim\limits_{y\to+0}u(x,y)=\varphi(x), \quad \lim\limits_{y\to+0}u_y(x,y)=\psi(x). \end{cases}$$

Proof. First, we show that (11) satisfies the initial conditions. We have

$$\int\limits_{-\infty}^{+\infty}y^{-\frac{\alpha}{4}}\phi\left(-\frac{\alpha}{4},-\frac{\alpha}{4}+1,\lambda_j\frac{|x-\xi|}{y^{\frac{\alpha}{4}}}\right)\varphi(\xi)\,d\xi=\left(j=1,2;\ t=\frac{|x-\xi|}{y^{\frac{\alpha}{4}}}\right)=$$

$$=\int\limits_{0}^{+\infty}\phi\left(-\frac{\alpha}{4},-\frac{\alpha}{4}+1,\lambda_j t\right)\left\{\varphi\left(x+y^{\frac{\alpha}{4}}t\right)+\varphi\left(x-y^{\frac{\alpha}{4}}t\right)\right\}dt,$$

now, taking into account (8), (9) and the restrictions on the function φ from the conditions of Theorem 2, we obtain

$$\lim_{y\to+0}\int\limits_{-\infty}^{+\infty}G_{-\frac{\alpha}{4}}(x-\xi,y)\,\varphi(\xi)\,d\xi=\varphi(x).$$

Furthermore, considering (5) and using (7), we have

$$\frac{\partial}{\partial y}\int\limits_{-\infty}^{+\infty}y^{-\frac{\alpha}{4}}\phi\left(-\frac{\alpha}{4},-\frac{\alpha}{4}+1,\lambda_j\frac{|x-\xi|}{y^{\frac{\alpha}{4}}}\right)\varphi(\xi)\,d\xi=$$

$$=\frac{-2\phi\left(-\frac{\alpha}{4},\frac{\alpha}{2},0\right)\varphi_{tt}(x)\,y^{-1+\frac{\alpha}{2}}}{\lambda_j^3}$$

$$+\frac{y^{-1+\alpha}}{\lambda_j^4}\int\limits_{0}^{+\infty}\left\{\varphi_{tttt}\left(x+y^{\frac{\alpha}{4}}t\right)+\varphi_{tttt}\left(x-y^{\frac{\alpha}{4}}t\right)\right\}\phi\left(-\frac{\alpha}{4},\frac{3\alpha}{4},\lambda_j t\right)dt,$$

now, taking into account (8)-(10), the restrictions on the function φ from the conditions of Theorem 2, and $\frac{1}{\lambda_1^2}+\frac{1}{\lambda_2^2}=0$, we obtain

$$\lim_{y\to+0}\frac{\partial}{\partial y}\int\limits_{-\infty}^{+\infty}G_{-\frac{\alpha}{4}}(x-\xi,y)\,\varphi(\xi)\,d\xi=0.$$

After performing similar transformations and calculations for the second term in representation (11), we obtain

$$\lim_{y\to+0}\int\limits_{-\infty}^{+\infty}G_{-\frac{\alpha}{4}+1}(x-\xi,y)\,\psi(\xi)\,d\xi=0,$$

$$\lim_{y\to+0}\frac{\partial}{\partial y}\int\limits_{-\infty}^{+\infty}G_{-\frac{\alpha}{4}+1}(x-\xi,y)\,\psi(\xi)\,d\xi=\psi(x).$$

Thus, representation (11) satisfies the initial conditions of the Cauchy problem.

Now we show that representation (11) satisfies the homogeneous equation (1). Taking into account (5) and formula [20]

$${}_CD_{0y}^{\alpha}f=D_{0y}^{\alpha}f-\frac{f(0)}{\Gamma(1-\alpha)}y^{-\alpha}-\frac{f'(0)}{\Gamma(2-\alpha)}y^{1-\alpha},$$

we have

$${}_CD_{0y}^{\alpha}u(x,y)=D_{0y}^{\alpha}\int\limits_{-\infty}^{+\infty}G_{-\frac{\alpha}{4}}(x-\xi,y)\,\varphi(\xi)\,d\xi-\frac{y^{-\alpha}}{\Gamma(1-\alpha)}\lim_{y\to+0}\int\limits_{-\infty}^{+\infty}G_{-\frac{\alpha}{4}}(x-\xi,y)\,\varphi(\xi)\,d\xi-$$

$$-\frac{y^{1-\alpha}}{\Gamma\left(2-\alpha\right)}\lim_{y\to+0}\frac{\partial}{\partial y}\int\limits_{-\infty}^{+\infty}G_{-\frac{\alpha}{4}}\left(x-\xi,y\right)\varphi\left(\xi\right)d\xi=$$

$$=\int\limits_{-\infty}^{+\infty}G_{-\frac{5\alpha}{4}}\left(x-\xi,y\right)\varphi\left(\xi\right)d\xi-\frac{y^{-\alpha}\varphi\left(x\right)}{\Gamma\left(1-\alpha\right)}. \tag{12}$$

Furthermore, by direct calculation we obtain

$$\frac{\partial^4}{\partial x^4}\left(\int\limits_{-\infty}^{+\infty}G_{-\frac{\alpha}{4}}\left(x-\xi,y\right)\varphi\left(\xi\right)d\xi\right)=$$

$$=\frac{y^{-\alpha}\varphi\left(x\right)}{\Gamma\left(1-\alpha\right)}-\int\limits_{-\infty}^{+\infty}y^{-\frac{5\alpha}{4}}\phi\left(-\frac{\alpha}{4},-\frac{5\alpha}{4}+1,\lambda_j\frac{\left|x-\xi\right|}{y^{\frac{\alpha}{4}}}\right)\varphi\left(\xi\right)d\xi. \tag{13}$$

From (12) and (13) we obtain

$${}_{C}D_{0y}^{\alpha}\left(\int\limits_{-\infty}^{+\infty}G_{-\frac{\alpha}{4}}\left(x-\xi,y\right)\varphi\left(\xi\right)d\xi\right)+\frac{\partial^4}{\partial x^4}\left(\int\limits_{-\infty}^{+\infty}G_{-\frac{\alpha}{4}}\left(x-\xi,y\right)\varphi\left(\xi\right)d\xi\right)=0.$$

It is shown similarly that

$${}_{C}D_{0y}^{\alpha}\left(\int\limits_{-\infty}^{+\infty}G_{-\frac{\alpha}{4}+1}\left(x-\xi,y\right)\psi\left(\xi\right)d\xi\right)+\frac{\partial^4}{\partial x^4}\left(\int\limits_{-\infty}^{+\infty}G_{-\frac{\alpha}{4}+1}\left(x-\xi,y\right)\psi\left(\xi\right)d\xi\right)=0.$$

Theorem 3 is proved.

Theorem 4. Let $f\left(x,y\right)=D_{0y}^{-\gamma}g\left(x,y\right)$, $\gamma>0$, $g\left(x,y\right)\in C\left(\overline{\Omega}\right)$, $\left|g\left(x,y\right)\right|\leq M=\text{const}$. Then the representation

$$u\left(x,y\right)=\int\limits_{0}^{y}d\eta\int\limits_{-\infty}^{+\infty}G_{\frac{3\alpha}{4}-1}\left(x-\xi,y-\eta\right)f\left(\xi,\eta\right)d\xi, \tag{14}$$

is a solution of the problem

$$\begin{cases} {}_{C}D_{0y}^{\alpha}u\left(x,y\right)+u_{xxxx}\left(x,y\right)=f\left(x,y\right), \\ \lim\limits_{y\to+0}u\left(x,y\right)=\lim\limits_{y\to+0}u_y\left(x,y\right)=0. \end{cases}$$

Proof. First, we show that representation (14) satisfies equation (1). We have

$$\frac{\partial}{\partial x^3}\int\limits_{0}^{y}d\eta\int\limits_{-\infty}^{+\infty}G_{\frac{3\alpha}{4}-1}\left(x-\xi,y-\eta\right)f\left(\xi,\eta\right)d\xi=$$

$$=\int\limits_{0}^{y}d\eta\int\limits_{-\infty}^{+\infty}\frac{\partial}{\partial x^3}G_{\frac{3\alpha}{4}-1}\left(x-\xi,y-\eta\right)f\left(\xi,\eta\right)d\xi,$$

taking into account the integration by parts formula [16]

$$\int\limits_{a}^{b}g\left(s\right)D_{as}^{\alpha}h\left(s\right)ds=\int\limits_{a}^{b}h\left(s\right)D_{bs}^{\alpha}g\left(s\right)ds,\quad \alpha\leq0,$$

we obtain

$$\frac{\partial}{\partial x}\int\limits_{0}^{y}d\eta\int\limits_{-\infty}^{+\infty}\frac{\partial}{\partial x^3}G_{\frac{3\alpha}{4}-1}\left(x-\xi,y-\eta\right)f\left(\xi,\eta\right)d\xi=$$

$$\frac{\partial}{\partial x}\int\limits_{0}^{y}d\eta\int\limits_{-\infty}^{+\infty}g\left(\xi,\eta\right)D_{y\eta}^{-\gamma}\left\{\frac{\partial}{\partial x^3}G_{\frac{3\alpha}{4}-1}\left(x-\xi,y-\eta\right)\right\}d\xi=$$

$$=f\left(x,y\right)-\int\limits_{0}^{y}d\eta\int\limits_{-\infty}^{+\infty}G_{\gamma-\frac{\alpha}{4}-1}\left(x-\xi,y-\eta\right)g\left(\xi,\eta\right)d\xi. \tag{15}$$

Next,

$$\frac{\partial^2}{\partial y^2}\int\limits_{-\infty}^{+\infty} d\xi \int\limits_0^y G_{\frac{3\alpha}{4}-1}\left(x-\xi, y-\eta\right) f\left(\xi,\eta\right) d\eta =$$

$$= \int\limits_{-\infty}^{+\infty} d\xi \int\limits_0^y G_{\frac{3\alpha}{4}-3+\gamma}\left(x-\xi, y-\eta\right) g\left(\xi,\eta\right) d\eta,$$

hence

$$D_{0y}^{\alpha-2}\int\limits_{-\infty}^{+\infty} d\xi \int\limits_0^y G_{\frac{3\alpha}{4}-3+\gamma}\left(x-\xi, y-\eta\right) g\left(\xi,\eta\right) d\eta =$$

$$= \int\limits_{-\infty}^{+\infty} d\xi \int\limits_0^y g\left(\xi,\eta\right) G_{-\frac{\alpha}{4}-1+\gamma}\left(x-\xi, t-\eta\right) d\eta. \tag{16}$$

From (15) and (16), it follows that

$$\left({}_C D_{0y}^{\alpha} + \frac{\partial^4}{\partial x^4}\right)\left\{\int\limits_0^y d\eta \int\limits_{-\infty}^{+\infty} G_{\frac{3\alpha}{4}-1}\left(x-\xi, y-\eta\right) f\left(\xi,\eta\right) d\xi\right\} = f\left(x,y\right).$$

We show that representation (14) satisfies the zero initial conditions. Let

$$I\left(x,y\right) = \int\limits_{-\infty}^{+\infty} d\xi \int\limits_0^y \left(y-\eta\right)^{\frac{3\alpha}{4}-1}\phi\left(-\frac{\alpha}{4}, \frac{3\alpha}{4}; \lambda_j \frac{|x-\xi|}{\left(y-\eta\right)^{\frac{\alpha}{4}}}\right) f\left(\xi,\eta\right) d\eta,$$

make the change of variables

$$z = \frac{|x-\xi|}{\left(y-\eta\right)^{\frac{\alpha}{4}}}, \quad \xi = x \pm z(y-\eta)^{\frac{\alpha}{4}}, \quad d\xi = \pm(y-\eta)^{\frac{\alpha}{4}} dz,$$

we have

$$I\left(x,y\right) = \int\limits_0^y \left(y-\eta\right)^{\alpha-1} d\eta \times$$

$$\int\limits_0^{+\infty} \phi\left(-\frac{\alpha}{4}, \frac{3\alpha}{4}; \lambda_j z\right)\left(f\left(x + z(y-\eta)^{\frac{\alpha}{4}}, \eta\right) + f\left(x - z(y-\eta)^{\frac{\alpha}{4}}, \eta\right)\right) dz,$$

hence

$$\lim_{y\to+0} I\left(x,y\right) = 0.$$

Similarly, we will have that

$$\lim_{y\to+0} \frac{\partial I\left(x,y\right)}{\partial y} = 0.$$

Theorem 4 is proved.

By Theorem 4, the function $G_{\frac{3\alpha}{4}-1}(x-\xi, y-\eta)$ is the fundamental solution of equation (1).

4. Conclusion

In this paper, we study the Cauchy problem for a fourth-order equation involving a fractional derivative in the sense of Caputo. In the case $\alpha = 2$, we have an equation for beam vibrations. The solution is constructed explicitly by finding Green's functions. Sufficient conditions for the existence and uniqueness of the solution are found. It should be noted that the question of the uniqueness of the solution to the Cauchy problem for the beam vibration equation remained open (see [3]). A fundamental solution to equation (1) is also constructed. In the future, the obtained results can be used to study boundary value problems for inhomogeneous linear and nonlinear equations, equations with lower-order terms, inverse problems with an unknown right-hand side, problems with nonlocal conditions, which have various applications in nanosystems. It should be noted that the problem under study has not only theoretical but also applied significance, since fractional integro-differential operators are widely used in mathematical models of nanosystem dynamics. In particular, among mathematical models of transport-diffusion, fractional differential calculus stands out as a tool for describing transport processes in media with a complex structure.

References

[1] Tarasov V.E. Review of some promising fractional physical models. *International Journal of Modern Physics B*, 2013, **27**(9), P. 1330005.

[2] Basharov A.M. The Stochastic foundation of the nanoparticle kinetic description by differential equations with fractional derivatives. *Nanosystems: Physics, Chemistry, Mathematics*, 2012, **3**(6), P. 47–63. (In Russ.)

[3] Sabitov K.B. Cauchy problem for the beam vibration equation. Differential Equations, 2017, **53**(5), P. 658–664.

[4] Selvamani R., Prabhakaran T., Yaylaci M. et al. Fractional nonlocal couple stress waves in magnetoelastic nanobeam using homotopy perturbation technique. Acta Mechanica, 2025, **236**, P. 5477-–5494.

[5] Abouelregal A.E., Marin M., Foul A. et al. Coupled responses of thermomechanical waves in functionally graded viscoelastic nanobeams via thermoelastic heat conduction model including Atangana–Baleanu fractional derivative. *Scientific Reports*, 2024, **14**(9122), P. 1–19.

[6] Lewandowski R. and Wielentejczyk P. Nonlinear vibration of viscoelastic beams described using fractional order derivatives. *Journal of Sound and Vibration*, 2017, **399**, P. 228–243.

[7] Eyebe G.J, Betchewe G., Mohamadou A., Kofane T.C. Nonlinear vibration of a nonlocal nanobeam resting on fractional-order viscoelastic Pasternak foundations. *Fractal and Fractional*, 2018, **2**(3), P. 21.

[8] Chong, N., Wang, L., Lei, D. et al. Nonlinear vibration of fractional viscoelastic piezoelectric nanobeams based on nonlocal theory. *Arch Appl Mech*, 2025, **95**(150), P. 1–18.

[9] Baltaeva U., Agarwal P., Khasanov B., Hayitbayev H., Hubert F. Inverse analysis of a loaded heat conduction equation. *Nanosystems: Physics, Chemistry, Mathematics*, 2025, **16**(6), P. 727–736.

[10] Kochubei A.N. Fractional-order diffusion. *Differential Equations*, 1990, **26**(4), P. 485—-492.

[11] Mainardi F., Rionero S., Ruggeri T. On the initial value problem for the fractional diffusion-wave equation. *Waves and stability in continuous media*, 1994, **7**, P. 246–251.

[12] Mainardi F. The time fractional diffusion-wave equation. *Radiophys Quantum Electron*, 1995, **38**(1-2), P. 13-–24.

[13] Mainardi F. The fundamental solutions for the fractional diffusion-wave equation. *Appl. Math. Lett.*, 1996, **9**(6), P. 23-–28.

[14] Voroshilov A.A., Kilbas A.A. The Cauchy problem for the diffusion-wave equation with the Caputo partial derivative. *Differ. Equ.*, 2006, **42**(5), P. 638-–649.

[15] Pskhu A.V. The fundamental solution of a diffusion-wave equation of fractional order. *Izvestiya: Mathematics*, 2009, **73**(2), P. 351-–392.

[16] Pskhu A.V. Fundamental solutions and Cauchy problems for an odd-order partial differential equation with. *Electronic Journal of Differential Equations*, 2019, **2019**(21), P. 1—13.

[17] Karasheva L.L. Cauchy problem for high even order parabolic equation with time fractional derivative. Sibirskie Elektronnye Matematicheskie Izvestiya [Siberian Electronic Mathematical Reports], 2018, **15**, P. 696–706. [In Russian].

[18] Baltaeva U., Alikulov Y., Baltaeva I.I., Ashirova A. Analog of the Darboux problem for a loaded integro-differential equation involving the Caputo fractional derivative. *Nanosystems: Phys. Chem. Math.*, 2021, **12**(4), P. 418–424.

[19] Karimov Sh., Mamajonova R. The Cauchy problem for a beam vibration equation involving the Caputo time-fractional operator. *Bull. Inst. Math.*, 2025, **8**(6), P. 154–160.

[20] Kilbas A.A., Srivastava H.M., Trujillo J.J. *Theory and Applications of Fractional Differential Equations. North-Holland Mathematics Studies*, 204. Elsevier, Amsterdam, 2006.

Submitted 30 January 2026; revised 14 March 2026; accepted 15 March 2026

Information about the authors:

B. Yu. Irgashev – University of Business and Science, Namangan, Uzbekistan; Institute of Mathematics named after V.I.Romanovsky of the Academy of Sciences of the Republic of Uzbekistan; ORCID 0000-0001-7204-9127; bahromirgasev@gmail.com

Conflict of interest: the authors declare no conflict of interest.

NANOSYSTEMS:
PHYSICS, CHEMISTRY, MATHEMATICS

Original article

Abdullaev J.I., et al. *Nanosystems: Phys. Chem. Math.*, 2026, **17** (2), 179–186.
http://nanojournal.ifmo.ru
DOI 10.17586/2220-8054-2026-17-2-179-186

Critical mass ratio and phase transition in three-particle lattice systems: comparison of bosonic and fermionic cases

Janikul I. Abdullaev[1,a], Abdumalik I. Eshniyozov[2,b], Mikhail V. Dolgopolov[3,c]

[1]Samarkand State University, Samarkand, Uzbekistan
[2]Gulistan State University, Gulistan, Uzbekistan
[3]Samara State Technical University, Samara, Russian Federation

[a]jabdullaev@mail.ru, [b]eshniyozovabdumalik75@gmail.com, [c]mvdolg@yandex.com

Corresponding author: M. V. Dolgopolov, mvdolg@yandex.ru

PACS 02.30.Tb

ABSTRACT We study three-particle Schrödinger operators on the two-dimensional lattice $\mathbb{Z}^2$ and show that a critical mass ratio $\gamma_c \approx 2.75194$ governs the existence of a bound trimer in the fermionic $2+1$ configuration (two identical fermions and a third particle). For $\gamma < \gamma_c$ there is a topological prohibition (Pauli suppression) of a three-body bound state, whereas for $\gamma > \gamma_c$ a doubly degenerate eigenvalue emerges below the essential spectrum with the strong-coupling asymptotics $z(\gamma, \lambda) = -\lambda + e_0(\gamma) + O(\lambda^{-1})$. Within a unified framework based on the Birman–Schwinger principle and strong-coupling asymptotic analysis, we compare this behaviour with the bosonic case of three identical particles, where two bound states exist below the essential spectrum and the ground-state energy satisfies $z_1^s(\mu) = -3\mu + C_2 + O(\mu^{-1})$. The resulting second-order phase transition with respect to the mass ratio γ is relevant for the design of experiments on fermionic trimers in optical lattices and for modelling excitonic complexes and defect-bound states in two-dimensional nanomaterials, where the critical value γ_c serves as a design guideline for the observability of three-body bound states. We also outline a modified three-particle lattice model with two competing interaction channels, for which the Birman–Schwinger analysis naturally leads to a Landau-type scenario of a first-order phase transition in the space of trimer bound states. In the bosonic case we prove a strong-coupling theorem describing the existence and asymptotics of trimer bound states, while in the fermionic $2+1$ case we establish a spectral phase-transition theorem that identifies an explicit critical mass ratio γ_c separating the trimer and non-trimer regimes.

KEYWORDS three-particle Schrödinger operator, lattice systems, bound states, bosons, fermions, critical mass ratio, phase transition, Birman–Schwinger principle.

ACKNOWLEDGEMENTS The first author is grateful to the Foundation for Fundamental Research of the Republic of Uzbekistan for financial support of the research (grant no. AL – 922 41 04 685)

FOR CITATION Abdullaev J.I., Eshniyozov A.I., Dolgopolov M.V. Critical mass ratio and phase transition in three-particle lattice systems: comparison of bosonic and fermionic cases. *Nanosystems: Phys. Chem. Math.*, 2026, **17** (2), 179–186.

1. Introduction

The study of few-particle bound states on quantum lattices is of fundamental interest both for mathematical physics and for applications in quantum simulation, condensed-matter physics, and nanotechnology; see, for example, Refs. [1–3]. Experiments with ultracold atoms in optical lattices make it possible to realize controllable quantum systems with tunable interaction parameters and geometry, which calls for precise theoretical predictions of their spectral properties.

In recent years, substantial progress has been made in the analysis of three-particle Schrödinger operators on lattices; see, e.g., [4–6]. In parallel, the spectral theory of lattice Schrödinger operators with a finite number of isolated levels has been actively developed: in particular, Ref. [7] establishes the existence of a maximal number of isolated eigenvalues for a broad class of lattice Schrödinger operators. The present work continues this line of research by turning to three-particle systems that exhibit critical phenomena with respect to the mass ratio. At the same time, the problem of critical behavior in fermionic systems with mass imbalance has remained insufficiently explored. In particular, it has been unclear whether there exists a threshold value of the mass ratio that separates qualitatively different regimes of existence of bound states. A related question of independent interest is whether suitable modifications of a multi-particle lattice model (for instance, by adding an external field or an additional interaction channel) can give rise to a first-order phase transition accompanied by a discontinuous rearrangement of the three-particle spectrum.

In this work, we perform a comparative analysis of the spectral properties of two principal classes of three-particle systems on a two-dimensional lattice: (i) three identical bosons and (ii) a fermionic $2+1$ configuration (two identical

TABLE 1. Position of the present work within the landscape of lattice few-body models.

Work	System	Dim.	Key feature
Two-particle lattice models [11]	dimer	$d = 2, 3$	threshold effects, monotonicity
Three-fermion models on $\mathbb{Z}$ [12]	trimer	$d = 1$	strong-coupling discrete spectrum
Fermionic 2+1 trimer (this work)	trimer	$d = 2$	critical γ_c, spectral phase transition
2+1 fermions [8]	trimer	$d = 3$	repulsive contact, critical $\gamma_s(K), \gamma_{as}(K)$

fermions and a third particle of a different nature). Employing a unified methodological framework based on the Birman–Schwinger principle and asymptotic analysis in the strong-coupling regime, we uncover fundamental differences induced by the quantum statistics of the particles. We prove a strong-coupling theorem for bosonic trimers and a spectral phase-transition theorem for the fermionic 2+1 trimer with an explicit critical mass ratio γ_c.

For a related three-particle 2+1 fermionic model on $\mathbb{Z}^3$ with repulsive contact interactions, Khalkhuzhaev et al. [8] introduced two critical mass ratios $\gamma_s(K)$ and $\gamma_{as}(K)$ that determine the number of eigenvalues lying to the right of the essential spectrum at strong coupling. Here we consider instead an attractive 2+1 model on $\mathbb{Z}^2$, where a single critical mass ratio γ_c controls the emergence of a low-energy trimer level below the essential spectrum and gives rise to a second-order spectral phase transition.

The application of this unified framework to concrete three-particle lattice models reveals deep structural distinctions that are entirely dictated by the underlying quantum statistics.

2. Comparative analysis of bosonic and fermionic trimers

We consider the Hamiltonian of a three-particle system on the two-dimensional lattice $\mathbb{Z}^2$ in the coordinate representation,

$$\hat{H} = \hat{H}_0 - \alpha \sum_{i<j} \hat{V}_{ij}, \tag{1}$$

where $\hat{H}_0$ is the kinetic-energy operator, $\alpha > 0$ is the coupling constant, and $\hat{V}_{ij}$ are zero-range pair potentials given by

$$(\hat{V}_{ij}\psi)(n_1, n_2, n_3) = \delta_{n_i,n_j}\, \psi(n_1, n_2, n_3).$$

The particle statistics is encoded in the choice of the Hilbert space: the symmetric subspace ℓ_s^2 for bosons and the antisymmetric subspace ℓ_a^2 for fermions (with respect to the coordinates of identical particles). For the fermionic $2 + 1$ system we introduce the mass ratio $\gamma = m_f/m_3$, where m_f is the fermion mass and m_3 is the mass of the third particle, and δ_{n_i,n_j} denotes the Kronecker delta.

2.1. Bosonic system: three identical bosons on a lattice

We consider a system of three identical bosons of unit mass on the two-dimensional lattice $\mathbb{Z}^2$. In the coordinate representation, the three-particle Hamiltonian takes the form

$$\hat{H}_\mu = \hat{H}_0 - \mu(\hat{V}_{12} + \hat{V}_{13} + \hat{V}_{23}), \qquad \hat{H}_\mu : \ell_s^2((\mathbb{Z}^2)^3) \to \ell_s^2((\mathbb{Z}^2)^3),$$

where $\mu > 0$ is the interaction strength and $\hat{H}_0$ denotes the free kinetic-energy Hamiltonian. Here $\ell_s^2((\mathbb{Z}^2)^3)$ is the subspace of square-summable symmetric functions on $(\mathbb{Z}^2)^3$, describing the states of three identical bosons on the lattice.

The Fourier transform on $\mathbb{Z}^2$ maps the coordinate-space Hamiltonian $\hat{H}_\mu$ into the momentum representation, in which the total Hamiltonian H_μ admits a direct-integral decomposition with respect to the total quasimomentum $\mathbf{K} \in \mathbb{T}^2$,

$$H_\mu = \int_{\mathbb{T}^2}^{\oplus} H_\mu(\mathbf{K})\, d\mathbf{K},$$

where, for each fixed $\mathbf{K}$, the fiber operator $H_\mu(\mathbf{K})$ acts in the symmetric subspace $L_s^2((\mathbb{T}^2)^2)$ and is given (see. [4,5]) by

$$\big(H_\mu(\mathbf{K})f\big)(\mathbf{p}, \mathbf{q}) = E_\mathbf{K}(\mathbf{p}, \mathbf{q}) f(\mathbf{p}, \mathbf{q}) - \mu(V_1 + V_2 + V_3) f(\mathbf{p}, \mathbf{q}), \qquad f \in L_s^2((\mathbb{T}^2)^2).$$

Here

$$E_\mathbf{K}(\mathbf{p}, \mathbf{q}) = \varepsilon(\mathbf{p}) + \varepsilon(\mathbf{q}) + \varepsilon(\mathbf{K} - \mathbf{p} - \mathbf{q}), \qquad \varepsilon(\mathbf{p}) = 2 - \cos p_1 - \cos p_2,$$

and

$$
\begin{aligned}
&(V_1 f)(\mathbf{p},\mathbf{q}) = \frac{1}{(2\pi)^2}\int\limits_{\mathbb{T}^2} f(\mathbf{p},\mathbf{s})\,d\mathbf{s}, \qquad (V_2 f)(\mathbf{p},\mathbf{q}) = \frac{1}{(2\pi)^2}\int\limits_{\mathbb{T}^2} f(\mathbf{s},\mathbf{q})\,d\mathbf{s},\\
&(V_3 f)(\mathbf{p},\mathbf{q}) = \frac{1}{(2\pi)^2}\int\limits_{\mathbb{T}^2} f(\mathbf{s},\mathbf{p}+\mathbf{q}-\mathbf{s})\,d\mathbf{s}.
\end{aligned}
\tag{2}
$$

2.2. Fermionic system: two identical fermions and a third particle

We consider a system of two identical fermions of unit mass and a third particle of mass m (a $2+1$ configuration) on the two-dimensional lattice $\mathbb{Z}^2$. Let $\ell^2\big((\mathbb{Z}^2)^3\big)$ denote the Hilbert space of square-summable functions of three lattice sites $\boldsymbol{n} = (\mathbf{n}_1, \mathbf{n}_2, \mathbf{n}_3) \in (\mathbb{Z}^2)^3$, and let

$$\ell^2_a\big((\mathbb{Z}^2)^3\big) \subset \ell^2\big((\mathbb{Z}^2)^3\big)$$

be its antisymmetric subspace with respect to the exchange of the fermionic coordinates $\mathbf{n}_1 \leftrightarrow \mathbf{n}_2$.

In the coordinate representation, the three-particle Hamiltonian is given by

$$\widetilde{H}_{\gamma,\lambda} = \hat{H}_0 - \lambda\big(\hat{V}_{13} + \hat{V}_{23}\big), \qquad \widetilde{H}_{\gamma,\lambda} : \ell^2_a\big((\mathbb{Z}^2)^3\big) \to \ell^2_a\big((\mathbb{Z}^2)^3\big),$$

where $\lambda > 0$ is the strength of the contact interaction and $\gamma{:=}m_f/m_3$ is the mass ratio (the ratio of the fermion mass to the mass of the third particle). Here ℓ^2_a denotes the antisymmetric subspace of ℓ^2 corresponding to the two identical fermions.

Passing to the momentum representation and fixing the total quasimomentum $\mathbf{K} = \mathbf{0}$, we arrive at the fiber Schrödinger operator

$$H_{\gamma,\lambda}(\mathbf{0}) = H_{\gamma,0}(\mathbf{0}) - \lambda\big(V_1 + V_2\big), \qquad H_{\gamma,\lambda}(\mathbf{0}) : L^2_a((\mathbb{T}^2)^2) \to L^2_a((\mathbb{T}^2)^2),$$

where $L^2_a((\mathbb{T}^2)^2)$ is the antisymmetric subspace in momentum space obtained as the image of $\ell^2_a((\mathbb{Z}^2)^2)$ under the three-particle Fourier transform,[1] and V_1 and V_2 are partial integral operators describing the contact interaction of the fermions with the third particle (see (2)). The operator $H_{\gamma,0}(\mathbf{0})$ acts as multiplication by the dispersion function

$$E_\gamma(\mathbf{p},\mathbf{q}) = \varepsilon(\mathbf{p}) + \varepsilon(\mathbf{q}) + \gamma\,\varepsilon(-\mathbf{p}-\mathbf{q}) = \varepsilon(\mathbf{p}) + \varepsilon(\mathbf{q}) + \gamma\,\varepsilon(\mathbf{p}+\mathbf{q}).$$

Remark. Due to the unitary equivalence $H_{\gamma,\lambda}(\mathbf{K}) \cong H_{\gamma,\lambda}(-\mathbf{K})$ via the transformation $f(\mathbf{p},\mathbf{q}) \mapsto f(-\mathbf{p},-\mathbf{q})$, it suffices to consider the total quasimomentum $\mathbf{K}$ in a fundamental domain of $\mathbb{T}^2$ modulo this involution. In this work we focus on the case $\mathbf{K} = 0$, which captures the essential spectral features; the extension to $\mathbf{K} \neq 0$ follows similar lines and will be addressed elsewhere.

2.3. General comments and development

The main analytical tool is the Birman–Schwinger principle [9, 10]. For energies z that are outside the essential spectrum of the operators $H_\mu(\mathbf{0})$ and $H_{\gamma,\lambda}(\mathbf{0})$, the corresponding eigenvalue problems

$$H_\mu(\mathbf{0})\psi = z\psi, \qquad H_{\gamma,\lambda}(\mathbf{0})\varphi = z\varphi$$

are reduced to fixed-point problems for compact self-adjoint Birman–Schwinger operators $B_\mu(z)$ and $B_{\gamma,\lambda}(z)$, respectively:

$$\psi \neq 0,\ H_\mu(\mathbf{0})\psi = z\psi \iff B_\mu(z)\psi^* = \psi^*, \qquad \varphi \neq 0,\ H_{\gamma,\lambda}(\mathbf{0})\varphi = z\varphi \iff B_{\gamma,\lambda}(z)\varphi^* = \varphi^*.$$

Moreover, for z below the bottom of the essential spectrum, the number of eigenvalues of $H_\mu(\mathbf{0})$ (respectively, $H_{\gamma,\lambda}(\mathbf{0})$) lying below z coincides with the number of eigenvalues of $B_\mu(z)$ (respectively, $B_{\gamma,\lambda}(z)$) that exceed one.

We emphasize that a key ingredient of our analysis is the detailed spectral information available for the two-particle lattice operator. In particular, the properties of the discrete spectrum of the two-particle Schrödinger operator on $\mathbb{Z}^d$ and its dependence on the total quasimomentum $\mathbf{k}$ have been studied in detail in [11], where the monotonicity of the eigenvalue branches $z_n(\mathbf{k})$ with respect to the components of $\mathbf{k}$ and bounds on the number of levels below the essential spectrum were established. In the present work, these results are used at a conceptual level to justify the robustness of two-particle threshold states, which enter the kernel of the Birman–Schwinger operator associated with the three-particle problem.

A related Birman–Schwinger type reduction combined with a finite-rank principal part has recently been employed for a different lattice few-body model, namely a system of three identical fermions on the one-dimensional lattice with nearest-neighbour attraction; in that setting, the discrete spectrum at strong coupling was analysed in [12], while the essential spectrum and further extensions to systems of identical particles were explicitly meant in the subsequent development, including in this research article. Although the underlying operator and statistics differ from our $2{+}1$ model, these works are methodologically close to our approach and provide complementary examples of how the Birman–Schwinger framework can be used to control the discrete spectrum of multi-particle lattice Schrödinger operators.

---

[1] The original coordinate-space Hilbert space is three-particle, while after fixing the center-of-mass quasimomentum the effective dimension is reduced.

As a natural generalization of the model (1), we consider a three-particle Hamiltonian with two competing interaction channels,

$$H_{\gamma,\lambda,\beta}(\mathbf{0}) = H_{\gamma,0}(\mathbf{0}) - \lambda \sum_{i<j} V_{ij}^{(0)} + \beta \sum_{i<j} V_{ij}^{(1)}, \tag{3}$$

where $V_{ij}^{(0)}$ describes a contact attractive interaction, while $V_{ij}^{(1)}$ accounts for a more long-ranged interaction between the particles (for instance, of Coulombic or polaronic type). For the Hamiltonian (3), the Birman–Schwinger operator $B_{\gamma,\lambda,\beta}(z)$ typically develops several qualitatively distinct eigenvalue branches associated with different spatial structures of trimer states (a localized versus an "extended" trimer). In the language of Landau's phenomenological theory, this leads to an effective potential for the order parameter η of the form

$$\mathcal{F}(\eta;\gamma,\lambda,\beta) = a(\gamma,\lambda,\beta)\,\eta^2 + b(\gamma,\lambda,\beta)\,\eta^4 + c(\gamma,\lambda,\beta)\,\eta^6 + \dots, \tag{4}$$

where the signs of the coefficients a, b, c are determined by the spectral characteristics of $B_{\gamma,\lambda,\beta}(z)$. In the regime $b < 0$, $c > 0$, two competing local minima $\eta = \eta_{1,2}$ emerge, and variations of the parameters (γ, λ, β) may induce an abrupt transition between them, corresponding to a first-order phase transition in the space of three-body bound states, in full agreement with the general principles of Landau's phenomenological theory of first- and second-order phase transitions [13, 14].

In the strong-coupling regime ($\mu \to \infty$ for the bosonic system and $\lambda \to \infty$ for the fermionic one), the operators $B_\mu(z)$ and $B_{\gamma,\lambda}(z)$ admit an asymptotic decomposition into a principal finite-rank part and a remainder of small norm. A spectral analysis of the principal part then yields precise asymptotics of the eigenvalues and provides conditions for the existence of bound states.

3. Main results

3.1. System of three identical bosons

For a system of three identical bosons with strong zero-range attraction ($\mu \to \infty$) in the sector of zero total quasimomentum, we obtain the following result.

Theorem 3.1 (Strong-coupling trimers in the bosonic case)**.** *For all sufficiently large $\mu > \mu_0$, the three-boson Schrödinger operator $H_\mu(\mathbf{0})$ has exactly two bound states below the essential spectrum. The ground-state energy admits the asymptotic expansion*

$$z_1^s(\mu) = -3\mu + C_2 + O(\mu^{-1}), \qquad \mu \to \infty,$$

where C_2 is a constant determined by the Green function of the free Hamiltonian. The first excited state $z_2^s(\mu)$ is a threshold resonance with the asymptotics

$$z_2^s(\mu) = -\mu + \mathrm{const} + O(\mu^{-1}), \qquad \mu \to \infty.$$

Thus, in the bosonic case bound states exist for arbitrarily weak and strong interactions, and their number and asymptotic behavior are governed purely by geometric and symmetry considerations.

3.2. Fermionic $2{+}1$ system

For the fermionic $2{+}1$ configuration, the picture is fundamentally different. The antisymmetry of the wave function under the exchange of the two identical fermions imposes strong constraints on the possibility of forming a bound state.

Theorem 3.2 (Spectral phase transition in the fermionic $2{+}1$ trimer)**.** *For the fermionic $2{+}1$ trimer on the two-dimensional lattice, there exists a critical mass ratio $\gamma_c > 0$ such that:*

1. *If $\gamma < \gamma_c$, then for any $\lambda > 0$ (equivalently, for arbitrarily large coupling) the operator $H_{\gamma,\lambda}(\mathbf{0})$ has no bound states (has no eigenvalues) below the bottom of the essential spectrum; this follows from the fact that the critical coupling diverges as $\gamma \to \gamma_c^-$.*
2. *If $\gamma > \gamma_c$, then there exists a threshold value $\lambda_0(\gamma)$ such that for all $\lambda > \lambda_0(\gamma)$ there appears exactly one doubly degenerate bound state with energy*

   $$z(\gamma,\lambda) = -\lambda + e_0(\gamma) + O(\lambda^{-1}), \qquad \lambda \to \infty.$$
3. *The function $\Delta E(\gamma) := z_0(\gamma,\lambda) - z(\gamma,\lambda)$ satisfies $\Delta E(\gamma) > 0$ for $\gamma > \gamma_c$, $\Delta E(\gamma) = 0$ for $\gamma \le \gamma_c$, and there exists $\nu > 0$ such that*

   $$\Delta E(\gamma) \sim C\,(\gamma - \gamma_c)^\nu, \qquad \gamma \downarrow \gamma_c,$$

   for some constant $C > 0$.

The critical value γ_c is determined by an integral equation that follows from the solvability condition of the Birman–Schwinger equation at the bottom of the essential spectrum:

$$\gamma_c^{-1} = \frac{1}{(2\pi)^2} \int\limits_{[-\pi,\pi]^2} \frac{(\sin q_1 + \sin q_2)^2}{4 - 2(\cos q_1 + \cos q_2)}\, dq_1 dq_2. \tag{5}$$

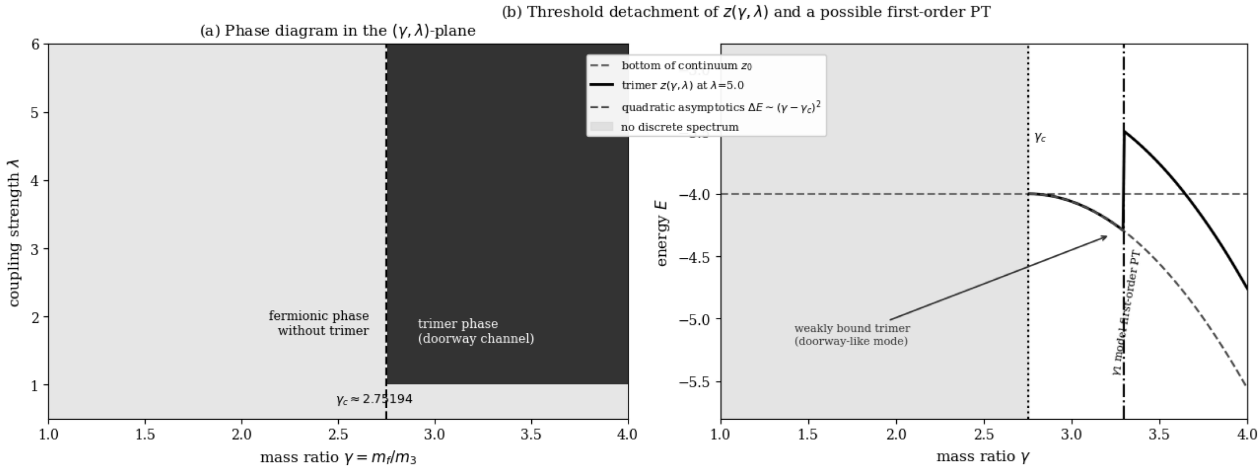

FIG. 1. (a) Schematic phase diagram in the (γ, λ)-plane for the fermionic 2+1 trimer at $\mathbf{K} = \mathbf{0}$. For $\gamma < \gamma_c$ the operator $H_{\gamma,\lambda}(\mathbf{0})$ has no three-body bound states for any λ (fermionic phase without a trimer). For $\gamma > \gamma_c$ and sufficiently large λ there exists a unique trimer bound state, corresponding to an effective doorway channel at the three-body level. (b) Trimer energy $z(\gamma, \lambda)$ at fixed sufficiently large λ near the critical mass ratio γ_c. As $\gamma \uparrow \gamma_c$ the level $z(\gamma, \lambda)$ approaches the bottom of the essential spectrum z_0, while for $\gamma > \gamma_c$ it separates from the threshold according to a quadratic law $\Delta E(\gamma) = z_0 - z(\gamma, \lambda) \sim C\,(\gamma - \gamma_c)^2$, which corresponds to a second-order phase transition in the spectral sense. The vertical line at γ_1 illustrates a possible, more intricate scenario with an additional first-order transition at larger γ, where the trimer level undergoes a discontinuous rearrangement (a model example for discussing multicritical behavior).

A numerical solution of equation (5) yields

$$\gamma_c \approx 2{,}75194 \pm 0{,}00001.$$

The transition at $\gamma = \gamma_c$ is of second order. As $\gamma \to \gamma_c^+$, the level $z(\gamma, \lambda)$ merges with the bottom of the essential spectrum, and the energy difference follows a power law $\Delta E \sim (\gamma - \gamma_c)^\nu$.

The physical mechanism behind this transition is the competition between two effects:

(1) Contact attraction, which tends to localize all three particles on the same lattice site and lower the energy of the system.

(2) Pauli repulsion, which forbids the two identical fermions from occupying the same state and increases the kinetic energy of the system.

For small γ (light fermions) the kinetic energy of the fermions is large, and Pauli repulsion suppresses the formation of a bound state. For $\gamma > \gamma_c$ the fermion mass is sufficiently large so that their kinetic energy becomes comparable to the interaction energy, which allows a trimer bound state to form.

Geometrically, the behavior of the lowest trimer level in a neighborhood of the critical mass ratio γ_c is illustrated in Fig. 1, which shows the separation of the energy $z(\gamma, \lambda)$ from the bottom of the essential spectrum z_0 for $\gamma > \gamma_c$ and the absence of a bound state for $\gamma < \gamma_c$ (Pauli-suppressed regime). This picture is consistent with a bifurcation scenario in which the contact attraction overcomes the effective Pauli repulsion only after the critical mass ratio γ_c is reached. In Fig. 1 this bifurcation is visualized as the detachment of the trimer level $z(\gamma, \lambda)$ from the threshold z_0 for $\gamma > \gamma_c$.

The second-order phase transition described in Theorem 3.2 can be visualized both in the parameter plane (γ, λ) and via the behavior of the trimer level at the threshold. In Fig. 1, panel (a) shows the domain of existence of the fermionic trimer for $\gamma > \gamma_c$, while panel (b) illustrates the quadratic detachment of the level $z(\gamma, \lambda)$ from the bottom of the essential spectrum z_0 and the corresponding second-order character of the transition. The model parameter γ_1 highlighted in panel (b) indicates a possible scenario of more complex (multicritical) behavior, with a first-order transition at larger mass ratios.

In this context, the trimer phase for $\gamma > \gamma_c$ plays the role of an effective doorway state on the lattice, analogous to the doorway modes controlling secondary electron emission in layered materials [15].

The spectral visualizations in Fig. 1 thus emphasize the qualitative difference between the fermionic and bosonic cases and, at the same time, illustrate how the proposed methodological approach captures a model scenario of a first-order phase transition built on top of the second-order bifurcation.

Remark. The exponent ν in the asymptotic law $\Delta E(\gamma) \sim C(\gamma - \gamma_c)^\nu$ is expected to be $1/2$, characteristic of a square-root bifurcation at a threshold. A rigorous determination of ν requires a refined analysis of the Birman–Schwinger kernel near the bottom of the essential spectrum and will be addressed in a forthcoming work.

4. Discussion and conclusions

The comparative analysis carried out in this work reveals a fundamental difference between the behaviors of bosonic and fermionic three-particle lattice systems:

- Bosons. Bound states exist for arbitrarily weak interactions; their number and properties are governed by the symmetry and geometry of the system.
- Fermions (2+1). A three-body bound state exists only if the mass ratio satisfies $\gamma > \gamma_c$, which reflects a *topological prohibition* imposed by the Pauli principle.

The critical phenomenon identified in the (γ, λ) parameter space can be interpreted as a *second-order phase transition*. It is characterized by a discontinuous change in the number of bound states upon crossing the critical line $\gamma = \gamma_c$. The critical value γ_c plays the role of a *universal constant of lattice geometry* that delineates two topologically distinct phases of trimer states.

A natural direction for further work is to investigate modified three-particle Hamiltonians of the type (3), where the presence of two competing interaction channels (such as short-range attraction combined with long-range repulsion or an external field) may lead to several local minima of the effective potential (4) and, consequently, to a *first-order* phase transition between different trimer phases.

The results obtained in this paper have important implications in several contexts:

(1) Quantum simulation in optical lattices. The value of γ_c provides a concrete "design rule" for experiments aiming at the observation of fermionic trimers: one has to choose atomic species with a mass ratio exceeding the threshold 2.75194 and tune the interaction into the strong-coupling regime (large λ), in which the asymptotics of $z(\gamma, \lambda)$ is realized.

(2) Condensed-matter physics. Similar three-particle models arise in the description of bound defect complexes in semiconductors and excitonic complexes in two-dimensional materials. The mechanism based on the competition between attraction and statistical constraints can manifest itself in these systems as well.

(3) Mathematical physics. This work demonstrates the efficiency of combining the Birman–Schwinger principle with asymptotic analysis for studying the spectral properties of discrete multi-particle operators. For two-particle systems, a closely related approach to the spectral structure and its parametric monotonicity was developed in [11], and here it is extended to the three-particle case with a critical phenomenon in the mass ratio. In Ref. [7], the existence of a maximum number of isolated eigenvalues of lattice Schrödinger operators under variations of the interaction parameters is analyzed, providing a natural two-particle analog of the three-body phase transitions studied in the present work. From a mathematical point of view, Theorem 3.2 gives the first example of a three-particle lattice system in which a critical value of a parameter (the mass ratio) produces a bifurcation of the discrete spectrum with an explicitly computable critical constant γ_c, while Theorem 3.1 describes the complementary strong-coupling behaviour in the purely bosonic case.

Promising directions for future research include:

- extending the present approach to systems with mixed statistics (Bose–Fermi mixtures);
- studying the influence of the lattice dimension and geometry on the critical value γ_c;
- analyzing the dynamical properties and stability of trimer states;
- relating the microscopic results obtained here to macroscopic phase diagrams of lattice models.

From the viewpoint of Landau's phenomenological theory of phase transitions [13], the mass ratio γ plays the role of a control parameter, whereas the quantity $\Delta E(\gamma) = z_0 - z(\gamma, \lambda)$ can be interpreted as an order parameter that vanishes in the limit $\gamma \to \gamma_c^+$. The behavior $\Delta E(\gamma) \sim (\gamma - \gamma_c)^\nu$ and the emergence of a doubly degenerate level below the essential spectrum for $\gamma > \gamma_c$ are characteristic of a second-order phase transition accompanied by symmetry breaking in the space of three-particle states.

4.1. Applied relevance for quantum nanosystems

The critical values obtained in this work have a direct experimental relevance for ultracold atomic systems in optical lattices. The value $\gamma_c \approx 2.75194$ provides a precise condition for the observability of fermionic trimers: one has to select combinations of atomic species such as $^6\mathrm{Li}$–$^{87}\mathrm{Rb}$ or $^{40}\mathrm{K}$–$^{133}\mathrm{Cs}$ with a mass ratio exceeding the threshold.

In condensed-matter physics, analogous three-particle models describe:

- triexciton states in monolayer WS_2 under resonant exciton–exciton attraction;
- bound defect complexes (vacancy–interstitial pairs) in MoS_2 and h-BN;
- spin-triplet states in quantum dots with a pronounced imbalance of effective masses or g-factors.

From the solid-state physics perspective, the level $z(\gamma, \lambda)$, which is separated from the essential spectrum and merges with its lower edge as $\gamma \to \gamma_c^+$, can be interpreted as an analog of a doorway state in the sense of Ref. [15], mediating the effective coupling between localized trimer configurations and the continuum of extended states. In particular, the threshold configuration corresponds to the condition

$$z(\gamma_c, \lambda) \;=\; E_{\mathrm{thr}}(\gamma_c), \qquad \det\nolimits_{\mathrm{Fred}}\big(\mathbb{I} - B_\gamma(z, \lambda)\big)\big|_{\gamma=\gamma_c, z=E_{\mathrm{thr}}(\gamma_c)} = 0,$$

which marks the onset of the trimer doorway mode at the three-body continuum threshold, where $E_{\text{thr}}(\gamma)$ denotes the lower edge of the essential spectrum of the three-body Hamiltonian $H_{\gamma,\lambda}(0)$ (the three-body continuum threshold) for a given mass ratio γ.

By analogy with the three-body lattice model, where the critical mass ratio γ_c controls the emergence or disappearance of a trimer bound state, mass (isotopic) effects in real crystals manifest themselves in the spectrum of collective excitations. In particular, Ref. [16] reports the experimental observation of a negative isotopic shift of the LO phonon in 3C–SiC, revealing a universal mechanism of mass-effect dominance in cubic lattices. This indicates that controlling the masses and isotopic composition, effectively tuning $\gamma = m_f/m_3$ in our terminology, can serve as a powerful tool for engineering spectral properties in nanostructures and hybrid energy sources. In particular, isotopic engineering allows one to tailor the phonon spectrum via shifts of the form

$$\Delta\omega_{\text{LO}} \;=\; \omega_{\text{LO}}(M_{\text{eff}}) - \omega_{\text{LO}}(M_{\text{ref}}),$$

where $\omega_{\text{LO}}(M)$ denotes the longitudinal optical phonon frequency for a crystal with an effective mass M of the vibrating sublattice, M_{eff} is the mass corresponding to a given isotopic configuration, and M_{ref} is a chosen reference mass (e.g., corresponding to the natural isotopic composition). This is directly analogous to the way the trimer energy $z(\gamma, \lambda)$ shifts relative to the three-body continuum threshold when the effective mass ratio γ is varied across the critical value γ_c.

The monotonicity of the eigenvalues of two-particle lattice Schrödinger operators established in [11] provides a complementary mechanism for the controllable rearrangement of the energy spectrum under variations of the total quasimomentum and lattice parameters. In particular, for the two-particle operator $H(\mathbf{k})$ on $\mathbb{Z}^3$, where $\mathbf{k} = (k_1, k_2, k_3)$ is the total quasimomentum, the paper [11] proves that the number $N(\mathbf{k})$ of eigenvalues below the essential spectrum is a nondecreasing function of each component $k_i \in [0, \pi]$, and, under additional assumptions on the interaction potential, each eigenvalue branch $z_n(\mathbf{k})$ satisfies

$$k_i^{(1)} \le k_i^{(2)} \quad\Longrightarrow\quad z_n\big(k_1, \dots, k_i^{(1)}, \dots, k_3\big) \;\ge\; z_n\big(k_1, \dots, k_i^{(2)}, \dots, k_3\big),$$

for fixed remaining components k_j, $j \neq i$. Here $z_n(\mathbf{k})$ denotes the n-th discrete eigenvalue of $H(\mathbf{k})$ and $N(\mathbf{k})$ is the total number of such eigenvalues, in the appropriate Brillouin-zone ordering, which allows one to shift bound levels spectrally by tuning the total quasimomentum $\mathbf{k}$ and the lattice geometry. Together with the mass- and isotope-controlled effects discussed above, this forms a robust toolbox for the spectral engineering of nanoscale quantum devices based on optical and solid-state lattices.

The proposed two-channel Hamiltonian opens a route toward realizing a first-order phase transition between distinct trimer phases, offering a microscopic realisation of Landau's phenomenological scenario in a few-body lattice system.

References

[1] Bloch I., Dalibard J., Zwerger W. Many-body physics with ultracold gases. *Rev. Mod. Phys.*, 2008, **80**(3), P. 885–964.

[2] Gross C., Bloch I. Quantum simulations with ultracold atoms in optical lattices. *Science*, 2017, **357**(6355), P. 995–1001.

[3] Atabaev B.G., Chepurnov V.I., Arutyunov N.Yu., Dolgopolov M.V., Juraev Kh.N., Radzhapov S.A. Rapid 3D defect mapping in SiC betavoltaics via positron annihilation tomography. *Physica Status Solidi (RRL) - Rapid Research Letters*, 2026, **20**(1), e202500356.

[4] Abdullaev Zh.I. Finiteness of discrete spectra for nontrivial values of the full quasi-momentum in the system of three bosons on a lattice. *Russian Math. Surveys*, 2007, **62**(1), P. 175—177.

[5] Lakaev S.N., Khalmukhamedov A.R., Khalkhuzhaev A.M. Bound states of the Schrödinger operator of a system of three bosons on a lattice. *Theoret. Math. Phys.*, 2016, **188**(1), P. 36–48.

[6] Muminov Z.I., Aktamova V.U. The point spectrum of the three-particle Schrödinger operator for a system comprising two identical bosons and one fermion on $\mathbb{Z}$. *Nanosystems: Physics, Chemistry, Mathematics*, 2024, **15**(4), P. 438–447.

[7] Lakaev S.N., Latipova D.A., Akhmadova M.O. On the existence of the maximum number of isolated eigenvalues for a lattice Schrödinger operator. *Nanosystems: Physics, Chemistry, Mathematics*, 2025, **16**(6), P. 737–748.

[8] Khalkhuzhaev A.M., Khayitova Kh.G., Khujamiyorov I.A. On the spectrum of the Schrödinger operator for a three-particle system on a lattice. *Uch. Zap. Kazan. Univ. Ser. Fiz.-Mat. Nauki*, (2025), **167**(3), P. 547–565.

[9] Birman M.Sh. On the spectrum of singular boundary-value problems. *Mat. Sb.*, 1961, **55(97)**(2), P. 125–174.

[10] Klaus M., Simon B. Coupling constant thresholds in nonrelativistic quantum mechanics. I. Short-range two-body case. *Ann. Phys.*, 1980, **130**(2), P. 251–281.

[11] Abdullaev J.I., Khalkhuzhaev A.M., Usmonov L.S. Monotonicity of the eigenvalues of the two-particle Schrödinger operator on a lattice. *Nanosystems: Physics, Chemistry, Mathematics*, 2021, **12**(6), P. 657–663.

[12] Abdullaev J.I., Ergashova S.H. Discrete Spectrum of the Schrödinger Operator of a System of Three Fermions on a One Dimensional Lattice. *Complex Anal. Oper. Theory*, 2025, **19**(6), P. 136.

[13] Landau L.D. On the theory of phase transitions. In: *Collected Papers of L. D. Landau*. Ed. by D. ter Haar. Pergamon Press, Oxford, Gordon & Breach, 1965, P. 193–216.

[14] Landau L.D., Lifshitz E.M. *Statistical Physics*. Part 1. Course of Theoretical Physics, Vol. 5. Pergamon Press, 1980.

[15] Niggas A., Hao M., Richter P., Simperl F., Blödorn F., Cap M., Kero J., Hofmann D., Bellissimo A., Burgdörfer J., Seyller T., Wilhelm R.A., Libisch F., Werner W.S.M. Identifying Electronic Doorway States in Secondary Electron Emission from Layered Materials. *Phys. Rev. Lett.*, 2025, **135**(16), 166401.

[16] Dolgopolov M.V., Chipura A.S. Negative isotopic shift of the LO phonon in 3C-SiC: A universal mechanism of mass effect dominance in cubic crystals. *JETP Lett.*, 2025, **122**(8), P. 500–506.

Submitted 1 February 2026; accepted 18 March 2026

Information about the authors:

Janikul I. Abdullaev – Samarkand State University named after Sharaf Rashidov, 15, University bul., Samarkand, 140129, Uzbekistan; ORCID 0009-0003-3315-8357; jabdullaev@mail.ru

Abdumalik I. Eshniyozov – Gulistan State University, 4th block of flats, Gulistan, 120100, Uzbekistan; ORCID 00009-0001-9357-5828; eshniyozovabdumalik75@gmail.com

Mikhail V. Dolgopolov – Samara State Technical University, 244, Molodogvardeyskaya st., Samara, 443100, Russian Federation.; ORCID 0000-0002-8725-7831; mvdolg@yandex.com

Conflict of interest: the authors declare no conflict of interest.

NANOSYSTEMS:
PHYSICS, CHEMISTRY, MATHEMATICS

Original article

Kuzmichev D.S., et al. *Nanosystems: Phys. Chem. Math.*, 2026, **17** (2), 187–192.
http://nanojournal.ifmo.ru
DOI 10.17586/2220-8054-2026-17-2-187-192

How to make opposite state store again

Dmitry S. Kuzmichev[1,a], Vyacheslav S. Konstantinov[1,2,b], Nikita A. Sizykh[1,c], Roman R. Khakimov[1,d]

[1]Moscow Institute of Physics and Technology, Dolgoprudny, Moscow region, Russia
[2]Molecular Electronics Research Institute, Zelenograd, Moscow, Russia

[a]kuzmichev.ds@mipt.ru, [b]vkonstantinov@niime.ru, [c]sizykh.na@mipt.ru, [d]khakimov.rr@mipt.ru

Corresponding author: Dmitry S. Kuzmichev, kuzmichev.ds@mipt.ru

PACS 85.50.Gk, 77.80.Fm

ABSTRACT The article shows the possibility of increasing the storage time of the opposite state (OS) at a temperature of 145 °C from 140 to 500 minutes in ferroelectric capacitors based on $Hf_{0.5}Zr_{0.5}O_2$ (HZO) by shift of current integration endpoint to right. Consideration of transient processes between measurement pulses after 500 minutes capacitors baking at 145 °C can enhance the OS retention from 21 to 35 % of the preheating state. Opposite trend detected for the same sate (SS) (decrease from 56 to 35 %) and new same state (NSS) (decrease from 63 to 45 %). It is also shown that the presence of a voltage shift caused by an imprint in some cases may not lead to a loss of polarization due to the current flowing during the flat part of the trapezoidal voltage pulse.

KEYWORDS TiN/HZO/TiN, retention, imprint, ferroelectric

ACKNOWLEDGEMENTS This work supported in part by the Foundation for Advanced Research (Project “Magnit”), in part by Ministry of Science and Higher Education of the Russian Federation in the scope of the government assignment (Agreement 075-03-2026-305 16.01.2026, project FSMG-2026-0021). The authors also acknowledge the MIPT Shared Facilities Center for access to the equipment. The authors are grateful to Andrey Markeev and Aleksey Azov for manufacturing support.

FOR CITATION Kuzmichev D.S., Konstantinov V.S., Sizykh N.A., Khakimov R.R. How to make opposite state store again. *Nanosystems: Phys. Chem. Math.*, 2026, **17** (2), 187–192.

1. Introduction

Ferroelectrics based on HfO_2 are perspective materials for non-volatile memory application due to high scalability and process compatibility with complementary metal oxide semiconductor (CMOS) technology, in contrast to conventional ferroelectric materials [1,2]. In the case of ferroelectrics-based random access memory (FeRAM), information is stored in the orientation of the polarization and can be read by unipolar voltage pulse [3] subsequent analysis of the received current response. Data retention is one of the key metrics of non-volatile memory. Reliability studies focusing on data retention of HfO_2-based devices report about critical role of imprint in retention degradation [4–11]. The imprint effect manifests itself as a shift of the hysteresis Polarization–Voltage (P–V) loop along the voltage axis. It occurs during thermal bake and is a major issue for FeRAM reliability as it reduces the memory window [12]. Also, in some cases, polarization loss can be observed follow a few seconds after removal of the external electric field and attributed to relaxation processes [5].

The retention of the memory window, in the case of a MFM (Metal–Ferroelectric–Metal) capacitor, can be estimated by calculating the charge in electrical circuit during the supply of voltage pulse sequences [4, 13]. Pulse sequences form states which can be evaluate before and after baking: same state (SS), opposite state (OS) [13] and, in some cases, new same state (NSS) [4, 10]. Usually, OS demonstrates higher degradation rate in contrast to SS and NSS which usually explained by imprint [4–11]. However, imprint also influences on SS and NSS [11] and in case of non-saturated loop SS and NSS degradation rate can be higher than for OS [4]. Therefore, the reason for the usually observed OS higher polarization loss is not fully understood, and further research is required to carefully investigate the imprint influence and methods employed in calculating polarization loss. In this work, for the first time, we evaluate influence of charge integration intervals duration used for SS, NSS and OS calculation in relaxation (25 °C) and retention loss (145 °C) processes for $Hf_{0.5}Zr_{0.5}O_2$ (HZO) based capacitors with TiN electrodes.

2. Experiments

To create TiN/HZO(10 nm)/TiN capacitors, magnetron sputtered was used to deposit TiN for both electrodes, and atomic layer deposition was used to grow HZO as a ferroelectric layer. After rapid thermal annealing in Ar atmosphere of 600 °C and 30 s capacitors with 250 μm^2 square were formed. The electric characteristics of the MFM devices were measured by Agilent B1500 semiconductor parameter analyzer. During all electric measurements, a voltage bias was applied to the top electrode and the bottom electrode was grounded and used for current measurements each 10 ns.

To evaluate retention loss and polarization relaxation of the TiN/HZO/TiN capacitors, pulse sequences "Cap 1" and "Cap 2" used for same-state (SS+), new same-state (NSS+) and opposite-state (OS+) determination accordance with [4, 10]. Pulses schemes used for these tests are illustrated in Fig. 1. According to [4], the polarization of SS+ was calculated as the difference between the polarizations of pulses 2_1 and 1_1, NSS+ – 2_3 and 1_2, and OS+ – 1_4 and 2_4 (Fig. 1). It is assumed that pulses 2_1, 2_3, and 1_4 contain a ferroelectric response (Data "1"), while pulses 1_1, 1_2, and 2_4 do not have a ferroelectric response (Data "0"). Polarization of each Data "1" and Data "0" pulses was calculated as total pulse charge normalized per MFM capacitor area. The charge, in turn, is calculated by integrating the current response. The time point at which integration begins corresponds to the start of the rise of the positive voltage pulse. The final time point of integration is specified separately.

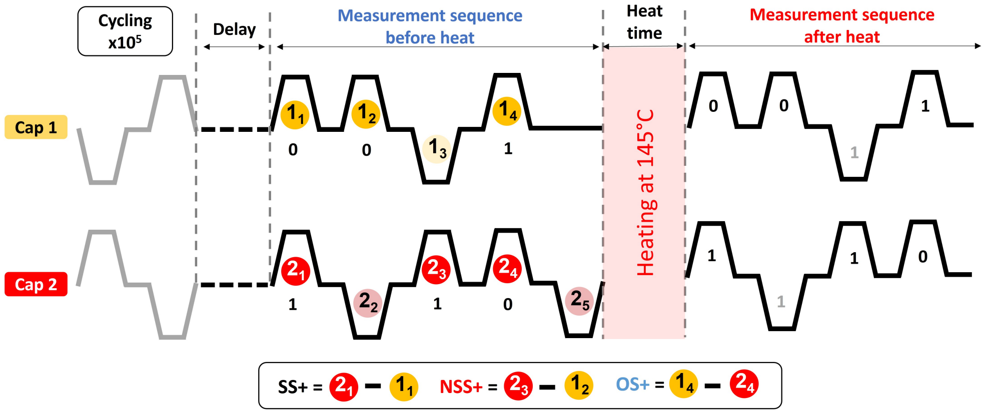

FIG. 1. Measurement sequences "Cap 1" and "Cap 2" used for relaxation and retention measurements

Before "Cap 1" and "Cap 2" sequences applying, were waked up by 10^5 cycles at room temperature (25 °C). For "Cap 1" and "Cap 2" sequences, last pulse of wake-up cycling was positive and negative, respectively. Than, to evaluate possible polarization relaxation before baking [5] "Cap 1" and "Cap 2" sequences were applied to capacitors with delay in the range from 1 μs to 100 s after wake-up cycling (Fig. 1). For retention measurements "Cap 1" and "Cap 2" sequences were applied to capacitors twice, first before baking (with delay of 1 μs after wake-up cycling at 25 °C) and second after 10, 40, 200 or 500 minutes of 145 °C baking according to [4]. At least 6 capacitors were used at each time point to calculate the polarization (3‘– for "Cap 1" and 3 for "Cap 2" sequences). 12 capacitors were used at 500 minutes of 145 °C baking time point (6 – for "Cap 1" and 6 for "Cap 2" sequences). Pulse amplitude and width for cycling and measurements sequences were equivalent and equal to 3 V and 3 μs respectively. Pulse shelf, rise and fall times were equal to 1 μs. Pulse separation was 1 μs. The pulse length and current measurement frequency were selected for more clear demonstration aspects of polarization calculation from current-time data for 250 μm^2 ferroelectric capacitors.

3. Results and discussion

Figure 2(a) shows evolution polarization values for all states in relaxation region at 25 °C and after baking at 145 °C. Charge integration range was 3.5 μs (pulse width and 500 ns after it) to take into account RC delay (Fig. S1(a), Supplementary materials). In relaxation region, polarization of SS+, NSS+ and OS+ after 1 μs delay is $\sim$30.2$\pm$0.8 μC/cm^2. After 100 s delay SS+, NSS+ and OS+ polarization demonstrate same values (negative states SS−, NSS− and OS− demonstrate similar trend in Fig. S2).

A noticeable drop in polarization is detected only after baking at elevated temperature. SS+, NSS+ and OS+ polarization after 10 minutes baking at 145 °C was 21, 22.5, and 18 μC/cm^2 respectively. Maximum degradation was achieved for 500 minutes baking at 145 °C, the values were 12.5, 15.5, and 9.5 μC/cm^2 for SS+, NSS+ and OS+ polarization, respectively. So, OS+ higher degradation is in accordance with previous research [5–8, 10, 14] and usually explained by shift of coercive fields (imprint), however, this effect also influences on SS and NSS [11]. Moreover, the imprint can start develop after 10^{-5} s [11], but in our case, polarizations values of all states do not change significantly even after 100 s. This raises two points that require clarification: the reason for the stronger effect of the imprint on OS compared to SS and NSS and the reason why the imprint does not result in a reduction in polarization during the relaxation process.

In order to do this, it is necessary to analyze the process of calculating polarization loss. First, it should be noted that usually reported only about polarization margin (Data “1” minus Data “0”) without separate analyzing of Data “1” and Data “0” [5–8, 14]. Second, time interval used for charge and polarization calculation measurement also usually is not specified. However, in real 1T-1C FeRAM devices, only after a certain time interval values Data “1” and Data “0” can be distinguished by the voltage difference on the bitline [9]. So, to recognize reasons of higher OS degradation, evolution of each pulse in “Cap 1” and “Cap 2” sequences and integration interval used for polarization calculation should be consider.

Figure 2(b) shows that in the relaxation region (25 °C) polarizations for all Data “0” and ”Data “1” values without any significant evolution are $\sim 0.4 \pm 0.4$ μC/cm^2 and $\sim 30 \pm 0.4$ μC/cm^2, respectively. The observed error is related to the accuracy of the measuring source (~ 1.5 μA), and not to the presence of a leakage current, since the current at maximum voltage on the pulse shelf after an RC delay is comparable to the current without voltage supply (Fig. S1(b)).

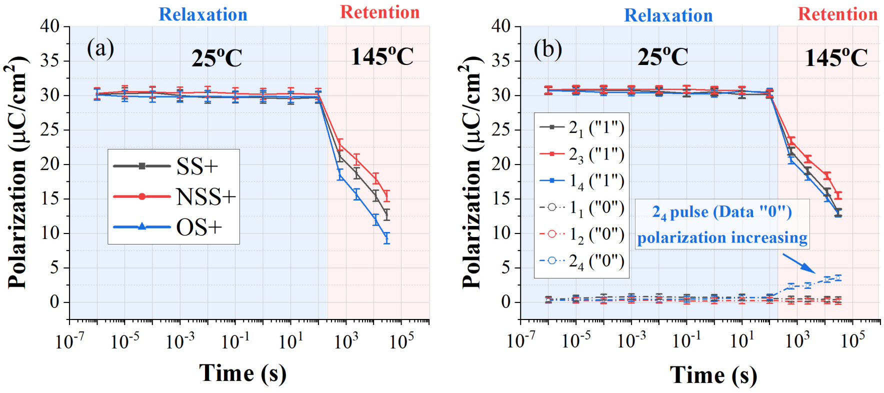

FIG. 2. Relaxation and Retention measurements of the TiN/HZO/TiN capacitors for (a) SS+, NSS+, OS+ and (b) pulses from “Cap 1” and “Cap 2” sequences. Charge measurement range was 3.5 μs (pulse width and 500 ns after it). The calculated values in each time point are in the ranges of ± 0.8 μC/cm^2 for (a) and ± 0.4 μC/cm^2 (b) and showed by error bars

Next, after 145 °C baking, Data “0” 2_4 pulse polarization demonstrate a noticeable increase – to 2.5 μC/cm^2 after 10 minutes, and 3.5 μC/cm^2 after 500 minutes baking. In contrast, other Data “0” pulses polarization (1_1 and 1_2 pulses) is not affected by baking. In turn, all ”Data “1” polarization values demonstrate degradation after baking. 2_1 (SS+), 2_3 (NSS+) and 1_4 (OS+) pulses polarizations after 10 minutes baking were 22, 23, and 20.5 μC/cm^2, respectively. Maximum degradation was achieved after heating for 500 minutes, the values were 13, 16, and 13 μC/cm^2 for SS+, NSS+ and OS+ polarization, respectively.

Thus, higher OS+ degradation in compare with SS+ during baking can be caused by polarization increasing of 2_4 pulse, because changes in 1_1 pulse (Data “0”) are insignificant and degradation ferroelectric 2_1 and 1_4 pulses is comparable. 2_3 pulse (NSS+) higher polarization value can be caused by recovery process after 2_1 and 2_2 pulses [14, 15]. It should be noted that effect of non-zero Data “0” current response detected on 2_4 pulse was reported previously and can be attributed to ferroelectric contribution [10].

Therefore, the analysis of current responses used in calculating the polarization can be useful in understanding the processes (imprint and ferroelectric contribution) taking place in the capacitor (Fig. 3). Changing dynamic of pulses responsible for SS+ and NSS+ are similar: first, there are no significant evolution in current responses of “Data 0” pulses (1_1 and 1_2), second, shifting maximum currents of “Data 1” pulses (2_1 and 2_3) to higher voltages during relaxation and retention measurements (Fig. 3(a–d)). After 100 s delay, maxima of ferroelectric current responses for 2_1 and 2_3 pulses shift to higher voltages on 0.5 and 0.3 V respectively in contrast to 1 μs delay (Fig. S3) and could be associated with imprint recovery for 2_3 pulse [14], however, this imprint does not lead to difference in polarization values (Fig. 2b).

Also, in both cases (2_1 and 2_3 pulses) increasing of backswitching effect detected during voltage fall after baking (Fig. 3(a,c)). For OS+ pulses (1_4 and 2_4) evolution processes show significantly different dynamic in contrast to SS+ and NSS+ pulses: shift current maxima of 1_4 pulse to lower voltages (Fig. 3(e)) and ferroelectric response detection in pulse 2_4 (Fig. 3(f)). In contrast to “Data 1” pulses for SS+ and NSS+ (2_1 and 2_3) there is no backswitching effect for “Data 1” pulses for OS+ (1_4 pulse) after baking. In turn, backswitching effect detected in “Data 0” pulse of OS+ (pulse 2_4). Also, it should be noted that for all pulses with backswitching effect (2_1, 2_3, 1_4) transient current after the pulse end is detected and may influence on polarization calculation [11].

To evaluate influence of transient currents on polarization calculation three time intervals were used: “I1” – 3 μs (only voltage pulse without RC-delay), “I2” – 3.5 μs (used in Fig. 2) and maximum “I3” – 4 μs (Fig. 4).

Increasing of time interval leads to a decrease of calculated polarization values for all pulses. In the relaxation region, calculated polarization for all Data “1” pulses decreases from ~ 33 μC/cm^2 for “I1” to ~ 31 μC/cm^2 for both “I2” and

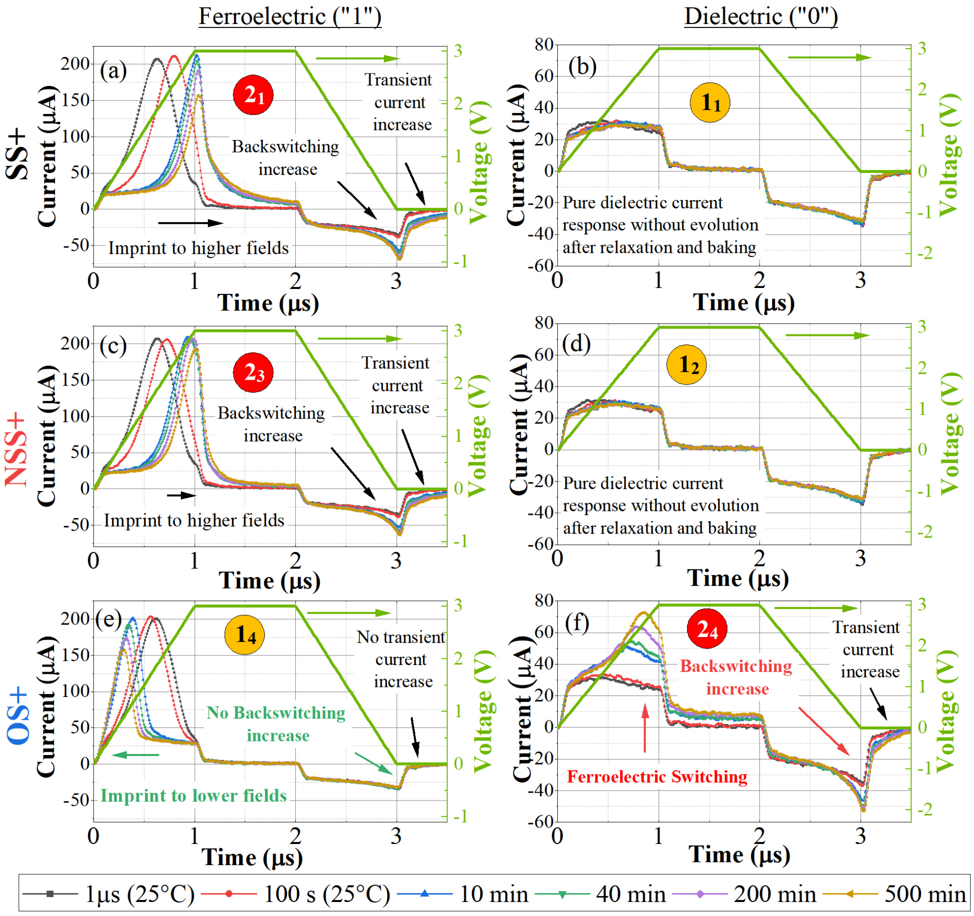

FIG. 3. Current responses of pulses from "Cap 1" and "Cap 2" sequences used for SS+ (a, b), NSS+ (c,d), OS+ (e,f) calculation

"I3". For all Data "0" pulses polarization decreases from ∼2 μC/cm^2 for "I1" to ∼0.8 μC/cm^2 for both "I2" and "I3" (Fig. 4 black and red curves). It is worth noting that Fig. 3(a) and Fig. 4(a) illustrate the reason for the lack of polarization loss during the observed imprint. In case of 1 μs delay most of the charge generated by the ferroelectric switching falls within the medium voltage rising range (∼ 1.9 V in Fig. S3, black curve). In contrast, for a delay of 100 seconds, the same charge flows at higher voltages (∼2.4 V Fig. S3, red curve) and on the flat part of the trapezoidal voltage pulse.

The changes in the integration interval are most pronounced when calculating the polarization after baking for pulses with backswitching (2_1, 2_3, 2_4) For pulse 2_1 after 500 min baking polarization decrease from 19 μC/cm^2 ("I1") to 12 μC/cm^2 ("I3") (Fig. 4a). For 2_4 pulse polarization decrease from 8 μC/cm^2 ("I1") to 2.8 μC/cm^2 ("I3") (Fig. 4d). Therefore, SS+ polarization value after 500 min baking is 17 μC/cm^2 in case of "I1" interval, 13 μC/cm^2 ("I2") and 11.5 μC/cm^2 ("I3"). OS+ polarization value after 500 min baking is 6 μC/cm^2 in case of "I1" interval, 9.5 μC/cm^2 ("I2") and 10.5 μC/cm^2 ("I3"). So, it shows practically equivalent polarization loss for SS+ and OS+ estimated by long pulse interval. The trend for NSS+ is similar to SS+ with effect of partial recovery (not shown).

Interval influence on normalized polarization loss after baking shows in Fig. 5 (SS+ and OS+) and Fig.S4 (NSS+). Maximum difference between states detected for I1 interval after 500 min backing: 56 %, 63 % and 21 % from initial polarization for SS+, NSS+ and OS+ respectively. An increase in the integration interval leads to reducing SS+, NSS+ and increasing OS+ values. The SS+ and OS+ normalized polarization values for I3 interval after 500 min backing practically the same and equal to ∼35 % from initial polarization. For NSS+ normalized polarization value for I3 interval is 45 % after 500 min backing.

It can be seen that an increase in the integration interval leads to an increase in OS+ storage time. At longer integration intervals, the levels of degradation of the SS+ and OS+ states become comparable (green lines in Fig. 5). The same level of normalized OS+ losses (35 % Fig. 5) for the short interval ("I1") it is achieved after ∼ 140 minutes of exposure at 145 ° C, and for the "I3" interval only in 500 minutes.

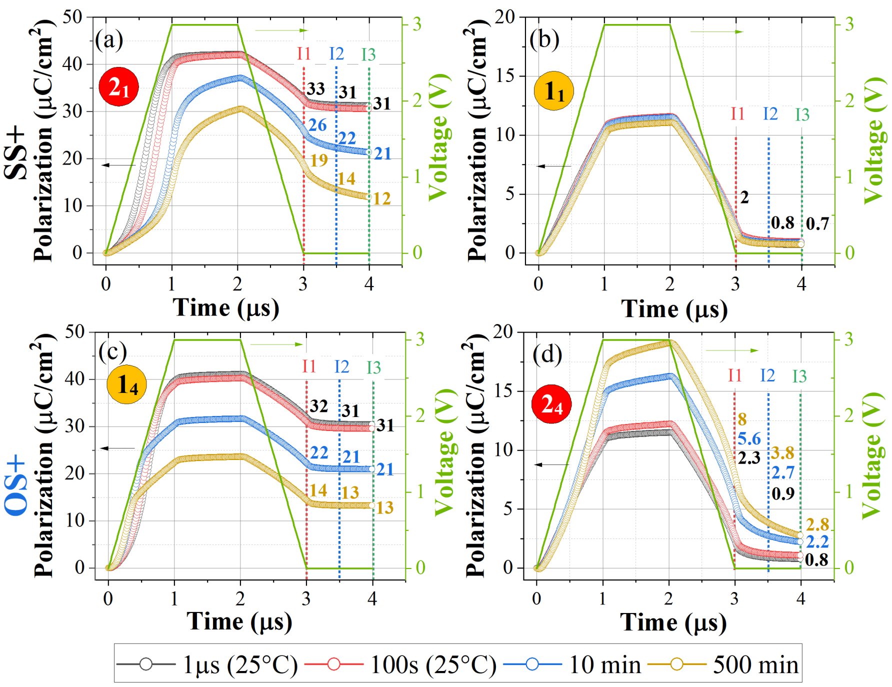

FIG. 4. Change of the polarization value depending on the integration interval for 2_1 (a), 1_1 (b), 1_4 (c) and 2_4 (d) pulses. Numbers indicate polarization values for “I1”, “I2” and “I3” intervals

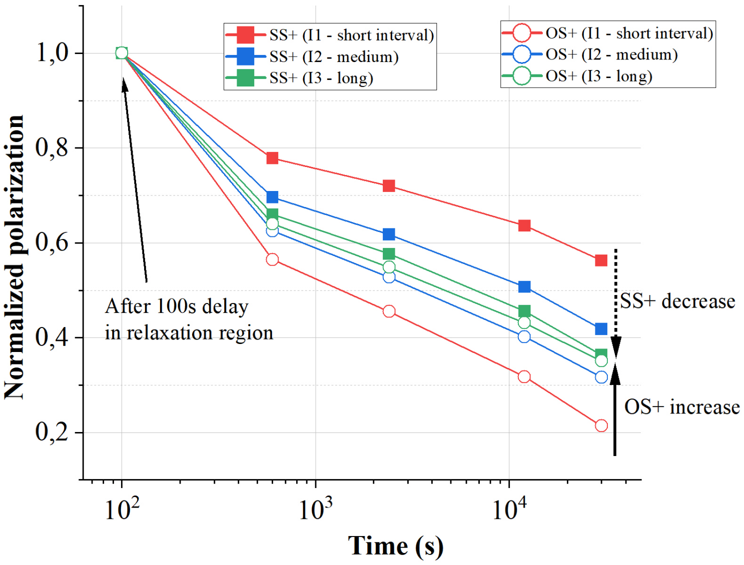

FIG. 5. Comparison of normalized polarization loss of SS+ (closed squares) and OS+ (open circles) for different integration intervals after baking at 145 °C

4. Conclusion

The results presented above show that the shift of the integration endpoint to longer times and the corresponding extension of the integration interval from 3 to 4 μs improve the OS+ retention time in ferroelectric TiN/HZO (10 nm)/TiN capacitors from ∼140 to 500 min at 145 °C. It is also shown that the coercive voltage shift, which is often cited as an unambiguous precursor to read polarization degradation, may not lead to polarization loss in the case of trapezoidal control pulses due to the charge flowing on the pulse shelf.

References

[1] Müller J., Polakowski P., Mueller S., Mikolajick T. Ferroelectric hafnium oxide based materials and devices: Assessment of current status and future prospects. *ECS Journal of Solid State Science and Technology*, 2015, **4** (5), P. N30–N35.

[2] Müller J., Böscke T. S., Bräuhaus D., Schröder U., Böttger U., Sundqvist J., Kücher P., Mikolajick T., Frey L. Ferroelectric $Zr_{0.5}Hf_{0.5}O_2$ thin films for nonvolatile memory applications. *Appl. Phys. Lett.*, 2011, **99** (11), 112901.

[3] Schenk T., Pesic M., Slesazeck S., Schroeder U., Mikolajick T. Memory technology – A Primer for material scientists. *Reports on Progress in Physics*, 2020, **83**, 086501.

[4] Mueller S., Müller J., Schroeder U., Mikolajick T. Reliability characteristics of ferroelectric Si:HfO2 thin films for memory applications. *IEEE Transactions on Device and Materials Reliability*, 2013, **13** (1), P. 93–97.

[5] Mehmood F., Hoffmann M., Lomenzo P.D., Richter C., Materano M., Mikolajick T., Schroeder U. Bulk depolarization fields as a major contributor to the ferroelectric reliability performance in lanthanum doped $Hf_{0.5}Zr_{0.5}O_2$ capacitors. *Adv. Mater. Interfaces*, 2019, **6** (21), P. 1–10.

[6] Mehmood F., Alcala R., Vishnumurthy P., Xu B., Sachdeva R., Mikolajick T., Schroeder U. Reliability improvement from La_2O_3 interfaces in $Hf_{0.5}Zr_{0.5}O_2$ -based ferroelectric capacitors. *Adv. Mater. Interfaces*, 2023, **10** (8), 2202151.

[7] Koroleva A.A., Chernikova A.G., Zarubin S.S., Korostylev E., Khakimov R.R., Zhuk M.Y., Markeev A. M. Retention improvement of HZO-based ferroelectric capacitors with TiO_2 insets. *ACS Omega*, 2022, **7** (50), P. 47084–47095.

[8] Khakimov R. R., Chernikova A. G., Lebedinskii Y., Koroleva A. A., Markeev A. M. Influence of the annealing temperature and applied electric field on the reliability of TiN/$Hf_{0.5}Zr_{0.5}O_2$/TiN capacitors. *ACS Appl. Electron. Mater.*, 2021, **3** (10), P. 4317–4327.

[9] Okuno J., Kunihiro T., Konishi K., Materano M., Ali T., Kuehnel K., Seidel K., Mikolajick T., Schroeder U., Tsukamoto M., Umebayashi T. 1T1C FeRAM memory array based on ferroelectric HZO with capacitor under bitline. *IEEE Journal of the Electron Devices Society*, 2022, **10**, P. 29–34.

[10] Laguerre J., Martin S., Coignus J., Carabasse C., Bocquet M., Andrieu F., Grenouillet L. Data retention insights from joint analysis on BEOL-integrated HZO-based scaled FeCAPs and 16kbit 1T-1C FeRAM arrays. *IEEE International Reliability Physics Symposium Proceedings*, 2024, P. 1–7.

[11] Mikheev V., Kondratyuk E., Chouprik A. Retention model and express retention test of ferroelectric HfO_2-based memory. *Phys. Rev. Appl.*, 2022, **18** (6), 064084.

[12] Okuno J., Kunihiro T., Yonai T., Ono R., Shuto Y., Alcala R., Lederer M., Seidel K., Mikolajick T., Schroeder U., Tsukamoto M., Umebayashi T. A highly reliable 1.8 V 1 Mb $Hf_{0.5}Zr_{0.5}O_2$-based 1T1C FeRAM array with 3-D capacitors. *2023 International Electron Devices Meeting (IEDM)*, 2023, P. 1–4.

[13] Rodriguez J., Remack K., Gertas J., Wang L., Zhou C., Boku K., Rodriguez-Latorre J., Udayakumar K. R., Summerfelt S., Moise T., Kim D., Groat J., Eliason J., Depner M., Chu F. Reliability of ferroelectric random access memory embedded within 130nm CMOS. *IEEE International Reliability Physics Symposium Proceedings*, 2010, P. 750–758.

[14] Chernikova A.G., Markeev A.M. Dynamic imprint recovery as an origin of the pulse width dependence of retention in $Hf_{0.5}Zr_{0.5}O_2$-based capacitors. *Appl. Phys. Lett.*, 2021, **119** (3), 032904.

[15] Yuan P., Mao G.Q., Cheng Y., Xue K.H., Zheng Y., Yang Y., Jiang P., Xu Y., Wang Y., Wang Y., Ding Y., Chen Y., Dang Z., Tai L., Gong T., Luo Q., Miao X., Liu Q. Microscopic mechanism of imprint in hafnium oxide-based ferroelectrics. *Nano Res.*, 2022, **15** (4), P. 3667–3674.

Submitted 23 October 2025; revised 17 March 2026; accepted 18 March 2026

Information about the authors:

Dmitry S. Kuzmichev – Moscow Institute of Physics and Technology, Institutskii per. 9, 141700 Dolgoprudny, Moscow region, Russia; ORCID 0000-0002-8901-5051; kuzmichev.ds@ mipt.ru

Vyacheslav S. Konstantinov – Moscow Institute of Physics and Technology, Institutskii per. 9, 141700 Dolgoprudny, Moscow region, Russia; Molecular Electronics Research Institute, Akademika Valieva st. 6/1, 124460 Zelenograd, Moscow, Russia; ORCID 0000-0002-9112-4898; vkonstantinov@niime.ru

Nikita A. Sizykh – Moscow Institute of Physics and Technology, Institutskii per. 9, 141700 Dolgoprudny, Moscow region, Russia; ORCID 0009-0000-0204-5104; sizykh.na@mipt.ru

Roman R. Khakimov – Moscow Institute of Physics and Technology, Institutskii per. 9, 141700 Dolgoprudny, Moscow region, Russia; ORCID 0000-0003-0707-8567; khakimov.rr@mipt.ru

Conflict of interest: the authors declare no conflict of interest.

NANOSYSTEMS:
PHYSICS, CHEMISTRY, MATHEMATICS

Original article

Nguyen Pham Quynh Anh *Nanosystems: Phys. Chem. Math.*, 2026, **17** (2), 193–199.
http://nanojournal.ifmo.ru
DOI 10.17586/2220-8054-2026-17-2-193-199

Dispersion analysis and tunable magnetic properties of a biaxial hyperbolic metamaterial based on n-GaAs/AlGaAs heterostructures

Nguyen Pham Quynh Anh

Faculty of Engineering and Technology, Saigon University, Cho Quan Ward, Ho Chi Minh City, Vietnam

npqanh@sgu.edu.vn

ABSTRACT This study presents the design and theoretical analysis of a tunable biaxial hyperbolic metamaterial (BHMM) constructed from a layered n-GaAs/AlGaAs heterostructure under an external magnetic field. The objective is to optimize the tunability in order to control the dispersion shape for applications in the terahertz (THz) frequency regime. The effective medium approximation (EMA) model is employed and demonstrates the coexistence of two wave modes, namely, a closed ellipsoidal and an open hyperboloidal isofrequency surface. The results reveal that the external magnetic field acts as a powerful tuning mechanism, enabling spectral shifting of the dispersion and active switching between Type-I and Type-II hyperbolic regimes. In addition, the conditions required to achieve extreme compression of the isofrequency surface (IFS), which is essential for beam steering control, are analyzed. This compression occurs when one component of the permittivity reaches extremely large values, leading to the formation of near-flat segments on the isofrequency surface.

KEYWORDS biaxial hyperbolic metamaterial, terahertz frequency regime, hyperboloidal isofrequency surface, effective medium approximation

FOR CITATION Nguyen Pham Quynh Anh Dispersion analysis and tunable magnetic properties of a biaxial hyperbolic metamaterial based on n-GaAs/AlGaAs heterostructures. *Nanosystems: Phys. Chem. Math.*, 2026, **17** (2), 193–199.

1. Introduction

The rapid advancement of materials science and nanotechnology has led to the emergence of metamaterials – artificially engineered composite structures exhibiting extraordinary electromagnetic properties that are not found in naturally occurring materials, such as negative refractive index and strongly anisotropic dispersion [1–8]. These materials serve as a fundamental platform for the development of compact, multifunctional photonic and electromagnetic devices, and are particularly significant for applications operating in the terahertz (THz) and infrared (IR) frequency regimes [9, 10].

Among anisotropic materials, hyperbolic metamaterials (HMMs) stand out due to their ability to exhibit strongly anisotropic dispersion. HMMs are characterized by an effective dielectric permittivity tensor ($\hat{\varepsilon}$) with principal components of opposite signs ($\varepsilon_\perp \cdot \varepsilon_{||} < 0$). This hyperbolic property enables HMMs to support high-wavevector ($k \to \infty$) modes, thereby overcoming the diffraction limit and significantly enhancing the photonic density of states (PDOS) [11,12]. HMMs have attracted considerable attention for a wide range of applications, including hyperlensing, perfect absorption, and terahertz (THz) biosensing [13].

Most current studies have predominantly focused on uniaxial hyperbolic metamaterials (HMMs), for which $\varepsilon_{xx} = \varepsilon_{yy} \neq \varepsilon_{zz}$. Such media exhibit only two singular points (where the two dispersion surfaces intersect, i.e., optical topological transitions or $\varepsilon \to 0/\infty$) along the symmetry axis, leading to iso-frequency surfaces with rotational symmetry around the optical (Z) axis [14]. Although this symmetry simplifies theoretical analysis, it significantly restricts the ability to manipulate wave propagation at arbitrary angles in three-dimensional space. Consequently, the flexibility in controlling energy flow (beam steering) and the multifunctionality of devices remain limited. To extend the controllability of electromagnetic waves in full three-dimensional space, recent research has shifted toward biaxial hyperbolic metamaterials, a class of media characterized by three distinct components of the effective dielectric permittivity tensor ($\varepsilon_{xx} \neq \varepsilon_{yy} \neq \varepsilon_{zz}$). This additional degree of freedom enables more flexible control of the energy flow with respect to the azimuthal angle [15, 16]. These metamaterials can support up to four potential singular points and possess more complex iso-frequency surfaces, thereby enabling multichannel device designs and improved polarization management, which are essential for advanced telecommunication and sensing applications [17].

Semiconductor-dielectric layered structures subjected to an external magnetic field constitute an effective approach for realizing biaxial hyperbolic metamaterials (BHMMs) and enabling magnetic-field tunability of their extreme dispersion characteristics [18]. Owing to their in-plane anisotropy, BHMMs allow significantly enhanced control of electromagnetic energy flow over a wide range of azimuthal angles. Kuznetsov E.V. and co-workers have optimized BHMM designs to achieve highly accurate energy distribution [19]. In recent years, research on biaxial hyperbolic metamaterials has progressed from proof-of-concept demonstrations toward performance optimization and enhanced tunability for practical applications [20].

Research on semiconductor-based hyperbolic metamaterials highlights that while these structures offer unique optical properties like infinite density of states, their performance depends heavily on the carrier concentration and layer thickness. However, a significant discrepancy exists between nominal design parameters and as-grown structures due to physical phenomena such as band bending and depletion effects at the interfaces. To accurately predict optical responses using effective medium theory, these practical changes in material properties must be integrated into the design process for optimized HMM applications [21]. Moreover, the synergistic coupling between the plasma response of heavily doped semiconductors and the phononic resonances of the crystal lattice indicates that hybrid BHMMs can support multiple dispersion regimes, including the biaxial hyperbolic regime, and offer substantially greater tunability than systems relying on a single physical mechanism (e.g., purely plasmonic platforms). This hybrid strategy represents a promising pathway for the development of multifunctional BHMM devices.

Although previous studies have confirmed the effectiveness of biaxial hyperbolic metamaterials (BHMMs) in controlling energy flow and wave propagation direction, a significant research gap remains in the design of BHMM structures that operate efficiently at room temperature while offering high integration capability. To address these challenges and expand the application potential of BHMMs in terahertz (THz) telecommunications and sensing, this work focuses on phase-transition phenomena in a novel n-GaAs/AlGaAs layered structure, an advanced material platform. The objective is to identify optimal operating conditions, including external magnetic field strength and layer thickness ratios that enable precise control over near-flat segments of the iso-frequency surface, thereby optimizing device performance for THz beam steering and sensing applications.

2. Effective model for n-GaAs/AlGaAs-based biaxial hyperbolic metamaterial

We employ the effective medium approximation (EMA) to investigate a novel multilayer system composed of n-GaAs (semiconductor) and AlGaAs (dielectric) layers. This material platform is deliberately chosen to enable room-temperature operation and enhanced integration capability, in contrast to earlier foundational studies that relied primarily on n-InSb and low-temperature operation. The EMA model is applied under the condition that the individual layer thicknesses are much smaller than the operating wavelength ($kd \leq 1$). The effective dielectric permittivity tensor ($\hat{\varepsilon}$) of the structure is determined by combining the Hall permittivity tensor of the semiconductor layer under an external magnetic field (applied along the Y-axis) with the isotropic dielectric constant (ε_d) of the dielectric layer. The alternating semiconductor (d_1) and dielectric (d_2) stacking induces an intrinsic anisotropy along the stratification (Z) direction, resulting in $\varepsilon_{yy} \neq \varepsilon_{zz}$ even in the absence of an external magnetic field. Regarding magneto-optical anisotropy (Hall effect), the application of an external magnetic field H_0 along the Y-axis renders the permittivity tensor of the semiconductor layer non-diagonal and non-symmetric, characteristic of a Hall-type tensor. However, within the effective medium approximation, this Hall tensor effectively reduces to a diagonal but fully biaxially anisotropic tensor for the composite structure ($\varepsilon_{xx} \neq \varepsilon_{yy} \neq \varepsilon_{zz}$) [18]:

$$\begin{pmatrix} \varepsilon_{xx} & 0 & 0 \\ 0 & \varepsilon_{yy} & 0 \\ 0 & 0 & \varepsilon_{zz} \end{pmatrix}, \tag{1}$$

with the components ε_{xx}, ε_{yy}, ε_{zz} equal to [22]:

$$\varepsilon_{xx} = \frac{w^4 a_1 - w^2 a_2 + a_3}{d w^2 (w^2 - w_H^2 - w_p^2)}, \quad \varepsilon_{yy} = \frac{w^2(\varepsilon_0 d_1 + \varepsilon_d d_2) - w_p^2 \varepsilon_0}{d w^2}, \quad \varepsilon_{zz} = \frac{\varepsilon_0 \varepsilon_d d (w^4 a_1 - w^2 a_2 + a_3)}{w^4 b_1 - w^2 b_2 + b_3},$$

$$a_1 = d_1 e_0 + d_2 e_d, \quad a_2 = w_H^2 a_1 + w_d^2 (d_1 e_0 + a_1), \quad a_3 = d_1 e_0 w_p^4, \quad b_1 = a_1 l_1, \quad l_1 = d_1 e_d + d_2 e_0,$$

$$b_2 = w_H^2 a_1 l_1 + w_p^2 e_0 S, \quad S = (d_2 a_1 + d_1 l_1), \quad b_3 = d_1 d_2 e_0^2 \left(2(w_g^2 + W_p^2) + w_p^4\right).$$

Here e_0 is the lattice dielectric frequency; m_{eff} is the effective mass; $w_H = H_0 e / m_{\text{eff}} c$ is the cyclotron frequency; w_p is the plasma frequency; $w_g = \sqrt{w_H^2 + w_p^2}$ is the hybrid resonance frequency.

Assuming the structure under consideration is non-absorbing ($\vec{J} = 0$, $\rho = 0$), non-magnetic ($\vec{B} = \mu_0 \vec{H}$) and linearly anisotropic ($\vec{D} = \varepsilon_0 \hat{\varepsilon} \vec{E}$. In the frequency domain, Maxwell's equations for harmonic plane waves ($\vec{E}_0 e^{i(\vec{k} \cdot \vec{r} - \omega t)}$) become as follows:

$$\nabla \times \vec{E} = -\frac{\partial \vec{B}}{\partial t} \quad \Rightarrow \quad i\vec{k} \times \vec{E} = i\omega \vec{B} \quad \Rightarrow \quad \vec{k} \times \vec{E} = \omega \vec{B} = \omega \mu_0 \vec{H}, \tag{2}$$

$$\nabla \times \vec{H} = \frac{\partial \vec{D}}{\partial t} \quad \Rightarrow \quad i\vec{k} \times \vec{H} = -i\omega \vec{D} \quad \Rightarrow \quad \vec{k} \times \vec{H} = -\omega \vec{D}. \tag{3}$$

From (2), we have:

$$\vec{H} = \frac{1}{\omega \mu_0} \left(\vec{k} \times \vec{E} \right). \tag{4}$$

Substitute (4) into equation (3), one obtains:

$$\vec{k} \times \left[\frac{1}{\omega\mu_0} \left(\vec{k} \times \vec{E} \right) \right] = -\omega\vec{D}, \tag{5}$$

$$\frac{1}{\omega\mu_0} \left[\vec{k} \times \left(\vec{k} \times \vec{E} \right) - \vec{E}k^2 \right] = -\omega\vec{D}. \tag{6}$$

Multiplying the both sides by $\omega\mu_0$ and setting $k_0^2 = \omega^2\mu_0\varepsilon_0 = \omega^2/c^2$, one comes to the expression:

$$k^2\vec{E} - \vec{k} \times \left(\vec{k} \times \vec{E} \right) = \omega^2\mu_0\vec{D} = \frac{\omega^2}{\varepsilon_0 c^2}\vec{D} = k_0^2\varepsilon_0^{-1}\vec{D}. \tag{7}$$

Due to the relation $\vec{D} = \varepsilon_0\hat{\varepsilon}\vec{E}$, we have:

$$k^2\vec{E} - \vec{k} \times \left(\vec{k} \times \vec{E} \right) = k_0^2\hat{\varepsilon}\vec{E}. \tag{8}$$

Equation (8) in matrix form is as follows:

$$\det \left[\begin{pmatrix} k^2 - k_x^2 & -k_xk_y & -k_xk_z \\ -k_yk_x & k^2 - k_y^2 & -k_yk_z \\ -k_zk_x & -k_zk_y & k^2 - k_z^2 \end{pmatrix} - k_0^2 \begin{pmatrix} \varepsilon_x & 0 & 0 \\ 0 & \varepsilon_y & 0 \\ 0 & 0 & \varepsilon_z \end{pmatrix} \right] = 0. \tag{9}$$

After performing a number of transformations, we obtain a normalized fourth-order equation for k:

$$\frac{k_x^2\varepsilon_x}{k^2 - k_0^2\varepsilon_x} + \frac{k_y^2\varepsilon_y}{k^2 - k_0^2\varepsilon_y} + \frac{k_z^2\varepsilon_z}{k^2 - k_0^2\varepsilon_z} = 0. \tag{10}$$

From Eq. (10), we see that for a given wave propagation direction (with a fixed ratio $k_x : k_y : k_z$), there are always two possible values for the magnitude of the wave vector (k_1 and k_2), corresponding to two orthogonally polarized wave modes in the biaxial medium:

$$k_{1,2}^2 = \frac{-B \pm \sqrt{B^2 - 4AC}}{2A}, \tag{11}$$

with $A = \sum\limits_{i=x,y,z} k_i^2$; $B = k_0^2 \left(\sum\limits_{i \neq j} k_i^2\varepsilon_i\varepsilon_j - k^2 \sum\limits_i \varepsilon_i \right)$; $C = k_0^4\varepsilon_{xx}\varepsilon_{yy}\varepsilon_{zz}$. Here, mode 1 corresponds to the first wave surface, while mode 2 (k_2) corresponds to the second wave surface. The solutions k_1^2 and k_2^2 determine the shapes of the two nested wave surfaces on the iso-frequency surface; both waves exhibit anomalous anisotropic behavior.

3. Dispersion analysis of the n-GaAs/AlGaAs-based biaxial hyperbolic metamaterial

Numerical calculations are performed for the semiconductor–dielectric multilayer structure n-GaAs/AlGaAs: $m_{\text{eff}} = 0.067\,m_0$, $\varepsilon_0 = 12.9$, $\omega_p = 5.3 \times 10^{12}$ rad/s, $\varepsilon_d = 11.8$.

Figure 1 illustrates the frequency dependence of the three components of the effective permittivity (ε_{xx}, ε_{yy}, ε_{zz}). The ε_{yy} component (red dashed line), oriented along the direction of the external magnetic field $\vec{B}$, exhibits the weakest dispersion and remains positive throughout the entire investigated frequency range, indicating that it is only weakly affected by hybrid resonances. In contrast, ε_{xx} (black solid line) and ε_{zz} (blue dotted line) show complex frequency dependences with multiple singularities, providing direct evidence of the BHMM characteristics. The ε_{xx} component exhibits poles where $\varepsilon_{ii} \to \pm\infty$ and zeros where $\varepsilon_{ii} = 0$. For example, ε_{xx} reaches a pole at $\omega \approx 5.6 \times 10^{12}$ s^{-1} (the hybrid resonance frequency) and a zero at $\omega \approx 3.5 \times 10^{12}$ s^{-1} (the effective plasma frequency). The presence of multiple poles and zeros in ε_{xx} arises from the complexity of the analytical expressions and the interlayer coupling, reflecting slow-wave modes characteristic of the layered structure.

The dispersion analysis of biaxial hyperbolic metamaterials (BHMMs) is carried out by means of examining the relationship between the frequency (ω) and the effective permittivity components (ε_{xx}, ε_{yy}, ε_{zz}), identifying the frequency regions where the sign of ε changes, thereby distinguishing between elliptic and hyperbolic dispersion regimes. Fig. 1 shows that ε_{yy} exhibits the weakest dispersion, whereas ε_{xx} and ε_{zz} display pronounced poles and zeros, indicating the strong influence of the hybrid resonance frequency (ω_g) and the plasma frequency (ω_p).

The coexistence of two wave modes (closed and open surfaces) is a characteristic feature of BHMMs. The shape of the iso-frequency surface (IFS) in wave-vector space $\vec{k}$ is classified into two main types according to the sign of the effective permittivity tensor: Type-I hyperbolic dispersion occurs when only one component in the set (ε_{xx}, ε_{yy}, ε_{zz}) is negative, whereas Type-II hyperbolic dispersion arises when two components of the permittivity tensor are negative. From Fig. 1, the structure exhibits Type-I hyperbolic behavior in the frequency range 3.5×10^{12} s^{-1} $< \omega <$ 3.8×10^{12} s^{-1}, with the permittivity components having the sign configuration (+, −, +). The corresponding iso-frequency surface is a double-sheet hyperboloid, compressed in the XZ plane and extended along the Y axis (Fig. 2a). Similarly, in the frequency range 4.9×10^{12} s^{-1} $< \omega <$ 5.6×10^{12} s−1, the structure shows a permittivity sign combination of (+, +, −), where

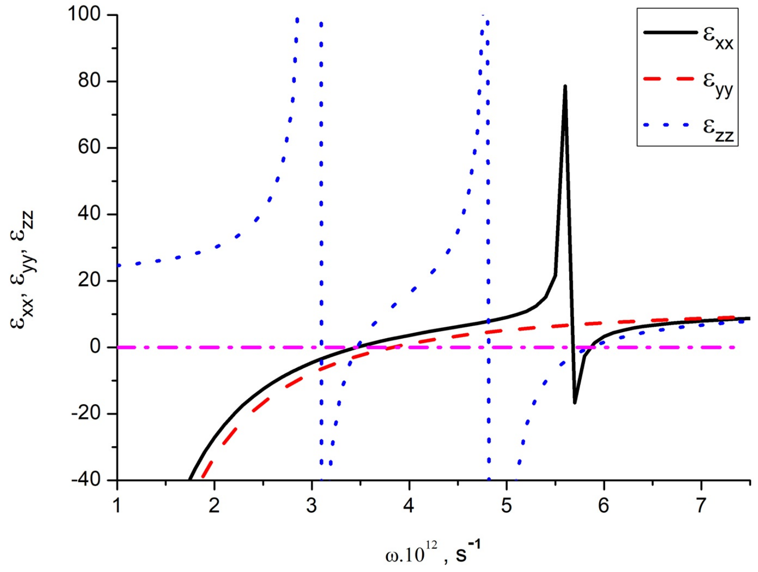

FIG. 1. Spectral dependences of the real parts of effective permittivities ε_{xx}, ε_{yy}, ε_{zz} of metamaterials made of semiconductor–dielectric multilayer structure n-GaAs/AlGaAs with $d_1 = d_2 = 4$ μm.

the iso-frequency surface is strongly compressed in the XY plane and extends infinitely along the Z axis (Fig. 2b). This configuration is highly relevant for hyper-lensing applications and for controlling the photonic density of states (PDOS). The Type-II hyperbolic region (single-sheet hyperboloid) corresponds to $\omega < 3.0 \times 10^{12}$ s^{-1} (Fig. 1). In this range, the permittivity components exhibit the sign configuration $(-, -, +)$, as both ε_{xx} and ε_{yy} take negative values, indicating metallic behavior along the X and Y directions, while retaining dielectric behavior along the Z direction (Fig. 2c). This region allows the propagation of evanescent waves.

The presence of multiple hyperbolic frequency regions indicates that the n-GaAs/AlGaAs BHMM supports multimode operation. The three-dimensional IFS results confirm that, by tuning physical parameters such as the external magnetic field (H_0) and the layer thickness ratio (d_1/d_2), the entire frequency spectrum can be shifted, enabling flexible switching between different BHMM regimes (Type I and Type II). This high degree of tunability is crucial for optimizing the IFS topology, particularly for achieving quasi-flat regions, which are essential for precise beam steering and active THz sensing applications.

The search for near-flat regions on iso-frequency surfaces is a central objective in hyperbolic metamaterial research, as it is directly related to the ability to achieve high-precision control of energy propagation direction, including beam collimation and steering. Based on three-dimensional simulation results obtained from different configurations of ε_{xx}, ε_{yy}, and ε_{zz} (Fig. 3), we analyze the physical conditions leading to the emergence of such near-flat regions. These regions, characterized by vanishing curvature, occur when the IFS is extremely compressed along a confined axis. In the BHMM model, this strong compression arises when the operating frequency ω approaches a pole of the permittivity tensor, causing the magnitude of one permittivity component ε_{ii} to diverge $(\pm\infty)$. As shown in Fig. 3b, the $(+, +, -)$ configuration with $\varepsilon = 8.318,\ 4.804,\ -814.889$ provides an optimal condition for achieving near-flatness. Because ε_{zz} attains a very large negative magnitude – several orders of magnitude larger than ε_{xx} and ε_{yy} – this component imposes an extreme compression of the IFS along the Z axis. Under such compression, the two-sheet hyperboloid IFS (Fig. 3b) is flattened into a highly anisotropic structure that lies close to the XY plane. In this strongly confined regime, the dependence of the dispersion relation on k_z becomes negligible, and the IFS asymptotically approaches the form of two parallel planes $(k_z \approx 0)$. This pronounced flattening constitutes a clear manifestation of near-flat regions, which are crucial for beam steering applications. For the Type-I hyperboloid opened along the Y direction (Fig. 3a), the $(+, -, +)$ configuration produces a relatively slender geometry with large curvature along the hyperbolic branches, and therefore does not generate sufficiently strong compression to induce surface flattening. In contrast, the single-sheet hyperboloid (Fig. 3c) with the $(-, -, +)$ configuration at frequencies close to the poles of ε_{xx} and ε_{yy} (e.g., $\varepsilon = -147.812, -168.831, 24.659$) develops a bottleneck-like shape, where the hyperbolic branches are strongly stretched and become nearly flat. This near-flatness emerges along the open hyperbolic branches when $|\varepsilon_{xx}|$ and $|\varepsilon_{yy}|$ reach extremely large values ($|\varepsilon_{xx}| \approx 148$, $|\varepsilon_{yy}| \approx 169$). As the IFS undergoes strong stretching, its curvature approaches zero. Fig. 3c clearly illustrates the formation of these tilted planar segments, which are of particular interest for beam steering, since the group velocity vector $(\vec{v}_g)$ is always normal to the IFS.

Figure 4 (a and b) illustrate the frequency dependence of ε_{xx} and ε_{yy} for three different values of the applied external magnetic field H_0 (9000 Oe, 7810 Oe, and 3000 Oe). In the considered model, the magnetic field H_0 is applied along the

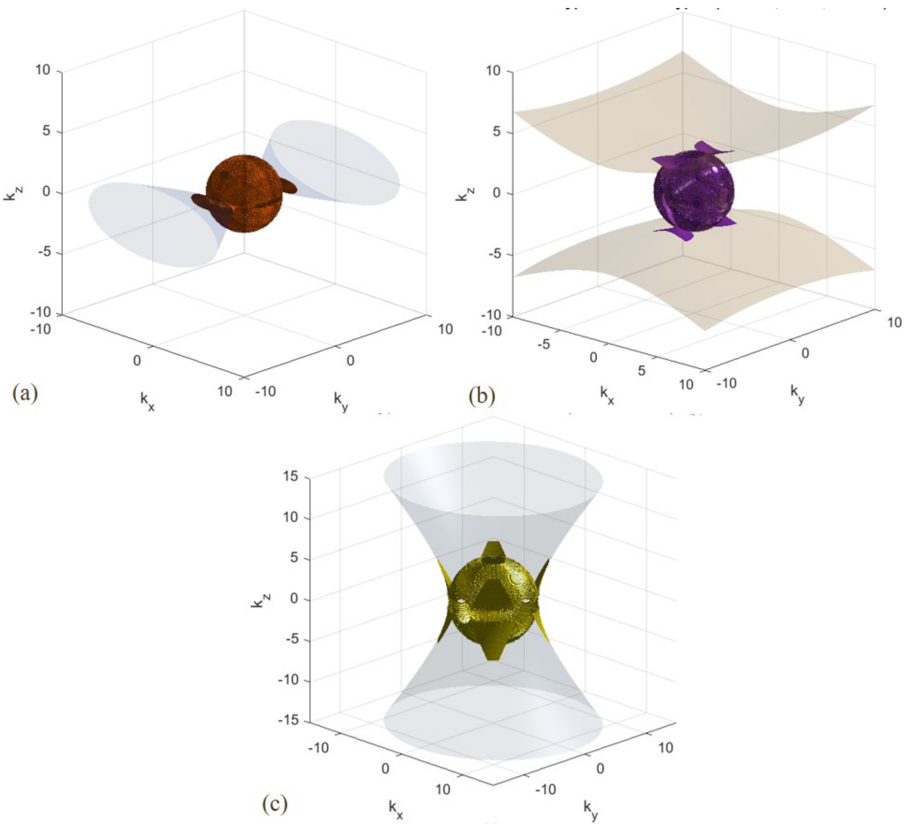

FIG. 2. Iso-frequency surfaces in the wave-vector space for biaxial hyperbolic metamaterials made of semiconductor–dielectric multilayer structure n-GaAs/AlGaAs with $d_1 = d_2 = 4$ μm: a) Biaxial Hyperbolic IFS type I (ε: 1.738; -0.885; 8.928); b) Biaxial Hyperbolic IFS type I (ε: 9.779; 5.384; -39.608); c) Biaxial Hyperbolic IFS dual mode (ε: -42; -50; 27)

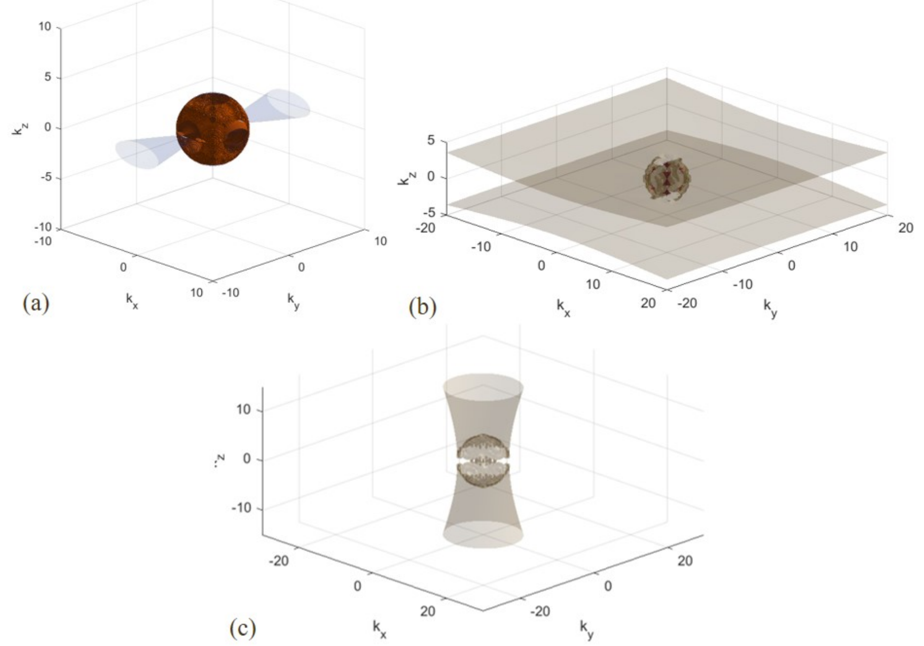

FIG. 3. Iso-frequency surfaces in the wave-vector space for a biaxial hyperbolic metamaterial based on an n-GaAs/AlGaAs multilayer structure ($d_1 = d_2 = 4$ μm), calculated as the operating frequency approaches the zeros – Biaxial Hyperbolic IFS type I (ε: 2.396, -0.197, 11.582) (a) or poles – Biaxial Hyperbolic IFS type I (ε: 8.318, 4.804, -814.889) (b), Biaxial Hyperbolic IFS dual mode (ε: -147.812, -168.831, 24.659) (c) of the effective permittivity tensor components

Y axis. For wave propagation (or electric-field polarization) parallel to the magnetic-field direction, the Hall effect, which is responsible for magnetically induced anisotropy, does not contribute.

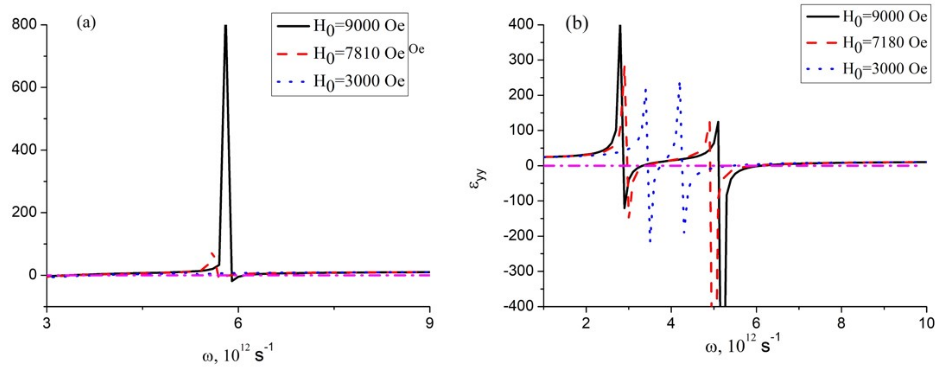

FIG. 4. Spectral dependences of the real parts of effective permittivities ε_{xx} (a), ε_{yy} (b) of metamaterials made of semiconductor–dielectric multilayer structure n-GaAs/AlGaAs ($d_1 = d_2 = 4$ μm) under the influence of an external magnetic field H_0

Nevertheless, both ε_{xx} and ε_{yy} exhibit pronounced shifts in their pole and zero frequencies as H_0 is varied. Specifically, when $H_0 = 9000$ Oe, the pole of ε_{xx} appears at the frequency $\omega = 5.8 \times 10^{12}$ s^{-1}; as H_0 is reduced to 7810 Oe, this pole shifts toward lower frequencies. The magnetic-field dependence of ε_{xx} is more intricate, yet it also displays similar pole–zero shifts, with particularly strong variations occurring around 4.5 – 5.5×10^{12} s^{-1}. This behavior can be attributed to the fact that the cyclotron frequency is proportional to H_0. As H_0 decreases, the cyclotron frequency ω_H is reduced, which in turn lowers the hybrid resonance frequency, leading to an overall redshift of the ε_{xx} and ε_{yy} spectra. Consequently, the magnetic-field-induced displacement of the pole and zero frequencies of ε_{xx} and ε_{yy} enable precise control over the positions of the hyperbolic and elliptic dispersion bands. At a fixed operating frequency (e.g., $\omega = 5 \times 10^{12}$ s^{-1}), the material can be switched between elliptic and hyperbolic dispersion regimes simply by tuning H_0.

This switching capability forms the foundation for active sensing devices and modulators. Another important implication is that tuning H_0 enables direct control over the geometric topology of the iso-frequency surfaces. The near-flat regions on the IFS, which are essential for high-precision beam control, emerge when the operating frequency approaches the hybrid resonance frequency ($\varepsilon \to \infty$). By appropriately adjusting H_0, the pole frequency can be shifted to coincide precisely with the desired operating frequency, thereby optimizing the degree of IFS flattening. This tunability allows for the design of BHMM structures capable of efficient energy collimation and directional wave propagation in the THz regime. Similar behavior is also observed when varying the layer thickness ratio from $0.5 \to 2$ (Fig. 5). As the relative thickness of the semiconductor layer increases with respect to the dielectric layer, the average electron concentration within the effective medium is enhanced, leading to a modification of the effective plasma frequency (ω_p^{eff}). The resulting shift in ω_p^{eff} induces a global redshift of the entire dispersion spectrum, further demonstrating the versatility of structural and magnetic-field tuning for controlling BHMM dispersion characteristics.

4. Conclusion

This study confirms the feasibility and advantages of employing n-GaAs/AlGaAs layered structures under an external magnetic field to implement biaxial hyperbolic metamaterials (BHMMs) operating in the THz frequency range. The effective medium approximation (EMA) has been successfully applied, demonstrating that the proposed structure behaves as a BHMM characterized by three distinct effective permittivity components ($\varepsilon_{xx} \neq \varepsilon_{yy} \neq \varepsilon_{zz}$). The analysis reveals that the external magnetic field H_0 serves as a powerful tuning parameter, enabling active switching among different dispersion regimes (elliptic, Type-I hyperbolic, and Type-II hyperbolic) at a fixed operating frequency through controlled shifts of the pole and zero frequencies of ε_{xx} and ε_{yy}. In addition, the layer thickness ratio d_1/d_2 is identified as a key structural design parameter for tailoring the degree of anisotropy and the extreme magnitude of the permittivity components, which ultimately governs the IFS topology. The combined tuning of magnetic and structural parameters demonstrates the ability to generate pronounced near-flat regions on the iso-frequency surfaces, particularly when one permittivity component attains an extremely large magnitude (e.g., $\varepsilon_{zz} = -815$), thereby producing the strong compression required for beam-steering applications. In conclusion, the use of n-GaAs together with its strong magnetically induced tunability establishes this BHMM architecture as a promising platform for next-generation photonic devices, capable of precise manipulation and steering of electromagnetic waves in the THz regime, with significant potential for high-speed communication systems and active sensing applications.

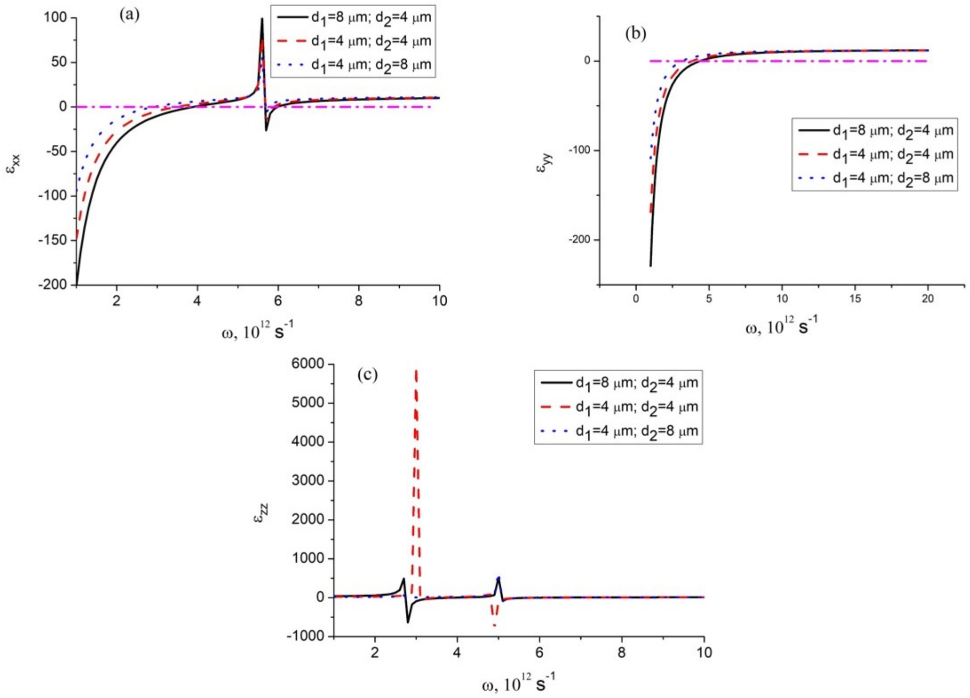

FIG. 5. Spectral dependences of the real parts of effective permittivities ε_{xx} (a), ε_{yy} (b), ε_{zz} (c) under the specified layer thickness ratio (d_1/d_2) of metamaterials made of semiconductor–dielectric multilayer structure n-GaAs/AlGaAs $(d_1 = d_2 = 50\ \mu\text{m})$

References

[1] Veselago V.G. The Electrodynamics of Substances with Simultaneously Negative Values of ε and μ. *Sov. Phys. Uspekhi*, 1968, **10** (4), P. 509–514.
[2] Smith D.R., et al. Metamaterials and Negative Refractive Index. *Science*, 2004, **305** (5685), P. 788–792.
[3] Krushynska A.O., et al. Fundamentals and applications of metamaterials: Breaking the limits. *App. Phys. Lett.*, 2023, **123**, 240401.
[4] Ritchie R.H. Plasma losses by fast electrons in thin films. *Phys. Rev.*, 1957, **106** (5), P. 874–881.
[5] Liu Y., Zhang X. Metamaterials: A new frontier of science and technology. *Chem. Soc. Rev.*, 2011, **40** (5), P. 2494–2507.
[6] Kshetrimayum R.S. A brief intro to metamaterials. *IEEE Potentials*, 2004, **23** (5), P. 44–46.
[7] Yan R., et al. High sensitive plasmonic nanorod hyperbolic metamaterial biosensor. *Photonics Research*, 2022, **10** (1), P. 84–95.
[8] Alù A., Silveirinha M.G., Saladrino A., Engheta N. Epsilon-near zero metamaterials and electromagnetic sources: Tailoring the radiation phase pattern. *Phys. Rev. B*, 2007, **75** (15), 155410.
[9] Chen H.T., et al. Active terahertz metamaterial devices. *Nature*, 2006, **444** (7119), P. 597–600.
[10] Ren Z., et al. Terahertz metamaterials inspired by quantum phenomena. *Research*, 2025, **8** (1), P. 1–28.
[11] Ma Q., Hu H., Huang E., Liu Z. Super-resolution imaging by metamaterial-based compressive spatial-to-spectral transformation. *Nanoscale*, 2017, **9** (46), P. 18268–18274.
[12] Khurgin J.B. Enhanced spontaneous emission inside hyperbolic metamaterials. *Opt. Express*, 2014, **22** (4), P. 4301–4306.
[13] Wang B. X., et al. Review of broadband metamaterial absorbers: From principles, design strategies, and tunable properties to functional applications. *Adv. Func. Mat.*, 2023, **33** (14), 2213818.
[14] Poddubny A., Iorsh I., Belov P., Kivshar Y. Hyperbolic metamaterials. *Nat. Photonics*, 2013, **7**, P. 948–957.
[15] Zheludev N.I., et al. The new phase of light. *Nat. Photonics*, 2020, **14**, P. 337–338.
[16] Chen B., et al. Hyperbolic metasurfaces enable enhancement and regulation of near-field radiative heat transfer. *Int. J. Heat Mass Transf.*, 2025, **169**, 109608.
[17] Chern R.-L, Yu Y.-Z. Chiral surface waves on hyperbolic-gyromagnetic metamaterials. *Opt. Expr.*, 2017, **25** (10), P. 11801–11812.
[18] Bulgakov A.A., Fedorin I. Surface electromagnetic waves in thin-layer biaxial structure in a magnetic field. *J. Electr. Mat.*, 2012, **54**, P. 1566–1574.
[19] Kuznetsov E.V., Merzlikin A.M. Light propagation in a magneto-optical hyperbolic biaxial crystal. *Opt. Comm.*, 2017, **405**, P. 164–170.
[20] Song X., Liu Z., Xiang Y., Aydin K. Biaxial hyperbolic metamaterials using anisotropic few-layer black phosphorus. *Opt. Express*, 2018, **26** (5), P. 5469–5477.
[21] Eylink K. G., et al. Determination of critical parameters for design of semiconductor hyperbolic metamaterials. *Opt. Materials*, 2021, **112**, 110576.
[22] Bulgakov A.A., Fedorin I.V. Electrodynamic properties of a thin-film periodic structure in an external magnetic field. *Opt., Quant. Electr.*, 2011, **56**, P. 510–514.

Submitted 6 January 2026; revised 26 February 2026; accepted 27 February 2026

Information about the authors:

Nguyen Pham Quynh Anh – Faculty of Engineering and Technology, Saigon University, 273 An Duong Vuong Street, Cho Quan Ward, Ho Chi Minh City, Vietnam; ORCID 0009-0009-4001-4873; npqanh@sgu.edu.vn

Conflict of interest: The author declares that he has no potential conflict of interests.

NANOSYSTEMS:
PHYSICS, CHEMISTRY, MATHEMATICS

Pleshakov I.V., et al. *Nanosystems: Phys. Chem. Math.*, 2026, **17** (2), 200–203.
http://nanojournal.ifmo.ru
DOI 10.17586/2220-8054-2026-17-2-200-203

Original article

Laser correlation spectroscopy of nanodispersed solutions in the region of transition to multiple light scattering

Ivan V. Pleshakov[1,a], Aleksey V. Soloviev[2,b], Arseniy A. Alekseev[3,c], Yakov A. Fofanov[4,d]

[1]Ioffe Institute, Saint Petersburg, Russia
[2]Independent researcher, Russia
[3]Peter the Great Saint Petersburg Polytechnic University, Saint Petersburg, Russia
[4]Institute for Analytical Instrumentation of RAS, Saint Petersburg, Russia

[a]ivanple@yandex.ru, [b]alexei.v.soloviev@gmail.com, [c]arseniy.alekseev98@gmail.com, [d]yakinvest@yandex.ru

Corresponding author: Ivan V. Pleshakov, ivanple@yandex.ru

PACS 42.62.-b, 42.68.Mj

ABSTRACT The work considers the application of laser correlation spectroscopy to the investigation of dispersed systems for such a case, which can be regarded as a transitional to the multiple scattering regime. It is shown that even a slight violation of the condition of single scattering by the increasing of concentration of scattering centers can affect the result of particle size measurements. It should be taken into account when studying colloids.

KEYWORDS aser correlation spectroscopy, multiple light scattering, nanoparticles

FOR CITATION Pleshakov I.V., Soloviev A.V., Alekseev A.A., Fofanov Y.A. Laser correlation spectroscopy of nanodispersed solutions in the region of transition to multiple light scattering. *Nanosystems: Phys. Chem. Math.*, 2026, **17** (2), 200–203.

1. Introduction

The laser correlation spectroscopy method (LCS), which is used in the study of various types of dispersed systems, had been developed primarily for the case of single-scattering of probing radiation [1,2]. However, the task of investigation of a structure with multiple scattering is also relevant, and LCS can be used here in one form or another, although artifacts are observed that significantly affect the determination of sample characteristics. Despite the existence of a number of works in the field, the theoretical understanding of such processes is still in progress.

This article discusses an important variant of LCS application: testing of the solutions at such particle concentrations for which the single light scattering transforms into multiple one. The theoretical results are compared with the experimental data obtained on polystyrene latex colloids, which serve as a model system for comprehension of the effects in this boundary region.

2. Theoretical analysis of the autocorrelation function of multiple scattered light

When finding the particles size by the LCS method, the autocorrelation function $G^{(2)}(\tau) = \langle I(t+\tau)I(t)\rangle$ of the scattered light intensity I is measured. Subtracting the base line $G^2(\infty)$ from it gives one the expression $G(\tau) = G^{(2)}(\tau) - G^{(2)}(\infty)$. Further we will refer to it simply as the autocorrelation function (ACF) of the scattered light.

It has been shown that if light is scattered by a colloidal solution with particles of radius r, the ACF depends on τ exponentially [1–3]:

$$G(\tau) = A\exp(-\Gamma\tau), \tag{1}$$

where

$$\Gamma = \frac{kTq^2}{3\pi\eta r}. \tag{2}$$

Here, k is the Boltzmann constant, T is the temperature, η is the viscosity of the carrier medium, and q is the length of the wave vector of the scattered radiation; $q = (4\pi n_0/\lambda)\sin(\theta/2)$, where n_0 is the refractive index of the medium, λ is the wavelength of the incident radiation, and θ is the scattering angle.

By determining Γ from the exponential approximation (1) of the experimental data and using expression (2), one can easily obtain the particle size in a monodisperse colloidal solution.

The ACF analysis can be performed in a more general form. Let us define the value of Γ as

$$\Gamma = -\frac{\partial \ln G(\tau)}{\partial \tau}\Big|_{\tau=0}. \tag{3}$$

For an exponential ACF, formula (3) provides the same value for Γ as earlier. It can be shown that in the case of a polydisperse system, when the ACF is nonexponential, determination Γ by expressions (3) and (2) gives the average value of the particle size [3,4].

Let Γ_1 be the value defined by the expression (3) for the ACF of light scattered at an angle of 90° in a dilute solution, when the scattering can be considered as single one. As the concentration of particles c increases, the mean free path of the photon l will decrease, and the scattering becomes multiple. For this case, we denote the value of Γ defined by (3) as Γ_m and represent it as $\Gamma_m = N\Gamma_1$, where N is the multiplicity of scattering.

It has been demonstrated previously [5,6] that when a spherical cuvette of diameter d is used to place the sample, and under the condition $l \ll d$, the value of N can be calculated by the following formula:

$$N = \frac{d^2}{l^2}(1-\bar{\mu})F(\theta), \tag{4}$$

where $\bar{\mu}$ is the average cosine of the angle of single scattering, and for $F(\theta)$, the expression was obtained:

$$F(\theta) = \frac{3}{2}\cos^2\frac{\theta}{2}\Big(1 - 4\cos\frac{\theta}{2}\int\limits_0^1 \frac{y^2dy}{\sqrt{1+2y^2\cos\theta + y^4}}\Big). \tag{5}$$

We would like to note that the integral in equation (5) can be expressed in terms of complete elliptic integrals of the first and the second kind $K(x)$ and $E(x)$:

$$\int\limits_0^1 \frac{y^2dy}{\sqrt{1+2y^2\cos\theta+y^4}} = \frac{1}{3\sin^2\frac{\theta}{2}}\Big[(1+\cos\theta)K(\sin\frac{\theta}{2}) - (3+\cos\theta)E(\sin\frac{\theta}{2})\Big].$$

Note that

$$l = \frac{1}{\sigma n} = \frac{m}{\sigma c}, \tag{6}$$

where σ is the cross-section of light scattering on a particle, n is the particle number concentration, m is the mass of the particle, c is the mass concentration of particles.

Assuming $\theta = 90°$ (herewith $F \approx 0.15$), from (4)–(6), it is easy to obtain the following formula

$$\Gamma_m \cong 0.15\, d^2\sigma^2\frac{c^2}{m^2}(1-\bar{\mu})\Gamma. \tag{7}$$

From this expression, it is clear that if the particle concentration increases, the value of Γ_m increases. Accordingly, this will lead to a decrease in the average particle radius, determined by formula (2).

At relatively small particle concentrations c, when the photon mean free path is comparable with the size of the scattering volume, expression (7) cannot be applied quantitatively. However, we assume that even in this case (i.e., in the transition regime between single- and multiple-scattering), an apparent decrease in the average particle size will also be observed for increasing c, since the probability of photon collisions with particles increases even with a slight increase in concentration. This leads to a broadening of the scattering spectrum, a more rapid decay of the ACF near zero, a growth of the value of Γ found by formula (3), and ultimately to the specified effect.

3. Effect of scattering centers concentration on LCS results

To verify experimentally the above statements, the standard LCS method was used [1]. The source of optical radiation was a He-Ne laser ($\lambda = 632.8$ nm), which was focused onto a center of a cuvette containing the solution under study. The cuvette had a rectangular cross-section with the size 10 × 10 mm (the results obtained with it, being qualitative, certainly can be compared with the conclusions of the theory developed for a spherical cuvette). The light scattered by the sample was transmitted to an optical fiber and, after passing through it, was recorded by a photodetector. The scattering angle was 90°. The signal was fed to an analog-to-digital converter and then to a computer, where it was processed, resulting in the ACF. A more detailed description of this setup can be found in articles [7,8], which describe experiments performed using the same approach as in this work.

Aqueous solutions containing polystyrene latex particles with a nominal radius of approximately 30 nm (this material is commercially available) were taken as test substances. The measurements were performed at the following solid phase concentrations: 0.1, 0.3, 1.0, 2.9, 8.2, and 41 mg/ml.

The calculations of Γ corresponding to the expression (3) were performed as follows. The logarithm of the ACF was approximated by a quadratic polynomial $f(\tau) = A + B\tau + C\tau^2$ using sixty initial points of the ACF, and Γ was taken to be $-B$. This value is more stable to ACF measurement errors than that found by the derivative of its logarithm over several points in the initial section of the linear approximation.

The concentration dependence of Γ is shown in Fig. 1. It can be seen that, as it follows from expression (7), Γ increases monotonically with increasing of c.

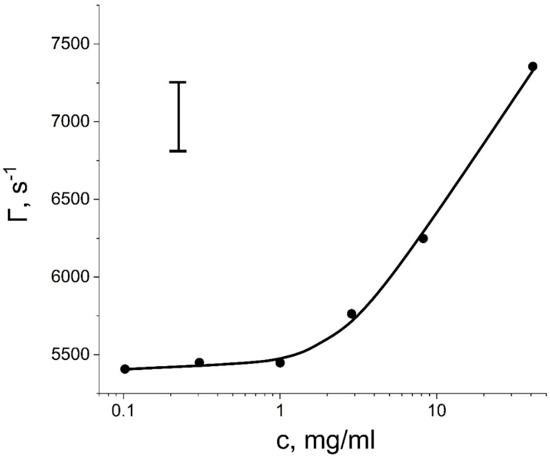

FIG. 1. Dependence of $\Gamma = -B$ on the concentration of particles

To estimate the photon mean free path l and the scattering multiplicity, an experiment on the attenuation of light was carried out, and the Bouguer–Lambert–Beer extinction law $I_d = I_0 \exp(-d/l)$ was used (I_0 and I_d are the intensities of the incident and transmitted light through the cuvette, respectively).

For the concentration of 41 mg/ml, $l \approx 4$ mm was obtained. In this case, at $d = 10$ mm, the value of N calculated by formula (4) is close to 1 (here the average cosine was taken $\bar{\mu} = 0.026$, that was found by Mie scattering theory). The calculated value of N means that for this and lower concentrations, the experiment was performed for the regime where the transition to multiple scattering is just beginning, and expressions (4)–(7) can only be applied qualitatively.

Substituting of Γ, determined as above, into (2) yields the dependence of the nominal values of the particle radius on the concentration, demonstrated in Fig. 2. It shows that the apparent value of R, measured by the LCS method, decreases with an increase in c. Since there is no actual change in the particle size, this phenomenon can only be attributed to a decrease in the photon mean free path and an increase in the scattering multiplicity of light in the colloidal solution. Note that knowledge of this fact especially can be useful in synthesizing and studying media such as magnetic fluids [9], where even a small deviation in particle size can lead to significant changes in macroscopic properties [10].

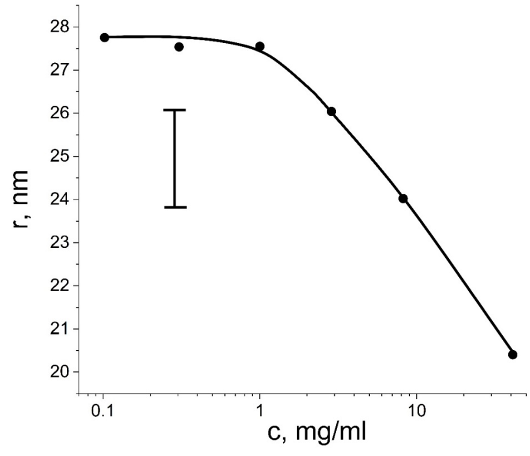

FIG. 2. Dependence of the calculated average radius of particles on their concentration

4. Conclusion

It has been established that when investigating dispersed systems using laser correlation spectroscopy, it is necessary to take into account the effect that, as the region of the multiple scattering of probing radiation approaches, the seeming size of the particles begins to depend on their concentration. It has been experimentally shown that this feature can already be observed even in regions where the scattering multiplicity only slightly differs from unity. This fact is important for examination the characteristics of colloids with relatively high solid phase content.

References

[1] Stetefeld J., McKenna S.A., Patel T.R. Dynamic light scattering: a practical guide and applications in biomedical sciences. *Biophys. Rev.*, 2016, **8** (4), P. 409–427.

[2] Nepomniashchaia E.K., Aksenov E.T., Bogomaz T.A., Velichko E.N. Use of laser correlation spectroscopy to investigate the parameters of biological suspensions. *J. Opt. Technol.*, 2015, **82** (3), P. 162–165.

[3] Cummins H.Z., Pike E.R. (Eds.) Photon Correlation and Light Beating Spectroscopy. Springer, Great-Malvern, 1974, 584 p.

[4] Dietz R. (Ed.) Industrial Polymers: Characterization by Molecular Weight. Transcripta Books, Teddington, 1975, 136 p.

[5] Ivanov D.Yu., Soloviev A.V. The effect of laser radiation on the temperature of highly scattering media, *Deposited scientific work*, Dep. in VINITI 22.04.1992, N 1357-B92, 19 p.

[6] Kostko A.F., Pavlov V.A. Location of the effective diffusing-photon source in a strongly scattering medium. *Appl. Opt.*, 1997, **36** (30), P. 7577–7582.

[7] Pleshakov I.V., Ryzhov V.A., Marchenko Ya.Yu., Alekseev A.A., Karseeva E.K., Nevedomskiy V.N., Prokof'ev A.V. Agglomeration of magnetite nanoparticles with citrate shell in an aqueous magnetic fluid. *Nanosystems: Phys. Chem. Math.*, 2023, **14** (3), P. 334–341.

[8] Pleshakov I.V., Alekseev A.A., Fofanov Ya.A. Observation of the processes of formation and growth of aggregates in a magnetic fluid by laser correlation spectroscopy. *Tech. Phys. Lett.*, 2025, **51** (8), P. 72–76.

[9] Pleshakov I.V., Alekseev A.A., Bibik E.E., Ilichev I.V., Prokof'ev A.V. Effect of laser radiation on magnetite nanoparticles in deposited ferrofluid. *Nanosystems: Phys. Chem. Math.*, 2024, **15** (3), P. 346–351.

[10] Punit T., Sarvendra K., Jitendra K., Singh S.P., Pant R.P. Finite size effect on structural, morphological, magnetic, and magneto-optical properties of Fe_3O_4 based nanofluids. *J. of Materials Science: Materials in Electronics*, 2025, **36** (36), 2310.

Submitted 1 March 2026; revised 13 March 2026; accepted 14 March 2026

Information about the authors:

Ivan V. Pleshakov – Ioffe Institute, Saint Petersburg, Russia; ORCID 0000-0002-6707-6216; ivanple@yandex.ru

Aleksey V. Soloviev – Independent researcher, Russia; ORCID 0009-0000-5368-6788; alexei.v.soloviev@gmail.com

Arseniy A. Alekseev – Peter the Great Saint Petersburg Polytechnic University, Saint Petersburg, Russia;
ORCID 0009-0000-5368-6788; arseniy.alekseev98@gmail.com

Yakov A. Fofanov – Institute for Analytical Instrumentation of RAS, Saint Petersburg, Russia; ORCID 0009-0004-2565-8834; yakinvest@yandex.ru

Conflict of interest: the authors declare no conflict of interest.

NANOSYSTEMS:
PHYSICS, CHEMISTRY, MATHEMATICS

Original article

Bakulin A.V., Kulkova S.E. *Nanosystems: Phys. Chem. Math.*, 2026, **17** (2), 204–209.
http://nanojournal.ifmo.ru
DOI 10.17586/2220-8054-2026-17-2-204-209

Elastic and mechanical properties of Ti–Nb–Zr based alloys

Alexander V. Bakulin[a], Svetlana E. Kulkova[b]

Institute of Strength Physics and Materials Science of the Siberian Branch of the Russian Academy of Science, Tomsk, Russia

[a]bakulin@ispms.ru, [b]kulkova@ispms.ru

Corresponding author: Alexander V. Bakulin, bakulin@ispms.ru

PACS 62.20.-x, 62.20.Dc, 62.20.Mk

ABSTRACT The elastic properties and mechanical characteristics of Ti–Nb_{22}–Zr_6 based alloys were calculated using the exact muffin-tin orbital method with the coherent potential approximation. Alloying by metals such as Hf, Mg and their combination were considered, and their concentration did not exceed 5 at.%. It was shown that addition of Hf and Mg leads to a decrease in Young's modulus due to both size effect and electronic factor. The calculated Young's modulus for the ternary Ti–Nb_{22}–Zr_6 alloy (70.1 GPa) is found in good agreement with experimental one (70 GPa). The smallest value of Young's modulus was calculated for the Ti–Nb_{22}–Zr_6–Hf_5–$Mg_{2.5}$ alloy, achieving 57 GPa. Further increase in Mg concentration leads to a negative C' and alloy destabilization. Additionally, alloying of the Ti–Nb_{22}–Zr_6 alloy results in a decrease in hardness, fracture toughness, but brittleness index is increased.

KEYWORDS titanium alloys, elastic moduli, mechanical properties, ab-initio calculations

ACKNOWLEDGEMENTS The work was performed according to the Government research assignment for ISPMS SB RAS, project FWRW-2026-0008.

FOR CITATION Bakulin A.V., Kulkova S.E. Elastic and mechanical properties of Ti–Nb–Zr based alloys. *Nanosystems: Phys. Chem. Math.*, 2026, **17** (2), 204–209.

1. Introduction

Ti–Nb based alloys are very promising materials for biomedical applications [1–7] because of their low Young's modulus (E) and biochemical compatibility with bone tissues. Our calculations of binary Ti–Me alloys (Me = V, Nb, Mo, Ta) demonstrated that near critical concentration of second component ($\beta \to \alpha$ transformation) all alloys have sharp decrease of E. However, prolonged contact of vanadium ions with biological tissues can provoke allergic reactions and have a negative effect on the nervous system [6]. Molybdenum, although is not considered cytotoxic, has an extremely detrimental effect on the rate of cell proliferation, mitochondrial activity and the volume of cells cultured on it [6]. So, the Ti–(Ta,Nb) based system can particularly suitable for orthopedic implants due to a reduced Young's modulus. Indeed, modern low-modulus alloys are mainly developed based on the Ti–Nb system with alloying elements such as Zr/Hf, Ta and Sn [5–7]. These elements, like Ti, are characterized by high biocompatibility and are β-stabilizing or neutral elements [6, 8]. Besides, the atomic radii of these elements exceed the size of the Ti atom that can also decrease the Young's modulus. At present, quantum mechanical methods allow one to calculate elastic moduli with sufficient accuracy and in a reasonable time in comparison with experiments and do not require significant expenditures. In order to estimate the elastic constants and moduli of disordered alloys several approaches are used. One of them is using the supercell approach, in which the larger the supercell, the lower the possible concentration of the alloying element [9, 10]. A significant drawback of this approach is the dependence of the total energy on the configuration of impurity atoms, although it is often neglected. Another approach is to use the so-called special quasirandom structures (SQS) [11]. In this case, supercells are generated to simulate a random distribution of atoms in terms of the correlation function, minimizing calculation errors relative to real random structures. Further, the exact muffin-tin orbital method with the coherent potential approximation (EMTO–CPA) [12] can be used also. This method is more suitable to structures with chemical disorder, since it eliminates the issue of configuration altogether, and calculations are performed for a unit cell containing a minimum number of atoms (one atom in the case of the β-phase). Nevertheless, studies using the EMTO–CPA method remain relatively rare. In any case, the problem to verification of obtained results is common one for all theoretical approaches. The latter is connected with a large scatter of experimental results, difference in the component concentration, the absence of information about phase compositions, etc. Recently the β-alloy with composition Ti–Nb_{22}–Zr_6 (at.%) was detailed studied in the paper [13]. Both experimental and theoretical values of Young's modulus are presented in this study.

The aim of this work is to study the electronic structure and mechanical characteristics of ternary β-Ti–Nb$_{22}$–Zr$_6$ alloy and to compare with available data as well as to investigate the influence of Hf and Mg on the lowering Young's modulus.

2. Method

Calculations of the electronic structure of disordered ternary and many component Ti–Nb$_{22}$–Zr$_6$ based alloys were performed using the exact MT-orbital method with the coherent potential approximation (EMTO–CPA) [12], which utilizes a random distribution of alloy atoms. The Green's function formalism and a $15\times15\times15$ k-point grid were used to calculate the total energies of alloys. The convergence criterion for the total energy was 10^{-7} Ry.

The finite displacement method was used to estimate the elastic constants. It is known that in the harmonic approximation, the change in total energy during deformation can be written as follows:

$$\Delta E\left(V,\{\varepsilon_i\}\right) = E\left(V,\{\varepsilon_i\}\right) - E\left(V_0,\ 0\right) = \frac{V_0}{2}\sum_{i,j=1}^{6} C_{ij}\varepsilon_i\varepsilon_j, \tag{1}$$

where $E(V,\ \varepsilon_i)$ and $E(V_0,\ 0)$ are the total energies of the deformed and equilibrium alloy cells with volumes V and V_0, respectively; ε_i is the strain; C_{ij} are the elastic constants. The total energies of the alloys, calculated for three different strains (isotropic, orthorhombic, and monoclinic), were used to estimate the bulk modulus (B) and the elastic constants C' and C_{44}, respectively. The other two elastic constants were calculated using the following formulas:

$$\begin{aligned} C_{11} &= B + 4C'/3, \\ C_{12} &= B - 2C'/3. \end{aligned} \tag{2}$$

Based on the elastic constants, the values of the shear and Young's moduli were calculated within the Voigt–Reuss–Hill approximation using standard formulas [14]:

$$\begin{aligned} G &= \frac{1}{2}\left[\frac{2C' + 3C_{44}}{5} + \frac{5C_{44}C'}{2C_{44} + 3C'}\right], \\ E &= \frac{9BG}{3B + G}. \end{aligned} \tag{3}$$

For the Vickers hardness (H_V) the following formula was used [15]:

$$H_V = \frac{E}{15.76}. \tag{4}$$

The choice of this expression is due to good agreement between the calculated value of 2.8 GPa for the Ti–Nb$_{20}$ alloy and the experimental values of 2.7 [16] and 2.8 GPa [17] for the Ti–Nb$_{21.7}$ alloy.

The fracture toughness was calculated using the formula [18]:

$$K_{IC} = (1 + \alpha)\sqrt{BGV_0^{1/3}}, \tag{5}$$

where V_0 is the volume per atom, and α is the enhancement factor due to peculiarities of metallic bond compared to covalent and ionic bonds.

Finally, the brittleness index M_{dt}, which reflects the machinability of the materials, can be defined as the ratio of the Vickers hardness to the fracture toughness [19]:

$$M_{dt} = \frac{H_V}{K_{IC}}. \tag{6}$$

3. Results and discussion

The calculated values of elastic constants and moduli for the binary alloys Ti–Nb$_{20}$ and Ti–Nb$_{25}$ are given in the Table 1. It is seen that the C' constant of the Ti–Nb$_{20}$ alloy has small negative value that indicates mechanical instability of the β-phase. Indeed, the critical concentration for the $\beta \to \alpha$ transformation is equal to 22.5 at.% of Nb in accordance with experimental data [20]. Further, the calculation of C' for Ti–Nb$_{25}$ demonstrates the positive value of 2.48 GPa that is in good agreement with estimation using C_{11} and C_{12} constants obtained in the paper [9]. In this paper [9] the elastic constants of β-Ti–Nb$_{25}$ alloy were calculated using the PAW method with 16-atom supercell constructed by SQS technique. It is seen from Table 1 that EMTO–CPA method overestimates C_{44} constant in comparison with results in [9, 10]. In the paper [10], the elastic properties of Ti–Nb alloys were also obtained within the supercell approach, and the electronic structure of the alloys was calculated using the augmented plane wave plus local orbital (APW+lo) method implemented in the Wien2k software code [21]. In general, calculated C_{11} and C_{12} constants and elastic moduli are also in good agreement with results obtained in earlier papers [9, 10]. Our value of the Young's modulus is between the values calculated in [9, 10]. However, it is lower than experimental value of 73.9 GPa obtained for Ti–Nb$_{25}$ alloy in [22] but closer to experimental value of 64 GPa [23] for the Ti–Nb$_{26}$ alloy.

TABLE 1. Lattice parameter (in Å), elastic constants and moduli (in GPa) and Poisson's ratio of Ti–Nb$_{22}$ based alloys

Alloy	a	C_{11}	C_{12}	C_{44}	C'	B	E	G	ν
Ti–Nb$_{20}$	3.338	125.0	128.1	59.3	−1.58	127.1	44.4	15.4	0.442
Ti–Nb$_{25}$	3.342	133.2	128.3	58.2	2.48	129.9	59.4	20.9	0.424
Ti–Nb$_{25}$ [9]	—	140±11	116±13	34±10	—	124±13	63±13	22±13	—
Ti–Nb$_{25}$ [10]	—	137.6	121.9	32.2	7.84	127.2	52.7	18.4	—
Ti–Nb$_{22}$–Zr$_6$	3.363	124.4	125.2	58.4	−0.40	125.0	48.7	17.0	0.435
Ti–Nb$_{22}$–Zr$_6$	3.304	157.7	150.4	65.7	3.6	152.9	70.1 70 [13]	24.6	0.424
Ti–Nb$_{22}$–Zr$_6$–Hf$_5$	3.329	147.9	146.6	65.4	0.6	147.1	58.7	20.5	0.433
Ti–Nb$_{22}$–Zr$_6$–Mg$_{2.5}$	3.307	152.8	147.4	66.6	2.7	149.2	67.5	23.7	0.425
Ti–Nb$_{22}$–Zr$_6$–Mg$_5$	3.311	150.1	146.0	67.2	2.0	147.4	65.4	22.9	0.426
Ti–Nb$_{22}$–Zr$_6$–Hf$_{2.5}$–Mg$_{2.5}$	3.320	138.9	136.2	66.3	1.3	137.1	62.0	21.7	0.425
Ti–Nb$_{22}$–Zr$_6$–Hf$_5$–Mg$_{2.5}$	3.333	144.5	144.3	65.9	0.1	144.4	57.0	19.9	0.434
Ti–Nb$_{22}$–Zr$_3$–Hf$_5$–Mg$_5$	3.325	142.8	143.0	66.7	-0.1	143.0	57.0	19.9	0.434

The theoretical lattice parameter obtained within PBE approximation for exchange-correlation functional is slightly higher than experimental value. In particular, the value of 3.304 Å given in the experimental paper [13] for the alloy Ti–Nb$_{22}$–Zr$_6$ is by 0.059 Å lower than that obtained by EMTO–CPA method (Table 1). The calculation of the ternary alloy with experimental lattice parameter leads to increase of both elastic constants and moduli. In particular, the theoretical value of 70.1 GPa the alloy Ti–Nb$_{22}$–Zr$_6$ is in good agreement with experimental one of 70 GPa [13].

Let us turn attention to experiments [13]. Two states of material were considered in this paper: 30 min heating at 600 °C to form the polygonized dislocation substructure (P state) with a subgrain size of $\sim$100 – 300 nm and 30 min heating at 750 °C to form the recrystallized structure (R state) with a grain size of $\sim$10 μm. To measure the Young's and shear moduli torsional pendulum experiment and mechanical test were performed. More details can be found in [13]. The value of $E = 110 \pm 10$ GPa obtained in the latter case is significant higher than that found by the torsional pendulum experiment. It should be noted that the obtained value mentioned above is a static "engineering" apparent elastic modulus which depends on the crystallographic texture and loading scheme and thus cannot be directly compared to its dynamical "physical" equivalent determined using a torsional pendulum or numerical simulations. The Poisson's ratio was also measured in [13] and the values of $\nu = 0.41 \pm 0.03$ (P state) and $\nu = 0.32 \pm 0.04$ (R state) were obtained. Our value (Table 1) is closer to one obtained in P state rather than in the R state.

The results of the atomistic simulations using molecular dynamic were also presented in the mentioned above paper [13]. Since the presence of lattice defects do not consider in the theoretical calculations, the comparison was made in the R state of the Ti–Nb$_{22}$–Zr$_6$ alloy. The atomistic simulation of Young's modulus allows one to obtain the value of 75±3 GPa within Voigt approach that is in good comparison with torsional pendulum experiment. However, it is higher by $\sim$55 GPa than that obtained within Reuss approach that leads to average value of $\sim$48 GPa at the low temperatures $\sim$50 °C. Besides, the values of elastic constants are significantly lower than those obtained in the present study. Thus, we can conclude that the present EMTO–CPA study with use of the Hill approach [14] allows obtaining Young's modulus for ternary Ti–Nb$_{22}$–Zr$_6$ alloy in good comparison with experiment. Therefore, we can consider the influence of some alloying elements on further lowering of E that is necessary for medical application of the Ti–Nb$_{22}$–Zr$_6$ based alloys.

In our previous paper [24], the influence of alloying elements on the Young's modulus was studied in the Ti–Mo$_5$–Me$_x$ ternary alloys. We considered Zr, Hf, In, Sn, Mg, Mn, Ta as alloying elements with concentration changed from 1 to 5 at.%. Only Zr, Hf and Mg were shown as elements which can lower the elastic moduli. This lowering was interpreted as a combined effect of size and electron factors. Therefore, in present paper we consider only Hf, Mg and their combinations. It is seen from Table 1 that all alloying elements lead to increase in the lattice parameter. As a result, alloying by 5 at.% of Mg or Hf causes a decrease in E with the most pronounced effect of Hf. In the case of alloying by Hf, we observe the lowering of C' up to 0.6 GPa. It is interesting that for the Ti–Nb$_{22}$–Zr$_6$–Hf$_5$ alloy size effect is most pronounced and both C' and C_{44} constants are lower in comparison with the ternary alloy. In the case of Mg, elastic constant C' decreases but, on the contrary, C_{44} is increased. This trend is valid for the alloy with both Hf and Mg alloying elements if their concentrations are 2.5 at.%. The growth of Hf concentration up to 5 at.% alongside with Mg alloying affects considerably C' constant, which lowers to 0.1 GPa. It should be noted that decrease in the concentration of Zr (Table 1) leads to instability of β-phase.

In the paper [25], it was demonstrated that some features of densities of states (DOS) can be connected with changes in C' and C_{44}. In particular, the first DOS peak near the Fermi level (E_F) reflects the changes in C', whereas the second peak shifted towards negative energy is connected with changes in C_{44}. Authors of [25] insist that hybridization of Nb with alloying elements and, as a consequence, increase of states in the second peak leads to stability of β-phase of the alloy. In turn, a decrease in the constant C' was associated by the authors [25] with a decrease in the states of *s*,*p*-metals at energies from -1.5 to 0.5 eV. Thus, the inverse relationship between the constants C_{44} and C' was explained by the opposite change in the peak heights upon alloying with *s*,*p*-elements. However, in the work [25], the change in the states under the DOS curves was estimated from the shape of the curves, and the division of the curves into two peaks was rather arbitrary. From Table 1 one can see that in the alloy with Mg the constant C' decreases, whereas C_{44} increases, but both constants are decreased in case of Hf as was mentioned above. Furthermore, a decrease in the number of states at the Fermi level indicates stabilization of the alloy and, consequently, an increase in C'.

Figure 1 shows the local DOS's of the Ti–Nb$_{22}$–Zr$_6$ alloys with alloying metals Hf and Mg. It is seen that the changes of the local DOS's at the Fermi level, $N(E_F)$, are insignificant in case of these elements. However, the addition of Hf in the alloy increases $N(E_F)$ more pronounced that *s*,*p*-element (lowest panel in Fig. 1). At the same time, the addition of fourth component means the decrease of Ti concentration. Since Ti contributes to a number of states at the Fermi level more than Hf or Mg, the alloying results in decrease of $N(E_F)$ shown in Fig. 2. This figure demonstrates difference of total DOS of doped and undoped ternary alloys. It is seen that decrease in $N(E_F)$ is significantly lower in the case of Hf. In general, states are decreased in the regions from -1.0 up to 0.5 eV and from -3.2 up to -1.7 eV, and they are increased in the region from -1.7 up to -1.0 and below -3.0 eV.

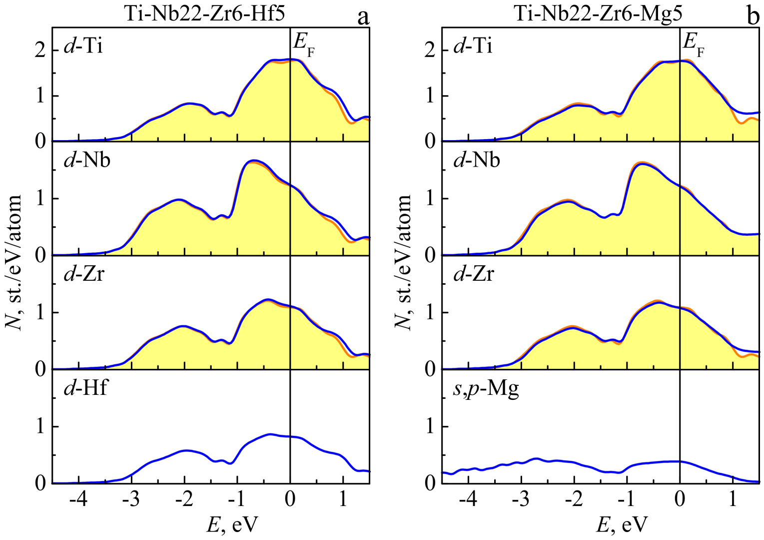

FIG. 1. Density of states of the Ti–Nb$_{22}$–Zr$_6$–Me$_5$ alloy components (blue line) in comparison with that of the Ti–Nb$_{22}$–Zr$_6$ alloy (orange line and yellow color fill): Me is Hf (a) and Mg (b)

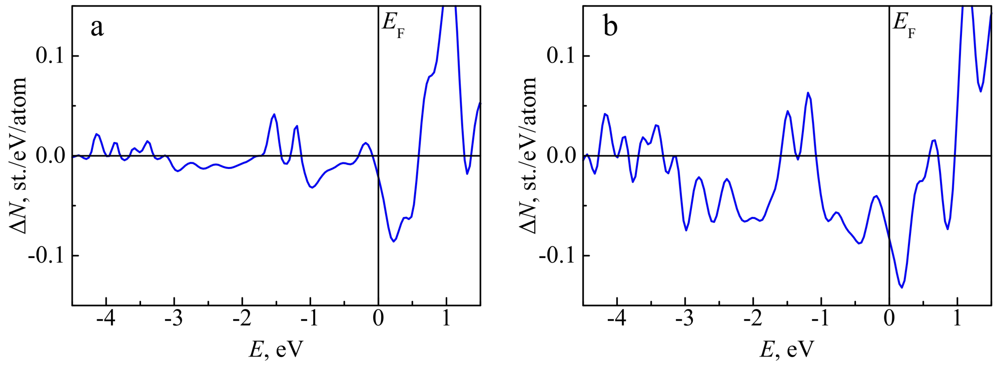

FIG. 2. Difference in the total DOS of the Ti–Nb$_{22}$–Zr$_6$–Me$_5$ alloy and Ti–Nb$_{22}$–Zr$_6$ one: Me is Hf (a) and Mg (b)

It should further be pointed out that in the case of Hf, the e/a concentration remains unchanged, whereas it decreases for the Mg doped alloy. It is seen from Table 1 that Hf, which is isoelectronic to Ti, causes a large decrease in E due to primarily its size effect. In the case of Mg doped alloys, the size effect is less pronounced in comparison with Hf but alongside with a decrease in the valence electron concentration, it contributes to a decrease in E as well.

The obtained results can be interpreted on the base of cluster-plus-glue-atom model, which was suggested in [26] for alloys with XY_3Ti_{11} composition, i.e. as approximately in our case. The basis of the structure is the cell (2×2×2) with the bcc Ti lattice. In the center of this cell, the Ti atom is replaced by an X element, and Y atoms are located in the middles of the cube edges with vacancies at the vertices. In our case, Y atoms are Nb ones, whereas X atom is Mg or Hf. A stronger bonding between X–Y atoms leads to a higher value of C_{44} in accordance with [25] and, as consequence, to stabilization of β-phase and to increase in E. However, the distance between X–Y atoms is great (Y is atom in the third coordination sphere in respect to X atom). So, their interaction can be indirect due to hybridization with Ti and Zr atoms. We have shown in [27, 28] that a weaker Y–Ti chemical bond leads to a lower value of E in the case of *s,p*-elements on X site, whereas in the case of *d*-elements on X site, a weak bonding X–Ti correlates also with a low value of E. Since Hf has larger atomic radius than Ti, its interatomic Hf–Ti bonds are weakening. In general, our simulations show that the smallest Young's modulus equaled to 57 GPa can be achieved for the Ti–Nb_{22}–Zr_6–Hf_5–$Mg_{2.5}$ alloy.

It should be noted that alloying of Ti–Nb_{22} alloy by 6 at.% Zr results in a decrease in hardness, fracture toughness but an increase in brittleness index (Table 2). Further addition of Hf and Mg in any combination enhances the changes in these mechanical characteristics. At the same time, the effect of Hf is more pronounced. The decrease in H_V is explained by the decrease in Young's modulus due to an increase in the metallic contribution in chemical bonding, while K_{IC} decreases due to a decrease in both factors in eq. (5). Since decrease in K_{IC} is larger than that in H_V, M_{dt} is increased. The highest value of M_{dt} obtained for the Ti–Nb_{22}–Zr_6–Hf_5–$Mg_{2.5}$ alloy, remains very low (0.279 $\mu\text{m}^{-1/2}$) that indicates high ductility of the alloys.

TABLE 2. Vickers hardness (H_V), fracture toughness (K_{IC}) and brittleness index (M_{dt}) for the Ti–Nb_{22} based alloys

Alloy	H_V, GPa	K_{IC}, MPa·$m^{1/2}$	M_{dt}, $\mu m^{-1/2}$
Ti–Nb_{22}	4.50	21.56	0.209
Ti–Nb_{22}–Zr_6	4.45	18.05	0.246
Ti–Nb_{22}–Zr_6–Hf_5	3.73	14.71	0.253
Ti–Nb_{22}–Zr_6–$Mg_{2.5}$	4.28	16.92	0.253
Ti–Nb_{22}–Zr_6–Mg_5	4.15	16.19	0.256
Ti–Nb_{22}–Zr_6–$Hf_{2.5}$–$Mg_{2.5}$	3.93	14.71	0.267
Ti–Nb_{22}–Zr_6–Hf_5–$Mg_{2.5}$	3.62	12.96	0.279
Ti–Nb_{22}–Zr_3–Hf_5–Mg_5	3.62	14.96	0.242

4. Conclusion

The elastic and mechanical properties of disordered titanium alloys Ti–Nb_{22}–Zr_6–Me alloyed with Hf, Mg and their combination were studied using the EMTO–CPA method. We demonstrate that the addition of Hf, which is isoelectronic to Ti, reduces Young's modulus by increasing the lattice parameter and weakening the chemical bonds. In the case of Mg, both structural and electronic factors also contribute to a reduction in Young's modulus. The smallest value of Young's modulus equaled to 57 GPa was calculated for the Ti–Nb_{22}–Zr_6–Hf_5–$Mg_{2.5}$ alloy. The decrease of Zr concentration and increase of Mg one leads to instability of β-phase of the alloy. The mechanical properties of the alloys, such as Vickers hardness, fracture toughness and brittleness index, were also calculated using the elastic moduli. It was shown that the hardness of the alloys decreases with the alloying by Hf and Mg, and effect of the former is more pronounced. Although the brittleness index increases for all alloying elements, its highest value, obtained for Ti–Nb_{22}–Zr_6–Hf_5–$Mg_{2.5}$, is only 0.28 $\mu\text{m}^{-1/2}$ indicating high ductility of the alloys.

References

[1] Niinomi M. Mechanical properties of biomedical titanium alloys. *Mater. Sci. Eng. A*, 1998, **243**, P. 231-236.

[2] Long M., Rack H.J. Titanium alloys in total joint replacement – a materials science perspective. *Biomater.*, 1998, **19**, P. 1621–1639.

[3] Geetha M., Singh A.K., Asokamani R., Gogia A.K. Ti based biomaterials, the ultimate choice for orthopaedic implants – A review. *Prog. Mater. Sci.*, 2009, **54**, P. 397–425.

[4] Niinomi M. Mechanical biocompatibilities of titanium alloys for biomedical applications. *J. Mech. Behav. Biomed. Mater.*, 2008, **1**, P. 30–42.

[5] Yu Z. *Titanium alloys for biomedical development and applications. Design, microstructure, properties, and application*. Elsevier, Amsterdam, 2022, 245 p.

[6] Biesiekierski A., Wang J., Gepreel M.A.H., Wen C. A new look at biomedical Ti-based shape memory alloys, *Acta Biomater.*, 2012, **8**, P. 1661–1669.

[7] Illarionov A.G., Nezhdanov A.G., Stepanov S.I., Muller-Kamskii G., Popov A.A. Structure, phase composition, and mechanical properties of biocompatible titanium alloys of different types. *Phys. Met. Metall.*, 2020, **121**, P. 367–373.

[8] Li Y., Yang C., Zhao H., Qu S., Li X., Li Y. New developments of Ti-based alloys for biomedical applications. *Materials*, 2014, **7**, P. 1709–1800.

[9] Marker C., Shang S.L., Zhao J.C., Liu Z.K. Effects of alloying elements on the elastic properties of bcc Ti-X alloys from first-principles calculations. *Comput. Mater. Sci.*, 2018, **142**, P. 215–226.

[10] Yao Q., Sun J., Xing H., Guo W. Influence of Nb and Mo contents on phase stability and elastic property of β-type Ti-X alloys. *Trans. Nonferrous Met. Soc. China.*, 2007, **17**, P. 1417–1421.

[11] Zunger A., Wei S.H., Ferreira L.G., Bernard J.E. Special quasirandom structures. *Phys. Rev. Lett.*, 1990, **65**, P. 353–356.

[12] Vitos L. *Computational quantum mechanics for materials engineers. The EMTO method and applications*. Springer, London, 2007, 238 p.

[13] Dubinskiy S., Baranova A., Markova G., Prokoshkin S., Zelenina A., Kolotova L., Starikov S., Korotitskiy A., Bazlov A., Brailovski V. Atypical intrinsic elinvar behavior of beta Ti-22Nb-6Zr alloy in high and wide temperature range: atomic mechanism and control of the effect. *Trans. Nonferrous Met. Soc. China*, 2026, in press.

[14] Hill R. The elastic behaviour of a crystalline aggregate. *Proc. Phys. Soc., Sect. A*, 1952, **65**, P. 349–354.

[15] Jiang X., Zhao J., Wu A., Bai Y., Jiang X. Mechanical and electronic properties of B_{12}-based ternary crystals of orthorhombic phase. *J. Phys.: Condens. Matter.*, 2010, **22**, 315503.

[16] Lee C.M., Ju C.P., Chern Linn J.H. Structure-property relationship of cast Ti–Nb alloys. *J. Oral Rehabil.*, 2002, **29**, P. 314–322.

[17] Fikeni L. *Microstructural evolution and its influence on mechanical properties of Ti–Nb binary alloys*. University of Pretoria, Pretoria, 2021, 95 p.

[18] Niu H., Niu S., Oganov A.R. Simple and accurate model of fracture toughness of solids. *J. Appl. Phys.*, 2019, **125**, 065105.

[19] Boccaccini A.R. Machinability and brittleness of glass-ceramics. *J. Mater. Process. Technol.*, 1997, **65**, P. 302–304.

[20] Lütjering G., Williams J.C. *Titanium*, second ed. Springer, Berlin, 2007, 442 p.

[21] Schwarz K., Blaha P., Madsen G.K.H. Electronic structure calculations of solids using the WIEN2k package for material sciences, *Comput. Phys. Commun.*, 2002, **147** (1–2), P. 71–76.

[22] Raabe D., Sander B., Friák M., Ma D., Neugebauer J. Theory-guided bottom-up design of β-titanium alloys as biomaterials based on first principles calculations: Theory and experiments. *Acta Materialia*, 2007, **55**, P. 4475–4487.

[23] Boyer R.R., Welsch G., Collings E.W. *Materials properties handbook: titanium alloys*. ASM Int., Mater. Park, 1994, 1176 p.

[24] Kasparyan S.O., Bakulin A.V., Kulkova S.E. The influence of alloying elements on the elastic properties of β-Ti. *J. Exp. Theor. Phys.*, 2026, **169**, P. 71–81. (in Russian)

[25] Kwasniak P., Wróbel J.S., Garbacz H. Origin of low Young modulus of multicomponent, biomedical Ti alloys – Seeking optimal elastic properties through a first principles investigation. *J. Mech. Behav. Biomed. Mater.*, 2018, **88**, P. 352–361.

[26] Hao C.P., Wang Q., Ma R.T., Wang Y.M., Qiang J.B., Dong C. Cluster-plus-glue-atom model in bcc solid solution alloys. *Acta Phys. Sin.*, 2011, **60** (11), 116101.

[27] Kasparyan S.O., Ordabaev A.E., Bakulin A.V., Kulkova S.E. Elastic and thermal properties of some ternary β-Ti based alloys. *Nanosystems Phys. Chem. Math.*, 2025, **16** (2), P. 225–234.

[28] Kasparyan S.O. *Electronic structure and elastic moduli of binary and ternary β-titanium alloys. Cand. Sci. (Phys.-Math.) Dissertation*. Nat. Res. Tomsk State Univ., Tomsk, 2025, 154 p. (in Russian).

Submitted 12 February 2026; revised 5 March 2026; accepted 10 March 2026

Information about the authors:

Alexander V. Bakulin – Institute of Strength Physics and Materials Science, Siberian Branch of Russian Academy of Sciences, Tomsk, 634055, Russia; ORCID 0000-0001-5099-3942; bakulin@ispms.ru

Svetlana E. Kulkova – Institute of Strength Physics and Materials Science, Siberian Branch of Russian Academy of Sciences, Tomsk, 634055, Russia; ORCID 0000-0002-7155-3492; kulkova@ispms.ru

Conflict of interest: the authors declare no conflict of interest.

NANOSYSTEMS:
PHYSICS, CHEMISTRY, MATHEMATICS

Almjasheva O.V., et al. *Nanosystems: Phys. Chem. Math.*, 2026, **17** (2), 210–217.
http://nanojournal.ifmo.ru
DOI 10.17586/2220-8054-2026-17-2-210-217

Original article

The role of dehydration-hydration in the formation of nanoparticles with a chrysotile structure during hydrothermal treatment of $Mg_{1-x}Ni_x(OH)_2$–SiO_2–H_2O(NaOH) systems

Oksana V. Almjasheva[1,2], Maria E. Kurguzkina[1], Victor V. Gusarov[1]

[1]NRC “Kurchatov Institute” – PNPI – IChS, Russia

[2]Saint-Petersburg Electrotechnical University, Russia

Corresponding author: Almjasheva O.V., almjasheva@mail.ru

ABSTRACT A thermodynamic analysis of hydroxide transformations in the $Mg_{1-x}Ni_x(OH)_2 - SiO_2 - H_2O$ system during the hydrothermal synthesis of nanotubular particles with a chrysotile structure has revealed the decisive role of the dehydration of initial reagents and the subsequent re-formation of hydroxides during hydrothermal treatment of reagents on the composition and morphological parameters of the target product. Depending on the composition of the hydroxide reagent and the *T–P* conditions in the reaction zone, three regions have been identified where the formation mechanism of nanotubular particles with a chrysotile structure changes dramatically. This is the direct cause of the non-monotonic dependence of the Mg/Ni ratio and the dimensional parameters of the $(Mg_{1-x}Ni_x)_3Si_2O_5(OH)_4$ nanotubes on the Mg/Ni ratio in the initial hydroxide.

KEYWORDS solid solutions, hydroxides, oxides, chrysotile, nanotubes, hydrothermal synthesis, thermodynamic calculations

ACKNOWLEDGEMENTS The work was supported by the Russian Science Foundation (RSF) project No. 24-13-00445.

FOR CITATION Almjasheva O.V., Kurguzkina M.E., Gusarov V.V. The role of dehydration-hydration in the formation of nanoparticles with a chrysotile structure during hydrothermal treatment of $Mg_{1-x}Ni_x(OH)_2$–SiO_2–H_2O(NaOH) systems. *Nanosystems: Phys. Chem. Math.*, 2026, **17** (2), 210–217.

1. Introduction

The hydrothermal formation of hydrosilicate nanotubes with a chrysotile structure, characterized by the general formula $Me_3Si_2O_5(OH)_4$, where Me is typically Mg, which can be partially or completely substituted by atoms such as Fe, Co, Ni, etc., has revealed a number of significant differences compared to the formation of oxide and hydroxide nanoparticles of other compositions and morphologies. For instance, while the hydrothermal synthesis of many simple and complex oxides and hydroxides can yield nanoparticles with a relatively narrow size distribution [1–7], the scientific literature reports no cases of forming hydrosilicate nanotubes with a narrow distribution in outer diameter, and especially in length, during the early stages of phase formation. This is despite wide variations in the *T–P* conditions of synthesis [8–18], the use of different precursors [8–11, 16–20], and hydrothermal media of various compositions [11, 20–23]. Only after prolonged hydrothermal treatment do the outer diameters, inner diameters, and lengths of the nanotubes become uniform [22, 24–28]. Numerous additional questions arise when attempting to synthesize nanotubes of variable composition, i.e., with partial substitution of cations in the octahedral and tetrahedral sublattices, as well as when substituting OH^- anions with F^- [20, 29–42]. Even more questions are prompted by the experimentally observed effect of non-uniform radial distribution of cations within the octahedral sublattice during the synthesis of variable-composition nanotubes with the chrysotile structure [41–43]. Potentially, this effect could be explained by the energetic preference of cations of different sizes for specific localization sites, depending on the radius of curvature of the cation sublattice within the nanotube (Fig. 1) [41, 43]. However, the influence of a kinetic factor on this cation distribution cannot be ruled out either, as observed, for example, in the synthesis of variable-composition orthophosphates with the rhabdophane structure [44]. It is also possible that both of these factors contribute to this effect. A separate question concerns the reasons for the diversity in the forms of nanotubular particles with the chrysotile structure, which is particularly pronounced in the initial stages of synthesis [9, 25, 35, 38, 45, 46]. Moreover, as shown in [38], the extent of this morphological heterogeneity of nanotubes may also depend on the degree of ion substitution in $(Mg_{1-x}Ni_x)_3Si_2O_5(OH)_4$.

The analysis conducted in [11] shows that the formation mechanism can significantly influence the morphology of nanotubes with a chrysotile structure. In this regard, study [47] analyzed the impact of using pre-synthesized hydroxides of variable composition, $(Mg_{1-x}Ni_x)(OH)_2$ [48], as reagents on the formation of $(Mg_{1-x}Ni_x)_3Si_2O_5(OH)_4$ nanotubes. However, several questions regarding the specific features of the formation of magnesium-nickel hydrosilicate nanotubes with the chrysotile structure in this system remain unclear. This pertains, in particular, to the significant discrepancy between the expected and actually observed differences in the morphological parameters of $(Mg_{1-x}Ni_x)_3Si_2O_5(OH)_4$ nanotubes depending on their composition [47]. Interest in the issues surrounding the formation of nanotubes with the

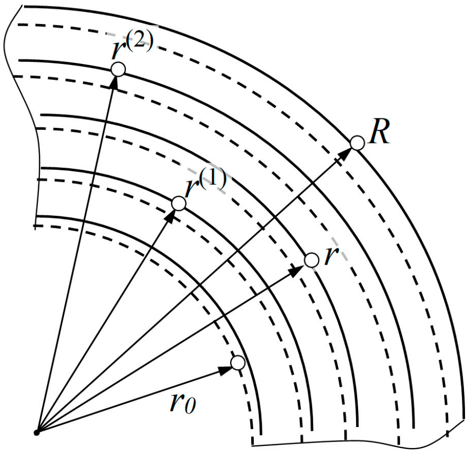

FIG. 1. Schematic diagram of a frontal section of a nanotube with a chrysotile structure. The solid circular lines represent the magnesium-nickel hydroxide layers; the dashed circular lines represent the layers based on silicon dioxide. $R = 0.5D$ and $r_0 = 0.5d$ correspond to the outer radius and diameter, and the inner radius and diameter of the nanotube, respectively; r denotes the radius of curvature of the magnesium-nickel hydroxide layer of chrysotile, with $r^1 < r^2$ representing the radii for which $x_{Ni}(r^1) < x_{Ni}(r^2)$, where $x_{Ni}(r^{\cdots})$ is the fraction of nickel ions in the corresponding layers of the compound $(Mg_{1-x}Ni_x)_3Si_2O_5(OH)_4$ [41]

chrysotile structure is sustained not only by the prospects for their application in various fields [10,49–58] but also by the significantly lower toxicity of synthetic chrysotile compared to its natural counterpart [58].

For these reasons, there is a need to continue both computational studies and a more detailed analysis of experimental results in the field of understanding the specific features of the formation process of nanotubes with the chrysotile structure under hydrothermal conditions, particularly when using a solid solution of composition $Mg_{1-x}Ni_x(OH)_2$ as one of the reagents. This work is dedicated to this very issue.

2. Calculations

Calculations of phase relations in the (*T–P*) coordinates within the $Mg_{1-x}Ni_xO$–H_2O system were performed by analyzing the dependence of the Gibbs energy change for the dehydration reaction of $(Mg_{1-x}Ni_x)(OH)_2$ under hydrothermal conditions, leading to the formation of a $Mg_{1-x}Ni_xO$ solid solution. The calculation was carried out neglecting the contributions of the Gibbs energy of mixing of the hydroxides and oxides of variable composition to the Gibbs energy of the dehydration process. Throughout the entire investigated range of temperature and pressure changes in the system, the hydroxide and oxide phases of variable composition remain homogeneous under equilibrium conditions, i.e., they do not decompose into two hydroxide or two oxide phases. This conclusion is based on available experimental data [48] and the fact that the molar enthalpy of mixing during the formation of the $Mg_{1-x}Ni_xO$ solid solution, according to [59, 60], is either negative or $\Delta H_m^M \approx 0$. The calculations were performed using the IVTANTHERMO database and software package [61].

3. Synthesis and analysis

The starting materials used in the synthesis of nanotubes with a chrysotile structure in the $(Mg_{1-x}Ni_x)O$–SiO_2–H_2O system were hydroxides of variable composition $(Mg_{1-x}Ni_x)(OH)_2$, with a nominal composition varying within the range ($x = 0.1$, ..., 0.9), and SiO_2 in the form of silica gel (GOST 3956-76, $n = 0.73$). The hydrothermal fluid contained a solution of 5 wt.% NaOH in distilled water. The hydroxides $(Mg_{1-x}Ni_x)(OH)_2$ with nominal values varying in the interval ($x = 0.1$, ..., 0.9) were obtained by the reverse deposition method, as described in [48].

Hydrothermal treatment of the reagent mixture, calculated for the stoichiometry of $(Mg_{1-x}Ni_x)_3Si_2O_5(OH)_4$ formation, was carried out in steel autoclaves. The temperature of the hydrothermal treatment was monitored based on the furnace temperature data. Due to the thermal inertia (heating/cooling) of the thick-walled steel autoclave, the temperature of the reaction zone differs significantly from the furnace temperature. To estimate the temperature in the reaction medium during autoclave heating, a calibration curve (Fig. 2) was used, obtained by comparing the temperature in the furnace and inside the autoclave. Using identical heating conditions and the same type of autoclaves in the experiment allows for predicting the temperature in the reaction space based on the furnace temperature data for all experiments. The pressure in the reaction medium was determined using Kennedy nomograms [62] based on data on the autoclave fill factor and the temperature of the hydrothermal fluid.

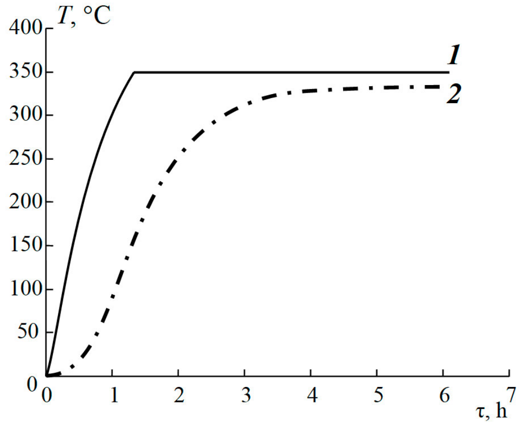

FIG. 2. Relationship between the temperature values in the furnace (1) and in the autoclave (2), according to the calibration experiment data

The hydrothermal treatment of the reagents, the post-hydrothermal operations with the resulting solid-phase products, and the analysis of the obtained samples were carried out in accordance with the methods described in [10, 47]. The dimensional parameters of the nanotubes were determined using data from transmission electron microscopy (JEM 2100-F microscope, $U = 200$ kV ($\lambda = 0.025$ Å)) and scanning electron microscopy (Hitachi S-570). To obtain statistically reliable information, random samples containing about 100 nanotubes were used in all cases, from which the average values of the outer diameter (D) and length (L) of the nanotubes were determined. The Mg/Ni ratios in the initial magnesium-nickel hydroxides and in the nanotubes were determined by EDX analysis using an attachment (Bruker Quantax 20) to a scanning electron microscope. The error in determining the Mg and Ni ratio was approximately 0.02 mole fraction.

4. Results and discussion

The results of thermodynamic calculations show that the initial mixed hydroxides $(Mg_{1-x}Ni_x)(OH)_2$, under hydrothermal treatment conditions, can dehydrate depending on their composition and temperature to form $Mg_{1-x}Ni_xO$ oxides (Fig. 3 – boundary of regions I and (II, III)). The Mg/Ni ratio in the oxide solid solution, as can be concluded from [48], will not change. This is primarily determined by the stability of $Mg_{1-x}Ni_xO$ solid solutions across the entire range of compositions down to very low temperatures, due to the fact that the molar enthalpy of mixing has negative values or is close to zero [59, 60]. Furthermore, the dehydration process can occur very quickly, as water escapes from the hydroxide nanoparticles with a layered structure through the interlayer spaces without any significant diffusion hindrance. This also contributes to preserving the Mg/Ni ratio in the oxide solid solution after dehydration of the $(Mg_{1-x}Ni_x)(OH)_2$ hydroxide.

A different situation arises during the hydration of $Mg_{1-x}Ni_xO$ under hydrothermal conditions. Despite the assumptions made based on thermodynamic calculations that, upon hydration of $Mg_{1-x}Ni_xO$ at the boundary of regions III and IV (Fig. 3), the Mg/Ni ratios in the hydroxide and oxide solid solutions should remain unchanged, the hydration reaction of $Mg_{1-x}Ni_xO$, a compound with a framework structure (periclase), will proceed significantly more slowly. In this case, on the surface of the $Mg_{1-x}Ni_xO$ crystals, for kinetic reasons, hydroxide particles enriched in magnesium ions will form first, since the driving force for the formation of such particles is significantly higher than the driving force for the formation of hydroxides enriched in nickel ions (Fig. 3). Consequently, at a certain stage of the hydration process of the $Mg_{1-x}Ni_xO$ solid solution, it can be expected that the formation reaction of “secondary” hydroxides will proceed as follows:

$$Mg_{1-x}Ni_xO + H_2O = (x_2 - x)/(x_2 - x_1)Mg_{1-x1}Ni_{x1}(OH)_2 + (x - x_1)/(x_2 - x_1)Mg_{1-x2}Ni_{x2}(OH)_2, \quad (1)$$

where $x_2 > x > x_1$. Moreover, the values of x_1 and x_2 can vary depending on the temperature and duration of the reaction (Fig. 3 and Fig. 4). In the limiting case, x_2 can equal unity. In this situation, the hydration of oxides enriched in NiO will occur very slowly or not at all (region II, Fig. 3). Furthermore, the interaction of NiO with silicon dioxide under hydrothermal conditions to form nickel hydrosilicate is known [11, 48] to be so difficult that $NiSiO_3$ is typically used as a reagent instead of NiO to obtain nanotubular $Ni_3Si_2O_5(OH)_4$.

Given that, according to the calculations performed, throughout the entire range of *T–P* conditions of hydrothermal treatment, hydroxides $Mg_{1-x}Ni_x(OH)_2$ are stable for $x <\sim (0.55 \pm 0.05)$, taking into account the kinetic factor, one likely scenario is the hydration of the $Mg_{1-x}Ni_xO$ solid solution at the boundary of regions III and IV (Fig. 3), leading to the formation of “secondary” hydroxides via the reaction:

$$Mg_{1-x}Ni_xO + 2(1-x)H_2O = 2(1-x)Mg_{\sim 0.45}Ni_{\sim 0.55}(OH)_2 + (2x - \sim 1.1)NiO. \quad (2)$$

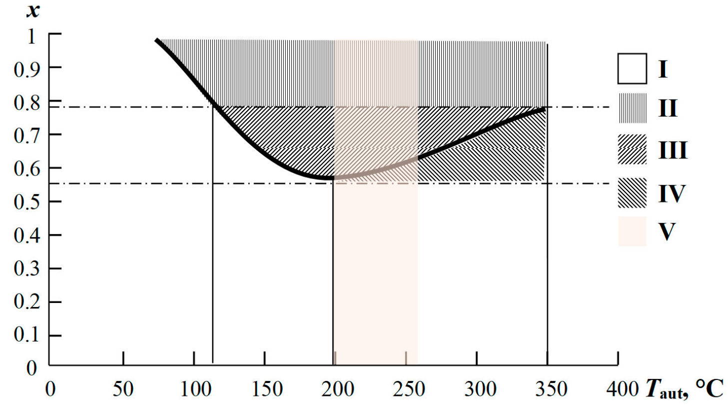

FIG. 3. Equilibrium phase state of reagent particles in the $Mg_{1-x}Ni_xO$-H_2O system according to thermodynamic calculation data, depending on the Mg/Ni ratio, temperature, and pressure in the autoclave (the pressure in the autoclave corresponding to each temperature was calculated using Kennedy nomograms [62]): I – region of existence of $(Mg_{1-x}Ni_x)(OH)_2$; II – region of formation of $Mg_{1-x}Ni_xO$ without further transformation into hydroxide; III – region of formation of $Mg_{1-x}Ni_xO$ with subsequent transformation into $(Mg_{1-x}Ni_x)(OH)_2$ upon changes in *T–P* conditions in the hydrothermal fluid; IV – region of formation of "secondary" hydroxide; V – temperature region in which the formation of chrysotile is activated [14]

As follows from (1) and (2) and is illustrated in Fig. 4, in the region of "secondary" hydration – II', for kinetic reasons, the hydroxides present will contain a smaller amount of Ni^{2+} than the original oxide. These hydroxides will be the first to interact with silicon dioxide to form nanotubes with a chrysotile structure. This conclusion is supported by the data illustrated in Fig. 3, which shows that the hydration region IV overlaps with the *T–P* region where chrysotile formation is activated.

In addition to the hydroxides in region II' (Fig. 4), one can expect to find nickel-enriched magnesium-nickel oxide solid solutions, and in the limiting case, NiO, in accordance with equation (2). During hydrothermal treatment, the components enriched in nickel oxide may either form outer layers on the surface of already formed nanotubes, initiate the formation of nanotubes significantly enriched in nickel oxide compared to the initial Mg/Ni ratio, or remain as a dispersed phase in the hydrothermal fluid due to their lower reactivity towards chrysotile formation [13]. In the latter case, they would be removed during decantation and washing of the target product precipitate.

It should be noted that the conclusions drawn from the analysis described above, within the error limits of the experiment and calculations, correlate well with the experimentally obtained data on the relationship between the composition of the initial hydroxide nanoparticles $Mg_{1-x}Ni_x(OH)_2$ and the composition of the resulting nanotubes with a chrysotile structure $(Mg_{1-y}Ni_y)_3Si_2O_5(OH)_4$ obtained using them as reagents (Fig. 5). The relationships $y(x)$ are qualitatively

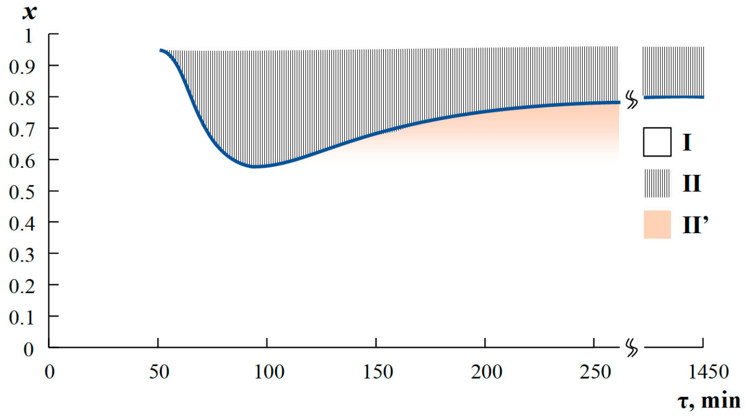

FIG. 4. Residence time of reagents in the form of hydroxide and oxide solid solutions during the hydrothermal synthesis of chrysotile for various compositions of initial hydroxides in the $Mg_{1-x}Ni_xO$–SiO_2–H_2O system. I – region of stable existence of $Mg_{1-x}Ni_x(OH)_2$; II – region of stable existence of $Mg_{1-x}Ni_xO$; II' – region of coexistence of "secondary" hydroxides and oxides in accordance with reactions (1) and (2)

divided into regions I, II, and III (Fig. 5). In terms of composition, region I (Fig. 5) corresponds to region I (Fig. 3 and Fig. 4), region II (Fig. 5) corresponds to region III (Fig. 3) and region II' (Fig. 4), and region III (Fig. 5) corresponds to region II (Fig. 3 and Fig. 4).

The characteristic feature of the dependence $y(x)$ in region II (Fig. 5) is explained by the fact that it is derived from processes preceding the formation of $(\mathrm{Mg}_{1-y}\mathrm{Ni}_y)_3\mathrm{Si}_2\mathrm{O}_5(\mathrm{OH})_4$ in this region: the decomposition of the hydroxide solid solution with the formation of $\mathrm{Mg}_{1-x}\mathrm{Ni}_x\mathrm{OH}$ (region II – Fig. 3 and Fig. 4) and subsequent hydration (region III – Fig. 3 and region II' – Fig. 4), with the composition of the resulting "secondary" hydroxides changing according to expressions (1) and (2).

Some systematic difference in the Mg/Ni ratio between the initial reagents and the reaction products in regions I and III (Fig. 5) may be associated both with the systematic error of EDX analysis in determining the elemental composition of objects of different nature and with energetic reasons [41,43]. When brucite-like nanoplates of $\mathrm{Mg}_{1-x}\mathrm{Ni}_x(\mathrm{OH})_2$ roll up during the formation of nanotubes with a chrysotile structure, for small values of the curvature radius – r (Fig. 1) of the brucite layer, the incorporation of Mg^{2+} ions into this layer is energetically preferable over Ni^{2+} ions [41,43].

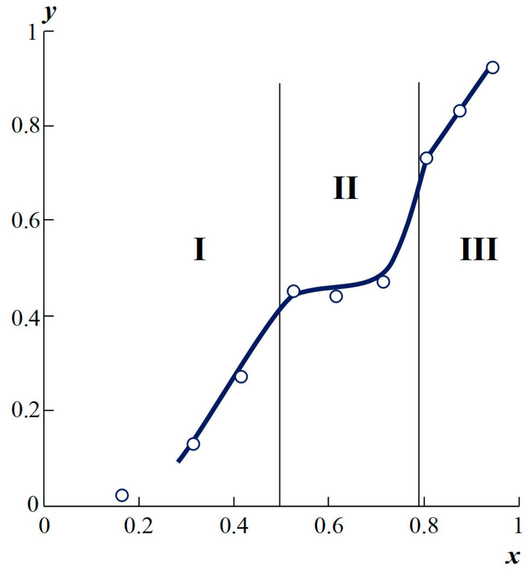

FIG. 5. Relationship between the composition of nanotubes $(\mathrm{Mg}_{1-y}\mathrm{Ni}_y)_3\mathrm{Si}_2\mathrm{O}_5(\mathrm{OH})_4$ and the initial hydroxides $\mathrm{Mg}_{1-x}\mathrm{Ni}_x(\mathrm{OH})_2$

Another confirmation of the concluded role of $\mathrm{Mg}_{1-x}\mathrm{Ni}_x(\mathrm{OH})_2$ dehydration and the formation of "secondary" hydroxides in the synthesis of magnesium-nickel nanotubes with a chrysotile structure is provided by the data on the dimensional parameters of the resulting nanotubes, presented in (Fig. 6). These data unequivocally show the presence of three types of characteristic dependencies of the average length (L) and outer diameter (D) of nanotubes on their composition – I, II, III (Fig. 6), the boundaries of which correlate with the boundaries of the hydroxide→oxide→hydroxide transformations for $\mathrm{Mg}_{1-x}\mathrm{Ni}_x(\mathrm{OH})_2$ solid solutions of different compositions under the conditions of their hydrothermal treatment during the experiment (Fig. 3, Fig. 4).

The sharp decrease in the size of nanotubes in region II (Fig. 6) compared to region I (Fig. 6) is explained by a sharp decrease in the formation rate of compounds with the chrysotile structure. The decrease in the formation rate of $(\mathrm{Mg}_{1-y}\mathrm{Ni}_y)_3\mathrm{Si}_2\mathrm{O}_5(\mathrm{OH})_4$ nanotubes for $y > (\sim 0.43)$ in region II (Fig. 6) may be related, firstly, to the fact that in region II' (Fig. 4) there is a significant proportion of oxides, which interact more slowly with SiO_2 under hydrothermal conditions than hydroxides [14]. Another reason for the sharp decrease in the nanotube growth rate in region II (Fig. 6) is the change in the Mg/Ni ratio during the formation of "secondary" hydroxides in accordance with equations (1) and (2) in region II' (Fig. 4) and, as a consequence, a decrease in the amount of nickel-enriched hydroxide reagents necessary for nanotube growth in region II (Fig. 6). The slow growth of nanotubes in region III (Fig. 6) is associated with the fact that they are formed not from hydroxides possessing a brucite structure, similar to the structure of the magnesium-nickel layer in chrysotile, but from $\mathrm{Mg}_{1-x}\mathrm{Ni}_x\mathrm{O}$ oxides – region II (Fig. 3 and Fig. 4). In this case, in the absence of a reagent with a layered structure, the formation of chrysotile proceeds significantly more slowly [11–18]. It should be noted that the results obtained in this work suggest that the change in the composition of $(\mathrm{Mg}_{1-y}\mathrm{Ni}_y)_3\mathrm{Si}_2\mathrm{O}_5(\mathrm{OH})_4$ nanotubes along their radius (Fig. 1), with enrichment of their peripheral regions with the nickel-containing component, may be associated not only with the energetic favorability of this state, as was shown in [41], but also with kinetic factors, at least for region II (Fig. 5) of $(\mathrm{Mg}_{1-y}\mathrm{Ni}_y)_3\mathrm{Si}_2\mathrm{O}_5(\mathrm{OH})_4$ solid solutions, due to the specific composition of the "secondary" hydroxides formed via reactions (1) and (2) in the region (IV – Fig. 3 and II' – Fig. 4).

5. Conclusion

It has been shown that during the hydrothermal synthesis of $(Mg_{1-y}Ni_y)_3Si_2O_5(OH)_4$ nanotubes with a chrysotile structure, their composition and dimensional parameters are determined not only by the composition and prehistory of the initial reagents but also by the possibility of reagent transformation during changes in the *T–P* conditions in the reaction medium upon heating the autoclave. The thermodynamic analysis performed on the dehydration processes of $Mg_{1-x}Ni_x(OH)_2$ solid solutions and the subsequent hydration of the resulting oxide solid solutions made it possible to explain a number of effects associated with the non-monotonic dependence of the nanotube dimensional parameters and the Mg/Ni ratio in $(Mg_{1-y}Ni_y)_3Si_2O_5(OH)_4$ on the Mg/Ni ratio in the initial $Mg_{1-x}Ni_x(OH)_2$ hydroxides. The obtained results have allowed for a broader perspective on the data, which were interpreted ambiguously in some studies, concerning the influence of the composition and structure of reagents on the formation of nanotubes with a chrysotile structure.

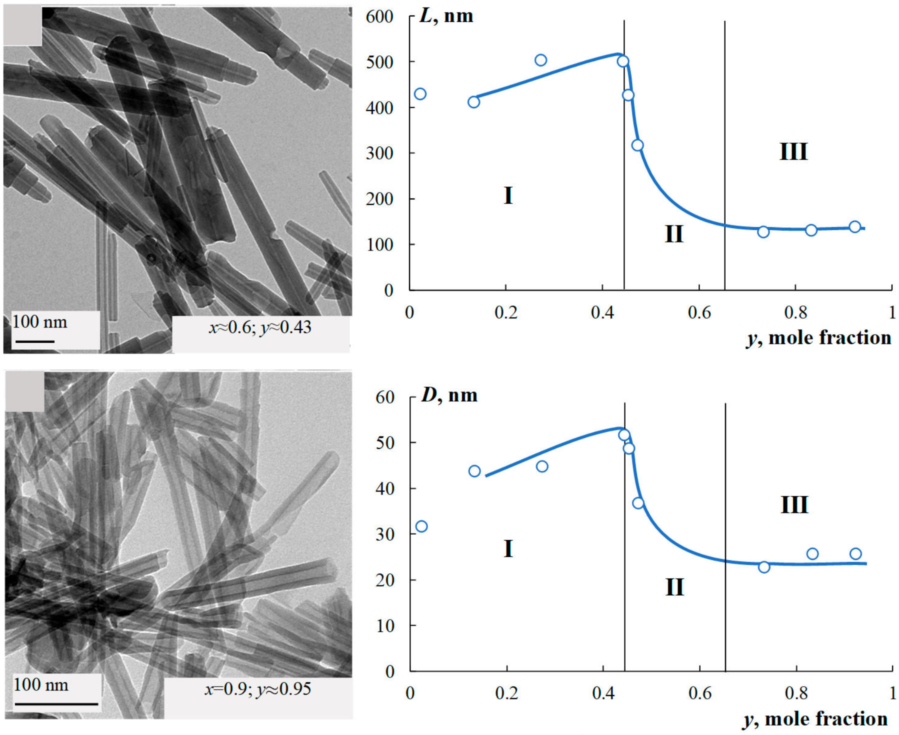

a *b*

FIG. 6. Electron micrographs of nanotube samples obtained using $Mg_{1-x}Ni_x(OH)_2$ hydroxides as reagents ($x \approx 0.6, 0.8, 0.9$; $y \approx 0.44, 0.7, 0.9$ – the corresponding Ni fraction in $(Mg_{1-y}Ni_y)_3Si_2O_5(OH)_4$) – a; average length – L, and outer diameter – D, of $(Mg_{1-y}Ni_y)_3Si_2O_5(OH)_4$ nanotubes versus the Ni fraction – y, in the brucite layer of the nanotubes

References

[1] Adschiri T., Kanazawa K., Arai K., Rapid and continuous hydrothermal crystallization of metal oxide particles in supercritical water. *J. Am. Chem. Soc.*, 1992, **75** (4), P. 1019–1022.

[2] Kwon S.G., Piao Y., Park J., Angappane S., Jo Y., Hwang N.-M., Park J.-G., Hyeon T. Kinetics of monodisperse iron oxide nanocrystal formation by "heating-up" process. *J. Am. Chem. Soc.*, 2007, **129** (41), P. 12571–12584.

[3] Ivanov V.K., Kopitsa G.P., Baranchikov A.E., Grigor'ev S.V., Runov V.V., Haramusc V.M. Hydrothermal growth of ceria nanoparticles. *Russ. J. Inorg. Chem.*, 2009, **54** (12), P. 1857–1861.

[4] Kießling J., Rosenfeldt S., Schenk A.S. Size-controlled liquid phase synthesis of colloidally stable Co_3O_4 nanoparticles. *Nanoscale Adv.*, 2023, **5** (15), P. 3942–3954.

[5] Fedorov P.P., Almyasheva O.V., Alexandrov A.A., Proydakova V.Yu., Korotkova N.A., Baranovskaya V.B. Gusarov V.V. Low-temperature phase formation in the ZrO_2–In_2O_3 system. *Mendeleev Commun.*, 2025, **35** (4), P. 376–378.

[6] Almjasheva O.V., Fedorov B.A., Smirnov A.V., Gusarov V.V. Size, morphology and structure of the particles of zirconia nanopowder obtained under hydrothermal conditions. *Nanosyst: Phys, Chem, Math.*, 2010, **1** (1), P. 26–37.

[7] Sharikov F.Yu., Almjasheva O.V., Gusarov V.V. Thermal analysis of formation of ZrO_2 nanoparticles under hydrothermal conditions. *Russ. J. Inorg. Chem.*, 2006, **51** (10), P. 1538–1542.

[8] Falini G., Foresti E., Gazzano M., Gualtieri A.F., Leoni M., Lesci I.G., Roveri N. Tubular-shaped stoichiometric chrysotile nanocrystals. *Chem. A Eur. J.*, 2004, **10** (12), P. 3043–3049.

[9] Bloise A., Belluso E., Fornero E., Rinaudo C., Barrese E., Capella S., Influence of synthesis conditions on growth of Ni-doped chrysotile. *Microporous Mesoporous Mater.*, 2010, **132** (1-2), P. 239–245.

[10] L´opez-Salinas E., Toledo-Antonio J.A., Manríquez M.E., Sanchez-Cantú M., Cruz Ramos I., Hernandez-Cortez J.G., Synthesis and catalytic activity of chrysotile-type magnesium silicate nanotubes using various silicate sources. *Micropor. Mesopor. Mater.*, 2019, **274**, P. 176–182.

[11] Korytkova E.N., Maslov A.V., Pivovarova L.N., Polegotchenkova Yu.V., Povinich V.F., Gusarov V.V. Synthesis of nanotubular $Mg_3Si_2O_5(OH)_4$-$Ni_3Si_2O_5(OH)_4$ silicates at elevated temperatures and pressures. *Inorg. Mater.*, 2005, **41** (7), P. 730–736.

[12] Jancar B., Suvorov D. The influence of hydrothermal-reaction parameters on the formation of chrysotile nanotubes. *Nanotechnology*, 2006, **17** (1), P. 25–29.

[13] Sharikov F.Yu., Korytkova E.N., Gusarov V.V. Effect of the thermal prehistory of components on the hydration and crystallization of $Mg_3Si_2O_5(OH)_4$ nanotubes under hydrothermal conditions. *Glass Phys. Chem.*, 2007, **35** (5), P. 515–520.

[14] Korytkova E.N., Pivovarova L.N. Hydrothermal synthesis of nanotubes based on $(Mg,Fe,Co,Ni)_3Si_2O_5(OH)_4$ hydrosilicates. *Glass Phys. Chem.*, 2010, **36** (1), P. 53–60.

[15] Maslennikova T.P., Korytkova E.N., Gatina E.N., Pivovarova L.N. Effect of temperature on the synthesis of nanoparticles with different morphology in the system $MgO–SiO_2–TiO_2–H_2O$ under hydrothermal conditions. *Glass Phys. Chem.*, 2016, **42** (6), P. 627–630.

[16] Devouard B., Baronnet A., Van Tendeloo G., Amelinckx S. First evidence of synthetic polygonal serpentines. *Eur. J. Mineral.*, 1997, **9** (3), P. 539–546.

[17] Ueno T., Furuta Y., Koyama T., Imada T. Phase relation among serpentine, brucite and forsterite from 200 to 500 atm water pressure. *Mineral. J.*, 1991, **15** (6), P. 276–281.

[18] Krasilin A.A., Almjasheva O.V., Gusarov V.V. Effect of the structure of precursors on the formation of nanotubular magnesium hydrosilicate. *Inorg. Mater.*, 2011, **47** (10), P. 1111–1115.

[19] Lafay R., Montes-Hernandez G., Janots E., Chiriac R., Findling N., Toche F. Nucleation and growth of chrysotile nanotubes in $H_2SiO_3/MgCl_2/NaOH$ medium at 90 to 300 °C. *Chemistry J.*, 2013, **19** (17), P. 5417–5424.

[20] Bloise A., Fuoco I., Apollaro C., Vespasiano G., Khrapova E., Krasilin A. Retrospective of chrysotile synthesis: From tough geoinspired process up to soft chemical design. *Applied Clay Science*, 2026, **281**, 108088.

[21] Khrapova E.K., Kozlov D.A., Krasilin A.A. Hydrothermal synthesis of hydrosilicate nanoscrolls $(Mg_{1-x}Co_x)_3Si_2O_5(OH)_4$ in a Na_2SO_3 solution. *Russ. J. Inorg. Chem.*, 2022, **67** (7), P. 839–849.

[22] Maslennikova T.P., Korytkova E.N. Influence of synthesis of physicochemical parameters on growth of $Ni_3Si_2O_5(OH)_4$ nanotubes and their filling with solutions of hydroxides and chlorides of alkaline metals. *Glass Phys. Chem.*, 2013, **39** (1), P. 67–72.

[23] Korytkova E.N., Brovkin A.S., Maslennikova T.P., Pivovarova L.N. Drozdova I.A. Influence of the Physicochemical Parameters of Synthesis on the Growth of Nanotubes of the $Mg_3Si_2O_5(OH)_4$ Composition under Hydrothermal Conditions. *Glas. Phys. Chem.*, 2011, **37** (2), P. 161–171.

[24] Chivilikhin S.A., Popov I.Yu., Svitenkov A.I., Chivilikhin D.S., Gusarov V.V. Formation and Evolution of Nanoscroll Ensembles Based on Layered-Structure Compounds. *Doklady Physics*, 2009, **54** (11), P. 491–493.

[25] Chivilikhin S.A., Popov I.Yu., Chivilikhin D.S., Gusarov V.V. Diffusion-controlled growth of a nanoscroll system. *Proceedings of Higher Educational Institutions. Physics*, 2010, **53** (3/2), P. 201–204. (In Russian)

[26] Levin A., Khrapova E., Kozlov D., Krasilin A., Gusarov V. Structure refinement, microstrains and crystallite sizes of Mg-Ni-phyllosilicate nanoscroll powders. *J. Appl. Crystallogr.*, 2022, **55** (3), P. 484–502.

[27] White R.D., Bavykin D.V., Walsh F.C. Morphological control of synthetic $Ni_3Si_2O_5(OH)_4$ nanotubes in an alkaline hydrothermal environment. *J. Mater. Chem. A*, 2013, **1** (3), P. 548–556.

[28] McDonald A., Scott B., Villemure G., Hydrothermal preparation of nanotubular particles of a 1:1 nickel phyllosilicate. *Micropor. Mesopor. Mater.*, 2009, **120** (3), P. 263–266.

[29] Thill A., Guiose B., Bacia-Verloop M., Geertsen V., Belloni L., How the diameter and structure of $(OH)_3Al_2O_3Si_xGe_{1-x}OH$ imogolite nanotubes are controlled by an adhesion versus curvature competition. *J. Phys. Chem. C*, 2012, **116** (51), P. 26841–26849.

[30] Khrapova E.K., Ivanova A.A., Kirilenko D.A., Krasilin A.A. Intermetallic compounds obtained from $Me_3Ge_2O_5(OH)_4$ (Me=Mg, Ni, Fe, Co) phyllogermanates: synthesis of single-phase precursors. *Nanosyst: Phys, Chem, Math.*, 2024, **15** (6), P. 821–836.

[31] Khrapova E.K., Ivanova A.A., Kirilenko D.A., Levin A.A., Bert N.A., Ugolkov V.L., Krasilin A.A. Phase transformations of $(Co_xMg_{1-x})_3Si_2O_5(OH)_4$ phyllosilicate nanoscrolls upon heating in Ar, O_2 and H_2 containing atmospheres. *Appl. Clay Sci.*, 2024, **250**, 107282.

[32] Khrapova, E.K., Omarov, S., Ivanova, A.A., Kirilenko, D.A., Kukushkina, Y., Krasilin, A. A. Mono- and bimetallic catalysts for the steam reforming of glycerol based on $(Co_xNi_{1-x})_3Si_2O_5(OH)_4$ phyllosilicate nanoscrolls. *Micropor. Mesopor. Mater.*, 2025, **389**, 113552.

[33] Ushio M., Saito H., Hydrothermal experiments on materials corresponding to fluor-hydroxyl chrysotile $[Mg_6Si_4O_{10}F_x(OH)_{8-x}]$. *J. Ceram. Soc. Jpn.*, 1970, **78** (11), P. 359–364.

[34] Foresti E., Hochella M. F., Kornishi H., Lesci I. G., Madden A.S., Roveri N., Xu H., Morphological and chemical/physical characterization of Fe-doped synthetic chrysotile nanotubes. *Adv. Funct. Mater.*, 2005, **15** (6), P. 1009–1016.

[35] Korytkova E.N., Pivovarova L.N., Drosdova I.A., Gusarov V.V. Hydrothermal Synthesis of Nanotubular Co-Mg Hydrosilicates with the Chrysotile Structure. *Rus. J. Gen. Chem.*, 2007, **77** (10), P. 1669–1676.

[36] Korytkova E.N., Semyashkina M.P., Maslennikova T.P., Pivovarova L.N., Al'myashev V.I., Ugolkov V.L. Synthesis and Growth of Nanotubes $Mg_3Si_2O_5(OH,F)_4$ Composition under Hydrothermal Conditions. *Glass Phys Chem.*, 2013, **39** (3), P. 294–300.

[37] Krasilin A.A., Suprun A.M., Gusarov V.V. Influence of component ratio in the compound $(Mg,Fe)_3Si_2O_5(OH)_4$ on the formation of nanotubular and platelike particles. *Russ J Appl Chem.*, 2013, **86** (11), P. 1633–1637.

[38] Krasilin A.A., Suprun A.M., Nevedomsky V.N., Gusarov V.V. Formation of conical $(Mg,Ni)_3Si_2O_5(OH)_4$ nanoscrolls. *Dokl Phys Chem.*, 2015, **460** (2), P. 42–44.

[39] Krasilin A.A., Gusarov V.V. Control over morphology of magnesium-aluminum hydrosilicate nanoscrolls. *Russ. J. Appl. Chem.*, 2015, **88** (12), P. 1928–1935.

[40] Krasilin A.A., Suprun A.M., Ubyivovk E.V., Gusarov V.V. Morphology vs. chemical composition of single Ni-doped hydrosilicate nanoscroll. *Materials Letters.*, 2016, **171**, P. 68–71.

[41] Krasilin A.A., Gusarov V.V. Redistribution of Mg and Ni cations in crystal lattice of conical nanotube with chrysotile structure. *Nanosyst: Phys, Chem, Math.*, 2017, **8** (5), P. 620–627.

[42] Krasilin A.A., Khrapova E.K., Nomine A., Ghanbaja J., Belmonte T., Gusarov V.V. Cations redistribution along the spiral of Ni-doped phyllosilicate nanoscrolls: energy modelling and STEM/EDS study. *ChemPhysChem.*, 2019, **20** (5), P. 719–726.

[43] Krasilin A.A., Gusarov V.V. Energy model of radial growth of a nanotubular crystal. *Tech. Phys. Lett.*, 2016, **42** (1), P. 55–58.

[44] Enikeeva M.O., Proskurina O.V., Gerasimov E.Yu., Gorshkova Yu.E., Naberezhnov A.A., Gusarov V.V. Gradient distribution of cations in rhabdophane $La_{0.27}Y_{0.73}PO_4{\cdot}nH_2O$ nanoparticles. *Physica B.*, 2025, **696**, Art. 416623.

[45] Lafay R., Fernandez-Martinez A., Montes-Hernandez G., Auzende A.L., Poulain A. Dissolution-reprecipitation and self-assembly of serpentine nanoparticles preceding chrysotile formation: Insights into the structure of proto-serpentine *American Mineralogist*, 2016, **101** (12), P. 2666–2676.

[46] Sprynskyy M., Niedojadło, J., Buszewski, B. Structural features of natural and acids modified chrysotile nanotubes. *J. of Physics and Chemistry of Solids*, 2011, **72** (9), P. 1015–1026.

[47] Kurguzkina M.E., Maslennikova T.P., Gusarov V.V. Formation, morphology, and size parameters of nanopowders based on $Mg_3Si_2O_5(OH)_4$–$Ni_3Si_2O_5(OH)_4$ nanoscrolls. *Inorg. Mater.*, 2023, **59** (10), P. 1111–1120.

[48] Kotova M.E., Maslennikova T.P., Ugolkov V.L., Gusarov V.V. Formation, structure, composition in the dispersed state, and behavior of nanoparticles heated in the $Mg(OH)_2$–$Ni(OH)_2$ system. *Nanosyst: Phys, Chem, Math.*, 2022, **13** (5), P. 514–524.

[49] Belotitskii V.I., Fokin A.V., Kumzerov Y.A., Sysoeva A.A. Optical properties of nanowires synthesized in regular nanochannels of porous matrices. *Opt. Quantum Electron.*, 2020, **52** (4), 218.

[50] Khrapova E.K., Ugolkov V.L., Straumal E.A., Lermontov S.A., Lebedev V.A., Kozlov D.A., Krasilin A.A. Thermal behavior of Mg-Ni-phyllosilicate nanoscrolls and performance of the resulting composites in hexene-1 and acetone hydrogenation. *ChemNanoMat.*, 2020, **7** (3), P. 257–269.

[51] Bian Z., Li Z., Ashok J., Kawi S. A highly active and stable Ni–Mg phyllosilicate nanotubular catalyst for ultrahigh temperature water-gas shift reaction. *Chem. Commun.*, 2015, **51** (91), P. 16324–16326.

[52] Yang Y., Liang Q., Li J., Zhuang, He Y., Bai B., Wang X. $Ni_3Si_2O_5(OH)_4$ multi-walled nanotubes with tunable magnetic properties and their application as anode materials for lithium batteries. *Nano Res.*, 2011, **4** (9), P. 882–890.

[53] Cheng L., Zhai L., Liao W., Huang X., Niu B., Yu Sh. An Investigation on the Behaviors of Thorium(IV) Adsorption onto Chrysotile Nanotubes. *J. Environ. Chem. Eng.*, 2014, **2** (3), P. 1236–1242.

[54] Chernyaev A.V., Mikhailin N.Yu., Shamshur D.V., Kumzerov Yu.A., Fokin A.V., Kalmykov A.E., Parfen’ev R.V., Sorokin L.M., Lashkul A. Electrical and magnetic properties of Pb and In nanofilaments in asbestos near the superconducting Transition. *Phys. Solid State*, 2018, **60** (10), P. 1935–1941.

[55] Yudin V.E., Otaigbe J.U., Svetlichnyi V.M., Korytkova E.N., Almjasheva O.V., Gusarov V.V. Effects of nanofiller morphology and aspect ratio on the rheo-mechanical properties of polimide nanocomposites. *Express Polym. Lett.*, 2008, **2** (7), P. 485–493.

[56] Gubanova G.N., Sukhanova T.E., Vylegzhanina M.E., Lavrentiev V.K., Romashkova K.A., Kutin A.A., Maslennikova T.P., Kononova S.V. Analysis of the surface morphology, structure and properties of polyamidoimide nanocomposites with tubular hydrosilicates. *J. Synch. Investig.*, 2017, **11** (5), P. 1022–1032.

[57] Krasilin A.A., Khrapova E.K., Maslennikova T.P. Review: Cation Doping Approach for Nanotubular Hydrosilicates Curvature Control and Related Applications. *Crystals*, 2020, **10** (8), 654.

[58] Skuland T., Maslennikova T., Låg M., Gatina E., Serebryakova M., Trulioff A., Kudryavtsev I., Klebnikova N., Kruchinina I., Schwarze P.E., Refsnes M. Synthetic hydrosilicate nanotubes induce low pro-inflammatory and cytotoxic responses compared to natural chrysotile in lung cell cultures. *Basic Clin Pharmacol Toxicol.*, 2020, **126** (4), P. 374–388.

[59] Heath K.D., Mackrodt W.C., Saundersb V.R., Causa Mauro Calculated Enthalpies of Mixing of MnO/MgO and NiO/MgO. *J. Mater. Chem.*, 1994, **4** (6), P. 825–829.

[60] Farina A., Neto F. Thermodynamic Assessment of NiO–MgO system, September 2016 Conference: Discussion Meeting on Thermodynamics of Alloys At: Santos – Brazil 2016.

[61] Belov G.V., Iorish V.S., Yungman V.S. IVTANTHERMO for Windows - database on thermodynamic properties and related software. *CALPHAD*, 1999, **23** (2), P. 173–180.

[62] Kennedy G.C. Pressure-volume-temperature relations in water at elevated temperatures and pressures. *Am. J. Sci.*, 1950, **248** (8), P. 540–564.

Submitted 14 April 2026; accepted 15 April 2026

Information about the authors:

Oksana V. Almjasheva – NRC “Kurchatov Institute” – PNPI – IChS, Russia, Saint-Petersburg Electrotechnical University, Russia; ORCID 0000-0002-6132-4178; almjasheva@mail.ru

Maria E. Kurguzkina – NRC “Kurchatov Institute” – PNPI – IChS, Russia; ORCID 0000-0002-5817-5247; kotovamaria715@gmail.com

Victor V. Gusarov – NRC “Kurchatov Institute” – PNPI – IChS, Russia; ORCID 0000-0003-4375-6388; victor.vladimirovich.gusarov@mail.ru

Conflict of interest: the authors declare no conflict of interest.

NANOSYSTEMS:
PHYSICS, CHEMISTRY, MATHEMATICS

Vinogradov V.Yu., et al. *Nanosystems: Phys. Chem. Math.*, 2026, **17** (2), 218–227.
http://nanojournal.ifmo.ru
DOI 10.17586/2220-8054-2026-17-2-218-227

Original article

Effect of hydroxide precursor synthesis conditions on the properties of $Gd_2Zr_2O_7$ spark plasma sintered ceramics

Vladimir Yu. Vinogradov[1,a], Dina V. Dudina[2,b], Maksim A. Esikov[2,c], Olga B. Shcherbina[1,d],
Vadim V. Efremov[3,e], Alexander M. Kalinkin[1,f]

[1]Tananaev Institute of Chemistry and Technology of Rare Elements and Mineral Raw Materials KSC RAS, Apatity, Russia

[2]Lavrentyev Institute of Hydrodynamics SB RAS, Novosibirsk, Russia

[3]Institute of North Industrial Ecology Problems KSC RAS, Apatity, Russia

[a]v.vinogradov@ksc.ru, [b]ddudina@hydro.nsc.ru, [c]esmax@ya.ru, [d]o.shcherbina@ksc.ru, [e]v.efremov@ksc.ru, [f]a.kalinkin@ksc.ru

Corresponding author: V.Yu. Vinogradov, v.vinogradov@ksc.ru

PACS 81.05.Je, 81.05.Hf, 81.16.Rt, 81.16.Tb, 81.40.Gh

ABSTRACT The paper presents the first comparative study of the microstructure and mechanical properties of gadolinium zirconate ceramics produced by spark plasma sintering of powders obtained using hydroxide precursors synthesized with and without mechanical activation. The initial precursor was prepared via reverse coprecipitation of hydroxides. Mechanical activation of the precursor was performed in an AGO-2 planetary mill at a centrifugal acceleration of 20 g for 30 min. X-ray phase analysis revealed that the resulting ceramics were nanocrystalline. The ceramics produced from the mechanically activated precursor demonstrated superior mechanical properties, including higher microhardness and Young's modulus, compared to those produced from the non-activated precursor.

KEYWORDS gadolinium zirconate, ceramics, mechanical activation, precursor, spark plasma sintering

ACKNOWLEDGEMENTS This research was conducted within the framework of the budget projects FMEZ-2025-0056 for the Tananaev Institute of Chemistry of the Federal Research Centre of Kola Science Centre of the Russian Academy of Sciences.

FOR CITATION Vinogradov V.Yu., Dudina D.V., Esikov M.A., Shcherbina O.B., Efremov V.V., Kalinkin A.M. Effect of hydroxide precursor synthesis conditions on the properties of $Gd_2Zr_2O_7$ spark plasma sintered ceramics. *Nanosystems: Phys. Chem. Math.*, 2026, **17** (2), 218–227.

1. Introduction

REE zirconates are complex oxides in binary systems of the type Ln_2O_3–MO_2 (where Ln represents rare-earth cations and M denotes Group IVB metal cations: Ti, Zr, Hf). These compounds typically adopt the general formula $Ln_2M_2O_7$ and most commonly crystallize in pyrochlore-type structures with varying degrees of disorder. The extent of structural disorder depends on intrinsic factors – such as chemical composition, bonding nature, and the ratio of cationic radii ($R_{\mathrm{Ln}}/R_{\mathrm{Zr}}$) – as well as extrinsic factors, including synthesis conditions [1, 2]. In terms of its structural and chemical characteristics, $Gd_2Zr_2O_7$ occupies a special position in the series of REE zirconates. The corresponding ratio of the radii of the REE and zirconium cations ($R_{\mathrm{Gd}}/R_{\mathrm{Zr}} = 1.462$) actually delimits two regions of stability: at $R_{\mathrm{Ln}}/R_{\mathrm{Zr}} \geq 1.46$, the pyrochlore structure (space group $Fd3\bar{m}$) is stable, and, at $R_{\mathrm{Ln}}/R_{\mathrm{Zr}} < 1.46$, the disordered fluorite structure (space group $Fm3\bar{m}$) becomes favorable [1, 3, 4]. At room temperature, $Gd_2Zr_2O_7$ typically adopts the stable pyrochlore phase (P-$Gd_2Zr_2O_7$), which transforms into a disordered fluorite modification (F-$Gd_2Zr_2O_7$) at $\sim$1550 °C. As the energy difference between these phases is small, fluorite-like $Gd_2Zr_2O_7$ can exist under standard conditions, which is facilitated by certain conditions of its synthesis [5, 6]. In this regard, REE zirconates, in particular $Gd_2Zr_2O_7$, are interesting from the point of view of the occurrence of a phase transition of the pyrochlore (order) – fluorite (disorder) type [1, 2].

At the same time, REE zirconates with both crystal structures exhibit a broad spectrum of physical and chemical properties, making them highly attractive for fundamental and applied research [7–10]. Their unique structural features and exceptional characteristics render them promising candidates for applications in electro/photocatalysis, magnetism, nuclear waste storage, thermal barrier coatings, sensors, catalysis, ionic conductors, oxygen monitoring, photoluminescent host materials, and solid electrolytes in high-temperature fuel cells [11–21]. In particular, $Gd_2Zr_2O_7$ demonstrates high thermal stability, chemical resistance, high thermal expansion coefficient ($11.09 \cdot 10^{-6}$ K^{-1} [22]), a high melting point

(2570 °C) [23], low thermal conductivity (1.5 – 2.0 W/(m·K) [5, 24]), and high ionic conductivity ($> 1 \cdot 10^{-3}$ Sm/cm at 800 °C [25, 26]).

In recent years, researchers have increasingly focused on enhancing the synthesis methods for nanoceramics based on REE zirconates. These materials exhibit superior properties compared to microcrystalline ceramics, including higher radiation resistance, lower thermal conductivity, and enhanced oxygen-ion conductivity [1, 4, 14, 27–36].

The properties and applicability of ceramics based on rare earth zirconates are directly influenced by the composition, size, shape, and morphology of their precursors, which can be synthesized through various methods [1, 4, 14, 37, 38]. Typically, precursors for rare earth zirconate nanoceramics – including $Gd_2Zr_2O_7$ – are prepared using wet chemistry techniques such as sol-gel synthesis, solvothermal, hydrothermal methods, and hydroxide coprecipitation [6, 11, 14, 30, 31, 39–41].

Another crucial step in ceramic production is selecting the consolidation method. Spark plasma sintering (SPS) has emerged as a promising technique for compacting and consolidating various materials. During SPS, an electric current passes through the tooling and the sample, rapidly heating them via the Joule effect. This allows the target processing temperature to be achieved in minimal time. Additionally, the applied pressure significantly enhances densification. Thus, SPS can consolidate powder system components at lower temperatures while suppressing excessive grain growth [42–44]. The key advantages of SPS technology include:

- High densification with controllable porosity.
- Elimination of pre-compaction or binders, simplifying the process.
- Homogeneous sintering of both similar and dissimilar materials.
- Rapid processing due to short cycle times.
- Minimal grain growth, preserving the microstructure [45, 46].

In this work, nanocrystalline $Gd_2Zr_2O_7$ ceramics were synthesized by SPS using a dried powder of hydroxide precursor prepared through the coprecipitation of gadolinium and zirconium hydroxides. For the first time, the influence of preliminary mechanical activation (MA) of the hydroxide precursor on the mechanical properties of the ceramics – specifically, microhardness and Young's modulus – was investigated.

2. Experimental

For the synthesis of the initial and MA-precursors of gadolinium zirconate, "chemically pure" gadolinium nitrate $Gd(NO_3)_3 \cdot 6H_2O$ ($\omega(Gd_2O_3)$ = 40.48 %), zirconium oxychloride $ZrOCl_2 \cdot 8H_2O$ ($\omega(ZrO_2)$ = 37.98 %) and ammonium hydroxide NH_4OH were used. The detailed synthesis method for the hydroxide precursor is described in the previously published work [47]. After obtaining the precursor, it was dried at 110 °C for 12 hours. This precursor is hereafter referred to as the initial precursor (IP).

The IP was subjected to mechanical activation. MA was performed in an AGO-2 centrifugal–planetary mill under ambient conditions. The process utilized zirconium dioxide–lined vials and 7 – 8 mm zirconium dioxide grinding balls [47]. The milling parameters were as follows: centrifugal acceleration – 20 g, duration – 30 min, and a ball-to-powder mass ratio of 20:1. To ensure homogeneity, the mill was paused every 60 seconds, and the contents were manually mixed using a spatula. The resulting mechanically activated precursor is hereafter denoted as MP. The IP and MP were not subjected to additional heat treatment before SPS.

SPS was performed on a SPS Labox 1575 apparatus (SINTER LAND Inc., Japan) using graphite tooling at temperatures of 1300 and 1550 °C (measured by a pyrometer focused on a hole in the wall of the die). The heating rate was $\sim$60 °/min, the applied pressure was 40 MPa. The samples were held for 5 min at the maximum temperature. Tablets with a diameter of 10 mm and a thickness of 2.0 – 2.5 mm were prepared from powders derived from IP and MP. After SPS, the samples were polished with sandpaper and ultrasonically cleaned in distilled water and alcohol to remove residual graphite from the surface [44]. To completely remove graphite, the tablets were calcined at 1000 °C for 3 hours.

For X-ray diffraction analysis (XRD), a Rigaku Miniflex-600 diffractometer (CuKα radiation) was used. XRD patterns were recorded at a rate of $2°(2\theta)$ per min. The cubic Fm3m structure of gadolinium zirconate $Gd_2Zr_2O_7$ was reliably identified in the diffraction patterns of the samples (PDF No. 04-006-1657). Full-profile analysis of the diffraction patterns using the Rietveld method was performed using SmartLab Studio II software, included with the MiniFlex-600 diffractometer. All reflections were used for the calculation. The initial structural model for the calculations was based on PDF card No. 04-006-1657, which closely matched the observed experimental profile. Angular correction (2θ correction) was performed using the external standard method, with silicon (NIST SRM 640) as the reference material. During full-profile analysis, the background, scale factor, and lattice parameters were refined using the initial parameters provided by the model. The peak profiles were fitted using a pseudo-Voigt function. Structural parameters – including atomic coordinates, site occupancies, and thermal displacement factors – were not refined. The refinement procedure was carried out sequentially as follows: background determination, refinement of the scale factor and lattice parameters, and finally, refinement of the profile function parameters.

The effective crystallite sizes for ceramics and the microstrains were calculated from the XRD data using Size-Microstrain (SSP) graphical method [48, 49]. In order to account for instrumental broadening, a Si (NIST SRM 640f) reference sample was used.

IR spectra were recorded on a Nicolet 6700 FT–IR Fourier spectrometer in KBr tablets.

The mechanical properties of $Gd_2Zr_2O_7$ ceramic samples prepared by SPS with and without preliminary MA of the IP were studied by the contact method using a NanoSkan probe microscope-nanohardness tester (FSBI TISNCM, Russia).

The microstructure of the $Gd_2Zr_2O_7$ ceramic samples obtained from IP and MP was analyzed by scanning electron microscopy (SEM) using a SEM LEO-1450 microscope. The images were processed by Scan Master program.

The density of the synthesized $Gd_2Zr_2O_7$ ceramics was determined using Archimedes' method. Prior to density measurements, all samples were annealed at 1000 °C for 3 hours to ensure the complete removal of residual graphite.

3. Results and discussion

Previous studies [47] demonstrated that both IP and MP, when heat-treated at 900 – 1200 °C, form disordered metastable fluorite-like $Gd_2Zr_2O_7$. The effective crystallite size increases with the calcination temperature, ranging from 10 to 48 nm for IP and from 17 to 56 nm for MP. Notably, the use of MA enables the synthesis of highly dispersed $Gd_2Zr_2O_7$ powders with a specific surface area 5 – 7 times greater than that of powders produced without MA. This enhancement can be attributed to the improved homogeneity of MP and more uniform $Gd_2Zr_2O_7$ crystallization during calcination [47].

Figure 1 presents the XRD patterns of the synthesized ceramics. All ceramic samples exhibit a disordered fluorite structure (PDF No. 04-006-1657) and are nanocrystalline in nature. The effective crystallite sizes for ceramics obtained by SPS IP and MP, as well as the microstrains and lattice parameters are given in Table 1. There was no significant deviation in the crystal lattice parameters of the ceramics produced by SPS IP and MP relative to the theoretical value (PDF No. 04-006-1657, Fd3m, $a = b = c = 5.25$ Å). This indicates that the chemical composition of the produced ceramics is close to $Gd_2Zr_2O_7$ (Gd:Zr mole ratio of 1:1). As an example, Fig. 2 presents experimental (black dots), calculated (red curve) and difference (blue curve) XRD patterns of $Gd_2Zr_2O_7$ ceramics synthesized by SPS at 1300 from MP. The small difference between the calculated and experimental XRD patterns confirms the formation of ceramics with the $Gd_2Zr_2O_7$ structure. To confirm the nanocrystalline structure of the obtained ceramics, further studies using transmission electron microscopy (TEM) are required.

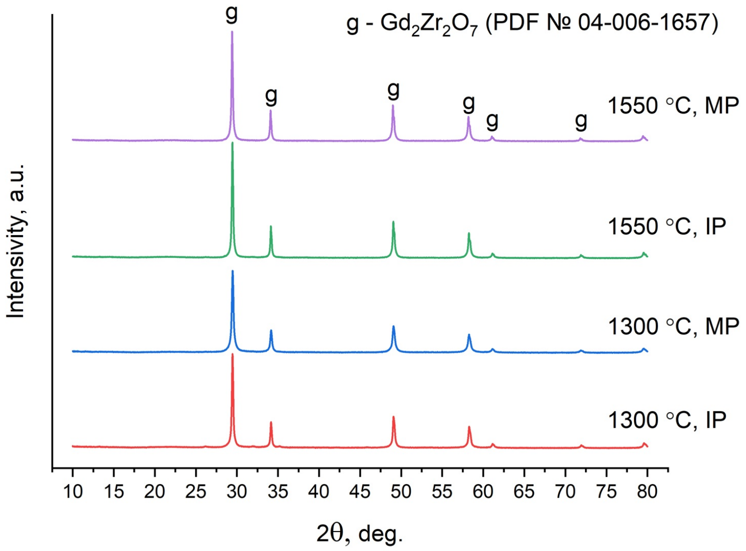

FIG. 1. XRD patterns of $Gd_2Zr_2O_7$ ceramics synthesized by SPS at 1300 and 1550 °C from IP and MP

As mentioned earlier, P-$Gd_2Zr_2O_7$ transforms into F-$Gd_2Zr_2O_7$ at approximately 1550 °C. However, depending on the synthesis method, the fluorite modification can be retained upon cooling. In such cases, an ordered pyrochlore phase may form within the fluorite phase as nanodomains, and the corresponding peaks are not detectable in the XRD patterns. According to the literature [50, 51], infrared spectroscopy is a highly sensitive method for identifying P-$Gd_2Zr_2O_7$ nanodomains within a F-$Gd_2Zr_2O_7$ matrix. The FTIR spectra of the ceramics studied here (Fig. 3) lack the characteristic pyrochlore absorption band at 510 cm^{-1}, which is associated with the $Gd_2Zr_2O_7$ pyrochlore lattice. This absence indicates that P-$Gd_2Zr_2O_7$ nanodomains are not present and that no fluorite-to-pyrochlore structural transition has occurred.

The microhardness (H, GPa) of $Gd_2Zr_2O_7$ ceramics was determined using the comparative sclerometry method, in which scratches are alternately applied to the test material and a reference standard of the known hardness [52]. A certified

TABLE 1. Lattice parameters, crystallite sizes and microstrains of $Gd_2Zr_2O_7$ ceramics

Sample	SPS temperature, °C	Lattice parameter, Å	Crystallite size, nm	Microstrain, %
IP	1300	5.2454	70±6	0.07±0.01
MP	1300	5.2519	64±5	0.07±0.01
IP	1550	5.2595	103±8	0.05±0.01
MP	1550	5.2457	123±10	0.03±0.01

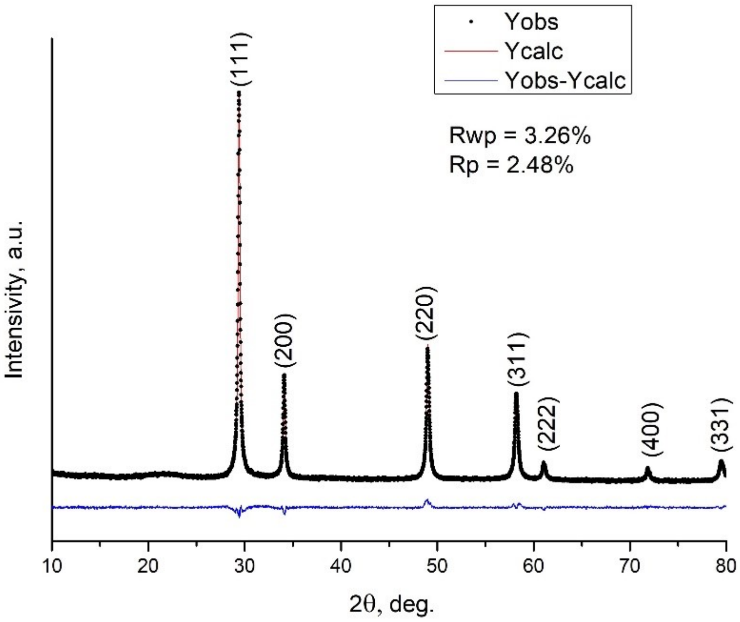

FIG. 2. Single-phase Rietveld refined XRD pattern of $Gd_2Zr_2O_7$ ceramics synthesized by SPS at 1300 °C from MP

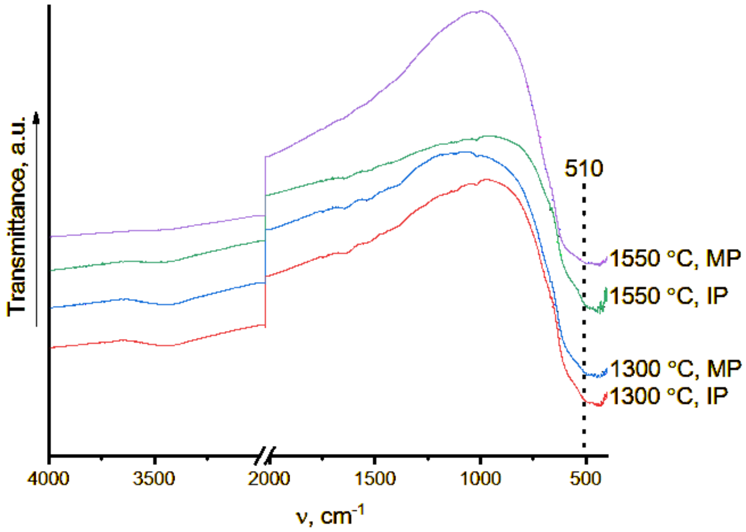

FIG. 3. FTIR spectra of $Gd_2Zr_2O_7$ ceramics synthesized by SPS at 1300 and 1550 °C from IP and MP

fused quartz sample calibrated against the State Hardness Standard (SHS 31-2006) at the Federal State Unitary Enterprise "Russian Metrological Institute of Technical Physics and Radio Engineering" (FSUE "VNIIFTRI") served as the hardness reference. Scratching of $Gd_2Zr_2O_7$ ceramics was performed at indenter loads of 5 – 20 mN using a Berkovich indenter – a triangular diamond pyramid probe with a tip curvature radius of $\sim$50 nm. The same probe was used to scan the scratched surface. As an example, Fig. 4 shows the resulting scratch topography of the ceramics prepared from IP and MP by SPS at 1300 °C.

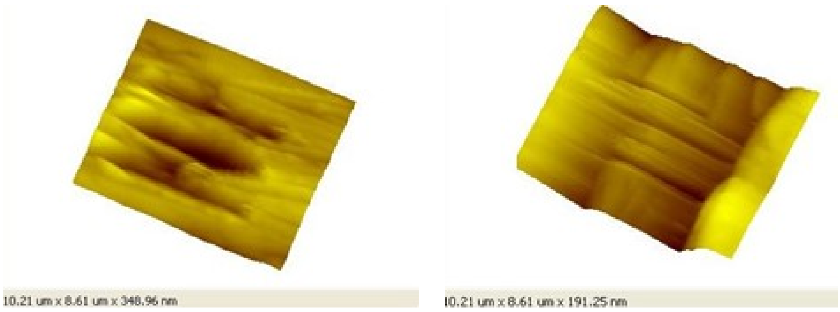

(a) (b)

FIG. 4. Surface morphology of $Gd_2Zr_2O_7$ ceramics prepared from IP (a) and MP (b) by SPS at 1300 °C after sclerometry

Since the forward motion of a Berkovich indenter at an acute angle during scratching resembles the extrusion of an imprint in a Vickers test, the calculations were based on a model for Vickers pyramid indentation [52–54]. The hardness of the material was determined using the following formula:

$$H = k \cdot \frac{P}{b^2}, \tag{1}$$

where P is the normal force with which the scratch was made, expressed in Newtons; b is the arithmetic mean of the scratch width, expressed in meters and k is the indenter shape factor for a given scratch width. The indenter shape factor k was determined by scratching a reference material with the known hardness and calculating it using the following formula:

$$k = \frac{H_c \cdot b^2}{P}, \tag{2}$$

where H_c is the hardness of the reference material.

To measure the absolute value of Young's modulus (E, GPa) of ceramics, force spectroscopy was employed [53–55]. This technique involves bringing an oscillating indenter into contact with the sample surface, where it vibrates normal to the surface with an amplitude of less than 10 nm and a frequency of $\sim$12 kHz. A triangular diamond pyramid with an apex angle of approximately 60° was used as the indenter needle featuring a tip curvature radius of $\sim$100 nm. The needle's Young's modulus (E) and Poisson's ratio (ν) were set to 1140 GPa and 0.07, respectively, in the calculations. As the indenter interacts with the material, the frequency of the probe oscillations increases upon contact with the surface. According to the Hertz model, the slope of the oscillation frequency versus penetration depth (approach curve) is proportional to the elastic modulus of the material [53, 54]. The elastic modulus was determined by comparing the slopes of the approach curves for the sample and a reference material. For each sample, the Young's modulus values were calculated as the average of 16 independent measurements.

The relative density of all prepared ceramics exceeds 90 %, reaching near-theoretical values [1] after SPS at 1550 °C (Table 2).

The data in Table 2 demonstrate that MA of the precursor enhances the mechanical properties of the gadolinium zirconate ceramics. For both SPS temperatures (1300 and 1550 °C), the microhardness and Young's modulus values of ceramics derived from the MP are significantly higher than those of ceramics produced from IP. For comparison, Table 2 presents the literature data on the properties of $Gd_2Zr_2O_7$ ceramics with a fluorite structure prepared via SPS [56] and conventional solid-phase free sintering [57, 58]. When consolidated by SPS, our precursor (MP) demonstrates advantages over the gel-drying and combustion-derived precursor, yielding ceramics with higher microhardness and density. The solid-phase method enables the production of ceramics with microhardness and Young's modulus values close to those obtained in our work. However, this method requires prolonged high-temperature calcination, which hinders the synthesis of nanocrystalline samples (Table 2).

The trends in the microhardness and Young's modulus for ceramics obtained by SPS of IP and MP can be explained as follows.

Young's modulus (elastic modulus) is a fundamental characteristic of a material, a measure of the interatomic bonding forces. It describes elastic deformation, which is reversible. In ceramics, pores are the primary factor weakening the elastic

TABLE 2. Relative density ($\rho_{\text{rel.}}$), microhardness (HV) and Young's modulus (E) of F-$Gd_2Zr_2O_7$ ceramics prepared by different methods

Precursor	Consolidation	$\rho_{\text{rel.}}$, %	HV, GPa	E, GPa	Ref.
IP	SPS: 1300 °C, 40 MPa, 5	95.9	6.2±1.3	205±3	This work
MP	SPS: 1300 °C, 40 MPa, 5	91.3	15.3±2.3	261±9	This work
IP	SPS: 1550 °C, 40 MPa, 5	98.9	8.2±1.4	272±3	This work
MP	SPS: 1550 °C, 40 MPa, 5	99.0	9.2±1.1	298±11	This work
Drying and combustion of gel	SPS: 1300 °C, 70 MPa, 5 min	97.4	8.8±0.4	—	[56]
Mixture of oxides	Solid-phase method: 1600 °C, 10 h	98.4	10.9±0.9	307±31	[57]
Mixture of oxides	Solid-phase method: 1650 °C, 10 h	99.0	6.0±0.3	214±5	[58]

modulus. They concentrate stress and do not contribute to the elastic stiffness of the material. As the sintering temperature increases, porosity decreases, the material becomes denser, and Young's modulus increases. As follows from Table 2, this trend is observed for IP and MP.

Microhardness is sensitive to (1) defects (porosity, cracks) and (2) grain size. When the sintering temperature increases, coalescence and grain growth occur. Fine grains create more boundaries, which act as obstacles to the movement of dislocations and the development of plastic deformation under the indenter. Large grains facilitate this movement, reducing microhardness. On the other hand, an increase in temperature is generally accompanied by an increase in density and the contact area between particles, leading to an increase in hardness. For IP, as the temperature increases, the hardness increases, which likely indicates the predominant influence of the first factor (density/contact area). In the case of MP, the situation is opposite, i.e., grain growth apparently plays the determining role.

Another notable feature of the data presented in Table 2 is that the relative density of the ceramics obtained at 1300 °C from the MP is lower than that of ceramics from the IP. Interestingly, despite this lower density, the microhardness of the ceramics prepared from MP is the highest. It was previously established that both hydroxide precursors (IP and MP) interact with atmospheric carbon dioxide during synthesis, leading to the formation of carbonate groups. In the case of MP, the decomposition of these carbonate groups with the release of CO_2 occurs at higher temperatures compared to IP [47]. We assume that this may be the reason for the reduced density of the MP-based ceramics sintered at 1300 °C. SPS is characterized by very rapid heating (within a few minutes) with simultaneous pressure application. Sintering is accompanied by the removal of volatile components – such as water and CO_2 – from the particle surfaces and from the pores within the sample under highly nonequilibrium conditions.

When the precursor is compacted, the closure of pores is inhibited by the pressure of gases trapped within them. As the removal of carbon dioxide from the MP is more difficult than from the IP, this can lead to a higher degree of closed porosity. However, when the SPS temperature is increased to 1550 °C, the negative factors that limit densification at 1300 °C are overcome. As a result, both the IP and MP achieve high and nearly equal relative densities (98.9 % and 99.0 %, respectively, as shown in Table 2). It is likely that the sample with a density of 91.3 % and maximum microhardness was sintered under optimal conditions for suppressing grain growth. A higher density (98 – 99 %) is achieved by increasing the sintering temperature, which inevitably leads to coalescence and grain growth. As previously noted, larger grains reduce hardness, while smaller grains create more grain boundaries. These boundaries act as obstacles to dislocation movement and hinder the development of plastic deformation beneath the indenter. A detailed clarification of the reasons for the different influence of sintering temperature on the microhardness of ceramics based on IP and MP requires additional research.

The microstructure of $Gd_2Zr_2O_7$ ceramic samples prepared by the SPS method with and without preliminary MA of the IP was analyzed using SEM imaging. The images were processed using Scan Master program, designed for the mathematical analysis of such micrographs. The program enables users to select objects within an image, analyze their characteristics, and perform the statistical processing on the set of selected objects based on the chosen criteria. In this case, parameter "Length" – defined as the maximum length among 18 projections of an object onto a plane – was selected as the criterion for evaluating the size of the ceramic particles.

SEM images of the $Gd_2Zr_2O_7$ ceramic material synthesized by SPS at 1300 °C using IP reveal a nearly pore-free surface with no discernible grains (Fig. 5). SEM images of the $Gd_2Zr_2O_7$ ceramic material synthesized by SPS at 1300 °C using MP is shown in Fig. 6.

Increasing the SPS temperature to 1550 °C results in grain growth. The $Gd_2Zr_2O_7$ ceramics synthesized from the IP at this temperature exhibit well-faceted grains ranging from 0.2 to 3.0 μm in size (Fig. 7), with an average grain size of 0.4 μm (Fig. 8). Microcracks are observed along the grain boundaries, but the ceramics are nearly pore-free.

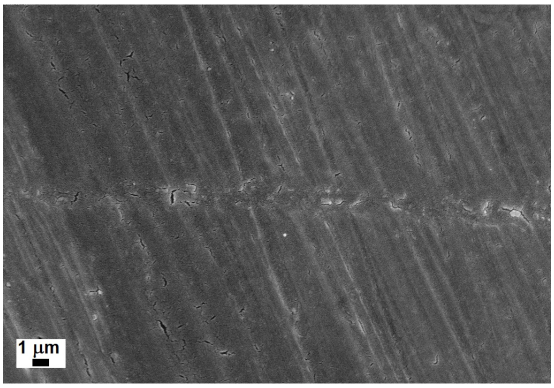

FIG. 5. SEM image of $Gd_2Zr_2O_7$ ceramic material prepared by the SPS at 1300 °C from IP (magnification 5000)

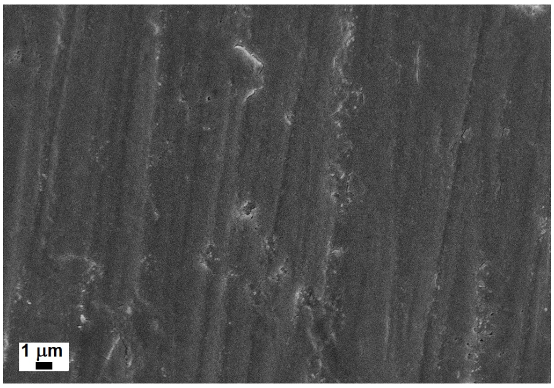

FIG. 6. SEM image of $Gd_2Zr_2O_7$ ceramic material prepared by the SPS at 1300 °C from MP (magnification 5000)

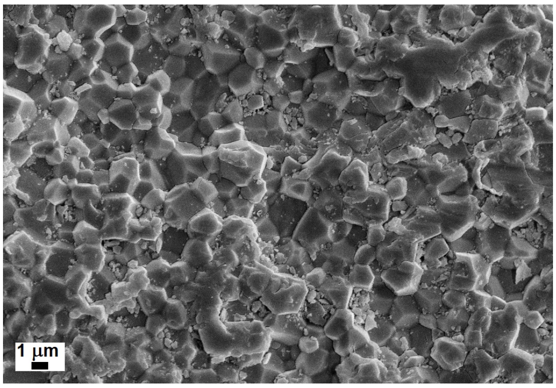

FIG. 7. SEM image of $Gd_2Zr_2O_7$ ceramic material prepared by SPS at 1550 °C from IP (magnification 5000)

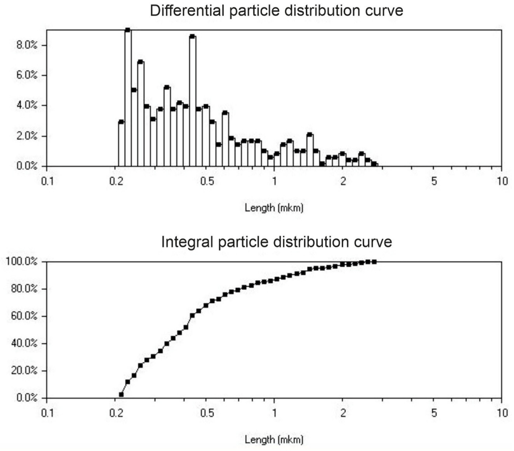

FIG. 8. Differential curve of grain distribution and integral curve of granulometric composition of $Gd_2Zr_2O_7$ ceramic material prepared by SPS at 1550 °C from IP

The $Gd_2Zr_2O_7$ ceramic samples prepared from MP at 1550 °C exhibit at least two distinct morphological structures (Fig. 9). These include regions composed of well-defined, faceted grains ranging from 0.1 to 1.5 μm in size and larger areas (up to 8 – 10 μm in length) lacking a pronounced grain structure (Figs. 9 and 10).

The SEM image of the $Gd_2Zr_2O_7$ ceramic material synthesized by SPS at 1550 °C (IP, higher magnification, Fig. 11) confirms a non-porous surface. The microstructure exhibits the features of brittle fracture, including a crystalline structure and intergranular cleavage facets. In contrast, the MP-based sample at the same magnification (Fig. 12) shows pronounced grain agglomeration. The intergranular boundaries are nearly invisible in the image, with the grains in close contact. The surface of this sample is smoother and exhibits fewer visible defects compared to the IP-based sample (Fig. 11). Cleavage predominantly occurs along intergranular contacts, while intragranular chips are extremely rare.

4. Conclusions

Nanocrystalline $Gd_2Zr_2O_7$ ceramics were synthesized by SPS using the hydroxide precursor with and without MA. The relative density of all the prepared ceramics is greater than 90 %. This value approaches the theoretical value after SPS at 1550 °C. MA of the initial precursor led to an increase in the microhardness and Young's modulus of the sintered ceramics. So, the highest values were achieved for the ceramics derived from the MP: a microhardness of 15.3±2.3 GPa (at 1300 °C) and a Young's modulus of 298±11 GPa (at 1550 °C). The comparison of the obtained results with the literature data on F-$Gd_2Zr_2O_7$ SPS-ceramics revealed that our MP precursor exhibits a higher efficiency in enhancing the microhardness of the ceramics compared to the precursor derived from gel drying and combustion. While conventional solid-phase synthesis of F-$Gd_2Zr_2O_7$ ceramics yields microhardness and Young's modulus values similar to our findings, this method requires prolonged high-temperature calcination, which prevents the formation of nanocrystalline materials. Although the crystallite size has a minimal direct impact on microhardness and Young's modulus, its control

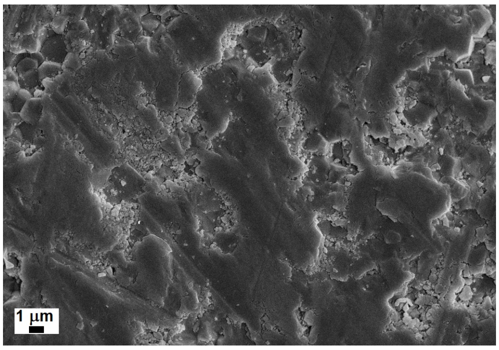

FIG. 9. SEM image of $Gd_2Zr_2O_7$ ceramic material prepared by SPS at 1550 °C from MP (magnification 5000)

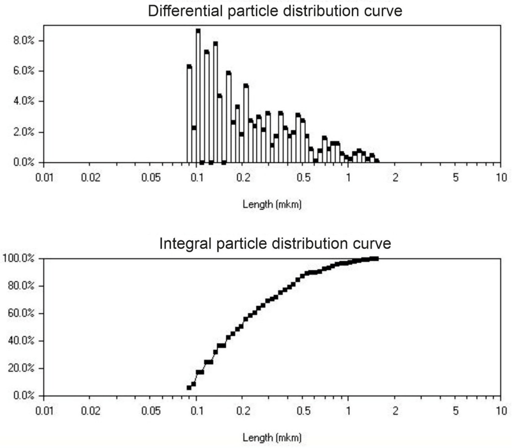

FIG. 10. Differential curve of grain distribution and integral curve of granulometric composition of $Gd_2Zr_2O_7$ ceramic material prepared by SPS at 1550 °C from MP

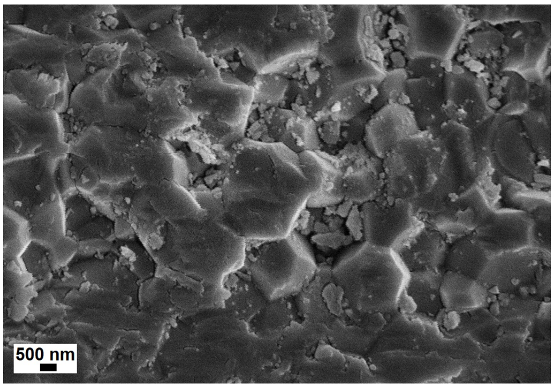

FIG. 11. SEM image of $Gd_2Zr_2O_7$ ceramic material prepared by SPS at 1550 °C from IP (magnification 10000)

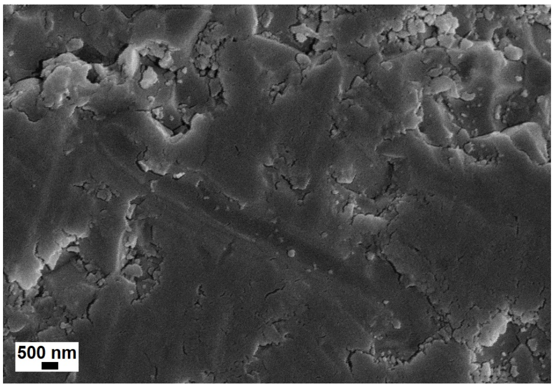

FIG. 12. SEM image of $Gd_2Zr_2O_7$ ceramic material prepared by SPS at 1550 °C from MP (magnification 10000)

remains crucial for practical applications. For instance, in functional materials like thermal barrier coatings, the production of nanocrystalline ceramics is highly important. This is because key physicochemical properties – such as thermal conductivity and heat capacity – are directly influenced by the crystallite size of the resulting ceramic material.

References

[1] Subramanian M., Aravamudan G., Subba Rao G.V. Oxide Pyrochlores – a Review. *Prog. Solid State Chem.*, 1983, **15** (2), P. 55–143.

[2] Pokhrel M., Alcoutlabi M., Mao Yu. Optical and X-ray Induced Luminescence from Eu^{3+} Doped $La_2Zr_2O_7$ Nanoparticles. *J. Alloy. Compd.*, 2017, **693**, P. 719–729.

[3] Zhang J., Guo X., Jung Ye.–G., Li L., Knapp J. Lanthanum Zirconate Based Thermal Barrier Coatings: A Review. *Surf. Coat. Technol.*, 2017, **323**, P. 1–12.

[4] Teymourinia H. Advanced Rare Earth–Based Ceramic Nanomaterials. Chapter 4 – Rare Earth Zirconate ($Re_2Zr_2O_7$) Ceramic Nanomaterials. *Elsevier Series on Advanced Ceramic Materials*, 2022, P. 77–103.

[5] Diaz-Guillen J.A., Dura O.J., Diaz-Guillen M.R., Bauer E., Lopez de la Torre M.A., Fuentes A.F. Thermophysical Properties of $Gd_2Zr_2O_7$ Powders Prepared by Mechanical Milling: Effect of Homovalent Gd^{3+} Substitution. *J. Alloys Compd.*, 2015, **649**, P. 1145–1150.

[6] Popov V.V., Menushenkov A.P., Yaroslavtsev A.A., Kulik E.S., Petrunin V.F., Korovin S.A., Zubavichus Ya.V., Trofmova N.N. Short and Long-Range Order Balance in Nanocrystalline $Gd_2Zr_2O_7$ Powders with a Fluorite-Pyrochlore Structure. *Russ. J. Inorg. Chem.*, 2014, **59**, P. 279–285.

[7] Fuentes A.F., Montemayor S.M., Maczka M., Lang M., Ewing R.C., Amador U. A Critical Review of Existing Criteria for the Prediction of Pyrochlore Formation and Stability. *Inorg. Chem.*, 2018, **57** (19), P. 12093–12105.

[8] Vassen R., Jarligo M.O., Steinke T., Mack D.E., Stöver D. Overview on Advanced Thermal Barrier Coatings. *Surf. Coat. Technol.*, 2010, **205**, P. 938–942.

[9] Feng J., Xiao B., Wan C. L., Qu Z. X., Huang Z. C., Chen J. C., Zhou R., Pan W. Electronic Structure, Mechanical Properties and Thermal Conductivity of Ln(2)Zr(2)O(7) (Ln = La, Pr, Nd, Sm, Eu and Gd) Pyrochlore. *Acta Mater.*, 2011, **59**, P. 1742–1760.

[10] Lang M., Zhang F., Zhang J., Wang J., Lian J., Weber W.J., Schuster B., Trautmann C., Neumann R., Ewing R.C. Review of A(2)B(2)O(7) Pyrochlore Response to Irradiation and Pressure. *Nucl. Instrum. Methods Phys. Res., Sect. B.*, 2010, **268**, P. 2951–2959.

[11] Duarte W., Vardelle M., Rossignol S. Effect of the Precursor Nature and Preparation Mode on the Coarsening of $La_2Zr_2O_7$ Compounds. *Ceram. Int.*, 2016, **42**, P. 1197–1209.

[12] Xu C., Wang L., Bai B., Peng L., Cai S. Rapid Synthesis of $Gd_2Zr_2O_7$ Ceramics by Flash Sintering and Its Aqueous Durability. *J. Eur. Ceram. Soc.*, 2020, **40**, P. 1620–1625.

[13] Sivakumar S., Praveen K., Shanmugavelayutham G. Preparation and Thermophysical Properties of Plasma Sprayed Lanthanum Zirconate. *Mater. Chem. Phys.*, 2018, **204**, P. 67–71.

[14] Zinatloo-Ajabshir S., Salavati-Niasari M., Sobhari A., Zinatloo-Ajabshir Z. Rare Earth Zirconate Nanostructures: Recent Development on Preparation and Photocatalytic Applications. *J. Alloys Compd.*, 2018, **767**, P. 1164–1185.

[15] Ewing R.C., Weber W.J., Lian J. Nuclear Waste Disposal-Pyrochlore ($A_2B_2O_7$): Nuclear Waste Form for the Immobilization of Plutonium and "Minor" Actinides. *J. Appl. Phys.*, 2004, **95**, P. 5949–5971.

[16] Zhou D., Mack D.E., Bakan E., Mauer G., Sebold D., Guillon O., Vaßen R. Thermal Cycling Performances of Multilayered Yttria–stabilized Zirconia/Gadolinium Zirconate Thermal Barrier Coatings. *J. Am. Ceram. Soc.*, 2020, **103**, P. 2048–2061.

[17] Brykała U., Diduszko R., Jach K., Jagielski, J. Hot pressing of gadolinium zirconate pyrochlore. *Ceram. Int.*, 2015, **41**, P. 2015–2021.

[18] Liu Z.G., Ouyang J.H., Zhou Y., Xia X.L. Electrical Conductivity of Defect Fluorite-Type $(Gd_{1-x}Yb_x)_2Zr_2O_7$ Solid Solutions. *J. Alloys Compd.*, 2010, **490**, P. 277–281.

[19] Srinivasulu K., Manisha Vidyavathy S. Effect of Different Calcination Techniques on the Morphology and Powder Flowability Characteristics of Rare-Earth Zirconates ($Re_2Zr_2O_7$; Re=La, Gd, Nd, Y) Synthesized by Solid-State High-Energy Milling Process. *J. Ceramic. Process. Res.*, 2019, **20**, P. 8–17.

[20] Keyvani A., Mahmoudinezhad P., Jahangiri A., Bahamirian M. Synthesis and Characterization of $((La_{1-x}Gd_x)_2Zr_2O_7;\ x = 0, 0.1, 0.2, 0.3, 0.4, 0.5, 1)$ Nanoparticles for Advanced TBCs. *J. Aust. Ceram. Soc.*, 2020, **56**, P. 1543–1550.

[21] Lei M., Weimin M., Xudong S., Jianan L., Lianyong J., Han S. Structure Properties and Sintering Densification of $Gd_2Zr_2O_7$ Nanoparticles Prepared via Different Acid Combustion Methods. *J. Rare Earths*, 2015, **33**, P. 195–201.

[22] Wang C., Guo L., Zhang Y., Zhao X., Ye F. Enhanced Thermal Expansion and Fracture Toughness of Sc_2O_3-doped $Gd_2Zr_2O_7$ Ceramics. *Ceram. Int.*, 2015, **41**, P. 10730–10735.

[23] Karaulov A.G., Zoz E.I., Shlyakhova T.M. Structure and Properties of Refractories Based on Zirconia Stabilized by Gadolinium Oxide. *Refract. Ind. Ceram.*, 1996, **37**, P. 83–87.

[24] Pan W., Phillpot S.R., Wan C.L., Chernatynskiy A., Qu Z.X. Low Thermal Conductivity Oxides. *Mater. Res. Bull.*, 2012, **37**, P. 917–922.

[25] Diaz-Guillen J.A., Fuentes A.F., Diaz-Guillen M.R., Almanza J.M., Santamaria J., Leon C. The Effect of Homovalent A-site Substitutions on the Ionic Conductivity of Pyrochlore-type $Gd_2Zr_2O_7$. *J. Power. Sources.*, 2009, **186**, P. 349–352.

[26] Cao X.Q., Vassen R., Stöver D. Ceramic Materials for Thermal Barrier Coatings. *J. Eur. Ceram. Soc.*, 2004, **24** (1), P. 1–10.

[27] Torres-Rodriguez J., Gutierrez-Cano V., Menelaou M., Kaštyl J., Cihlář J., Tkachenko S., González J.A., Kalmár J., Fábián I., Lázár I., Čelko L., Kaiser J. Rare-Earth Zirconate $Ln_2Zr_2O_7$ (Ln: La, Nd, Gd, and Dy) Powders, Xerogels, and Aerogels: Preparation, Structure, and Properties. *J. Inorg. Chem.*, 2019, **58** (21), P. 14467–14477.

[28] Kong S.L., Karatchevtseva I., Gregg D.J., Blackford M.G., Holmes, R., Triani, G. $Gd_2Zr_2O_7$ and $Nd_2Zr_2O_7$ Pyrochlore Prepared by Aqueous Chemical Synthesis. *J. Eur. Ceram. Soc.*, 2013, **33**, P. 3273–3285.

[29] Kaliyaperumal C., Sankarakumar A., Paramasivam T. Grain Size Effect on the Electrical Properties of Nanocrystalline $Gd_2Zr_2O_7$ Ceramics. *J. Alloys Compd.*, 2020, **813**, 152221.

[30] Li W., Zhang K., Xie D., Deng T., Luo B., Zhang H., Huang X. Characterizations of Vacuum Sintered $Gd_2Zr_2O_7$ Transparent Ceramics Using Combustion Synthesized Nanopowder. *J. Eur. Ceram. Soc.*, 2020, **40**, P. 1665–1670.

[31] Yang Y., Huang Z., Shi C., Duan J., Cheng G., Wang H., Wu D., Qi J., Lu T. Liquid-Solid-Solution Synthesis of Ultrafine $Gd_2Zr_2O_7$ Nanoparticles with Yield Enhancement. *Ceram. Int.*, 2020, **46**, P. 1216–1219.

[32] Yan C.-H., Yan Z.-G., Du Ya-P., Shen J., Zhang C., Feng W. Controlled Synthesis and Properties of Rare Earth Nanomaterials. *Handbook on the Physics and Chemistry of Rare Earths*, 2011, **41**, P. 275–472.

[33] Zinatloo-Ajabshir S., Niasari-Salavati M., Zinatloo-Ajabshir Z. $Nd_2Zr_2O_7$–Nd_2O_3 Nanocomposites: New Facile Synthesis, Characterization and Investigation of Photocatalytic Behaviour. *Mater. Lett.*, 2016, **180**, P. 27–30.

[34] Zinatloo-Ajabshir S., Niasari-Salavati M., Zinatloo-Ajabshir Z. Facile Size–Controlled Preparation of Highly Photocatalytically Active Praseodymium Zirconate Nanostructures for Degradation and Removal of Organic Pollutants. *Sep. Pur. Technol.*, 2017, **177**, P. 110–120.

[35] Sytschev A.E., Merzhanov A.G. Self-propagating high-temperature synthesis of nanomaterials. *Russ. Chem. Rev.*, 2004, **73** (2), P. 147–159.

[36] Belyakov A.V. *Methods for Obtaining Inorganic Non–metallic Nanoparticles*. RSTU n.a. D.I. Mendeleev Publishing House, Moscow, 2003, 80 p.

[37] Zhong F., Zhao J., Shi L., Xiao Y., Cai G., Zheng Y., Long J. Alkaline-earth Metals-doped Pyrochlore $Gd_2Zr_2O_7$ as Oxygen Conductors for Improved NO_2 Sensing Performance. *Sci. Rep.*, 2017, **7**, 4684.

[38] Jiang L., Wang C., Wang J., Liu F., You R., Lv S., Zeng G., Zijie Yang, He J., Liu A. Yan X., Sun P., Zheng J., Lu G. Pyrochlore Ca-doped $Gd_2Zr_2O_7$ Solid State Electrolyte Type Sensor Coupled with ZnO Sensing Electrode for Sensitive Detection of HCHO. *Sensor. Actuat. B-chem.*, 2020, **309**, 127768.

[39] Sevastyanov V.G., Simonenko E.P., Simonenko N.P., Sakharov K.A., Kuznetsov N.T. Synthesis of Finely Dispersed $La_2Zr_2O_7$, $La_2Hf_2O_7$, $Gd_2Zr_2O_7$ and $Gd_2Hf_2O_7$ Oxides. *Mendeleev Commun.*, 2013, **23**, P. 17–18.

[40] Tang Z., Huang Z., Qi J., Guo X., Han W., Zhou M., Penga S., Lu T. Synthesis and Characterization of $Gd_2Zr_2O_7$ Defect-fluorite Oxide Nanoparticles via a Homogeneous Precipitation-solvothermal Method. *RSC Adv.*, 2017, **7**, P. 54980–54985.

[41] Liu S., Jiang K., Zhang H., Liu Y., Zhang L., Su B., Liu Y. Nano-nano Composite Powders of Lanthanum-gadolinium Zirconate and Gadolinia-stabilized Zirconia Prepared by Spray Pyrolysis. *Surf. Coat. Technol.*, 2013, **232**, P. 419–424.

[42] Wei X., Back C., Izhvanov O., Khasanov O.L., Haines C.D., Olevsky E.A. Spark Plasma Sintering of Commercial Zirconium Carbide Powders: Densification Behavior and Mechanical Properties. *Materials.*, 2015, **8** (9), P. 6043–6061.

[43] Yurlova M.S., Demenyuk V.D., Lebedeva L.Y., Dudina D.V., Grigoryev E.G., Olevsky E.A. Electric Pulse Consolidation: An Alternative to Spark Plasma Sintering. *J. Mater. Sci.*, 2014, **49**, P. 952–985.

[44] Maslennikov D.V., Matvienko A.A., Sidelnikov A.A., Dudina D.V., Esikov M.A., Belosludov R.V., Kato H. Effect of the Synthesis Conditions of $Ce_{0.9}Gd_{0.1}O_{1.95}$ Powder on its Morphology and Characteristics of the Oxygen Ion-conducting Ceramics Obtained by Spark Plasma Sintering. *Ceram. Int.*, 2021, **47** (2), P. 2557–2564.

[45] Papynov E.K., Shichalin O.O., Mayorov V.Yu., Tkachenko I.A., Golub A.V., Tananaev I.G., Avramenko V.A. Spark Plasma Sintering as Prospective Solution for Fabrication of the Functional Nanostructured Ceramics. *FEB RAS Bull.*, 2016, **6** (190), P. 15–30.

[46] Sorokin O.Yu., Solntsev S.S., Evdokimov S.A., Osin I.V. Hybrid Spark Plasma Sintering Method: Principle, Posiibilities, Future Prospects. *AMIT*, 2014, **S6**, P. 11–16.

[47] Kalinkin A.M., Vinogradov V.Yu., Kalinkina E.V., Nevedomskii V.N. Preparation of nanocrystalline $Gd_2Zr_2O_7$ from mechanically activated coprecipitated precursor. *Chem. Pap.*, 2020, **74**, P. 1161–1170.

[48] Terlan B., Levin A.A., Börrnert F., Simon F., Oschatz M., Schmidt M., Cardoso-Gil R., Lorenz T., Baburin I.A., Joswig J.-O., Eychmüller A. Effect of Surface Properties on the Microstructure, Thermal, and Colloidal Stability of VB_2 Nanoparticles. *Chem. Mater.*, 2015, **27**, P. 5106–5115.

[49] Terlan B., Levin A.A., Börrnert F., Zeisner J., Kataev V., Schmidt M., Eychmüller A. A Size-Dependent Analysis of the Structural, Surface, Colloidal, and Thermal Properties of $Ti_{1--x}B_2$ ($x = 0.03$–0.08) Nanoparticles. *Eur. J. Inorg. Chem.*, 2016, **6**, P. 3460–3468.

[50] Klee W.E., Weitz G. Infrared spectra of ordered and disordered pyrochlore-type compounds in the series $RE_2Ti_2O_7$, $RE_2Zr_2O_7$ and $RE_2Hf_2O_7$. *J. Inorg. Nucl. Chem.*, 1969, **31** (8), P. 2367–2372.

[51] Sanjay Kumar N.R., Chandra Shekar N.V., Sahu P.C. Pressure Induced Structural Transformation of Pyrochlore $Gd_2Zr_2O_7$. *Solid State Commun.*, 2008, **147** (9–10), P. 357–359.

[52] Oliver W.C., Pharr G.M. Measurement of Hardness and Elastic Modulus by Instrumented Indentation: Advances in Understanding and Refinements to Methodology. *J. Mater. Res.*, 2004, **19** (1), P. 3–20.

[53] Useinov A.S. A Nanoindentation Method for Measuring the Young Modulus of Superhard Materials Using a NanoScan Scanning Probe. *Instrum. Exp. Tech.*, 2004, **47** (1),P. 119–123.

[54] Maslenikov I.I., Reshetov V.N., Useinov A.S. Mapping the Elastic Modulus of a Surface with a NanoScan 3D Scanning Microscope. *Instrum. Exp. Tech.*, 2015, **58**, 711.

[55] Malygin G.A Plasticity and Strength of Micro- and Nanocrystalline Materials. *Phys. Solid State*., 2007, **49** (6), P. 1013–1033.

[56] Huang Z., Cao Z., Shi K., Qi J., Zhou M., Tang Z., Han W., Diao X., Tang J., Lu T. Synthesis and Densification of $Gd_2Zr_2O_7$ Nanograin Ceramics Prepared by Field Assisted Sintering Technique. *J. Nucl. Mater.*, 2017, **495**, P. 164–171.

[57] Tuncer R., Karabaş M., Gökçe H., Kayali Y. Effect of Yb, Fe and Mo, Ti Co-doping on Thermal and Mechanical Properties of $Gd_2Zr_2O_7$ ceramics. *Ceram. Int.*, 2025, **51** (19), P. 28678–28688.

[58] Zhao M., Ren X., Pan W. Mechanical and Thermal Properties of Simultaneously Substituted Pyrochlore Compounds $(Ca_2Nb_2O_7)_x(Gd_2Zr_2O_7)_{1-x}$. *J. Eur. Ceram. Soc.*, 2015, **35** (3), P. 1055–1061.

Submitted 18 July 2025; revised 11 November 2025; accepted 4 March 2026

Information about the authors:

Vladimir Yu. Vinogradov – Tananaev Institute of Chemistry and Technology of Rare Elements and Mineral Raw Materials of the Kola Science Centre of the Russian Academy of Sciences, Akademgorodok, 26a, Apatity, 184209, Russia; ORCID 0000–0002–3335–5778; v.vinogradov@ksc.ru

Dina V. Dudina – Lavrentyev Institute of Hydrodynamics of the Siberian Branch of the Russian Academy of Sciences, Academician Lavrentyev Av., 15, Novosibirsk, 630090, Russia; ORCID 0000–0003–0010–4638; ddudina@hydro.nsc.ru

Maksim A. Esikov – Lavrentyev Institute of Hydrodynamics of the Siberian Branch of the Russian Academy of Sciences, Academician Lavrentyev Av., 15, Novosibirsk, 630090, Russia; ORCID 0000–0002–4845–148X; esmax@ya.ru

Olga B. Shcherbina – Tananaev Institute of Chemistry and Technology of Rare Elements and Mineral Raw Materials of the Kola Science Centre of the Russian Academy of Sciences, Akademgorodok, 26a, Apatity, 184209, Russia; ORCID 0000–0001–9591–0274; o.shcherbina@ksc.ru

Vadim V. Efremov – Institute of North Industrial Ecology Problems of the Kola Science Centre of the Russian Academy of Sciences, Akademgorodok, 14a, Apatity, 184209, Russia; ORCID 0000–0003–2407–7304; v.efremov@ksc.ru

Alexander M. Kalinkin – Tananaev Institute of Chemistry and Technology of Rare Elements and Mineral Raw Materials of the Kola Science Centre of the Russian Academy of Sciences, Akademgorodok, 26a, Apatity, 184209, Russia; ORCID 0000–0002–3668–8578; a.kalinkin@ksc.ru

Conflict of interest: the authors declare no conflict of interest.

NANOSYSTEMS:
PHYSICS, CHEMISTRY, MATHEMATICS

Original article

Kozlova T.O., et al. *Nanosystems: Phys. Chem. Math.*, 2026, **17** (2), 228–235.
http://nanojournal.ifmo.ru
DOI 10.17586/2220-8054-2026-17-2-228-235

Redox behaviour of nanoscale $ACe_2(PO_4)_3$ (A = NH_4^+, K^+, Rb^+) double ceric phosphates

Taisiya O. Kozlova[1,a], Madina M. Sozarukova[1,b], Daniil A. Kozlov[1,c], Ekaterina D. Sheichenko[1,2,d], Anzhelika O. Bedarkova[1,e], Darya N. Vasilyeva[1,2,f], Alexander E. Baranchikov[1,g], Vladimir K. Ivanov[1,h]

[1]Kurnakov Institute of General and Inorganic Chemistry of the Russian Academy of Sciences, Leninsky prospect, 31, Moscow, 119991, Russia
[2]HSE University, Moscow, Myasnitskaya str., 20, 101000, Russia

[a]taisiya@igic.ras.ru, [b]s_madinam@bk.ru, [c]kozlov@igic.ras.ru, [d]edsheychenko@edu.hse.ru,
[e]a.bedarkova@igic.ras.ru, [f]dnvasileva_1@edu.hse.ru, [g]a.baranchikov@yandex.ru, [h]van@igic.ras.ru

Corresponding author: T. O. Kozlova, taisiya@igic.ras.ru

PACS 61.66.Fn; 68.65.-k; 81.70.-q; 82.39.-k

ABSTRACT A comparative study of the redox behaviour of nanocrystalline isostructural $ACe_2(PO_4)_3$ (A = NH_4^+, K^+, Rb^+) double ceric phosphates was performed. It has been established that with respect to alkylperoxyl radicals or hydrogen peroxide as reactive oxygen species, all the double ceric phosphates acted as antioxidants or prooxidants, respectively. The antioxidant activity towards alkylperoxyl radicals was found to be the higher for the phosphates containing potassium or rubidium. Notably, for $KCe_2(PO_4)_3$ and $RbCe_2(PO_4)_3$ an inverse dependence of catalytic activity on concentration in the reaction with H_2O_2 was found, in contrast to $NH_4Ce_2(PO_4)_3$. The redox behaviour of nanoscale cerium dioxide used for comparison was similar to that of ammonium ceric phosphate, but significantly lower in absolute values. This was explained by the suppressive effect of phosphate anions presented in the buffer solutions.

KEYWORDS radical-scavenging ability; prooxidant activity; chemiluminescence; isostructurality.

ACKNOWLEDGEMENTS This work was supported by Russian Science Foundation (Grant no. 23-73-10088, https://rscf.ru/en/project/23-73-10088/) using the equipment of the JRC PMR IGIC RAS.

FOR CITATION Kozlova T.O., Sozarukova M.M., Kozlov D.A., Sheichenko E.D., Bedarkova A.O., Vasilyeva D.N., Baranchikov A.E., Ivanov V.K. Redox behaviour of nanoscale $ACe_2(PO_4)_3$ (A = NH_4^+, K^+, Rb^+) double ceric phosphates. *Nanosystems: Phys. Chem. Math.*, 2026, **17** (2), 228–235.

---

1. Introduction

Inorganic phosphates comprise both natural and synthetic compounds. They exist in the form of minerals [1], constitute the basis of mammalian bone tissue [2], and are utilized as luminophores [3], ceramics [4,5], ionic conductors [6], etc. Nowadays, over 200 structural types of inorganic phosphates are known [7]. This crystallochemical diversity arises from a large number of cations that can bind with phosphate tetrahedra in different ways, as well as the ability to substitute or incorporate other anions and molecules (such as H_2O) into the structure [8].

Several studies have been devoted to investigating the influence of cation composition on the functional properties of isostructural compounds [9–13], including inorganic phosphates. In particular, Gautier et al. [14] demonstrated an increase in the second harmonic generation response values for compounds with the composition $A(VO_2)_2(PO_4)\cdot 3H_2O$ (where A = Rb^+, NH_4^+ and K^+). Zhen et al. [15] found the different thermal expansion behavior of isostructural $AZr_2(PO_4)_3$, A = Na^+, K^+, Rb^+, Cs^+. In a similar series, Sukhanov et al. [16] observed a decrease in catalytic activity for methanol dehydration in the order $NaZr_2(PO_4)_3 > KZr_2(PO_4)_3 > CsZr_2(PO_4)_3 \gg RbZr_2(PO_4)_3$. Patkare et al. [17] evaluated the adsorption capacity for uranyl ions from aqueous solutions for a series of isostructural double thorium phosphates, finding the following trend: $RbTh_2(PO_4)_3 < CsTh_2(PO_4)_3 < KTh_2(PO_4)_3$.

Despite the extensive knowledge of compounds with the general formula $AM_2^{IV}(PO_4)_3$ (where A = Li–Cs and M = Ti, Zr, Hf or Th, U, Np, Pu), it has not been possible until recently to establish similar composition–structure–property relationships for the M = Ce^{IV} series. This limitation existed due to a lack of information on even one complete structural series of double ceric phosphates. Only in 2025 were the data on the synthesis of $RbCe_2(PO_4)_3$ [18] reported; this compound turned out to be isostructural with two previously known analogues, $NH_4Ce_2(PO_4)_3$ [19] and $KCe_2(PO_4)_3$ [20].

It is known that ceric compounds, primarily nanocrystalline CeO_2, can act as efficient inorganic nanozymes [21–23]. At the same time, cerium(IV) phosphates, owing to their biocompatibility and expected stability in biological environments [24], are equally important to investigate with regard to their biological behavior. So, this study presents the first comparative analysis of the radical-scavenging ability and redox activity of nanoscale isostructural ceric phosphates with the composition $ACe_2(PO_4)_3$ (A = NH_4^+, K^+, Rb^+).

2. Experimental Section

The following materials were used as received, without further purification: $Ce(NO_3)_2\cdot 6H_2O$ (pure grade, Lanhit Russia), potassium hydroxide (pure grade, Sigma Aldrich), rubidium hydroxide (pure grade, Novosibirsk Rare Metals Plant, Russia), aqueous ammonia (25 wt.%, extra-pure grade, Khimmed Russia), phosphoric acid (85 wt.% aq, extra-pure grade, Komponent-Reaktiv, Russia), isopropanol (extra-pure grade, Khimmed Russia), 2,2′-azobis(2-amidinopropane) dihydrochloride (Sigma, #440914), luminol (Sigma, #123072), hydrogen peroxide (extra-pure grade, Khimmed Russia), distilled water.

Previously, using $NH_4Ce_2(PO_4)_3$ and $KCe_2(PO_4)_3$ [25], we developed a synthetic approach to obtain these compounds in a nanoscale state. In the present study, we have accordingly adapted this method to synthesize $RbCe_2^{IV}(PO_4)_3$. First, nanocrystalline (4–5 nm) cerium dioxide (0.100 g) obtained by precipitation from $Ce(NO_3)_3$ aqueous solution was dissolved in concentrated phosphoric acid (5 ml) at 80°C. The cooled solution was placed into an ultrasonic bath Bandelin Sonorex Longlife RK 1050 for 30 min, and then mixed with 35 ml of 1 M KOH, NH_4OH or RbOH aqueous solutions. The obtained gels ($\sim$40 mL) were sonicated using Bandelin Sonopuls HD 3200 homogenizer equipped with titanium horn (TT-13 titanium tip) operated at 20 kHz (amplitude 20%) for 1 h. The resulting suspensions were placed in 100 ml Teflon autoclaves and treated under hydrothermal-microwave (HTMW) conditions at 180°C for 1 h. After cooling the autoclaves, the precipitates were repeatedly washed using distilled water and dried at 60°C in air.

Powder X-ray diffraction (PXRD) patterns were acquired with a DX-2700BH (Haoyuan, China) diffractometer, using Cu $K_{\alpha 1,2}$ radiation in the 2θ range of 5°–80° with 0.02° 2θ steps and a counting time of no less than 1 s per step. The full-profile analysis of diffraction patterns was performed using the Rietveld method realized in the MAUD software (version 2.99) [26]. The diffraction peak profiles were fitted using a pseudo-Voigt function. The sizes of coherent scattering domains (crystallite sizes) and particle anisotropy were estimated using the Lorentzian component of peak broadening and the approach proposed by Popa [27]. For all samples, the crystallite sizes along the (001) direction and in the perpendicular direction were calculated.

Scanning electron microscopy (SEM) images were obtained using an Amber GMH (Tescan, Czech Republic) microscope operated at an accelerating voltage of 5 kV using a secondary electron (Everhart–Thornley) detector. Energy-dispersive X-ray spectroscopy (EDX) was performed using an Ultim Max 100 (Oxford Instruments, UK) detector at an accelerating voltage of 20 kV. Particle size was determined from SEM data using Gwyddion software. To account for anisotropy, the dimensions of each particle were measured in two perpendicular directions. The particle sizes were fitted by a lognormal distribution function.

Analysis of double ceric phosphates redox behaviour in relation to alkylperoxyl radicals or hydrogen peroxide was conducted by chemiluminescent method [28]. Nanocrystalline cerium dioxide powder which was used for the synthesis of double ceric phosphates (see above) was analysed as a control. Directly before the measurements, suspensions of the materials under study were prepared with a concentration of 0.01 M. For this purpose, the powders were dispersed in 5 ml of deionized water and sonicated for 10 min.

Alkylperoxyl radicals were generated by the thermal decomposition of 2,2′-azobis(2-amidinopropane) dihydrochloride (AAPH). For this, 2.5 μM AAPH and 2.0 μM luminol were added to a cuvette containing 100 mM phosphate buffer solution (pH 7.4, 37°C). In experiments with H_2O_2, a reaction mixture of phosphate buffer (100 mM, pH 7.4), hydrogen peroxide (10 mM) and luminol (50 μM) was used. The baseline chemiluminescence signal was monitored for 60–90 s. Upon stabilization of the chemiluminescent signal, the aliquot of ceric phosphate or ceria aqueous dispersion was added.

Detection of the chemiluminescence signal was carried out using a DISoft (Russia) Lum-1200 instrument equipped with 12 detection channels. The experiments were performed with three replicates for each sample. The results were processed using PowerGraph software (version 3.3).

3. Results and discussion

The isostructural nature of the compounds obtained was confirmed by X-ray phase analysis (Fig. 1). The calculated unit cell parameters for the synthesised double ceric phosphates are given in Table 1 and agree well with previously reported data [18–20]. From the data presented in Table 1 it follows that an increase in the cation size ($K^+ < NH_4^+ < Rb^+$ [14, 29, 30]) results in the expansion of the volumes of the corresponding unit cells due to the increase in the a and b parameter values. The crystallite sizes calculated in two crystallographic directions were found to be less than 100 nm (Table 1), with the smallest value for the $RbCe_2(PO_4)_3$ phase, and the largest for the $NH_4Ce_2(PO_4)_3$ phase. Scanning electron microscopy images confirm particle anisotropy, and the particle sizes were found to be close to the XRD data (Fig. 2). The chemical composition was confirmed by EDX analysis.

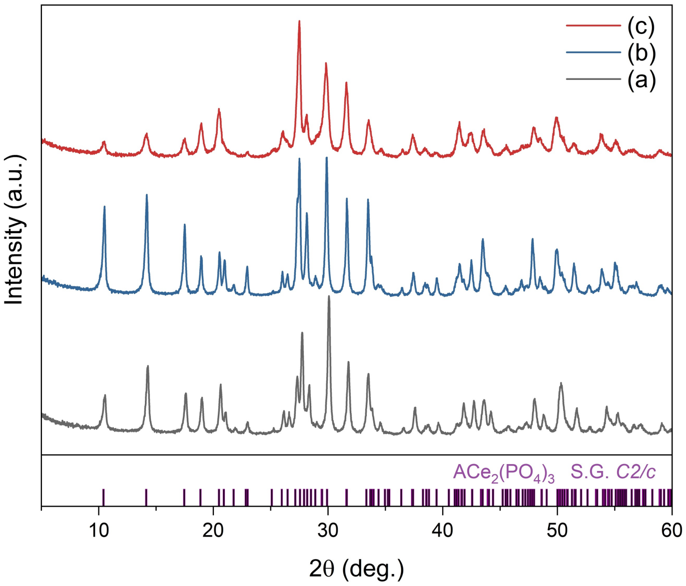

FIG. 1. Powder X-ray diffraction patterns of the products of HTMW treatment of ceric phosphate gels formed upon the addition of 1 M KOH (a), NH_4OH (b) or RbOH (c) aqueous solutions to ceric phosphate solutions. The corresponding Bragg peak positions for $ACe_2(PO_4)_3$ (A = NH_4^+, K^+, Rb^+) are shown below

TABLE 1. Structural parameters and crystallite sizes for the products of HTMW treatment of ceric phosphate gels formed upon the addition of 1 M KOH, NH_4OH or RbOH to ceric phosphate solutions

Sample	KCeP	NCeP	RbCeP
Precipitating agent	1 M KOH aqueous solution	1 M NH_4OH aqueous solution	1 M RbOH aqueous solution
Phase composition	$KCe_2(PO_4)_3$	$NH_4Ce_2(PO_4)_3$	$RbCe_2(PO_4)_3$
Lattice parameters	S.G. *C2/c* $a = 17.3764(8)$ Å $b = 6.7316(3)$ Å $c = 7.9700(4)$ Å $\beta = 102.292(3)°$	S.G. *C2/c* $a = 17.4749(7)$ Å $b = 6.7711(3)$ Å $c = 7.9988(3)$ Å $\beta = 102.794(3)°$	S.G. *C2/c* $a = 17.502(1)$ Å $b = 6.7804(6)$ Å $c = 7.9867(7)$ Å $\beta = 102.847(5)°$
Crystallite size, nm	$\langle D\rangle_{001} = 60 \pm 3$ $\langle D\rangle_{110} = 70 \pm 3$	$\langle D\rangle_{001} = 110 \pm 5$ $\langle D\rangle_{110} = 78 \pm 2$	$\langle D\rangle_{001} = 28 \pm 2$ $\langle D\rangle_{110} = 36 \pm 3$

The redox behaviour of the synthesized isostructural compounds was evaluated in model systems. Experiments were based on monitoring the chemiluminescence intensity from the oxidation of luminol by alkylperoxyl radicals (ROO•) or hydrogen peroxide decomposition products.

In the first assay, introducing the samples into a reaction solution resulted in a decrease in luminol-dependent chemiluminescence compared to the control (Fig. 3). The degree of chemiluminescence inhibition varied among the samples, reflecting their different radical-scavenging capacities (Fig. 3a). Overall, the observed kinetic profiles are characteristic of long-acting antioxidants that scavenge free radicals at a relatively low rate [31].

To quantitatively evaluate the radical-scavenging properties of the nanoscale $NH_4Ce_2(PO_4)_3$, $KCe_2(PO_4)_3$ and $RbCe_2(PO_4)_3$ samples, the areas of the luminescence suppression region (S_{CL}, a.u.) were calculated. This parameter is proportional to the number of the scavenged radicals and reflects the antioxidant capacity of a material (Fig. 3b).The $KCe_2(PO_4)_3$ and $RbCe_2(PO_4)_3$ samples showed the most pronounced antioxidant activity against organic radicals compared to the ammonium-containing analogue. This difference is likely attributable to the smaller particle size of the potassium and rubidium ceric phosphates, which leads to a higher concentration of surface-active sites (e.g., Ce^{3+}/Ce^{4+}

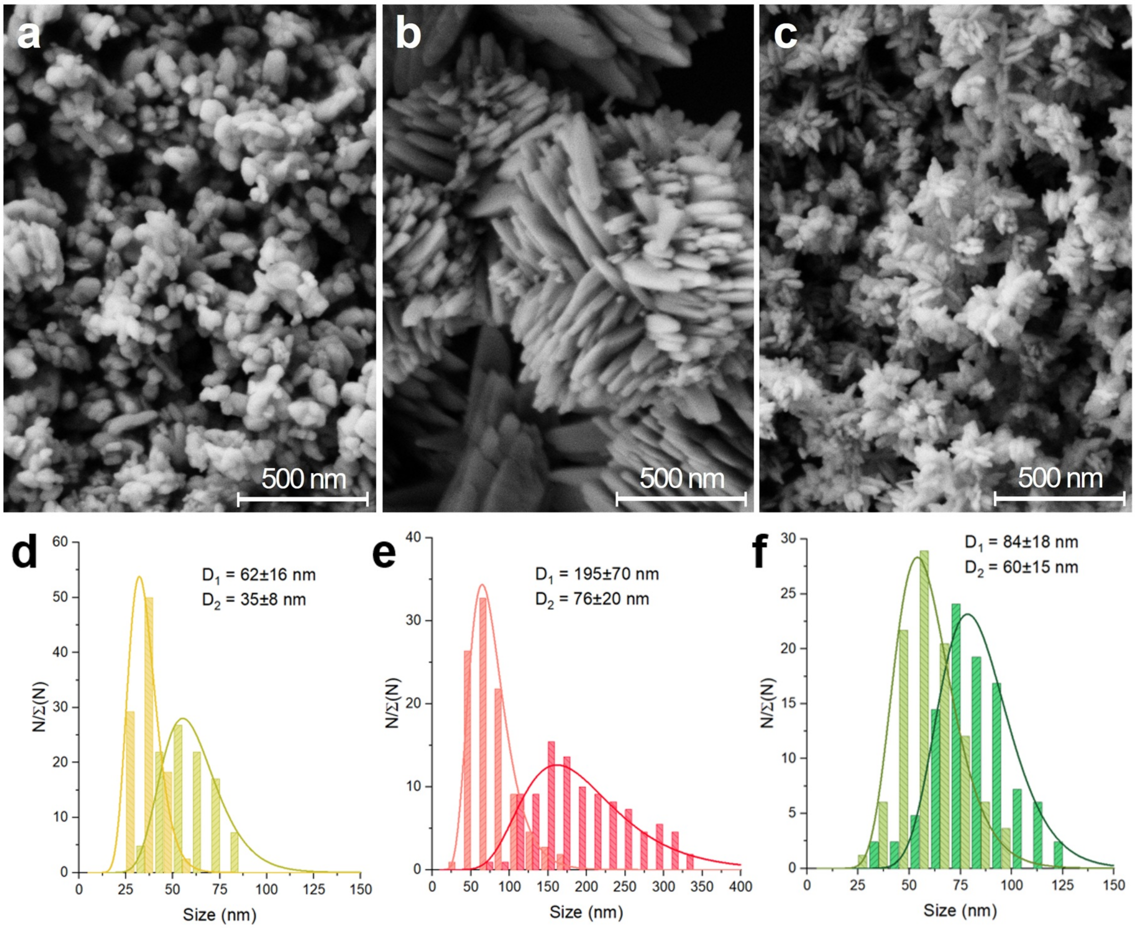

FIG. 2. SEM images and corresponding particle size distribution of KCeP (a,d), NCeP (b,e), RbCeP (c,f)

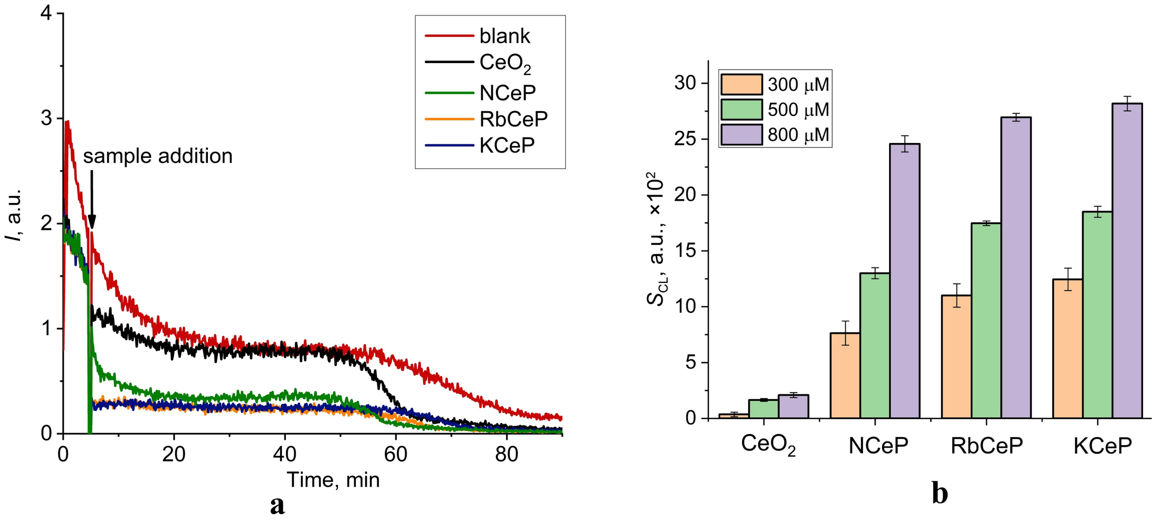

FIG. 3. a) Chemiluminograms characterising the radical-scavenging properties of CeO_2, $NH_4Ce_2(PO_4)_3$, $KCe_2(PO_4)_3$ and $RbCe_2(PO_4)_3$ (800 μM); b) histograms of chemiluminescence suppression (S_{CL}, a.u.) for ceric samples

ratio, oxygen vacancies and hydroxyl groups) [32–35] available for interaction with the components of the studied mixture, including free radicals. Nanocrystalline cerium dioxide (4–5 nm) demonstrated the weakest antioxidant effect, in contrast to the ceric phosphate suspensions. Since chemiluminescence was recorded under physiologically relevant conditions (100 mM PBS, pH 7.4), this result aligns with literature reports on the inhibitory effect of phosphate ions on CeO_2 activity. Inorganic phosphates and phosphate-containing molecules, which are abundant in biological environments, are known to adsorb onto the surface of ceria nanoparticles and significantly suppress their catalytic properties [36–38].

Fig. 4 shows chemiluminograms obtained by adding suspensions of double ceric phosphates or cerium dioxide to a reaction mixture containing H_2O_2 and luminol (pH 7.4, phosphate buffer solution).

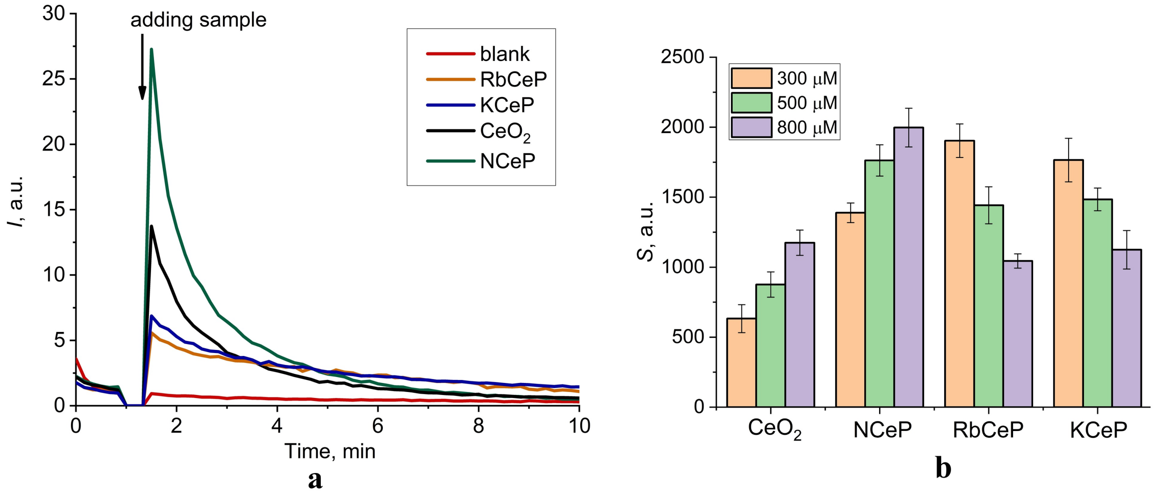

FIG. 4. a) Chemiluminograms characterising prooxidant activity of the of CeO_2, $NH_4Ce_2(PO_4)_3$, $KCe_2(PO_4)_3$ and $RbCe_2(PO_4)_3$ (800 μM); b) light sums (*S*) as a function of ceric samples concentrations

Upon addition of the studied samples, a sharp, exponentially decaying increase in luminol-dependent chemiluminescence was observed (Fig. 4a). This luminescence burst, caused by the generation of reactive oxygen species (ROS), indicates the prooxidant properties of the compounds, consistent with data reported for other ceria-based nanomaterials [39, 40]. Notably, the samples exhibit two distinct types of chemiluminescence kinetics: CeO_2 and $NH_4Ce_2(PO_4)_3$ show a sharp exponential decay whereas $RbCe_2(PO_4)_3$ and $KCe_2(PO_4)_3$ produce flatter curves. The flatter profiles for the rubidium and potassium ceric phosphates likely result from their lower reaction rate with hydrogen peroxide compared to CeO_2 and $NH_4Ce_2(PO_4)_3$.

For the quantitative assessment of prooxidant properties, we used the integral area under the chemiluminescence curve (*S*) over a selected 5-minute period. This value is proportional to the amount of ROS generated. The data in Fig. 4b show a dose-dependent increase in chemiluminescence for CeO_2 and $NH_4Ce_2(PO_4)_3$ nanoparticles. In contrast, the $RbCe_2(PO_4)_3$ and $KCe_2(PO_4)_3$ samples exhibited a decrease in prooxidant activity with increasing suspensions concentration. This inverse relationship between prooxidant activity and nanoparticle concentration is unusual. The most probable reasons for this behavior, found in isolated examples from the literature, include the aggregation of nanoparticles, leading to a decrease in the number of available surface-active sites [41], or ROS scavenging at high concentrations of compounds [42–44]. The first explanation is unlikely, as such a reversible concentration-dependent relationship was not observed in experiments with alkylperoxyl radicals. Therefore, we hypothesize that for potassium and rubidium ceric phosphates, an increase in concentration promotes the scavenging of reactive oxygen species, which competes with the decomposition of H_2O_2.

Thus, using two model systems, we have demonstrated for the first time the difference in redox behavior between $NH_4Ce_2(PO_4)_3$ and its isostructural potassium or rubidium analogues. Although the precise reasons for their different redox activities cannot yet be definitively established, they are likely related to the cation type (NH_4^+ or K^+, Rb^+) [45,46]. Several studies have demonstrated differences in the physicochemical properties of isostructural compounds containing ammonium or alkali metal cations. For instance, it was shown that $NH_4Zn_2BO_3Cl_2$ exhibits superior nonlinear optical properties compared to its $KZn_2BO_3Cl_2$ or $RbZn_2BO_3Cl_2$ analogues, attributed to a higher interlayer binding energy [47]. In another study, Johnson [48] calculated the solubility of ammonium perrhenate (H_4ReO_4) to be considerably greater than that of the potassium and rubidium salts (0.274, 0.0410, and 0.037 mol/kg, respectively). It is also necessary to pay attention to the different thermal behavior of $NH_4Ce_2(PO_4)_3$ compared to $KCe_2(PO_4)_3$ and $RbCe_2(PO_4)_3$. Thus, during the thermolysis of $NH_4Ce_2(PO_4)_3$, only $CePO_4$ formation and NO release were observed, presumably due to the oxidation of ammonia by redox active species, such as ceric cations [19]. In contrast, the thermolysis of the potassium and rubidium analogues leads to the crystallization of monazite ($CePO_4$) alongside KPO_3 [20] or $RbPO_3$ [18] polyphosphates, respectively.

The results obtained in this study indicate that nanocrystalline double ceric phosphates $ACe_2(PO_4)_3$ ($A = NH_4^+, K^+, Rb^+$) exhibit dual concentration-dependent antioxidant/prooxidant behaviour. These findings provide a starting point for further in-depth study of ceric phosphates redox activity, which could contribute to developing new approaches for preventing and treating diseases associated with oxidative stress [49, 50].

4. Conclusions

This study represents the first comparative analysis of the redox activity of isostructural double ceric phosphates, containing a monovalent cation. Compounds with the general composition $ACe_2^{IV}(PO_4)_3$ ($A = NH_4^+, K^+, Rb^+$) and particle sizes less than 100 nm were successfully synthesized under hydrothermal-microwave treatment. Chemiluminescence analysis using two model test systems demonstrated that the nature of the second cation in the studied ceric phosphates significantly influences their redox properties. Specifically, suppression of chemiluminescence induced by alkylperoxyl radicals was found to be more pronounced for potassium and rubidium ceric phosphates than for their ammonium counterpart. A qualitative difference in the behavior of the studied compounds was observed in the chemiluminescent reaction of H_2O_2 catalytic decomposition. Thus, $NH_4Ce_2(PO_4)_3$ demonstrated an increase in prooxidant activity with concentration growth, while $KCe_2(PO_4)_3$ and $RbCe_2(PO_4)_3$ showed an unusual inverse dose-response relationship. These results highlight the important role of the cation composition in modulating the biochemical properties of cerium-containing nanomaterials, expanding the potential for their use as controlled pro-/antioxidant agents.

References

[1] Achary S.N., Bevara S., Tyagi A.K. Recent Progress on Synthesis and Structural Aspects of Rare-Earth Phosphates. *Coord. Chem. Rev.*, 2017, **340**, P. 266–297.

[2] Lukaviciute L., Ganceviciene R., Tsuru K., Ishikawa K., Yang J.-C., Grigoraviciute I., Kareiva A. Cationic Substitution Effects in Phosphate-Based Bioceramics – A Way towards Superior Bioproperties. *Ceram. Int.*, 2024, **50**, P. 34479–34509.

[3] Peter A.M., Kailasnath M. Perspectives of Low Dimensional Luminescent Rare Earth Phosphates: Applications and Challenges. In *Low-Dimensional Materials, Systems and Applications*, Volume 1, Elsevier, 2026, P. 443–478.

[4] Clavier N., Podor R., Dacheux N. Crystal Chemistry of the Monazite Structure. *J. Eur. Ceram. Soc.*, 2011, **31**, P. 941–976.

[5] Neumeier S., Arinicheva Y., Ji Y., Heuser J.M., Kowalski P.M., Kegler P., Schlenz H., Bosbach Di. Deissmann G. New Insights into Phosphate Based Materials for the Immobilisation of Actinides. *Radiochim. Acta*, 2017, **105**, P. 961–984.

[6] Chiang S.-J., Kaduk J.A., Shaw L.L. High Ionic Conducting NaSICON Enabled by Mechanical Activation Enhanced Reaction. *Mater. Chem. Phys.*, 2024, **312**, P. 128656.

[7] Ameen S., Shaheer Akhtar M. Introductory Chapter: An Overview of Phosphate Mineral and Electrochemical Detection of Phosphate for Environmental Remediation. In *Functional Phosphate Materials and Their Applications*, IntechOpen, 2023.

[8] Attfield J.P. Phosphates: Solid-State Chemistry. In *Encyclopedia of Inorganic and Bioinorganic Chemistry*, Wiley, 2004, P. 1–16.

[9] Pet'kov V.I., Shipilov A.S., Sukhanov M. V. Thermal Expansion of $MZr_2(AsO_4)_3$ and $MZr_2(TO_4)_x(PO_4)_{3-x}$ (M = Li, Na, K, Rb, Cs; T = As, V). *Inorg. Mater.*, 2015, **51**, P. 1079–1085.

[10] Huang H., Kong X., Zhao H., Ye N., Hu Z., Li C. A-Site Cation Substitution toward Structural Transformation in Phosphates Exhibiting Short UV Transparency and Second Harmonic Response. *Inorg. Chem.*, 2025, **64**, P. 17083–17090.

[11] Ermilova M.M., Sukhanov M.V., Borisov R.S., Orekhova N.V., Pet'kov V.I. Novikova S.A., Il'in A.B., Yaroslavtsev A.B. Synthesis of the New Framework Phosphates and Their Catalytic Activity in Ethanol Conversion into Hydrocarbons. *Catal. Today*, 2012, **193**, P. 37–41.

[12] Slobodin V., Surat L.L., Zubkov V.G., Tyutyunnik A.P., Berger I.F., Kuznetsov M.V., Perelyaeva L.A., Shein I.R., Ivanovskii A.L., Shulgin B.V., Solomonov V. I., Svensson G., Forslund B., Sayagués M. J. Structural, Luminescence, and Electronic Properties of the Alkaline Metal-Strontium Cyclotetravanadates $M_2Sr(VO_3)_4$, (M=Na, K, Rb, Cs). *Phys. Rev. B*, 2005, **72**, P. 155205.

[13] Wen M., Wu H., Wu X. Influence of Cation on the Anion Frameworks and Properties of Four Lead Phosphates, $A_2PbBi_2(PO_4)_2(P_2O_7)$ (A = Rb, Cs) and $A_2PbP_2O_7$ (A = K, Rb). *Inorg. Chem.*, 2020, **59**, P. 2945–2951.

[14] Gautier R., Auguste S., Clevers S., Dupray V., Coquerel G., Le Fur E. Influence of the Cation Size on the Second Harmonic Generation Response of Chiral $A(VO_2)_2(PO_4)\cdot 3H_2O$ ($A = K^+$, $NH_4{}^+$ and Rb^+). *CrystEngComm*, 2014, **16**, P. 10902–10906.

[15] Zhen X., Sanson A., Sun Q., Liang E., Gao Q. Role of Alkali Ions in the Near-Zero Thermal Expansion of NaSICON-Type $AZr_2(PO_4)_3$ (A=Na, K, Rb, Cs) and $Zr_2(PO_4)_3$ Compounds. *Phys. Rev. B*, 2023, **108**, P. 144102.

[16] Sukhanov M.V., Ermilova M.M., Orekhova N.V., Pet'kov V.I., Tereshchenko G.F. Catalytic Properties of Zirconium Phosphate and Double Phosphates of Zirconium and Alkali Metals with a $NaZr_2(PO_4)_3$ Structure. *Russ. J. Appl. Chem.*, 2006, **79**, P. 614–618.

[17] Patkare G., Shafeeq M., Sengupta A., Keskar M., Phatak R., Kannan S. Investigation of the Thermal Properties of Alkali Metal Thorium Phosphates and Their Application for the Sorption of Uranyl Ion from Acidic Medium. *Eur. J. Inorg. Chem.*, 2023, **26**, P. 202300140.

[18] Vasilyeva D.N., Kozlov D.A., Protsenko M.R., Simonenko N.P., Kozlova T.O. Ivanov V.K. Structure and Thermal Behavior of Novel Double Ceric Phosphates $RbCe_2(PO_4)_3$and $Rb_2Ce(PO_4)_2 \cdot xH_2O$. *Russ. J. Inorg. Chem.*, 2025, **70**, P. 943–951.

[19] Shekunova T.O., Istomin S.Y., Mironov A. V., Baranchikov A.E., Yapryntsev A.D., Galstyan A.A., Simonenko N.P., Gippius A.A., Zhurenko S.V., Shatalova T.B., et al. Crystallization Pathways of Cerium(IV) Phosphates Under Hydrothermal Conditions: A Search for New Phases with a Tunnel Structure. *Eur. J. Inorg. Chem.*, 2019, **2019**, P. 3242–3248.

[20] Kozlova T.O., Vasilyeva D.N., Kozlov D.A., Teplonogova M.A., Baranchikov A.E., Simonenko N.P., Ivanov V.K. Synthesis and Thermal Behavior of $KCe_2(PO_4)_3$, a New Full-Member in the $A^IM^{IV}{}_2(PO_4)_3$ Family. *Nanosyst. Physics, Chem. Math.*, 2023, **14**, P. 112–119.

[21] Pansambal S., Oza R., Borgave S., Chauhan A., Bardapurkar P., Vyas S., Suresh G. Bioengineered Cerium Oxide (CeO_2) Nanoparticles and Their Diverse Applications: A Review. *Appl. Nanosci.*, 2023, **13**, P. 6067–6092.

[22] Nag S., Mitra O. P, S., Bhattacharjee A., Mohanto S., Gowda B.H.J., Kar S., Ramaiah S., Anbarasu A., Ahmed M.G. Exploring the Emerging Trends in the Synthesis and Theranostic Paradigms of Cerium Oxide Nanoparticles (CeONPs): A Comprehensive Review. *Mater. Today Chem.*, 2024, **35**, P. 101894.

[23] Lord M.S., Berret J.F., Singh S., Vinu A., Karakoti A.S. Redox Active Cerium Oxide Nanoparticles: Current Status and Burning Issues. *Small*, 2021, **17**, P. 2102342.

[24] Kozlova T.O., Popov A.L., Kolesnik I. V., Kolmanovich D.D., Baranchikov A.E., Shcherbakov A.B., Ivanov V.K. Amorphous and Crystalline Cerium(IV) Phosphates: Biocompatible ROS-Scavenging Sunscreens. *J. Mater. Chem. B*, 2022, **10**, P. 1775–1785.

[25] Kozlova T.O., Sheichenko E.D., Vasilyeva D.N., Kozlov D.A., Kolesnik I.V., Tronev I.V, Teplonogova M.A., Baranchikov A.E., Ivanov V.K. Ultrasonic-Assisted Hydrothermal Synthesis of Nanoscale Double Ceric Phosphates. *Nanosyst. Physics, Chem. Math.*, 2024, **15**, P. 215–223.

[26] Lutterotti L. Total pattern fitting for the combined size-strain-stress-texture determination in thin film diffraction. *Nucl. Instrum. Methods Phys. Res. B*, 2010, **268**, P. 334–340.

[27] Popa, N.C. The (hkl) Dependence of Diffraction-Line Broadening Caused by Strain and Size for all Laue Groups in Rietveld Refinement. *J. Appl. Crystallogr*, 1998, **31**, P. 176–180.

[28] Alekseev A.V., Proskurnina E.V., Vladimirov Y.A. Determination of Antioxidants by Sensitized Chemiluminescence Using 2,2'-Azo-Bis(2-Amidinopropane). *Moscow Univ. Chem. Bull.*, 2012, **67**, P. 127–132.

[29] Sidey V. On the Effective Ionic Radii for Ammonium. *Acta Crystallogr. Sect. B Struct. Sci. Cryst. Eng. Mater.*, 2016, **72**, P. 626–633.

[30] Shannon R.D., Prewitt C.T. Effective Ionic Radii in Oxides and Fluorides. *Acta Crystallogr. Sect. B Struct. Crystallogr. Cryst. Chem.*, 1969, **25**, P. 925–946.

[31] Vladimirov G.K., Sergunova E. V., Izmaylov D.Y., Vladimirov Y.A. Chemiluminescent Determination of Total Antioxidant Capacity in Medicinal Plant Material. *Bull. Russ. State Med. Univ.*, 2016, P. 62–68.

[32] Lee S.S., Song W., Cho M., Puppala H.L., Nguyen P., Zhu H., Segatori L., Colvin V.L. Antioxidant Properties of Cerium Oxide Nanocrystals as a Function of Nanocrystal Diameter and Surface Coating. *ACS Nano*, 2013, **7**, P. 9693–9703.

[33] Ghosalya M.K., Li X., Beck A., van Bokhoven J.A., Artiglia L. Size of Ceria Particles Influences Surface Hydroxylation and Hydroxyl Stability. *J. Phys. Chem. C.*, 2021, **125**, P. 9303–9309.

[34] Römer I., Briffa S.M., Arroyo Rojas Dasilva Y., Hapiuk D., Trouillet V., Palmer R.E., Valsami-Jones E. Impact of Particle Size, Oxidation State and Capping Agent of Different Cerium Dioxide Nanoparticles on the Phosphate-Induced Transformations at Different PH and Concentration. *PLoS One*, 2019, **14**, P. e0217483.

[35] Listova A.L., Kuzenkova A.S., Gerasimov M.A., Kulikova E.S., Svetogorov R.D., Novichkov D.A., Averin A.A., Yapaskurt V.O., Romanchuk A.Y., Kalmykov S.N., Plakhova T.V. Comprehensive Dissolution Study on Two Double Ce(IV) Phosphates with Evidence of Secondary CeO_2 Nanoparticle Formation. *Molecules*, 2025, **30**, P. 2105.

[36] Ta K.M., Neal C.J. Coathup M.J., Seal S., Phillips R.M., Molinari M. The Interaction of Phosphate Species with Cerium Oxide: The Known, the Ambiguous and the Unexplained. *Biomater. Adv.*, 2025, **166**, P. 214063.

[37] Singh S., Dosani T., Karakoti A.S., Kumar A., Seal S., Self W.T. A Phosphate-Dependent Shift in Redox State of Cerium Oxide Nanoparticles and Its Effects on Catalytic Properties. *Biomaterials*, 2011, **32**, P. 6745–6753.

[38] Singh R., Singh S. Role of Phosphate on Stability and Catalase Mimetic Activity of Cerium Oxide Nanoparticles. *Colloids Surfaces B Biointerfaces*, 2015, **132**, P. 78–84.

[39] Sozarukova M.M., Proskurnina E.V, Ivanov V.K. Prooxidant Potential of CeO_2 Nanoparticles towards Hydrogen Peroxide. *Nanosyst. Physics, Chem. Math.*, 2021, **12**, P. 283–290.

[40] Sozarukova M.M., Kozlova T.O., Beshkareva T.S., Popov A.L., Kolmanovich D.D., Vinnik D.A., Ivanova O.S., Lukashin A. V., Baranchikov A.E., Ivanov V.K. Gadolinium Doping Modulates the Enzyme-like Activity and Radical-Scavenging Properties of CeO_2 Nanoparticles. *Nanomaterials*, 2024, **14**, 769.

[41] Xu C., Qu X. Cerium Oxide Nanoparticle: A Remarkably Versatile Rare Earth Nanomaterial for Biological Applications. *NPG Asia Mater.*, 2014, **6**, P. e90.

[42] Joubert El., Winterton P., Britz T.J., Gelderblom W.C.A. Antioxidant and Pro-Oxidant Activities of Aqueous Extracts and Crude Polyphenolic Fractions of Rooibos (Aspalathus Linearis). *J. Agric. Food Chem.*, 2005, **53**, P. 10260–10267.

[43] Nowak M., Tryniszewski W., Sarniak A., Wlodarczyk A., Nowak P.J., Nowak D. Concentration Dependence of Anti- and Pro-Oxidant Activity of Polyphenols as Evaluated with a Light-Emitting Fe^{2+}-Egta-H_2O_2 System. *Molecules*, 2022, **27**, P. 3453.

[44] Stoeva S., Hvarchanova N., Georgiev K.D., Radeva-Ilieva, M. Green Tea: Antioxidant vs. Pro-Oxidant Activity. *Beverages*, 2025, **11**, P. 64.

[45] Hoard J.L., Blair V. The Crystal Structures of Rubidium and Ammonium Fluoborates. *J. Am. Chem. Soc.*, 1935, **57**, P. 1985–1988.

[46] Aydin F., Zhan C., Ritt C., Epsztein R., Elimelech M., Schwegler E., Pham T.A. Similarities and Differences between Potassium and Ammonium Ions in Liquid Water: A First-Principles Study. *Phys. Chem. Chem. Phys.*, 2020, **22**, P. 2540–2548.

[47] Yang G., Gong P., Lin Z., Ye N. $AZn_2BO_3X_2$ (A = K, Rb, NH_4; X = Cl, Br): New Members of KBBF Family Exhibiting Large SHG Response and the Enhancement of Layer Interaction by Modified Structures. *Chem. Mater.*, 2016, **28**, P. 9122–9131.

[48] Johnson D.A. Thermochemistry of Ammonium and Rubidium Perrhenates, and the Effect of Hydrogen Bonding on the Solubilities of Ammonium Salts. *J. Chem. Soc. Dalt. Trans.*, 1990, P. 3301–3304.

[49] Castañeda-Arriaga R., Pérez-Gonzalez A., Reina M., Alvarez-Idaboy J.R., Galano A. Comprehensive Investigation on the Antioxidant and Pro-Oxidant Effects of Phenolic Compounds: A Double-Edged Sword in the Context of Oxidative Stress? *J. Phys. Chem. B*, 2018, **122**, P. 6198–6214.

[50] Samrot A.V., Singh S.P.R., Deenadhayalan R., Rajesh V.V., Padmanaban S., Radhakrishnan K.K. Nanoparticles, a Double-Edged Sword with Oxidant as Well as Antioxidant Properties – A Review. *Oxygen*, 2022, **2**, P. 591–604.

Submitted 17 February 2026; revised 31 March 2026; accepted 1 April 2026

Information about the authors:

Taisiya O. Kozlova – Kurnakov Institute of General and Inorganic Chemistry of the Russian Academy of Sciences, Leninsky prospect, 31, Moscow, 119991, Russia; ORCID 0000-0002-9757-9148; taisiya@igic.ras.ru

Madina M. Sozarukova – Kurnakov Institute of General and Inorganic Chemistry of the Russian Academy of Sciences, Leninsky prospect, 31, Moscow, 119991, Russia; ORCID 0000-0002-5868-4746; s_madinam@bk.ru

Daniil A. Kozlov – Kurnakov Institute of General and Inorganic Chemistry of the Russian Academy of Sciences, Leninsky prospect, 31, Moscow, 119991, Russia; ORCID 0000-0003-0620-8016; kozlov@igic.ras.ru

Ekaterina D. Sheichenko – Kurnakov Institute of General and Inorganic Chemistry of the Russian Academy of Sciences, Leninsky prospect, 31, Moscow, 119991, Russia; HSE University, Moscow, Myasnitskaya str., 20, 101000, Russia; ORCID 0000-0003-3485-1842; edsheychenko@edu.hse.ru

Anzhelika O. Bedarkova – Kurnakov Institute of General and Inorganic Chemistry of the Russian Academy of Sciences, Leninsky prospect, 31, Moscow, 119991, Russia; ORCID 0000-0003-4346-5644; a.bedarkova@igic.ras.ru

Darya N. Vasilyeva – Kurnakov Institute of General and Inorganic Chemistry of the Russian Academy of Sciences, Leninsky prospect, 31, Moscow, 119991, Russia; HSE University, Moscow, Myasnitskaya str., 20, 101000, Russia; ORCID 0009-0004-3560-4178; dnvasileva_1@edu.hse.ru

Alexander E. Baranchikov – Kurnakov Institute of General and Inorganic Chemistry of the Russian Academy of Sciences, Leninsky prospect, 31, Moscow, 119991, Russia; ORCID 0000-0002-2378-7446; a.baranchikov@yandex.ru

Vladimir K. Ivanov – Kurnakov Institute of General and Inorganic Chemistry of the Russian Academy of Sciences, Leninsky prospect, 31, Moscow, 119991, Russia; ORCID 0000-0003-2343-2140; van@igic.ras.ru

Conflict of interest: the authors declare no conflict of interest.

Paper abstracts in Russian / Аннотации статей

Двухфермионные решёточные операторы Шрёдингера с взаимодействиями между ближайшими и вторыми ближайшими узлами

Лакаев С.Н., Абдухакимов С.Х., Хасанов А.Б.

Мы исследуем операторы Шрёдингера $H_{\lambda\mu}(K)$, ассоциированные с двухфермионной системой на трёхмерной решётке T^3 при фиксированном полном квазиимпульсе $K \in T^3$, где частицы взаимодействуют посредством связей с ближайшими и вторыми ближайшими узлами с константами взаимодействия $\lambda, \mu \in \mathbb{R}$. Для случая $K = 0$ установлено, что оператор $H_{\lambda\mu}(0)$ допускает приведённое инвариантное подпространство, ограничение на которое зависит только от параметра $\mu \in \mathbb{R}$. Показано, что μ-параметрическая прямая содержит две критические точки, соответствующие нижнему и верхнему порогам спектра; в каждой из этих точек определитель Фредгольма приведённого оператора обращается в нуль. Каждая из критических точек разбивает параметрическую прямую на два бесконечных интервала, на которых число собственных значений, расположенных ниже (соответственно, выше) существенного спектра, остаётся постоянным. В зависимости от значения параметра μ соответствующий приведённый оператор имеет ровно одно дискретное собственное значение, расположенное либо ниже нижней границы, либо выше верхней границы существенного спектра. Кроме того, получена нижняя оценка на число дискретных собственных значений оператора $H_{\lambda\mu}(K)$ для всех $K \in T^3$.

Ключевые слова: двухфермионная система; решёточный оператор Шрёдингера; дискретные собственные значения; существенный спектр; приведённое инвариантное подпространство.

Слабо периодическая мера и фазовый переход: q-состояния и p-адическая модель Поттса на дереве Кэли порядка k

Тухтабаев А.М.

В данной работе исследуются слабо периодические p-адические квазигиббсовские меры для модели Поттса с q состояниями на дереве Кэли порядка k. Кроме того, продемонстрировано, что для всех q, не меньших 3, и k, не меньших 2, существуют такое простое число p и параметр, которые гарантируют возникновение фазового перехода.

Ключевые слова: p-адические числа; модель Поттса; p-адическая квазигиббсовская мера; трансляционно-инвариантные, периодические, слабо периодические меры Гиббса; фазовый переход.

Результаты анализа колебаний для дифференциального уравнения второго порядка с запаздыванием и несколькими отклоняющимися аргументами

Анбарасу П., Сактивел Р.

Исследуется колебательное поведение всех решений дифференциального уравнения второго порядка с запаздыванием, имеющего несколько отклоняющихся аргументов и неотрицательных коэффициентов. Получены некоторые достаточные условия для колебаний. Приведен также пример, иллюстрирующий значимость наших основных результатов.

Ключевые слова: второй порядок; немонотонные аргументы; уравнения с запаздыванием; колебательное решение

Задача Коши для уравнения четвертого порядка с дробной производной в смысле Капуто

Иргашев Б.Ю.

В данной статье исследуется задача Коши в полуплоскости для неоднородного уравнения четвертого порядка с дробной производной в смысле Капуто. Единственность решения показывается с помощью преобразования Лапласа. При построении решения сначала находятся частные решения, выраженные через функции Райта. Затем с помощью этих частных решений строятся функции Грина. Решение строится в явном виде с использованием функции Грина. Также получен явный вид фундаментального решения.

Ключевые слова: уравнение четвертого порядка, задача Коши, производная Капуто, функция Райта, асимптотика, фундаментальное решение, существование, единственность.

Критическое отношение масс и фазовый переход в трёхчастичных решёточных системах: сравнение бозонного и фермионного случаев

Абдуллаев Д.И., Эшниязов А.И., Долгополов М.В.

Мы изучаем трёхчастичные операторы Шрёдингера на двумерной решётке $\mathbb{Z}^2$ и показываем, что критическое отношение масс $\gamma_c \approx 2.75194$ определяет существование связанного тримера в фермионной 2+1 конфигурации (два тождественных фермиона и третья частица). При $\gamma < \gamma_c$ имеется топологическое запрещение (подавление Паули) трёхчастичного связанного состояния, тогда как при $\gamma > \gamma_c$ возникает дважды вырожденное собственное значение ниже существенного спектра с асимптотикой сильной связи $z(\gamma, \lambda) = -\lambda + e_0(\gamma) + O(\lambda^{-1})$. В рамках единого подхода, основанного на принципе Бирмана–Швингера и асимптотическом анализе в режиме сильной связи, мы сравниваем это поведение с бозонным случаем трёх тождественных частиц, где два связанных состояния существуют ниже существенного спектра и энергия основного состояния удовлетворяет $z_1^s(\mu) = -3\mu + C_2 + O(\mu^{-1})$. Возникающий фазовый переход второго рода по отношению масс γ важен для планирования экспериментов по фермионным тримерам в оптических решётках и для моделирования экситонных комплексов и дефектно-связанных состояний в двумерных наноматериалах, где критическое значение γ_c служит ориентиром для наблюдаемости трёхчастичных связанных состояний. Мы также намечаем модифицированную трёхчастичную решёточную модель с двумя конкурирующими каналами взаимодействия, для которой анализ Бирмана–Швингера естественным образом приводит к сценарию Ландау фазового перехода первого рода в пространстве тримерных связанных состояний. В бозонном случае мы доказываем теорему о сильной связи, описывающую существование и асимптотику тримерных связанных состояний, а в фермионном 2+1 случае устанавливаем теорему о спектральном фазовом переходе, которая даёт явное критическое отношение масс γ_c, разделяющее тримерный и бестримерный режимы.

Ключевые слова: трёхчастичный оператор Шрёдингера, решёточные системы, связанные состояния, бозоны, фермионы, критическое отношение масс, фазовый переход, принцип Бирмана–

Швингера.

Как вновь заставить хранить инверсное состояние

Кузьмичев Д.С., Константинов В.С., Сизых Н.А., Хакимов Р.Р.

В настоящей статье показана возможность увеличить время хранения инверсного состояния OS с 140 до 500 мин при 145 °C в сегнетоэлектрических конденсаторах на основе $Hf_{0.5}Zr_{0.5}O_2$ (HZO) путем сдвига вправо конечной точки интегрирования тока. Учет переходных процессов между управляющими импульсами после отжига в течение 500 мин при температуре 145 °C позволяет повысить сохраняемость состояния OS с 21 % до 35 % от начального значения. Противоположная тенденция выявлена для состояний SS (снижение с 56 % до 35 %) и NSS (снижение с 63 % до 45 %). Также показано, что наличие сдвига напряжения, вызванного эффектом импринта, в некоторых случаях может и не приводить деградации поляризации благодаря току, который протекает на полке максимального напряжения управляющего импульса.

Ключевые слова: TiN/HZO/TiN, сохраняемость, импринт, сегнетоэлектрик.

Дисперсионный анализ и регулируемые магнитные свойства двуосного гиперболического метаматериала на основе гетероструктур n-GaAs/AlGaAs

Нгуен Фам Куинь Ань

В данном исследовании представлены проектирование и теоретический анализ перестраиваемого двуосного гиперболического метаматериала (БГММ), построенного из слоистой гетероструктуры n-GaAs/AlGaAs под воздействием внешнего магнитного поля. Цель состоит в оптимизации перестраиваемости для управления формой дисперсии в терагерцовом (ТГц) диапазоне частот. Используется модель приближения эффективной среды (ПЭС), демонстрирующая сосуществование двух волновых мод, а именно замкнутой эллипсоидальной и открытой гиперболоидальной изочастотной поверхности. Результаты показывают, что внешнее магнитное поле действует как мощный механизм настройки, позволяющий осуществлять спектральный сдвиг дисперсии и активное переключение между гиперболическими режимами типа I и типа II. Кроме того, анализируются условия, необходимые для достижения экстремального сжатия изочастотной поверхности (ИЗП), что имеет важное значение для управления направлением луча. Это сжатие происходит, когда одна из компонент диэлектрической проницаемости достигает чрезвычайно больших значений, что приводит к образованию почти плоских сегментов на изочастотной поверхности.

Ключевые слова: двухосный гиперболический метаматериал, терагерцовый частотный диапазон, гиперболоидальная изочастотная поверхность, приближение эффективной среды.

Лазерная корреляционная спектроскопия нанодисперсных растворов в области перехода к многократному рассеянию света

Плешаков И.В., Соловьев А.В., Алексеев А.А., Фофанов Я.А.

В работе рассматривается применение лазерной корреляционной спектроскопии к исследованию дисперсных систем для такого случая, который можно рассматривать как переходный к режиму многократного рассеяния. Показано, что даже незначительное нарушение условия од-

нократного рассеяния за счет увеличения концентрации рассеивающих центров может привести к эффекту, который изменит результат измерения размера частиц. Это следует учитывать при изучении коллоидов.

Ключевые слова: лазерная корреляционная спектроскопия, многократное светорассеяние, наночастицы.

Упругие и механические свойства сплавов на основе Ti–Nb–Zr

Бакулин А.В., Кулькова С.Е.

Упругие свойства и механические характеристики сплавов на основе $Ti–Nb_{22}–Zr_6$ были рассчитаны методом точных маффин-тин орбиталей в приближении когерентного потенциала. Рассматривалось легирование металлами, такими как Hf, Mg и их комбинациями, при этом их концентрация не превышала 5 ат.%. Было показано, что добавление Hf и Mg приводит к понижению модуля Юнга как из-за размерного эффекта, так и из-за электронного фактора. Рассчитанный модуль Юнга для тройного сплава $Ti–Nb_{22}–Zr_6$ (70.1 ГПа) хорошо согласуется с экспериментальным значением (70 ГПа). Наименьшее значение модуля Юнга было рассчитано для сплава $Ti–Nb_{22}–Zr_6–Hf_5–Mg_{2.5}$, достигая 57 ГПа. Дальнейшее увеличение концентрации Mg приводит к отрицательному значению *C'* и дестабилизации сплава. Кроме того, легирование сплава $Ti–Nb_{22}–Zr_6$ приводит к снижению твердости и трещиностойкости, но при этом повышается индекс хрупкости.

Ключевые слова: сплавы титана, упругие модули, механические свойства, *ab-initio* расчеты

Роль дегидратации-гидратации в формировании наночастиц со структурой хризотила при гидротермальной обработке систем $Mg_{1-x}Ni_x(OH)_2$–SiO_2–$H_2O(NaOH)$

Альмяшева О.В., Кургузкина М.Е., Гусаров В.В.

Термодинамический анализ трансформаций гидроксидов в системе $Mg_{1-x}Ni_x(OH)_2–SiO_2–H_2O$ при гидротермальном синтезе нанотубулярных частиц со структурой хризотила показал решающую роль процессов их дегидратации и повторного образования гидроксидов в ходе гидротермальной обработки реагентов на состав и морфологические параметры целевого продукта. В зависимости от состава гидроксидного реагента и *T–P*-условий в реакционной среде зоне выделены три области, в которых резко изменяется механизм формирования нанотубулярных частиц со структурой хризотила, что и является непосредственной причиной немонотонной зависимости Mg/Ni соотношения и размерных параметров нанотрубок $(Mg_{1-x}Ni_x)_3Si_2O_5(OH)_4$ от Mg/Ni соотношения в исходном гидроксиде.

Ключевые слова: твёрдых растворы, гидроксиды, оксиды, хризотил, нанотрубки, гидротермальный синтез, термодинамические расчёты

Влияние условий синтеза порошка $Gd_2Zr_2O_7$ на свойства керамики на его основе, полученной методом электроискрового спекания

Виноградов В.Ю., Дудина Д.В., Есиков М.А., Щербина О.Б., Ефремов В.В., Калинкин А.М.

В работе впервые проведено сравнительное исследование микроструктуры и механических свойств керамики цирконата гадолиния, полученной методом электроискрового спекания из гидроксидных прекурсоров, синтезированных без и с использованием механоактивации. Исходный прекурсор был получен методом обратного соосаждения гидроксидов. Механоактивация (МА) прекурсора проводилась в планетарной мельнице АГО-2 при центробежном факторе 20 g в течение 30 мин. С помощью рентгенофазового анализа показано, что керамика является нанокристаллической. Механические свойства (микротвердость и модуль Юнга) керамики, полученной на основе механоактивированного прекурсора, превосходят аналогичные показатели керамики на основе исходного прекурсора.

Ключевые слова: цирконат гадолиния, керамика, механоактивация, прекурсор, электроискровое спекание

Редокс поведение наноразмерных двойных ортофосфатов церия(IV) состава $ACe_2(PO_4)_3$ ($A = NH_4^+, K^+, Rb^+$)

Козлова Т.О., Созарукова М.М., Козлов Д.А., Шейченко Е.Д., Бедарькова А.О., Васильева Д.Н., Баранчиков А.Е., Иванов В.К.

Проведено сравнительное исследование окислительно-восстановительного поведения нанокристаллических изоструктурных двойных ортофосфатов церия(IV) состава $ACe_2(PO_4)_3$ ($A = NH_4^+$, K^+, Rb^+). Установлено, что по отношению к алкилпероксильным радикалам или пероксиду водорода в качестве активных форм кислорода все двойные фосфаты церия(IV) действовали как антиоксиданты или прооксиданты, соответственно. Антиоксидантная активность по отношению к алкилпероксильным радикалам оказалась выше у фосфатов, содержащих калий или рубидий. Примечательно, что для $KCe_2(PO_4)_3$ и $RbCe_2(PO_4)_3$ была обнаружена обратная зависимость каталитической активности от концентрации в реакции с H_2O_2, в отличие от $NH_4Ce_2(PO_4)_3$. Окислительно-восстановительное поведение наноразмерного диоксида церия, использованного для сравнения, было аналогично поведению ортофосфата церия(IV)-аммония, но значительно ниже в абсолютных значениях. Это было объяснено подавляющим эффектом фосфат-анионов, присутствующих в буферных растворах.

Ключевые слова: радикал-перехватывающая способность, прооксидантная активность, хемилюминесценция, изоструктурность.

NANOSYSTEMS:
PHYSICS, CHEMISTRY, MATHEMATICS

INFORMATION FOR AUTHORS

The journal publishes research articles and reviews, and also short scientific papers (letters) which are unpublished and have not been accepted for publication in other magazines. Articles should be submitted in English. All articles are reviewed, then if necessary come back to the author to completion.

The journal is indexed in Web of Science Core Collection (Emerging Sources Citation Index), Chemical Abstract Service of the American Chemical Society, Zentralblatt MATH and in Russian Scientific Citation Index.

Author should submit the following materials:

1. Article file in English, containing article title, the initials and the surname of the authors, Institute (University), postal address, the electronic address, the summary, keywords, MSC or PACS index, article text, the list of references.
2. Files with illustrations, files with tables.
3. The covering letter in English containing the article information (article name, MSC or PACS index, keywords, the summary, the literature) and about all authors (the surname, names, the full name of places of work, the mailing address with the postal code, contact phone number with a city code, the electronic address).
4. The expert judgement on possibility of publication of the article in open press (for authors from Russia).

Authors can submit a paper and the corresponding files to the following addresses:
nanojournal.ifmo@gmail.com, popov1955@gmail.com.

Text requirements

Articles should be prepared with using of text editors MS Word or LaTeX (preferable). It is necessary to submit source file (LaTeX) and a pdf copy. In the name of files the English alphabet is used. The recommended size of short communications (letters) is 4–6 pages, research articles – 6–15 pages, reviews – 30 pages.

Recommendations for text in MS Word:

Formulas should be written using Math Type. Figures and tables with captions should be inserted in the text. Additionally, authors present separate files for all figures and Word files of tables.

Recommendations for text in LaTeX:

Please, use standard LaTeX without macros and additional style files. The list of references should be included in the main LaTeX file. Source LaTeX file of the paper with the corresponding pdf file and files of figures should be submitted.

References in the article text are given in square brackets. The list of references should be prepared in accordance with the following samples:

1. Surname N. *Book Title*. Nauka Publishing House, Saint Petersburg, 2000, 281 pp.
2. Surname N., Surname N. Paper title. *Journal Name*, 2010, **1** (5), P. 17–23.
3. Surname N., Surname N. Lecture title. In: Abstracts/Proceedings of the Conference, Place and Date, 2000, P. 17–23.
4. Surname N., Surname N. Paper title, 2000, URL: http://books.ifmo.ru/ntv.
5. Surname N., Surname N. Patent Name. Patent No. 11111, 2010, Bul. No. 33, 5 pp.
6. Surname N., Surname N. Thesis Title. Thesis for full doctor degree in math. and physics, Saint Petersburg, 2000, 105 pp.

Requirements to illustrations

Illustrations should be submitted as separate black-and-white files. Formats of files – jpeg, png, eps, tiff.